ISTANBUL TECHNICAL UNIVERSITY ★ GRADUATE SCHOOL

THE SPATIO-TEMPORAL DYNAMICS OF AEROSOLS IN THE MARMARA REGION AND IMPACT OF LAND COVER/USE ON ATMOSPHERIC ENVIRONMENT

Ph.D. THESIS

Paria ETTEHADI OSGOUEI

Department of Communication Systems

Satellite communication and Remote Sensing Programme

JUNE 2023

ISTANBUL TECHNICAL UNIVERSITY ★ GRADUATE SCHOOL

THE SPATIO-TEMPORAL DYNAMICS OF AEROSOLS IN THE MARMARA REGION AND IMPACT OF LAND COVER/USE ON ATMOSPHERIC ENVIRONMENT

Ph.D. THESIS

Paria ETTEHADI OSGOUEI
(705152002)

Department of Communication Systems

Satellite Communication and Remote Sensing Programme

Thesis Advisor: Prof. Dr. Şinasi KAYA

JUNE 2023

ISTANBUL TEKNİK ÜNİVERSİTESİ ★ LİSANSÜSTÜ EĞİTİM ENSTİTÜSÜ

MARMARA BÖLGESİNDEKİ AEROSOLLERİN MEKANSAL-ZAMANSAL DİNAMİKLERİ VE ARAZİ ÖRTÜSÜ/KULLANIMININ ATMOSFERİK ORTAM ÜZERİNDEKİ ETKİSİ

DOKTORA TEZİ

Paria ETTEHADI OSGOUEI
(705152002)

İletişim Sistemleri Anabilim Dalı

Uydu Haberleşme ve Uzaktan Algılama Programı

Tez Danışmanı: Prof. Dr. Şinasi KAYA

HAZİRAN 2023

Paria ETTEHADI OSGOUEI, a Ph.D. student of ITU Graduate School student ID 705152002, successfully defended the thesis/dissertation entitled “THE SPATIO-TEMPORAL DYNAMICS OF AEROSOLS IN THE MARMARA REGION AND IMPACT OF LAND COVER/USE ON ATMOSPHERIC ENVIRONMENT”, which she prepared after fulfilling the requirements specified in the associated legislations, before the jury whose signatures are below.

Thesis Advisor : **Prof. Dr. Şinasi KAYA** ....
İstanbul Technical University

Jury Members : **Prof. Dr. Elif SERTEL** ....
Istanbul Technical University

Prof. Dr. Cem GAZİOĞLU ....
Istanbul University

Prof. Dr. Nebiye MUSAOĞLU ....
Istanbul Technical University

Prof. Dr. Füsun BALIK ŞANLI ....
Yildiz Technical University

Date of Submission : 26 May 2023
Date of Defense : 16 June 2023

To my beloved Mom and Dad,

FOREWORD

It is with great pleasure and gratitude that I present this thesis, which represents the culmination of years of hard work, research, and dedication. As I reflect on the journey that has led me to this moment, I am reminded of the many people who have supported and encouraged me along the way.

First and foremost, I would also like to extend my gratitude to my parents, who have been my constant source of inspiration and motivation throughout my academic journey. Their unwavering support, encouragement, and belief in me have been instrumental in shaping who I am today. I am deeply grateful for their sacrifices and their unwavering love.

I would like to express my heartfelt thanks to my supervisor, Prof. Dr. Şinasi KAYA. Without his guidance and unwavering support, this thesis would not have been possible. His invaluable feedback and encouragement have helped shape my research.

Last but not least, I would like to thank my husband, Sepehr FIROUZI, for his unwavering love and support throughout this stressful journey. His patience, encouragement, and unwavering belief in me have been the driving force behind my success. Without his support, I would not have been able to navigate the challenges and obstacles that come with pursuing an advanced degree.

I am humbled and grateful to have had the support of such incredible individuals who have helped me reach this point. Their support, encouragement, and belief in me have been instrumental in shaping me into the scholar I am today. I hope this thesis will serve as a fitting tribute to their unwavering support and belief in me.

May 2023

Paria ETTEHADI OSGOUEI
(Remote Sensing Specialist)

TABLE OF CONTENTS

Page

ABBREVIATIONS

AAE : Absorption AE
AAE : Absorption Ångström Exponent
AE : Ångström Exponent
AERONET : AErosol RObotic NETwork
AQM : Air Quality Monitoring
ATSR-2 : Along Track Scanning Radiometer-2
AVHRR : Advanced Very-High-Resolution Radiometer
CART : Regression tree
CHIRPS : Climate Hazards Group InfraRed Precipitation with Station data
CLC : CORINE Land Cover
CO : Carbon monoxide
CORINE : Coordination of Information on the Environment
COVID-19 : COronaVIrus Disease of 2019
DB : Deep Blue
DJF : December-January-February
DT : Dark Target
EAE : Extinction AE
EEFIS : European Forest Fire Information System
EPDK : Enerji Piyasası Düzenleme Kurumu
FMF : Fine Mode Fraction
HQ : High-Quality
IMS-METU : Institute of Marine Sciences-Middle East Technical University
JJA : June-July-August
LCU : Land Cover/Use
MAIAC : Multi-Angle Implementation of Atmospheric Correction
MAM : March-April-May
MB : Mean Bias
MERIT: : Multi-Error-Removed Improved-Terrain
MNDWI : Modified Normalized Difference Water Index
MODIS : Moderate Resolution Imaging Spectroradiometer
NDTI : Normalized Difference Tillage Index
NDVIre : red-edge-based Normalized Difference Vegetation Index
NIR : Near-Infrared
NN : Neural Network
NO_2 : Nitrogen dioxide
O_3 : Ozone
PLDR : Particle linear depolarization ratio
PM : Particulate Matter
POLDER : POLarization and Directionality of the Earth's Reflectances
PW : Precipitable Water
QA : Quality Assurance

QF : Quality Flag
RF : Random Forest
RH : Relative Humidity
RMSE : Root-Mean-Squared Errors
ROI : Region of interest
SAR : Synthetic aperture radar (SAR)
SN : Sinusoidal
S-NPP : Suomi National Polar-orbiting Partnership
SO_2 : Sulfur dioxide
SOA : Secondary organic aerosol
SOAR : Satellite Ocean Aerosol Retrieval
SON : September-October-November
SRC : Spectral Regression Coefficient
SSA : Single-Scattering Albedo
SVM : Support Vector Machine
SWIR : **S**hortwave Infrared
T : Temperature
TEOM : Tapered_Element Oscillating Microbalance
THEP : Temız Hava Eylem Planı
TOA : **T**op-of-the-atmosphere
TOM : Total Ozone Mapping Spectrometer
TUIK : Türkiye Istatistik Kurumu
VIIRS : Visible Infrared Imaging Radiometer Suite
VOC : volatile organic compounds
WD : Wind Direction
WHO : World Health Organization
WS : Wind Speed

LIST OF TABLES

Page

LIST OF FIGURES

Page

THE SPATIO-TEMPORAL DYNAMICS OF AEROSOLS IN THE MARMARA REGION AND IMPACT OF LAND COVER/USE ON ATMOSPHERIC ENVIRONMENT

SUMMARY

The impacts of urbanization and industrialization on air quality are well known, and air pollution control strategies have been implemented, but the effectiveness of these strategies is limited to developed countries. Developing countries continue to rely on fossil fuels and experience air pollution from agriculture emissions, crop residue burning, biomass fuel, and low-quality coal combustion. Air pollution contributes to health, visibility, ecosystems, and climate change. Solid air pollutants, also known as particulate matter (PM) consist of tiny particles suspended in the air has the most severe health impacts. Governments need to measure, monitor, and control the concentration of air pollutants and maintain the pollution levels under the values defined by the World Health Organization (WHO). There have been some efforts to reduce air pollution in developing countries. However, there is still a long way to go in terms of clean air in many developing countries.

The data collected from air quality monitoring (AQM) stations are commonly used to study the impacts of air pollution on human health. However, the initial investment and maintenance of ground-based AQM stations are expensive. The limited quantity of air quality monitoring stations on the ground poses a hindrance to conducting thorough research into the effects of elevated levels of air pollution on the environment. Measurements from earth-observing satellites can be a useful substitute for ground-based data in environmental studies. Although ground-based data are often more detailed and accurate, satellite data provide a broader view of larger spatial extents. The advantages of satellite data collection over a lengthy period allow for long-term monitoring of environmental trends and changes.

Aerosols, tiny particles that are suspended in the Earth's atmosphere can be of natural or human-made origin. The impact of atmospheric aerosol loading on various aspects of the Earth's climate and environment cannot be overstated. Besides its adverse effect on human health, it affects global temperature, atmospheric radiation, the Earth's albedo, and terrestrial heat budget, as well as clouds and precipitation processes, and ecological systems. Therefore, understanding atmospheric aerosols is essential for comprehending Earth's climate and ecosystem. The columnar aerosol pollution or the number of microscopic aerosol particles in a vertical slice of the atmosphere can be measured by satellite sensors. The main remotely sensed geophysical quantity and column-effective particle property is total column aerosol optical depth (AOD). The AOD is a measure of how much sunlight is absorbed or scattered by aerosol particles in the atmosphere, and it provides information on the concentration and distribution of atmospheric aerosols. The concentrations of PM and AOD are important measures of air pollution. They represent the amount of particulate matter present in the air and are strongly correlated with each other. While ground-based air pollutant concentration

records show the concentration of pollutants near the Earth`s surface, satellite-based and ground-measured AOD data provide a measure of the total column amount of aerosols from the Earth's surface up to the top of the atmosphere. Satellite-based AOD measurements can identify hotspots of particle pollution and short-term spikes, which can then be targeted for more detailed ground-based measurements of air pollution.

Space-based remote sensing plays a vital role in characterizing the spatial and temporal distributions of atmospheric aerosols from the local to global scale. The popularity of satellite aerosol products has led to the development of various aerosol retrieval algorithms. To ensure the accuracy of satellite aerosol data in interpreting regional and global aerosol patterns, it's crucial to evaluate the performance of the retrieval algorithms. Validation using accurate ground-based AOD measurements is employed for this purpose. AErosol RObotic NETwork (AERONET) program is a federation of ground-based remote sensing aerosol networks, a vital worldwide network for monitoring aerosols that employ numerous sun-photometers stationed across the globe to measure various aerosol optical and microphysical characteristics, such as AOD. It's important to note that the efficacy of satellite aerosol products may vary depending on factors such as geography, climate, and weather conditions. Thus, it's essential to identify the most reliable algorithm by validating satellite AOD retrievals against the nearest ground-based data to the region of interest.

The primary aim of this research is to better understand the behavior of aerosols in the atmosphere and gain insight into the spatial distribution and temporal variability of aerosols in the region, as well as to identify the factors that influence the magnitude of AOD and its correlation with land cover/use (LCU). This understanding will aid in devising an efficient strategy to manage environmental air pollution. Furthermore, by gathering, verifying, and analyzing appropriate data through particular techniques, the alterations in aerosol concentrations over a prolonged period will be assessed. For this major objective, the study is divided into three key sections. First, various aerosol products are evaluated for their accuracy and reliability by comparing satellite-derived AODs with AERONET AOD measurements at three different sites. The most effective AOD product were determined by comparing the performances of aerosol data sets. In this context, multiple Moderate Resolution Imaging Spectroradiometer (MODIS) and Visible Infrared Imaging Radiometer Suite (VIIRS) AOD products were compared with AERONET AOD measurements at various surface classes/types (i.e. land, ocean, coastal) in the eastern Mediterranean over five years (2014-2018) and the results were validated. MODIS aerosol products based on Dark Target (DT), Deep Blue (DB), and Multi-Angle Implementation of Atmospheric Correction (MAIAC) are available at different spatial resolutions (1 km, 3 km, and 10 km), while the VIIRS aerosol product has a resolution of 6 km. To obtain VIIRS AOD values, the improved DB approach was used for land and the Satellite Ocean Aerosol Retrieval (SOAR) method for the ocean. The best-performing products over the urban/land surface are the MODIS MAIAC and VIIRS DB aerosol products with Root-Mean-Squared Errors (RMSE) of 0.048-0.061 and a higher percentage (81%-89%) of retrievals falling within the expected error for land. This is while the MODIS MAIAC AOD data also has the advantage that it has a better spatial resolution of 1 km, which enables it to capture sub-grid aerosol features and a higher number of AOD retrievals.

In the second section, I focus on the spatiotemporal variation of MODIS MAIAC AOD over the Marmara region. The objective of this section is to pinpoint areas within a region that have high AOD levels and examine how various environmental factors such as seasonal weather patterns, local emission sources, and LCU are linked to the presence of aerosol pollution in those areas. Our study area was the Marmara region because it is subject to the production of aerosols originating from diverse sources, both natural and anthropogenic. The Marmara Region is the country's most populous region, despite being the second smallest geographically. This is due to Istanbul being located there. The region also contains other important developing cities like Bursa, Kocaeli, and Tekirdag. It is a significant economic center with a lot of agricultural, commercial, and industrial activity. Aerosol formation in the region is influenced by a range of sources, including sea salt, agricultural practices, maritime transport, industrial activities, and the seasonal transportation of dust from the Sahara Desert.

To accomplish the objective of the study's second part, I analyzed the MODIS MAIAC AOD data at annual, monthly, and seasonal scales between 2000 and 2021 to investigate the spatiotemporal variability of AOD in the Marmara region. The monthly mean AOD increases gradually from January to May and fluctuates between May and August and reaches its highest value in August. The monthly mean AOD decreases after August and reaches its lowest monthly mean at the end of the year during December. Seasonal variation in AOD is significant: summer (0.148) > spring (0.136) > autumn (0.116) > winter (0.09). According to an analysis of the AOD's multi-year variation, there were two maxima for the AOD between 2000 and 2010 with values of 0.146 and 0.137 in 2002 and 2008, respectively. AOD exhibits a decreasing tendency from 2000 to 2021, with a 0.005/yearly decline. Using the MODIS MAIAC AOD data at a 1-km scale, I performed a comprehensive assessment of aerosol loading and statistical-visual analyses highlighting the influence of land use/cover on aerosol properties. The findings revealed that there are significant regions with high aerosol concentrations across the region and that these regions show significant temporal variations. The aerosol loading was higher over the western side of the Marmara region (Edirne, Tekirdag, Kırklareli, Canakkale, Istanbul, Kocaeli) until 2011 while the eastern part of the region (Bursa, Sakarya, and Balikesir) was exposed to higher aerosol concentrations after 2016. From 2000 to 2021 the largest number of days with lower aerosol pollution is seen in Bilecik (≈ 35%) while Edirne experienced the highest percentage of days with the highest aerosol pollution level (≈ 9%). In the region, aerosols are mostly generated by urban activities and industries, as well as mineral aerosols originating from soils.

Finally, a novel approach to LCU classification is proposed. The last part of the paper proposes a strategy to identify and distinguish different LCU patterns in Mediterranean cities. The focus was on separating built-up areas from bare land, which can be challenging due to urban landscape complexity and heterogeneity. Separation is also necessary since urbanized/industrialized zones and bare soil areas contribute significantly to atmospheric aerosol pollution. For this purpose, the separation of these two classes was well-addressed by using the proposed multi-index methods on satellite image data. The multi-index combination of the normalized difference tillage index (NDTI), the red-edge-based normalized vegetation index (NDVIre), and the modified normalized difference water index (MNDWI) showed outstanding overall performance with 93% accuracy and a 0.91 kappa value for all LCU classes. The improvement achieved in separating built-up regions from bare land is of substantial significance, as it significantly reduces the misclassification of bare land as built-up regions. This is particularly important for aerosol studies in the study region, where the two factors with the highest impact on aerosol loading are found. The enhanced accuracy of land cover classification provided by this improvement can greatly enhance the reliability and precision of aerosol studies in the area.

MARMARA BÖLGESİNDEKİ AEROSOLLERİN MEKANSAL-ZAMANSAL DİNAMİKLERİ VE ARAZİ ÖRTÜSÜ/KULLANIMININ ATMOSFERİK ORTAM ÜZERİNDEKİ ETKİSİ

ÖZET

Kentleşme ve sanayileşmenin hava kalitesi üzerindeki etkileri bilinmektedir. Gelişmiş ülkelerde hava kirliliği kontrol stratejileri uygulandığı için stratejilerin etkinliği bu ülkelerle sınırlıdır. Gelişmekte olan ülkeler fosil yakıtlara güvenmeye devam etmekte ve tarım emisyonları, mahsul kalıntılarının yakılması ve biyokütle yakıtı ve düşük kaliteli kömür yanmasından kaynaklanan hava kirliliği yaşamaktadır. Hava kirliliği sağlığa, görünürlüğe, ekosistemlere ve iklim değişikliğine neden olmaktadır. Partikül madde (PM) olarak da bilinen katı hava kirleticileri sağlık üzerinde en ciddi olumsuz etkilere sahiptir ve hava kirliliğine maruz kalmak hükümetlerin başta 2,5 mikron ve daha küçük parçacıklar ($PM_{2.5}$) ve 10 mikron ve daha küçük parçacıklar (PM_{10}) olmak üzere hava kirleticilerinin konsantrasyonunu ölçmesi, izlemesi ve kontrol etmesi ve kirlilik seviyelerini dünya sağlık örgütü tarafından tanımlanan değerlerin altında tutması gerekmektedir. Hava kalitesi izleme ağları mevcut olmasına rağmen, Afrika ve Orta Doğu'daki şehirler en kötü etkilenenler olmak üzere, dünya genelinde hava kirliliği düzeyleri birçok ülke ve kentte halen kabul edilen sınırların üzerinde seyretmektedir. 2020'de COVID-19 ile ilgili karantinalar yıllık hava kirletici seviyelerinde önemli bir düşüşe neden olsa bile, hava kirliliği hâlâ dünya'daki en büyük çevresel tehdit olarak kabul edilmektedir.

Hava kalitesi izleme istasyonlarından toplanan veriler, hava kirliliğinin insan sağlığı üzerindeki etkilerini incelemek için yaygın olarak kullanılmaktadır. Hava kalitesi izleme ağları, hava kirliliğinin izlenmesi için gerekli olan kirleticilerin kimyasal bileşimleri ve meteorolojik parametreler hakkında önemli bilgiler sağlar ancak bu istasyonların ilk yatırımı ve bakımı pahalıdır ve yerel ve bölgesel ölçekte makul hava kirliliği tahminleri üretmek için konumları dikkatlice planlanmalıdır. Hava kalitesi izleme istasyonları, hava kirleticilerinin mekansal dağılımını doğru bir şekilde temsil etmek için en uygun konumlara yerleştirilmelidir. Düşük maliyetli hava kalitesi izleme sensörleri popüler hale gelmiş olsa da, yer tabanlı istasyonlara kıyasla bazı yetersizlikleri vardır. Ayrıca, Hava kalitesi izleme istasyonları tüm hava kirleticilerinin mekansal değişkenliğini yakalayamayabilir ve temsiliyetleri dikkatle incelenmelidir. Maliyetli istasyonlar yanlış yerleştirildiğinde ve hava kalitesi verilerini kopyaladığında istasyon fazlalığı sorunu da ortaya çıkmaktadır. Havadakı partiküllerin konsantrasyonlarını ölçen yer tabanlı hava kalitesi izleme istasyonlarının sayısının yetersiz olması, yüksek partikül konsantrasyon seviyelerinin çevre üzerindeki etkilerine ilişkin kapsamlı çalışmaları engellemektedir. Partikül madde konsantrasyonunu ölçmek için çeşitli mekanik, elektrikli ve radyoaktif aletler mevcut olsa da, hataları önlemek için düzeltme faktörlerine ve kalibrasyonlara ihtiyaç vardır.

Bu nedenlerden dolayı, yer gözlem uydularından elde edilen veriler/ölçümler, çevresel çalışmalarda yer tabanlı verilerin yerine kullanılabilir. Yere dayalı veriler genellikle daha ayrıntılı ve doğru olmasına rağmen, uydu görüntü verileri daha geniş mekansal kapsamlar üzerinde daha geniş bir görünüm sağlar. Uydu verileri aynı zamanda uzun zaman dilimlerinde veri toplama avantajına sahip olup, çevresel eğilimlerin ve değişimlerin uzun vadeli analizine olanak tanır ve pahalı yer tabanlı ölçüm araçlarına uygun maliyetli bir alternatif sağlayabilir.

Aerosoller, Dünya atmosferinde asılı duran küçük parçacıklardır. Doğal veya insan kaynaklı olabilirler ve çeşitli boyut ve bileşimlere sahiptirler. Atmosferik aerosol yükünün Dünya'nın ikliminin ve çevresinin çeşitli yönleri üzerindeki etkisi yatsınamaz. Küresel sıcaklığı, atmosferik radyasyonu, Dünya'nın albedosunu ve karasal ısı bütçesini, ayrıca bulutları ve yağış süreçlerini ve ekolojik sistemleri etkiler. Bu nedenle, atmosferik aerosollerin rolünü anlamak, Dünya'nın iklimini ve ekosistemini kapsamlı bir şekilde anlamak için çok önemlidir.

Atmosferin dikey bir dilimindeki mikroskobik aerosol parçacıklarının veya damlacıklarının miktarı hem yer tabanlı aletler hem de uydu sensörleri tarafından ölçülebilir. Atmosferik aerosol tespiti için kullanılan ilk uydu aracının fırlatılmasından bu yana otuz yıldan fazla zaman geçti. Uzaktan algılanan ana jeofiziksel miktar ve sütun/kolon etkili parçacık özelliği, toplam sütun orta görünür aerosol optik derinliğidir (AOD). AOD, güneş ışığının atmosferdeki aerosol parçacıkları tarafından ne kadar emildiğinin veya saçıldığının bir ölçüsüdür ve atmosferik aerosollerin konsantrasyonu ve dağılımı hakkında bilgi sağlar.

PM ve AOD konsantrasyonları hava kirliliğinin önemli ölçütleridir. Havada bulunan partikül madde miktarını temsil ederler ve birbirleriyle güçlü bir şekilde ilişkilidirler. Yere dayalı hava kirletici konsantrasyonu olgusu, atmosferin yaklaşık 1 ila 2 kilometre yüksekliğe kadar Dünya yüzeyi ile etkileşime giren kısmı olan atmosferik sınır tabakasındaki kirletici konsantrasyonunu gösterirken, uydu tabanlı AOD veriler, Dünya yüzeyinden atmosferin tepesine kadar olan aerosollerin toplam sütun miktarının bir ölçüsünü sağlar. Uydu tabanlı AOD ölçümleri, partikül kirliliğinin yoğun olduğu bölgeleri ve kısa vadeli ani artışları belirleyebilir ve daha sonra daha ayrıntılı yer tabanlı hava kirliliği ölçümler için hedeflenebilir ve bu ölçüm çabalarının optimize edilmesine yardımcı olur. Ayrıca, uydu tabanlı AOD ölçümleri uygun maliyetlidir ve ölçüm çabalarını daha verimli bir şekilde hedeflemek için önemli bilgiler sağlayabilir.

Uzay tabanlı uzaktan algılama yöntemleri ile elde edilen uydu AOD verileri, atmosferik aerosollerin mekansal ve zamansal dağılımlarının sürekli ve yerelden küresele farklı ölçeklerde karakterize edilmesinde hayati bir rol oynamaktadır. Uydu bazlı aerosol ürünlerinin popülerliği, çeşitli geri alma algoritmalarının geliştirilmesine yol açmıştır. Uydu aerosol gözlemleri iklim çalışmaları, hava kalitesi çalışmaları ve su döngüsü çalışmaları gibi birçok alanda yaygın olarak kullanılmaktadır.

Bölgesel ve küresel aerosol modellerinin yorumlanmasında uydu aerosol verilerinin doğruluğunu sağlamak için, aerosol algoritmalarının performansını değerlendirmek çok önemlidir. Yer tabanlı güneş fotometrelerinden elde edilen doğru ve ayrıntılı AOD verilerini kullanılarak yapılan doğrulama bu amaçla kullanılmaktadır. AErosol RObotic NETwork (AERONET) programı, AOD gibi çeşitli aerosol optik ve mikrofiziksel özelliklerini ölçmek için dünyanın dört bir yanına yerleştirilmiş çok sayıda güneş fotometresi kullanan aerosolleri izlemek için dünya çapında hayati bir ağ olan yer tabanlı uzaktan algılama aerosol ağlarının bir federasyonudur.

Uydu aerosol ürünlerinin etkinliğinin coğrafya, iklim ve hava koşulları gibi faktörlere bağlı olarak değişebileceğini unutmamak gerekir. Bu nedenle, uydu AOD alımlarını ilgi bölgemizde en yakın mesafede bulunan AERONET sahalarından alınan AOD ölçümleriyle doğrulayarak ve mevcut aerosol ürünlerini karşılaştırarak en güvenilir algoritmayı belirlemek çok önemlidir.

Bu çalışmanın temel amacı, aerosol konsantrasyonlarını ve ortam hava kirliliğini kontrol altına almak ve etkili bir plan oluşturmak için aerosol konsantrasyonunu etkileyen faktörleri anlamaktır. Bunun yanı sıra, ilgili verilerin toplanması, doğrulanması ve özel yöntemler kullanılarak analiz edilmesi yoluyla, aerosol konsantrasyonlarının uzun dönemdeki değişimleri belirlenmeye çalışılacaktır. Bu amaç doğrultusunda, çalışma üç ana bölümden oluşmaktadır. İlk olarak, çeşitli uydu aerosol ürünleri, Akdeniz bölgesi ve Karadeniz'de doğrulukları ve uygunlukları açısından, uydudan türetilen AOD'ler ile AERONET AOD ölçümleri kara, okyanus ve kıyı olmak üzere üç farklı konumda karşılaştırılarak değerlendirilmiştir. En etkili AOD verisi elde etme algoritması ve uydu sensörü, birincil uydu aerosol veri setlerinin karşılaştırılması yoluyla belirlenmiştir. Bu kapsamda, Beş yıllık bir süre boyunca (2014-2018), doğu Akdeniz'deki çeşitli yüzey sınıfları/türlerinde (yani kara, okyanus, kıyı) AERONET AOD ölçümlerini ile çoklu Moderate Resolution Imaging Spectroradiometer (MODIS) ve Visible Infrared Imaging Radiometer Suite (VIIRS) AOD ürünleri karşılaştırıldı ve çıkan sonuçlar doğrulandı. Dark Target (DT), Deep Blue (DB) ve Multi-Angle Implementation of Atmospheric Correction (MAIAC) dayanan MODIS aerosol ürünleri farklı mekansal/uzamsal çözünürlüklerde (1 km, 3 km ve 10 km) mevcutken, VIIRS aerosol ürünü 6 km çözünürlüğe sahiptir. VIIRS AOD değerlerini elde etmek için kara için geliştirilmiş DB yaklaşımı, okyanus için ise SOAR yöntemi kullanılmıştır. Kentsel/kara yüzeyi üzerinde en iyi performans gösteren ürünler, 0,048-0,061 Root-Mean-Squared Errors (RMSE) ile MODIS MAIAC ve VIIRS DB aerosol ürünleridir ve kara için beklenen hata içinde kalan geri alımların daha yüksek bir yüzdesi (%81-%89) vardır. MODIS MAIAC AOD verilerinin 1 km'lik daha iyi bir mekansal çözünürlüğe sahip olması nedeniyle avantajlıdır ve bu da alt-grid aerosol özelliklerini yakalamasını ve daha fazla sayıda AOD alımı sağlar.

İkinci bölümde, Marmara bölgesi üzerinde MODIS MAIAC tabanlı AOD'nin mekansal-zamansal değişimi ve etki faktörleri analizine odaklanıyorum. Bu bölümün amacı, bir bölge içinde normalden daha yüksek AOD seviyelerine sahip alanları belirlemek ve mevsimsel hava düzenleri, yerel emisyon kaynakları ve arazi örtüsü ve kullanımı gibi çeşitli çevresel faktörlerin bu alanlardaki aerosol kirliliğinin varlığıyla nasıl bağlantılı olduğunu incelemektir. Marmara bölgesini çalışma bölgemiz olarak seçmemizin nedeni, bölgenin çeşitli doğal ve antropojenik kaynaklardan aerosol oluşumuna maruz kalmasıdır. Türkiye'nin kuzeybatısında olan Marmara bölgesi, coğrafi olarak en küçük ikinci bölge olmasına rağmen, ülkenin en kalabalık bölgesidir. Bunun nedenlerinden biri, Türkiye'nin en büyük şehri ve dünyanın en büyük şehirlerinden biri olan İstanbul'un burada bulunmasıdır. Bölge, ayrıca Bursa, Kocaeli ve Tekirdağ gibi diğer gelişen şehirleri de içerdiği gibi ticari ve endüstriyel faaliyetlerin yoğun olduğu önemli bir ekonomik merkezdir. Bölge, deniz tuzu, tarımsal faaliyetler, deniz taşimaciliği, endüstriyel faaliyetler ve mevsimsel Sahra tozu taşımacılığı dahil olmak üzere çeşitli kaynaklardan aerosol oluşumunun etkisi altındadır.

Çalışmanın ikinci bölümünde amaçlanan hedefi gerçekleştirmek için, çalışma süresince MODIS MAIAC uydu verilerini yıllık, aylık, mevsimsel ve günlük olarak inceleyerek bölgedeki AOD'nin mekânsal ve zamansal değişkenliği incelenmiştir. Aylık ortalama AOD Ocak ayından Mayıs ayına kadar kademeli olarak artmakta, Mayıs ve Ağustos ayları arasında dalgalanmakta ve Ağustos ayında en yüksek değerine ulaşmaktadır. Aylık ortalama AOD Ağustos ayından sonra azalır ve yıl sonunda Aralık ayında en düşük aylık ortalamaya ulaşır. AOD'nin mevsimsel değişimi önemlidir: yaz (0.148) > ilkbahar (0.136) > sonbahar (0.116) > kış (0.09). AOD'nin çok yıllı değişiminin incelenmesi, 2000 ve 2010 yılları arasında AOD'nin sırasıyla 2002 ve 2008 yıllarında 0,146 ve 0,137 değerleriyle iki maksimuma sahip olduğunu göstermektedir. 2000-2021 yılları arasında, AOD yıllık 0,005/a'lık bir düşüşle azalma eğilimindedir. 1km ölçekte MODIS MAIAC AOD veriler kullanarak aerosol yüklemesinin kapsamlı bir değerlendirmesi ve arazi kullanımının/örtüsünün aerosol özellikleri üzerindeki etkisini vurgulayan istatiksel-görsel analizler yapılmıştır. Elde edilen bulgular, bölge genelinde yüksek aerosol konsantrasyonuna sahip önemli bölgeler olduğunu ve bu bölgelerin belirgin zamansal değişimler gösterdiği ortaya konmuştur. Aerosol yüklemesi 2011 yılına kadar Marmara bölgesinin batı yakasında (Edirne, Tekirdağ, Kırklareli, Çanakkale, İstanbul, Kocaeli) daha yüksekken, 2016 yılından sonra bölgenin doğu kısmı (Bursa, Sakarya ve Balıkesir) daha yüksek aerosol konsantrasyonlarına maruz kalmıştır.

2000-2021 yılları arasında aerosol kirliliğinin en düşük olduğu gün sayısı Bilecik'te görülürken (≈%35), Edirne en yüksek aerosol kirliliği seviyesine sahip günlerin en yüksek yüzdesini (≈%9) yaşamıştır. Bölgede aerosollerin ana kaynakları kentsel faaliyetler ve endüstrilerden kaynaklanan emisyonların yanı sıra topraktan kaynaklanan mineral aerosollerdir.

Son olarak, arazi örtüsü/arazi kullanımı sınıflandırması için yeni bir yaklaşım önerilmektedir. Çalışmanın son bölümünde, Akdeniz şehirlerindeki farklı arazi örtüsü ve arazi kullanımı modellerini belirlemek ve ayırt etmek için bir strateji önerilmektedir. Kentsel peyzajların karmaşık ve morfolojik olarak heterojen doğası nedeniyle zor olabilen yapılaşmış alanları çıplak araziden ayırmaya odaklanılmıştır. Ayrıca, kentleşmiş/sanayileşmiş bölgelerin ve çıplak toprak alanlarının atmosferik aerosol yüküne olan büyük katkısı nedeniyle de bu ayrıma ihtiyaç duyulmaktadır. Bu amaçla, uydu görüntü verileri üzerinde önerilen çoklu indeks yöntemleri kullanılarak bu iki sınıfın ayrılması iyi bir şekilde ele alınmıştır. Normalleştirilmiş fark tillage indeksi (NDTI), kırmızı kenar tabanlı normalleştirilmiş bitki örtüsü indeksi (NDVIre) ve modifiye edilmiş normalleştirilmiş fark su indeksinden (MNDWI) oluşan çoklu indeks kombinasyonu, tüm LCU sınıfları için %93 doğruluk ve 0,91 kappa değeri ile olağanüstü bir genel performans göstermiştir. Yerleşik bölgeleri çıplak araziden ayırmada elde edilen iyileşme, çıplak arazilerin yerleşik bölgeler olarak yanlış sınıflandırılmasını önemli ölçüde azalttığı için büyük önem taşımaktadır. Bu durum, aerosol yüklemesi üzerinde en yüksek etkiye sahip iki faktörün bulunduğu çalışma bölgesindeki aerosol çalışmaları için özellikle önemlidir. Bu iyileştirme ile sağlanan arazi örtüsü sınıflandırmasının artan doğruluğu, bölgedeki aerosol çalışmalarının güvenilirliğini ve hassasiyetini büyük ölçüde artırabilir.

1. INTRODUCTION

1.1 Rapid Industrialization-Urbanization and Increasing Air Pollution

The impacts of urbanization and industrialization on air quality have been widely known (S. Wang, Gao, Li, & Feng, 2020). The intensification of human activity in urban areas is a major cause of air pollution. The consciousness of environmental degradation has increased and some effective air pollution control strategies have been taken to alleviate air pollution such as the utilization of renewable and clean energy for heating and developed public transportation systems. However, the clean air policies have been effective just in developed modern countries with higher income-levels (Saint Akadiri, Alola, Akadiri, & Alola, 2019; Shahsavari & Akbari, 2018). Degradation of air quality in developing countries in which the deceleration of unplanned urbanization and industrialization is improbable has been helpless (Nahar, Mahiuddin, & Hossain, 2021; Yuan Shi, Bilal, Ho, & Omar, 2020). The reliance of the economic development of today's developing countries on fossil fuels contributes significantly to air pollution and climate change (Asongu, Agboola, Alola, & Bekun, 2020). Agriculture emissions and particularly air pollutant emissions from crop residue burning are other big sources of air pollution in the developing world (Haider, Bashir, & Husnain, 2020). The use of biomass fuel and low-quality coal combustion for cooking and heating are the leading causes of air pollution in less-industrialized rural areas (Yun et al., 2020). Besides local air pollutant emissions, the air quality of a region is affected by the long-range transport of anthropogenic and natural particles from regions in neighboring countries or relatively distant continents. Therefore, aerosols can affect the atmosphere not only on a local scale but also on a regional and global scale. This highlights the importance of monitoring and controlling local-scale air pollution (Q. Zhang et al., 2017).

Air pollution can contribute to health, visibility, ecosystems, and climate change (Y. Lu et al., 2018; Manisalidis, Stavropoulou, Stavropoulos, & Bezirtzoglou, 2020). In recent decades policymakers are becoming increasingly alarmed at how ambient air pollution leads to serious health effects. The effects of air pollutants on human health and well-being have been covered in many studies and the necessity of controlling air pollutant emissions, implementation of policies for taking actions on air pollution, and setting limits on certain air pollutants has been exposed (Nowak, Hirabayashi, Doyle, McGovern, & Pasher, 2018). The man-made particulate matter (PM) containing carbon and can absorb high concentrations of chemical substances, organic compounds, salt, and toxic metal. Among air pollutants, PM has the most severe health impacts (W. Yang et al., 2021). Besides the well-known cardiovascular and respiratory diseases caused by the inhalable PMs (PMs with aerodynamic diameter ≤2.5 μm ($PM_{2.5}$) and ≤10 μm (PM_{10})) (Rajagopalan, Al-Kindi, & Brook, 2018), researchers claimed that exposure to air pollutants may promote the development of Parkinson disease (Jo et al., 2021), they bring up the link between the higher air pollutant concentration and higher odds of diabetes (B.-Y. Yang et al., 2020), and they confirmed the negative effects of exposure to the polluted air to the maternal and perinatal health (Bekkar, Pacheco, Basu, & DeNicola, 2020). Due to the wide range of health impacts of exposure to air pollution governments need to measure, monitor, and control the concentration of air pollutants and maintain the pollution levels under the values which are defined as an ambient air quality standard set by the World Health Organization (WHO). Regular levels of pollution are essential for individuals or groups which are most vulnerable such as people with heart or lung diseases, children, and older adults to avoid exposure to air pollutants. The widespread air quality monitoring networks have been constructed and maintained to keep track of air quality and alert people in high-pollution episodes. Air quality monitoring (AQM) stations measure the criteria air pollutants including $PM_{2.5}$ and PM_{10}, CO (carbon monoxide), NO_2 (nitrogen dioxide), SO_2 (sulfur dioxide), and O_3 (ozone). The air quality monitoring networks, consisting of several stations located consistently across the region are used for mapping and managing regional air pollution. Based on the report by 'IQAir-AirVisual' which is based on the air quality data captured at AQM stations across the globe with high data availability during 2018, 64% of the stations at 3000 cities of 69 countries measuring the $PM_{2.5}$ mass exceeded the WHO's recommended limits of $PM_{2.5}$. This is while for cities within the Africa and Middle East, the percentage of regions that exceeded the target value is almost 100%. They claimed that the number of regions that are coping with the high $PM_{2.5}$ levels is expected to be higher but the information is scarce from areas in which the air quality information is not available for public use (IQAir, 2018). Although significant reductions happened in annual $PM_{2.5}$ levels in 2020 due to the COVID-related lockdowns, 5%, 0%, and 1.6% of regional cities of Africa, West Asia, Central & South Asia met the WHO's PM2.5 target, respectively (IQAir, 2020). The air quality over cities in Europe and Northern America with 50.7% and 65% of regional cities meeting the Who's $PM_{2.5}$ limits, respectively, are better compared to Asia and Africa. Silver et al. (2018) reported an increase in O_3 concentration and a decrease in $PM_{2.5}$ and SO_2 concentrations in China using a three-year (2015–2017) dataset from the comprehensive air AQM network consisting of over 1000 AQM stations across China (Silver, Reddington, Arnold, & Spracklen, 2018). Fan et al. (2020) showed the same decrease in PMs and pollutant gases (CO, NO_2, and SO_2) in China using the concentrations measured from May 2014 to December 2018 at AQM stations located in more than 300 cities and also, highlighted the differences of the spatial distribution of each air pollutant over central, Northeast, and Northwest China (H. Fan, Zhao, & Yang, 2020). Sicard et al. (2016) utilized the O_3 measurements from 2005 to 2014 at 300 AQM stations located in rural districts and 808 urban-background stations in the United Kingdom, the United States, France, South Korea Canada, Germany, Italy, and Japan to study the effectiveness of control policies of the O3 precursors' emissions on ground-level O3 concentrations. They highlighted the necessity for additional research for detecting the sources of air pollution in major cities (Sicard et al., 2016). Kahya et el. (2017) reported an increasing $PM_{2.5}$ concentration over the Marmara region/Turkey, studying the $PM_{2.5}$ measurement from March 2013 to February 2014 at 13 AQM stations located in Marmara region (Kahya, Balcik, Oztaner, Ozcomak, & Seker, 2017). Yurtseven et al. (2018) evaluated the dataset from AQM stations located in mega city Istanbul/Turkey and they claimed decrease of three criteria air pollutants (PM, SO_2, and CO) in 10 pilot districts of city between 2003 and 2013 (Yurtseven, Vehid, Bosat, Koksal, & Yurtseven, 2018). Shrestha et al. (2020) studied the information on air pollutants measured at AQM station in 1,000 major cities on six continents and they claimed that COVID-19 lockdown caused global air pollution declines (Shrestha et al., 2020).

1.2 In Situ Measurements of Air Pollutants

The data from AQM stations are largely used for studying the impacts of air pollution on human health. Gorai et al. (2016) used the $PM_{2.5}$ and ground-ozone measurements at 99 monitoring stations located in different counties of the eastern part of Texas to study the impacts of exposure to air pollutants on asthma prevalence (Gorai, Tchounwou, & Tuluri, 2016). Popov et al. (2020) utilized the datasets from the local AQM stations located in Kyiv, Ukraine and they asserted rising adverse environmental health issues in Kyiv city from 2016–2017 (Popov et al., 2020). Similar studies have been conducted in different cities located in Turkey, utilizing the local and regional air quality data for assessing the relationship between exposure to air pollutants and human diseases (Baltaci, Arslan, & Akkoyunlu, 2022; Capraz & Deniz, 2021; Mentese, Bakar, Mirici, Oymak, & Otkun, 2018; Saygın et al., 2017). AQM networks provide valuable information on air quality and are utilized widely to study the high episodes of air pollution, and chemical compositions of air pollutants, to examine the temporal variation of pollutants concentration, and to detect the location of hotspots of air pollution. Other than the information about the gaseous pollutants such as sulfur dioxide (SO_2), nitrogen dioxide (NO_2), nitrogen oxides (NO_X), ozone (O_3), CO, and particle matters (PM_{10} and $PM_{2.5}$), AQM stations also provide the daily meteorological parameters such as temperature (T), wind direction (WD), wind speed (WS), and Relative Humidity (RH). Tracking the meteorological parameters is essential for monitoring air pollution since the various weather condition which is resulted from the combination of lower/higher precipitation, T, AP, RH, and WS can be effective in changing the air quality scenarios while there is no change in the pollution sources and concentration levels (J. He et al., 2017; Sezer Turalıoğlu, Nuhoğlu, & Bayraktar, 2005; H. Zhang, Wang, Hu, Ying, & Hu, 2015). The weather conditions that prevailed were either suitable for dispersion, transmission, or the elimination of pollutants. Although the air quality data from stations are precise and useful, the initial investment and maintenance of the ground-based stations are both expensive. Ngo et al. (2019) pointed out the scarcity of air quality data in Africa due to the high costs of equipment and data processing (Ngo, Asseko, Ebanega, Allo'o Allo'o, & Hystad, 2019). Low-cost sensors are put forward as an alternative means for long-term air quality monitoring which are majorly invested privately and applied for private uses which can make a network providing an opportunity to monitor air pollution in outdoor air and study the spatial pattern of air pollution in a particular region (Popoola et al., 2018). Despite the increasing availability and popularity of low-cost air quality monitoring sensors, there are some insufficiencies in the performance of the sensors compared to concise reference sensors at ground-based stations (Karagulian et al., 2019).

The locations to install the ground-based AQM stations which are mostly limited in number should be studied and planned carefully. The AQM networks in which the stations are located consistently and accurately represent the spatial distribution of air pollutants at a local and regional scale are scarce. AQM stations should be sited in their optimal locations to produce reasonable estimates of air pollution at a local- and regional scale. However, AQM stations are commonly positioned in areas of interest or mostly polluted regions (hot spots). Several studies tried to assess the area of representativeness of the AQM stations and they showed that the station networks which are mostly placed without prior investigation and optimal design do not capture the spatial variability of all air pollutants. Yatkin et al. (2020) claimed that the stations in their study area, an urban region in Italy are not homogenously distributed through the area in a way that accurately represents the spatial distribution of anthropogenic and natural air pollutants (Yatkin et al., 2020). Duyzer et al. (2015) mentioned that data on air pollutants measured at AQM stations located in Barcelona and Stuttgart are not suitable to examine the exposure of the general population (Duyzer, van den Hout, Zandveld, & van Ratingen, 2015). While a limited number of AQM stations can create a network not representing a spatial variation of air pollution, there is an issue of station redundancy that occurs when the costly stations are located improperly and duplicate the air quality data (Martin, Fileni, Palomino, Vivanco, & Garrido, 2014).

1.3 Satellite Data and Products for Studying Aerosol Pollution (Why do we need alternatives?)

The importance of controlling the levels of particle pollution concentrations due to the adverse effects of exposure to high particle matter (PM) concentrations on human health has caused a rising need for consistent PM measurements. However, not all stations measure the PM concentrations and the long-term, precise measurements of $PM_{2.5}$ is rare. Riojas et al. (2016) claim the inadequacy of the number of stations in Latin American countries providing official air quality data; none of those stations measures the concentrations of PM and the CO measurements were rare (Riojas-Rodríguez, da Silva, Texcalac-Sangrador, & Moreno-Banda, 2016). The comprehensive study of the impacts of high levels of PM concentrations on human health and the environment is limited in number due to the lack of PM measurements at air quality monitoring stations.

Mostly the policymakers dealing with air pollution majorly focused on the levels of gaseous pollutants particularly NO_x, SO_2, concentrations, dust transportation, and soot emissions (H. He et al., 2014). As PM pollution seems to be worsening with time and it has gradually become a major environmental issue with a growing industrial sector in developing countries, the methods to estimate PM concentration and monitor the temporal variations of PMs get more crucial (Kulshrestha, Satsangi, Masih, & Taneja, 2009). The environmental planners should access accurate PM data with a high temporal resolution to efficiently contribute to the environmental impact assessment of air pollution. The tapered_element oscillating microbalance (TEOM) is one of the mechanical-based instruments which is typically used for measuring the real-time PM mass. There are other instruments that are based on electrical and radioactive principles. The PM concentration calculation in these devices is a fairly complicated process and labor-intensive (Grover et al., 2005). The performance of the mechanical-based instruments which are widely used could be affected by various factors such as humidity changes, changes in filter pressure, and temperature fluctuations. There is a need to apply various correction factors and calibrations for correcting every possible calculation error including flowrate, temperature, and pressure calibrations and leak checks. The standardized measurement techniques at AQM stations provide hourly PM data 24hr/day even in cloudy and fuggy days.

To attain high-resolution spatial variation of PM concentrations and classify the long-term human exposure to this air pollutant which extremely impacts human health we need a sufficient number of AQM stations monitoring the PM levels within a wider area which are placed optimally in a way that they can be a good representation of concentration distribution of PM pollutants. Although the AQM stations provide precise PM data, the point measurements from an inadequate number of sparse AQM stations monitoring PM concentrations are not feasible to map large spatial areas. PM measurements from ground stations are restricted to the sampling area of measurement and do not provide a largescale picture of air pollution; i.e., the measured high/low PM concentrations in observation spots which are located in the area where the concentration of PM was higher/lower than other spots within an area during the period of observation can be misleading. Although extreme air pollution levels are monitored at stations, examining the origin-destination patterns of air pollution is not practicable by insufficient and widely spaced point measurements. Local, regional, and national governments address the lack of ambient stations by expanding the network of conventional AQM stations monitoring PM levels. They implemented a number of new microsensors and used the PM data to predict particle pollution levels over a long-term period (Lin et al., 2020). Utilizing mobile monitoring devices individually and in combination with fixed stations is another solution to cope with a lack of ground-based pollution monitoring stations which is widely validated for monitoring air pollution emissions in developing countries (B. Chen et al., 2018).

The 'IQAir' studied the number of government stations monitoring particle pollution at a global scale. Although the number of AQM stations has increased significantly with more than 30,000 known air quality monitoring stations in the world, other than the United States, China, and Japan which have the luxury of having comprehensive ground-based monitoring stations most countries do not have an adequate number of well-distributed ground monitors to create the air pollution maps at high spatial resolution. The number of AQM stations in Turkey has increased from 253 stations in 2016 to 313 stations in 2018 and 357 stations in 2020. According to the air pollution report 2020 by the TMMOB, while the PM10 (i.e. inhalable particles, with diameters that are generally 10 micrometers) mass has been measured in 141 out of 357 stations, the number of stations that measuring $PM_{2.5}$ (i.e. fine inhalable particles, with diameters that are generally 2.5 micrometers and smaller) mass concentrations is just 131 out of 357 with 41 stations out of 131 stations providing reliable $PM_{2.5}$ data and this means just 14% of reliable $PM_{2.5}$ across Turkey. In just three out of 31 stations in megacity Istanbul $PM_{2.5}$ concentration is measured (Air pollution report, 2020). Long-term assessments of PM impacts are not practical because the tracing of PM has been done across the Marmara region since March 2013 and before this date the data of $PM_{2.5}$ is unavailable. The AQM stations in Turkey are mostly clustered in the most populated regions with an urban background. To assess the variations of particle pollution in wider spatial coverage and examine the adverse health outcomes of air pollution exposure we need stations located homogenously across an area with stations performing air pollutant measurements at suburban regions, industrial zones, agricultural areas, vegetated lands, marine conditions, and traffic-related regions beside those sited in mostly urbanized regions.

The valued alternative for the particle matter measurements is the satellite and ground-based remote sensing of aerosol optical and physical properties. The Satelite aerosol dataset contains the characteristics of particles in the atmosphere which are retrieved from satellite observations using a variety of methods. The remotely sensed aerosol datasets have been used to study the aerosol−cloud radiative effects (Seinfeld et al., 2016), to estimate the radiative forcing of aerosols (D. G. Kaskaoutis et al., 2013), to characterize the aerosol types (K. Raghavendra Kumar, Kang, & Yin, 2018; Yousefi, Wang, Ge, & Shaheen, 2020), to study the spatiotemporal variability of dust aerosols and quantify the dust aerosol load impact (Denjean et al., 2016). These datasets provide information on aerosol optical depth (AOD) which is a measurement of the amount of aerosol in the atmosphere. AOD retrieved from satellite observation has been used to address various climate and air quality research. With air pollution started becoming a global environmental issue in the last decades, long-term satellite measurements of aerosol properties have been used widely for studying and monitoring air pollution (Al-Saadi et al., 2005; Hoff & Christopher, 2009; L. Shen et al., 2020; Zoogman et al., 2017). The free satellite aerosol data with higher spatial coverage provide the opportunity to study the spatial distribution of air pollution at regional and global scales which is not feasible with a limited number of costly ground-based AQM stations which are mostly clustered in most polluted areas.

With growing worldwide concerns about elevated air pollutant levels, studies focused on utilizing the potential of satellite aerosol datasets to monitor atmospheric aerosol pollution. The ground observed and satellite retrieved AOD, a unitless value referring to the columnar measure of light extinction by aerosol absorption and scattering between the earth's surface and the top of the atmosphere, can be used to study the atmospheric loading of aerosols, estimate air quality, and manage atmospheric pollution.

1.4 In Situ Measurements of Aerosol Optical Properties

Other than it's direct effects on air quality, atmospheric aerosol loading has been an important topic due to its direct and indirect effects on the Earth's climate, global temperature, atmospheric radiation, the Earth's albedo, and terrestrial heat budget, clouds and precipitation processes, and ecological system. Other than satellite-derived aerosol information, the ground-based instruments have measured atmospheric aerosol properties. The Aerosol Robotic Network (AERONET) is a comprehensive network of ground-based Cimel Electronique Sun–sky radiometers that measure columnar aerosol properties at worldwide locations for more than two decades (Holben et al., 1998). Other than AOD measurements, the AERONET provides various optical and radiative aerosol properties such as Ångström exponent (AE), fine mode fraction (FMF), single-scattering albedo (SSA), and absorption Ångström exponent (AAE). The accurate measurement of AOD from AERONET has been utilized widely to characterize atmospheric aerosols and study the various environmental impacts of aerosol loading (Anoruo, 2021; Arola, Eck, Kokkola, Pitkänen, & Romakkaniemi, 2017; Basart, Pérez, Cuevas, Baldasano, & Gobbi, 2009; Kambezidis & Kaskaoutis, 2008; Jaehwa Lee et al., 2010; J. Li, Carlson, Dubovik, & Lacis, 2014; Maghrabi & Alotaibi, 2018; Pérez-Ramírez et al., 2017; Prasad & Singh, 2007; Russell et al., 2010; Schafer, Eck, Holben, Artaxo, & Duarte, 2008; Science, 2014; Toledano, Cachorro, Berjon, et al., 2007).

1.5 A Need for the Assessment of Satellite Aerosol Products

Due to the popularity of satellite aerosol products, various retrieval algorithms have been developed to retrieve AOD from satellite measurements. The retrieval algorithms have been developed, changed, updated, and optimized over time to apply to various satellite sensor measurements, reduce the uncertainties and retrieve AOD over various surface backgrounds. The AERONET observations are the most widely used ground-truth AOD measurements for the evaluation of the performances of the retrieval algorithms and validation of AOD retrievals from satellite measurements (Bright & Gueymard, 2019; Kahn et al., 2005; L. A. Remer et al., 2005; Wei et al., 2020). The performance of aerosol retrieval algorithms varied over different surface types and the AOD uncertainties can be different in the various climatic zone with different aerosol types. Aerosol products are highly consistent globally but exhibit certain differences on regional and site scales. Wei et al. (2019) compared aerosol distribution derived from the multiple satellite aerosol dataset and highlighted certain differences in spatial aerosol variations on regional and site scales despite the globally consistent manner (Wei, Peng, Mahmood, Sun, & Guo, 2019). The best-performer retrieval algorithm should be defined for a geographical region. Evaluation of satellite-derived aerosol products is an essential step for understanding the suitability of the product for further studies such as air quality or climate studies. Reliable remote sensing aerosol observations can be utilized for monitoring atmospheric aerosol loading. The appropriate satellite aerosol dataset is an exceptional data source to study the spatial distribution and the temporal trend of the aerosol loadings and define the major aerosol emissions at a regional scale.

Researches from multiple fields benefit the satellite aerosol dataset. The daily aerosol data from earth-viewing satellite sensors an opportunity to examine the impacts of aerosols on climate systems. Impacts of the aerosols differ with the aerosol type and therefore the altering composition of atmospheric aerosols due to the intensifying industrial activities should be tracked continuously to accurately monitor the impacts on the climate systems (Quaas, Boucher, Bellouin, & Kinne, 2008). The aerosol composition alteration mainly modifies the impacts of aerosols on cloud condensation nuclei, cloud properties, and precipitation. Therefore, the opportunity for consistent monitoring of the aerosol types utilizing satellite aerosol data makes the study of aerosol impacts on the water cycle and the world's water supply possible (Yoram J. Kaufman, Tanré, & Boucher, 2002). The characteristics and distribution of aerosols over the ocean can be different from those over the land. Monitoring the spatial distribution and temporal variation of aerosol loadings over the ocean is as important as those over the land. The independent satellite aerosol retrieval algorithms are proposed to derive the aerosol characteristics over the land and oceans separately (L. A. Remer et al., 2002; Tanré, Kaufman, Herman, & Mattoo, 1997). Reus et al. (2001) studied the difference in aerosol properties at different atmospheric layers and altitudes over the northern Indian Ocean using remote sensing aerosol data (de Reus et al., 2001). Smirnof et al. (2002) study the systematic characteristics of aerosol over the oceans by examining the comprehensive optical and physical properties of aerosol at five AERONET stations located in islands (Smirnov et al., 2002). Satellite aerosol observations have been widely used to study the spatial-temporal distribution of dust loading, particularly over arid and semiarid regions (Chudnovsky, Koutrakis, Kostinski, Proctor, & Garshick, 2017; Song et al., 2018). A satellite aerosol dataset with global spatial coverage has been majorly helpful for tracking the pattern of dust transportation and its effects on regional air pollution (Badarinath et al., 2010; Moulin et al., 1998; Tao et al., 2021). Examining changes in aerosol emissions from human activities after the lockdowns due to the COVID-19 pandemic attracts researchers' attention. Several studies conducted on reviewing the effects of lockdowns on aerosol properties and air pollution and the accessible satellite aerosol observations have been the most used dataset (Acharya et al., 2021; Dimitris G. Kaskaoutis et al., 2021; Ranjan, Patra, & Gorai, 2020). Several studies focused on the factors affecting the spatial variation variations of aerosol loading including local, regional, and global trends and temporal variation of aerosol loading including inter-, intra-annual, monthly, and seasonal variations.

Knowing the factors affecting aerosol concentration is needed to effectively plan for controlling and reducing aerosol concentrations and ambient air pollution. Some studies claimed that aerosol concentration is positively associated with socio-economic activities (Q. He, Zhang, & Huang, 2016; L. Li & Wang, 2014) and others introduced the contributions of topography as the main factor predominating the aerosol loading and its spatial distribution (Cheng et al., 2019; C. Wang, Wang, Myint, & Wang, 2017). The intense land cover and land use conversions are caused by human activities along with huge population growth and industrial development (Ettehadi Osgouei & Kaya, 2017; Ettehadi Osgouei, Kaya, Sertel, & Alganci, 2019). How the transformation in the natural landscape affects the aerosol loadings and which LCU is more potent in causing aerosol pollution at local, regional, and global scales? Answers to these questions are the needed information for urban planners and policymakers to choose the best urban development strategies and control human exposure to air pollution. Besides considering the social and economic benefits of industrial development, industrial development, and factory enhancement should be planned sensibly by examining the suitability of topographical and meteorological properties of an area to control the aerosol pollution in the region and reduce human exposure to hazardous air pollutants. Several studies focused on aerosol and LCU interactions (Artaxo et al., 2013; Q. Xie & Sun, 2021; J. Xu, Jiang, Zhang, Lu, & Peng, 2014). For the sustainable management of environmental protection and air quality, the interactions of land use/cover with the atmospheric environment is crucial. LCU is a factor affecting the abundance and distribution of natural and anthropogenic aerosols. In conjunction with records of aerosol properties obtained from observations made using satellite instruments, a detailed map of an area's land use could be useful for identifying land cover/uses that are more significant in contributing to aerosol pollution at local and global scales, locating aerosol hotspots, and suggesting potential solutions for better managing and reducing aerosol emissions at regional or global scales.

The Marmara region, located in the northwest of Turkey, has one-third of Turkey's population with half of it living in the metropolitan city of Istanbul. Other than Istanbul, the 5th biggest city and one of the most industrialized cities in Turkey, Bursa is also within the boundaries of the Marmara region. Owing to its extraordinary marine transportation and accession due to straits (Istanbul and Çanakkale Straits) and ports and unusual geographic location and land formation, favorable for land and air transportation, the Marmara region maintains a strong economic structure which is mainly based on industry-related export and services sector. Immigrants including domestic and international ones have long been drawn to the Marmara region due to the remarkable industrial development and economic growth along with agricultural development owing to favorable climate, land, and soil structure. The economic heartland of Turkey lies within the Marmara region, which is recognized for its significant contribution to the production of wheat and sunflower plants. The population growth in the Marmara region has increased aerosol emissions significantly due to rising energy consumption while the increase in car ownership within the region intensifies the traffic-related emissions. The swift growth of urbanization and economic development, rapid industrialization, increased human activities leading to significant pollutant emissions, and the intricate topography in this area have contributed to a high AOD and inferior atmospheric conditions. The Marmara region houses the major sources of aerosols including emissions from human, agricultural, mining, and industrial activities. Across the Marmara region, massive burning of solid fuels, particularly the poor-quality coal for use in energy generation at thermal power plants and residential heating and cooking leads to additional air pollutant emissions in the atmosphere. Besides, the use of traditional cookstoves in rural homes and combustion technologies and processes in industry exacerbate the air pollution in the region. The air quality of provinces and cities in the Marmara region is affected by several factors (Arslan & Akyürek, 2018; Kahya et al., 2017; Kasparoglu, Incecik, & Topcu, 2018). The relationship between industrial development, economic growth, and environmental degradation particularly the air quality of the region should be analyzed at a local scale along with considering the topographical parameters. Policymakers and governments should impose appropriate and optimal policies to monitor and protect the atmospheric environment along with economic and industrial developments. In addition to land-surface emissions, the sea surfaces and coastal area of the Marmara region are largely affected by the ship-sourced emissions from maritime traffic (C. Deniz & Durmusoglu, 2008; Ülker, Bayırhan, Mersin, & Gazioğlu, 2021; Viana et al., 2015). The factors affecting the over-sea aerosols and their effect on human health and climate are as important as the over-land ones (Bucak, Arslan, Demirel, & Balın, 2021). The daily accessible satellite aerosol observations will serve as a convenient data source to observe, monitor, control, and predict atmospheric pollution and detect conditions and factors that cause a high level of air pollution, and plan for active and effective air quality policies.

The present study can be divided into three major parts. In the first step, the availability and suitability of different satellite aerosol products are assessed by evaluation of the satellite-derived AODs over different surface types in the Mediterranean region and the black sea compared to AERONET AOD measurement at three different stations over the land, ocean, and coastal site. The best performer aerosol retrieval algorithm and satellite sensor are identified by the inter-comparison of major satellite aerosol datasets.

In the second part, the spatiotemporal distribution and variation of aerosol loadings over the regions in the Marmara region between 2000-2021 are studied and the hotspots are identified. It investigated how land uses and cover relates to aerosol pollution over the Marmara region. Besides, an improved approach to process a satellite image for land cover and land use mapping and to understand the impact of land use on aerosol emissions in highly urbanized areas.

2. AEROSOL LOADING AND SATELLITE-DERIVED AEROSOL PRODUCTS

2.1 Background Information

2.1.1 Atmospheric aerosols and AOD

Aerosols are tiny solid, liquid, or mixed particles that are suspended in the atmosphere and can be dispersed and transported broadly vertically and horizontally through atmospheric movement. Although aerosols with sizes ranging from a few nanometres up to 1 μm suspended in the atmosphere are not detectable individually, a high concentration of aerosols can reduce the visibility and affect the earth's climate by interacting with incoming solar radiations and outgoing Earth’s surface radiation.

Natural and anthropogenic sources emit aerosol particles into the atmosphere. The main natural sources of atmospheric aerosols are arid zones (dust), sea surfaces (sea sprays and sea salt), volcanos, terrestrial and marine ecosystems, biosphere (pollen, virus, and bacteria), and forest fires. Megacities, domestic activities related to cooking and heating, industrial, mining, and agricultural activities, transportation, and energy production/consumption are responsible for anthropogenic aerosol emissions. The chemical component and size distribution of aerosols varied significantly. Major contributors to aerosol particles in urbanized areas are inorganic ions and total carbon (Bae, Kim, Kim, Yoo, & Kim, 2020; Ma et al., 2019). The aerosol emissions from post-harvest biomass burning rise the carbonaceous species and an increase in the potassium ratio of the aerosol composition is a good indicator for biomass burning (K. Huang et al., 2013; Ryu, Kwon, Kim, Kim, & Chun, 2007). Several studies focus on the chemical composition of aerosols over coastal sites since it benefits the analysis of the coastal ecosystem and examination of the atmospheric substances transported from the continents to the ocean (H. Wang et al., 2018; L. Xia & Gao, 2010). Chianese et al. (2019) claimed that the variation of air mass trajectories can change the chemical composition of the aerosols in a region based on the type of prevailing air pollutants in air mass origin. A chemical component of particle matter can be an indicator of air pollution events (Chianese, Tirimberio, & Riccio, 2019). Galindo et al. (2020) linked the increase of crystal elements especially Titanium in PM to the Saharan dust events. The chemical composition of the particle matters varies from season to season based on the prevailing source of emissions (Galindo et al., 2020). While aerosol particles are affected by biomass burning in spring, the emissions from fossil fuel burning for heating are dominant in cold seasons (Bencharif-Madani et al., 2019; Samek et al., 2020; Yunhong Zhou et al., 2020).

Other than the type of sources that gives the characteristics of aerosols, the formation mechanism of the aerosol can be determinative of the aerosol properties. Primary particles are emitted directly into the atmosphere from both natural and anthropogenic sources, while secondary particles are formed as a result of chemical reactions and interaction of primary gaseous pollutants (i.e. precursors) with each other in the atmosphere. The SO_2, nitrogen oxides, carbon oxides, and volatile organic compounds (VOC) emitted from industries and automobiles are among the major precursors. SO_2 is one of the important precursors which contributes to secondary PM formation which has significant adverse effects on human health. SO_2 is mostly produced during the burning of oil and coal in industrial activities and the burning of wood and biomass residues resulting from domestic and agricultural activities. Policies for controlling air pollution and emission of the primary particle into the atmosphere should company the policies for emission mitigation of the pollutant gases, specifically SO_2 and NO_X to achieve the ideal solutions (L. Wang, Yu, Huang, Zhang, & Li, 2020; X. Wang et al., 2019).

2.1.2 Multiple impacts of atmospheric aerosols and AOD

Aerosols as important components of Earth's climate system, play a critical role in the Earth's energy balance and can affect cloud formation indirectly (J. Fan, Wang, Rosenfeld, & Liu, 2016; J. Li et al., 2014). Additionally, atmospheric aerosol pollution affects the ambient air, and ambient air pollution in large concentrations is among the major factors that are responsible for human disease. The ways aerosols affect the climate, environment, and human health needs an examination in detail. Understanding how atmospheric aerosol affects the climate condition necessitates the characterization of aerosol distribution and monitoring the temporal changes. One of the aerosol properties commonly utilized for studying atmospheric aerosol loading and monitoring the spatiotemporal change in atmospheric pollution is AOD. AOD has become one common property of aerosols suggesting itself when studying the multiple impacts of aerosols.

The AOD is a unitless parameter describing the amount of light reflected or absorbed by aerosols in an entire air column. In other words, the AOD is a quantification of the vertical concentration of atmospheric aerosol. The aerosol confined in a column can be of any type including haze, dust, sea spray and fire smoke, and a mixture of aerosols. Measuring the AOD helps us to characterize multiple aerosol types and understand the role of aerosol particles in precipitation, radiation, and climate forcing (Attwood et al., 2014; Che et al., 2018; Eck et al., 2014; Ng, Li, Raghavan, & Liong, 2017). AOD has been validated and studied as the most comprehensive variable to remotely assess the aerosol burden in the atmosphere. In addition, AOD has become one of the important tools for monitoring air pollution due to its reliable correlation with surface particle matter concentrations. Higher AODs represent the greater amount of aerosol particles in the air, which may indicate the areas has higher levels of air pollution.

2.1.3 Ground-based measurements of aerosol optical properties

2.1.3.1 AERONET

Although satellite sensors have observed aerosol loading in the atmosphere since the late 1980s, a global database of the microphysical and optical properties of atmospheric aerosols was lacking. Scientists need a comprehensive database of detailed properties of aerosol particles to understand the aerosol influence on climate, clouds, precipitation, and ambient air quality. Likewise, although ground-based instrumentations such as rotating shadow band radiometers, spectrobolometer, analog sunphotometers, and lidar systems have been used for aerosol observation since the first half of the 20 century, researchers would benefit from the usage of long-term aerosol information from standard and automatic-tracking Sun- and sky-scanning radiometers for studying the atmospheric aerosols in detail and examining the temporal variation of aerosol loading at inter-and intra-annual scales. The aerosol optical properties of the well-calibrated instruments and standard processing systems, mutual analysis method, and quality controls would also be helpful for the validation of aerosol retrievals from various satellite sensor data.

The NASA AERONET (Holben et al., 1998) program was one of the first atmospheric observing projects that located a large number of uniform automatic robotic sunphotometers at national and international scales to provide free-of-charge quality-assured aerosol optical properties. The AERONET grew into a widespread ground-based network of aerosol remote sensing through expansion across the world with national and international collaborations. As of 2018, the number of AERONET sites which were located in different regions around the world reached 600 by the end of 2018 (Giles et al., 2019). Routine instrument calibrations (both before deployment in the field and post-deployment), standard measurement protocols, a processing system, and a user-friendly graphical interface makes the AERONET network the most used aerosol data as a ground-truth aerosol measurement (Holben et al., 1998). The AERONET becomes the main aerosol network to obtain quality-controlled datasets of aerosol characteristics including AOD having over 25 years of records.

The Cimel CE318 is an automatic sun-and-sky scanning radiometer (e.g. sunphotometer) that is utilized by the AERONET program to measure the physical and optical properties of atmospheric aerosol. A sunphotometer retrieves information about aerosol properties from spectral measurements of direct and diffuse radiation. AOD as a very useful aerosol characteristic and a crucial parameter for several aerosol-related studies is calculated from the radiance measurements by sunphotometers. To measure the AOD, a sun photometer points at the sun and measures the direct spectral transmission of solar radiation through the atmosphere. Atmospheric aerosol contribution to solar radiation including the scattering and absorption causing the light extinction (e.g. loss of light) between the top and bottom of the atmosphere is measured by the instrument by comparing the difference between the measured energy at the Earth's surface and the well-known energy of the sun at the top of the atmosphere. The solar irradiance I at any given wavelength λ can be expressed as equation 2.1

$$I_\lambda = I_{0\lambda} \exp(-m\tau) \tag{2.1}$$

where I_0 is the solar irradiance at the top of the atmosphere, m is the air mass, and τ is the total optical depth. The aerosols are not the only component in atmospheric columns. The trace gases also absorb solar radiation while the radiation is scattered by gaseous molecules (e.g. Rayleigh scattering). To measure the exact amount of aerosol contribution to solar radiation, the well-measured contributions of the Rayleigh, gases (ozone, mixed gases, trace gases), and water vapor are subtracted from the total optical depth, τ, and the optical depth of the aerosols are retrieved (Holben et al., 1998). The AERONET sunphotometer calculates the AOD for eight wavelengths with measurements of direct sun radiance in eight spectral bands between 340-1020 nm at 15-minute intervals. The eight spectral bands are at 340, 380, 440, 500, 675, 870, 940, and 1020 nm. The measurement at 940 nm, the only available water vapor channel between 340-1020 is used to retrieve the columnar water vapor content (e.g. precipitable water (PW)). The measurements of radiance (triple measurements within a minute) at 15-minute intervals not only provide a longer temporal frequency but also allows cloud screening based on the significant variations caused by clouds in measurements of radiance compared to aerosols (Dubovik et al., 2002). The contribution of clouds to the total optical depth is detected and removed based on the unexpected differences (0.02 (for τ less than 0.667) or 0.03 % (for τ greater than 0.667)) between triple measurements within a minute. The precision and accuracy of AERONET AOD measurements are provided by tracking the uncertainties due to instrumental calibrations, clouds, and random errors. The AERONET AOD measurements uncertainties related to calibration uncertainties for the field instruments are <±0.01 for wavelengths greater than 440 nm and <±0.02 for shorter wavelengths. This is while the uncertainties for optical depth of water vapor at 940 nm is about 10% due to the higher variability of water content at different atmospheric profiles. The type of aerosol (fine mode anthropogenic aerosols, course mode dust aerosol, and mixed aerosols) could also affect the uncertainties in AOD measurements. A comprehensive analysis of possible errors in the AOD measurements based on the aerosols of different types was conducted by Dubovik and King (2000) and Dubovik et al. (2002) (Dubovik et al., 2002; Dubovik & King, 2000). New approaches are proposed and applied to reduce the uncertainties in the retrieved aerosol properties. Sinyuk et al. (2020) discuss the latest changes and additions to the last version (version 3) of the AERONET aerosol retrieval algorithm aimed to reduce the uncertainties of the optical properties measurements (Sinyuk et al., 2020).

Other than AOD and water vapor measurements using the solar extinction the AERONET provides the data archive of aerosol parameters that are derived by inversion strategies from the combined use of calculated spectral optical thickness measurements and the angular distribution of sky radiance almucantar measurements at different wavelengths (Dubovik & King, 2000). These aerosol parameters include particle size distribution, and derived AE (i.e., the spectral dependence of the AOD) including Absorption AE (AAE) and Extinction AE (EAE), aerosol columnar size distribution (CSD), SSA, asymmetry parameter, refractive index, fine and coarse-mode AODs.

Several studies have utilized the AERONET data archive focusing on aerosol-type classification (Ali et al., 2020; Bibi, Alam, & Bibi, 2016, p. 20; Gobbi, Kaufman, Koren, & Eck, 2007; Kanike Raghavendra Kumar, Sivakumar, Reddy, Gopal, & Adesina, 2014; Jaehwa Lee et al., 2010; Logothetis, Salamalikis, & Kazantzidis, 2020; L. Zhang & Li, 2019). Omar et al. (2005) classified over 143,000 records at AERONET sites around the world into six main categories of polluted marine, biomass burning, desert dust, urban industrial pollution, rural background, and dirty pollution based on the microphysical properties of each aerosol type. They represent the mean properties of six main aerosol models (Omar et al., 2005). Shin et al. (2019) defined subcategories for the desert dust aerosol model utilizing the particle linear depolarization ratio (PLDR) provided in the AERONET version 3 aerosol dataset. They benefit from the data from AERONET sites located in East Asia which are frequently affected by Asian dust (Shin, Tesche, Noh, & Müller, 2019). They classified the dust aerosols into pure dust, dust-dominated mixed plume, and pollutant-dominated mixed plume. Giles et al. (2012) validated the retrieved AOD and SSA from 19 AERONET sites around the world to identify main aerosol types and they suggest the use of the absorption and size relationship to meaningfully cluster aerosols (Giles et al., 2012). Stefan et al. (2020) used the AERONET data from the stations located at the Black Sea Coast to identify the dominant aerosol types over a coastal region and study the seasonal variations of the aerosol characteristics over water bodies (Stefan, Voinea, & Iorga, 2020). They focused on the effects of humidity on the optical properties of aerosols. Fan et al. (2021) utilized the AERONET data from stations located in China and they established eight aerosol models based on the physical and optical properties of aerosols over China and used these models to analyze the spatial-temporal distribution of aerosols in China (Y. Fan, Sun, Huang, Ti, & Liu, 2021). Farahat et al. (2016) focused on the possibilities and mechanism of long-range transportation of aerosol loading among different locations by utilizing the aerosol information from AERONET stations located in eight different cities in North Africa and the Middle East between 1999-2015 (Farahat, El-Askary, Adetokunbo, & Fuad, 2016). They claimed that the dominant aerosol type of different locations can be changed in the case of aerosol transport which significantly changes the optical properties (i.e. AOD and AE) of the local aerosol at specific times of the year. Ozdemir et al. (2020) utilized the AERONET version 3 aerosol information to identify the dominant aerosol types over the eastern Mediterranean and the Black Sea and they study the spatiotemporal variation of aerosol properties (Ozdemir, Tuna Tuygun, & Elbir, 2020).

Monitoring the impacts of aerosols on climate necessitates the constant study of microphysical and chemical properties of aerosols at local and global scales. AERONET data have been used by numerous researchers to examine aerosol characteristics and composition. Eck et al. (2005) utilized the aerosol optical properties provided by the AERONET sites located in different regions of the central-eastern region of Asia and the mid-tropical Pacific and investigated the temporal variation of dominant aerosol type. They highlighted the importance of the constant investigation of the aerosol properties at a local scale, especially for highly populated and industrialized regions in which the unceasing increases in fossil fuel combustion may lead to significant impacts on the regional and global climate (Eck et al., 2005). Kaskaoutis et al. (2013) studied the seasonal behavior in aerosol loading trends and their size distribution (e.g. trends of fine and coarse particles) over the Indo-Gangetic plains, from 2001 to 2010 utilizing the AOD and Ångström exponent data provided by the AERONET site located in India at Kanpur city (D. G. Kaskaoutis et al., 2013). Xu et al. (2020) studied the optical properties of aerosols over the Middle East and Eastern Mediterranean Sea utilizing the aerosol dataset (AOD, AE, SSA) from seven AERONET sites during 2010–2017. They studied the seasonal variation of aerosol characteristics, identify the dominant aerosol type, and examine the aerosol radiative forcing based on aerosol types. They review the causes for the increase and/or decrease of the volume of aerosol loading and variation of size distributions utilizing the aerosol information provided by the AERONET sites (X. Xu et al., 2020).

The atmospheric aerosol is one of the main factors affecting the energy balance of the earth-atmosphere system by absorbing or reflecting the only source of energy, the sun. Studying the direct and indirect radiative aerosol forcing is possible by examining the aerosol information from AERONET stations. Some studies focused on the assessment of direct aerosol radiative forcing utilizing the aerosol information provided by the AERONET stations around the world (Alam, Trautmann, & Blaschke, 2011; Arkian & Nicholson, 2018; H. Chen, Xia, Wang, & Zhang, 2007; Chin et al., 2009; D. G. Kaskaoutis et al., 2013; Mao, Zhang, Chen, Huang, & Yuan, 2019; Prasad & Singh, 2007; X. Xia et al., 2007). Garcia et al. (2012) evaluated the long-term aerosol retrievals at the AERONET stations located in various regions around the world to analyze the aerosol radiative forcing and their effects on the energy balance of the Earth based on the dominant aerosol condition of regions in which the AERONET sites are located including desert dust, biomass burning, continental background, the urban-industrial and oceanic troposphere (García et al., 2012). Khan et al. (2020) conducted a similar study about the contribution of different aerosol types to direct radiative forcing using the AERONET data between 2007 and 2018 over urban-industrial (Lahore) and coastal (Karachi) cities located in Pakistan (Khan, Kumar, Zhao, & Ali, 2020).

Mineral dust as one of the most abundant aerosol types in the global atmosphere could have a significant impact on the Earth's energy budget, cloud microphysical properties, and though on climate. The AERONET sun-photometer data has been widely used to study and characterize the optical and physical properties of desert dust aerosols (Koven & Fung, 2006; Lyamani, Olmo, & Alados-Arboledas, 2005; Shin et al., 2018; Su & Toon, 2011; Toledano, Cachorro, de Frutos, et al., 2007). Kim et al. (2011) examined the aerosol properties of the dust aerosols over North Africa and the Arabian Peninsula utilizing the aerosol products at 11 AERONET sites and they label the annual means and standard deviations for aerosol optical properties including SSA, asymmetry parameter, real refractive index, and imaginary refractive index to characterize the Saharan and Arabian desert dust (Kim et al., 2011). Velasco-Merino et al. (2018) validated the aerosol data from the Caribbean AERONET sites and western Africa AERONET sites to examine possible alterations in the physical and optical properties of dust aerosols transported from western Africa to the Caribbean site across the Atlantic ocean (Velasco-Merino et al., 2018). Guirado et al. (2014) validated the aerosol information of the Saharan AERONET site Tamanrasset to characterize dust aerosols and they study the factors affecting the annual variability of AOD and AE over an arid region. They claimed that the thermodynamic feature of the convective boundary layer (CBL) and the appearance of the transported fine-mode aerosols could change the pattern of AOD and AE in a region with the dominant aerosol type of pure dust aerosol (Guirado et al., 2014). The effect of dust events on the optical and physical properties of the local aerosol profile has been studied utilizing the AERONET aerosol measurements (Fernández et al., 2017; Gharibzadeh, Alam, Bidokhti, Abedini, & Masoumi, 2017; Prasad et al., 2007; Verma et al., 2013).

2.1.3.2 AERONET sites in Turkey

The IMS METU Erdemli (e.g., Erdemli) AERONET station is located in a rural site on the southeastern coast of Turkey. The sunphotometer is instrumented on the roof of the Institute of Marine Sciences-Middle East Technical University (IMS-METU) in Mersin province. The Erdemli station is the only AERONET station located in Turkey that is providing continuous aerosol data since 1999. Figure 2.1 shows the location of the Erdemli station. The station is exposed to rural aerosol emissions from the rural settlements and agricultural activities and to sea spray aerosols from the Eastern Mediterranean Sea.

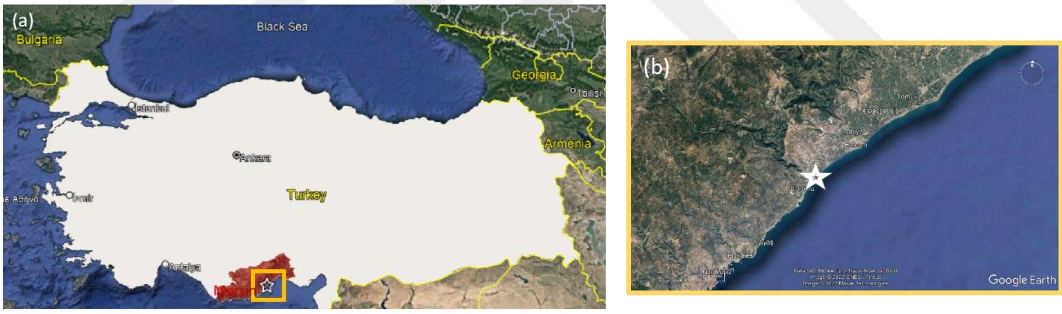

Figure 2.1 : Location of Erdemli AERONET station in Turkey. (a)Mersin on Turkey map. (b)location of Erdemli station in Mersin.

The AOD measurements at Erdemli AERONET stations have been validated for different objectives. The long-term AOD dataset of the Erdemli station has been evaluated to investigate mineral dust events in Eastern Mediterranean (Agacayak et al., 2015; Kubilay, Cokacar, & Oguz, 2003), to characterize the aerosol loading in the Eastern Mediterranean Basin (Fotiadi et al., 2006; Tutsak & Koçak, 2019, 2020; X. Xu et al., 2020), to classify aerosol particles utilizing the microphysical and optical properties of aerosol particles (Ozdemir et al., 2020), and to study the temporal variation of aerosol loading over an urban coastal region (Tuna Tuygun & Elbir, 2020), etc.

2.1.4 Satellite-based measurements of aerosol properties

Although well-calibrated AERONET AOD measurements have taken an important place in aerosol research and well served the decision-makers in aerosol-related climate and air quality issues, the limited spatial coverage of point ground measurements especially in regions with an inadequate number of ground-based AOD measurement stations restricted the observation and examination of the aerosol loading at a national and international scale. Whilst the ground-based aerosol monitoring stations provide accurate observations with a high temporal resolution over a limited spatial extent, satellite aerosol observations offer the advantage of synoptic estimates over larger spatial coverage. Scientists have the opportunity of capturing the dynamics of the atmospheric aerosols and they can monitor aerosol concentration and their spatial distribution at larger spatial coverage over the land and ocean utilizing satellite aerosol observations. Aerosol observations collected by various satellite instruments provide the transport pattern of aerosol loading not only on a regional scale but also on an intercontinental scale owing to their large spatial coverage and consistent frequent measurements (Alam et al., 2011; Che et al., 2019; Aristeidis K. Georgoulias et al., 2016; Guo et al., 2011; J. He et al., 2017; Lorraine A. Remer et al., 2008) Monitoring the aerosol events at a larger scale by satellite sensors offers the chance to study the role of aerosols in the earth-atmosphere system and understand how the aerosols are distributed in the atmosphere over both land and ocean surfaces (Myhre et al., 2005). Atmospheric models would benefit from the aerosol information provided by satellite sensors that cover the earth's land and ocean at a global scale to characterize aerosols (Collins et al., 2001).

Having a wide variety of benefits makes a huge interest in retrieving the AOD from space utilizing satellite data. In the last few decades, many satellite sensors and aerosol retrieval methods have been proposed and implemented, but a renewed interest has emerged in constructing innovative satellite sensors and developing more advanced retrieval algorithms to measure AOD from space.

2.2 Satellite Sensors for Aerosol Observations

Deriving records of AOD from satellite data has a long history of research, application, improvements, and modifications. Since the late 20th century, aerosol concentrations have been retrieved from satellite sensor data. Some of these sensors are including the

AVHRR-Advanced Very-High-Resolution Radiometer (Husar, Prospero, & Stowe, 1997), ATSR-2-Along Track Scanning Radiometer-2 (Veefkind, de Leeuw, & Durkee, 1998), and TOM-Total Ozone Mapping Spectrometer (Herman et al., 1997). Although it was feasible to get the aerosol information from the atmospheric data captured by these satellite sensors, the SeaWiFS (Gordon & Wang, 1994) and POLDER-POLarization and Directionality of the Earth's Reflectances (Deuzé et al., 2001) were the first sensors that were designed and launched with aerosol retrieval purposes in mind. The Moderate Resolution Imaging Spectroradiometer (MODIS) which was launched in 1999 on the Terra and Aqua satellites was one of the first sensors designed specifically for aerosol remote sensing carrying developed technologies to improve the accuracy of aerosol parameter retrievals over both the land and ocean surfaces based on prior findings on aerosol remote sensing (King, Kaufman, Tanré, & Nakajima, 1999). MODIS provides the opportunity for consistent aerosol retrievals over both the land and ocean surfaces being the very first sensor with onboard calibrators and wide spectral range and high spatial resolution. The existing long-term aerosol record from the continuous multi-decadal MODIS data records led to examine the short- and long-term effects of atmospheric aerosols on the environment, climate, and human health. The Visible Infrared Imager Radiometer Suite (VIIRS), a cross-track scanning radiometer operated aboard the Suomi National Polar-orbiting Partnership (S-NPP) satellite, is designed to provide continuity to MODIS aerosol observations and extend the long-term aerosol data records by MODIS.

The optical characteristics of atmospheric aerosols such as AOD have been obtained from satellite data by applying different methods of aerosol detection. The signal received by the satellite sensors is the combination of the surface reflectance and atmospheric aerosol scattering contribution. Aerosol retrieval algorithms are applied to separate the amount of solar irradiance on the top of the atmosphere scattered by aerosols. The ground surface and aerosols affect the spectral band differently. The Shortwave Infrared (SWIR) wavelength is assumed to be unaffected by the aerosols and the correlation of the reflectances in the visible and SWIR wavelength band has been utilized to estimate the surface reflectance values and retrieve the aerosol contribution (L. A. Remer et al., 2005).

Numerous aerosol retrieval algorithms have been designed and applied to multiple satellite sensors, producing various aerosol products. The Dark Target (DT) and Deep

Blue (DB) aerosol retrieval algorithms are the most used and well-performed algorithms. The DT and DB algorithms have been applied to Aqua and Terra MODIS to produce the MODIS aerosol products (L. A. Remer et al., 2005).

MODIS has been generating AOD datasets for more than two decades. The MODIS AOD retrievals are provided at 10 (km) spatial resolution over land (Y. J. Kaufman, Tanré, Remer, et al., 1997; Levy et al., 2013) and ocean (Jeffrey Lee, Gill, Mulligan, Dominguez Acosta, & Perez, 2009; Sayer et al., 2014; Tanré et al., 1997). The MODIS AOD retrievals can be classified based on the surface type and retrieval algorithms, AOD over dark surfaces and oceans is retrieved using the DT algorithm (Y. J. Kaufman, Tanré, Remer, et al., 1997; Lorraine A. Remer & Kaufman, 1998) while the DB algorithm is applied to retrieve AOD over bright surfaces with higher surface reflectance such as arid (deserts), semi-arid and urban regions (Hsu, Tsay, King, & Herman, 2004). The second generation of MODIS AOD products tried to improve the spatial resolution of AOD retrievals and the MODIS DT AOD product at a finer spatial resolution of 3 (km) has been provided over land and the ocean (Levy et al., 2013; L. A. Remer, Mattoo, Levy, & Munchak, 2013). The MODIS DB algorithm which was designed to retrieve AOD over bright surfaces in its earlier version has been enhanced to the next generation of the DB algorithm namely the 'enhanced DB' method to retrieve aerosol properties not only over bright surfaces but also over dark ones. This provides the MODIS DB AOD product with higher spatial coverage (Hsu et al., 2013). The MODIS operational aerosol products provide spectral AOD retrievals at three visible wavelengths (0.47, 0.55, and 0.66 μm) over land using the DB and DT land algorithms, whilst, over the ocean, spectral AOD retrievals are provided at seven wavelengths from 0.47 μm to 2.13 μm by the DT ocean algorithm (Levy et al., 2013; L. A. Remer et al., 2005, 2013, 2002). The attempt to retrieve AOD at better spatial resolution has been sustained until the Multi-Angle Implementation of Atmospheric Correction (MAIAC) algorithm has been proposed and applied to MODIS radiance measurements. The MODIS MAIAC AOD product provides aerosol retrievals at a 1-km spatial resolution. Same as MODIS DT and DB AOD products, the MODIS MAIAC AOD product provides AOD retrievals over dark and bright surfaces (A. Lyapustin et al., 2011; Alexei Lyapustin, Martonchik, Wang, Laszlo, & Korkin, 2011a; Alexei Lyapustin, Wang, Korkin, & Huang, 2018).

The VIIRS aerosol product which is aimed to provide the continuity for the decadal aerosol retrievals of MODIS instrument follows the principles of its predecessor MODIS AOD algorithms (H. Liu et al., 2014). Same as MODIS aerosol products, the DT algorithm is primarily applied to the VIIRS radiance measurements to provide the VIIRS DT AOD product. The VIIRS DT AOD retrievals were restricted to dark land and non-sunglint-affected ocean surfaces (Jackson et al., 2013). The later VIIRS DB aerosol product extended the spatial coverage of VIIRS aerosol product to both dark and bright land surfaces (Hsu et al., 2019). In addition to land AOD retrievals, the VIIRS AOD product provides AOD retrievals over the ocean surface. In the VIIRS AOD products, the AODs over water surfaces are provided by the Satellite Ocean Aerosol Retrieval (SOAR) algorithm (Sayer et al., 2012; Sayer, Hsu, Lee, Bettenhausen, et al., 2018).

In the following section, the steps which are taken to retrieve AOD by different algorithms including DT, DB, MAIAC, and SOAR are discussed briefly.

2.2.1 MODIS DT algorithm

The MODIS DT algorithm uses the calibrated L1B MODIS reflectance data which are corrected for the gas and water vapor contamination and organized into retrieval windows of N × N pixels (N = 20 or 6) at 500 m resolution. The windows are masked out if pixels within them are cloud contaminated, or contain shallow/inland water, or snow/ice pixels (R.-R. Li, Kaufman, Gao, & Davis, 2003; Martins et al., 2002). Cloud contamination is one of the greatest uncertainties in retrieving aerosol properties (e.g. AOD), especially over the ocean (Y.J. Kaufman et al., 2005; J. Zhang, Reid, & Holben, 2005) where it can lead to consistent overestimation of satellite-retrieved AODs if not adequately removed (L. Remer et al., 2012). Whilst cloud contamination causes significant errors in AOD retrievals, applying stringent cloud masks results in the greater omission of cloud-free pixels. Modifications of the cloud masks used in MOD04 Collection 6 (C6) increased the number of aerosol retrievals (e.g. by 5% for example granules over northeastern South America) (Hsu et al., 2013; Levy et al., 2013). Further updates to the cloud mask algorithm in C6.1 enabled AOD retrievals of smoke through its improved discrimination from a cloud (Levy et al., 2013). Collection 6.1 also upgraded the sediment mask which reduced the bias in coastal regions with high sediment concentration in which the near-zero water-leaving radiances are not valid (R.-R. Li et al., 2003). Increases in the spatial resolution (250 m) of the water mask reduced the uncertainty in AOD retrievals in regions with heterogeneous land/water cover or complicated structures such as coastal regions, lakes, and river basins (Carroll, Townshend, DiMiceli, Loboda, & Sohlberg, 2011).

2.2.1.1 MODIS DT land algorithm

The underlying basis of the DT algorithm is that top-of-the-atmosphere (TOA) radiance is influenced least by surface reflectance and that the atmospheric contribution is higher over the regions which look dark in the visible (VIS; 0.4–0.7 μm) spectrum (Tanré et al., 1997). To filter out bright land surfaces, a threshold is applied to the reflectance at 2.12 μm (between 0.01 and 0.25), and of these pixels, the brightest 50% and darkest 20% of pixels at 0.66 μm are discarded. After discarding all inappropriate bright pixels from each 10 km × 10 km block, the surface reflectance is estimated using the relationship between surface reflectance at 0.47, 0.65, and 2.11 μm wavebands (“VISvs2.1”) (Y. J. Kaufman, Tanré, Gordon, et al., 1997). In C6, the static value of VISvs2.1 was redefined to be a function of scattering angle and $NDVI_{SWIR}$ values. In C6.1, to improve the AOD retrievals over urban areas, the urban land cover percentage (UP) is incorporated into the calculation of surface reflectance if the urban percentage cover exceeds 20% (Gupta, Levy, Mattoo, Remer, & Munchak, 2016). Look-up tables (LUT) for MODIS DT represent five aerosol models, four of them reflecting the properties of fine and spherical type particles (non-dust) and one reflecting the properties of coarse and spheroid type particles (dust) (Levy, Remer, & Dubovik, 2007). Finally, the average surface reflectance of remaining pixels (at least 12 out of 400 pixels) at 0.47 μm, 0.65 μm is calculated and compared to the assumed TOA reflectance in pre-calculated LUTs and the match with minimum residual is used to retrieve the AOD (Levy, Remer, Mattoo, Vermote, & Kaufman, 2007).

2.2.1.2 MODIS DT OCEAN algorithm

If all pixels in a 10-km × 10-km area are water pixels, the DT algorithm for the ocean is applied. In the DT ocean algorithm, the brightest and darkest 25% of pixels within a box at 0.86 μm waveband are discarded (L. A. Remer et al., 2005; L. Remer et al., 2012). The surface reflectance is calculated for six wavelengths (0.55, 0.65, 0.86, 1.24, 1.63, and 2.11 μm) which is then used to find the best match in the LUTs which calculate aerosol retrievals using the weighted combination of nine aerosol models (modes: four fine, five coarse). Additionally, in C6, the influence of wind speed is accounted for when interpolating the LUT using data from the National Centers for Environmental Prediction (NCEP) at 1° × 1° spatial resolution rather than assuming a constant 6 m s^{-1} wind speed (Levy et al., 2013).

2.2.2 MODIS DB algorithm

The need for retrieving aerosol properties over bright surfaces such as deserts, semi-deserts, and urban areas necessitated the development of the DB algorithm (Hsu et al., 2004; Hsu, Tsay, King, & Herman, 2006). The primary DB algorithm retrieves AODs just over bright surfaces, whilst the enhanced DB method retrieves aerosols over arid, semi-arid, vegetated, and built-up areas. In the enhanced DB method, the surface reflectance is estimated by applying one of three schemes depending on the underlying surface type using a pre-constructed global surface reflectance database (Hsu et al., 2013). In the database, surface reflectance is determined at multiple viewing and illumination geometries which accounts for surface bidirectional reflectance distribution function (BRDF) effects which can lead to high bias in a retrieved AOD (Hsu et al., 2006). For the vegetated surfaces, the surface reflectance is estimated using the VISvs2.1 relationship at multiple subgroups depending on $NDVI_{SWIR}$ values and seasons. The surface reflectance for urban surfaces is determined by applying one of the above approaches or a combination of them (Hsu et al., 2013). LUTs for the enhanced DB method are calculated for multiple viewing geometries, aerosol loadings, and surface conditions. Selection of the best match between the estimated and measured surface reflectance is carried out by computing the mixing ratio between the dust and smoke aerosol models. By utilizing the best match, the aerosol optical properties are retrieved for both dust-dominated and mixed aerosol (dust and fine-dominated) cases (Hsu et al., 2004, 2006).

2.2.3 MODIS MAIAC product (MCD19A2)

The MAIAC AOD dataset provides a 1-km spatial resolution of AOD retrievals at a daily temporal frequency (A. Lyapustin et al., 2011; Alexei Lyapustin, Martonchik, Wang, Laszlo, & Korkin, 2011b). In the MAIAC algorithm, the L1B MODIS data are gridded to a 1-km resolution where cloud-contaminated pixels are removed whilst retaining smoke/dust pixels (A. Lyapustin, Korkin, Wang, Quayle, & Laszlo, 2012; A. Lyapustin, Wang, Laszlo, & Korkin, 2012; A. Lyapustin et al., 2014; Alexei Lyapustin et al., 2018). The MAIAC algorithm utilizes a time series of multi-angle observations acquired over four days at the polar regions and 16 days at the equator) to characterize the BRDF. The Lambertian equivalent reflector (LER) surface model is used to estimate the surface reflectance at 0.47 μm and 2.13 μm from which a spectral regression coefficient (SRC) between the surface reflectance (B3/B7) is calculated for each observation. To optimize surface reflectance estimation, the SRC over bright surfaces is computed for additional three-view angles. One of the most important developments in the C6 MAIAC algorithm compared to its earlier versions is that the surface reflectance is estimated at a pixel scale rather than within the 25×25 km windows which reduces the AOD "Blockiness" which is caused by random SRC bias (Alexei Lyapustin et al., 2018). Eight LUTs are used for aerosol retrievals which are based on eight regional aerosol models that are representative of the AERONET regional climatology (A. Lyapustin et al., 2011; Alexei Lyapustin et al., 2011b). Following the MAIAC AOD retrieval, a mesoscale AOD-based cloud mask is applied to detect subpixel clouds (Alexei Lyapustin et al., 2018).

2.2.4 VIIRS DB product (AERDB_L2)

The VIIRS aerosol algorithm utilizes the M-bands (M1-M7), covering a spectral range between 0.41 and 2.25 μm which have a higher signal-to-noise ratio (SNR) at low radiance values, to retrieve aerosol properties (Cao et al., 2013). The primary VIIRS aerosol retrieval algorithm is based on the MODIS DT aerosol retrieval algorithm heritage with some alterations in the surface reflectance estimation and aerosol model assumption (H. Liu et al., 2014). Similar to the MODIS aerosol retrieval procedure, the VIIRS DT algorithm uses empirically derived relationships between surface reflectance in the visible and SWIR bands (M1/M5 = 0.513, M11/M5 = 1.788) to estimate aerosol during the day over dark land and non-sunglint affected ocean surfaces (Jackson et al., 2013). The primary VIIRS DT aerosol product displays similar performance to MODIS DT against AERONET measurements with about 50–75% of retrievals falling within the expected uncertainty range, performing better over highly vegetated surfaces (J. Huang et al., 2016; H. Liu et al., 2014; Wei & Sun, 2017). The enhanced DB algorithm providing aerosol products over vegetated surfaces as well as the brighter surfaces (deserts) and built-up areas has been applied to VIIRS data (Hsu et al., 2013, 2019). The VIIRS AOD product provides retrievals over the ocean using the SOAR algorithm, providing full coverage over the land and ocean (Sayer et al., 2012; Sayer, Hsu, Lee, Bettenhausen, et al., 2018; Sayer, Hsu, Lee, Kim, et al., 2018). The VIIRS aerosol retrieval is performed at the pixel level and produces aerosol retrievals with a spatial resolution of 0.75 km which are then aggregated to 6 km (8 × 8 pixels) resolution at nadir (Jackson et al., 2013).

2.3 Accuracy of Satellite AOD Data and Validation Against AERONET AOD Measurements

The use of AOD retrievals from satellite data requires the assessment of the performances of retrieval algorithms. The reliability of the satellite aerosol dataset for the interpretation of the regional and global aerosol variability should be evaluated carefully. The AERONET AOD measurements are widely used for the validation of satellite AOD retrievals. Numerous studies have validated AOD measurements at AERONET sites to examine the performances of the satellite aerosol retrieval algorithms (Chu et al., 2002; de Leeuw et al., 2015; Gueymard & Yang, 2020; J. Huang et al., 2016; Kahn et al., 2005; H. Liu et al., 2014; L. A. Remer et al., 2005, 2002; H. Shi, Xiao, Zhan, Ma, & Tian, 2019; Wei, Li, Peng, & Sun, 2019). MODIS AOD retrievals in various parts of the earth have been validated using the AERONET AOD measurements. Bibi et al. (2015) found reasonable agreement between MODIS DT/DB and AERONET AODs over sites on the Indo-Gangetic plains ($r > 0.73$) (Bibi et al., 2015). Over AERONET sites in Alaska, McPhetres and Aggarwal (2018) (McPhetres & Aggarwal, 2018) reported a moderate correlation ($r > 0.67$), between MODIS DT (10-km and 3-km) and AERONET AOD datasets, with higher correlations for the 10-km compared to the 3-km product but with differences in AOD magnitude. Che et al. (2019) found the DT retrievals achieved a satisfactory retrieval accuracy (70.2% within EE) over the forest, cropland, and grassland but lower performance over urban surfaces (within EEs <61%) (Che et al., 2019). By evaluating the MODIS DB dataset at a global scale, Wei et al. (2019) reported satisfactory performance of the DB product not just over bright surfaces but also over medium or densely vegetated regions (Wei, Li, et al., 2019). Shi et al. (2019) reported a positive bias for the DT dataset, indicating an overestimation relative to AERONET AOD and a negative bias for the DB product which were lower in magnitude (0.0045) than the DT dataset (0.001–0.035) (H. Shi et al., 2019). Likewise, Bilal et al. (2016) and Xiao et al. (2016) reported high positive bias for MODIS DT AOD products compared to AERONET

AOD measurements over sites in Pakistan and East Asia, respectively, despite high correlations (r > 0.89) (Bilal, Nichol, & Nazeer, 2016; Xiao et al., 2016). Over India, Tripathi et al. (2005) and Prasad and Singh (2007) reported a significant overestimation of MODIS DT during the dust-loading seasons (Prasad et al., 2007; Tripathi et al., 2005). Over the Mediterranean basin, Papadimas et al. (2007) reported good agreement between the MODIS DT and AERONET AOD (r = 0.76) although with overestimation (underestimation) of AERONET AODs smaller (larger) than 0.25. The discrepancies were attributed to uncertainties in the surface reflectance especially the over brighter surfaces that exhibit higher surface albedos. Tuna Tuygun et al. (2020) found MODIS DT AOD at 10-km and 3-km resolutions overestimated AOD during both low and high aerosol loadings, particularly over urban areas where 48–62% of the retrievals fell above the expected error (Tuna Tuygun, Ozdemir, & Elbir, 2020). Georgoulias et al. (2016) found good agreement between MODIS DT/DB AOD and AERONET AOD (within EE > 66%), with lower correlations between MODIS DB AOD retrievals (r < 0.60) compared to DT AOD retrievals (r > 0.86) (A. K. Georgoulias et al., 2016). Several studies have assessed the performance of MODIS Terra and Aqua AOD products against independent datasets. Gupta et al. (2018) found similar correlations between Aqua and Terra MODIS 3-km DT AOD but that higher positive bias was found with Terra MODIS AODs (Gupta, Remer, Levy, & Mattoo, 2018). Wei et al. (2019) also found that Aqua AOD products were more accurate than Terra AOD products in terms of the annual mean AOD loadings over the land surface at a global scale (Wei, Li, et al., 2019). However, Bilal et al. (2021) reported equal performance for Aqua and Terra AOD products in terms of correlation and the percentage of retrievals within the EE in Pakistan (Bilal et al., 2021).

The VIIRS DB and VIIRS SOAR aerosol products have also been validated against AERONET AOD measurements globally over the land and ocean surface with the results indicating a high percentage of retrievals over land fall within the EE (78–80%) but with lower performances over sites with low aerosol loading (Bilal, Nazeer, & Nichol, 2017; Hsu et al., 2019; Sayer, Hsu, Lee, Kim, & Dutcher, 2019). Over the ocean, the SOAR AOD retrievals were strongly correlated with AERONET AOD measurements (r > 0.86) which improved the quality and quantity of AOD retrievals over shallow coastal water by applying an alternative algorithm (Sayer et al., 2012; Sayer, Hsu, Lee, Kim, et al., 2018).

In addition to AOD validation against AERONET AOD measurements, numerous studies have carried out intercomparisons between AOD retrieval algorithms. Comparisons between the MODIS DT and DB AOD retrievals have been carried out globally (Bilal, Nichol, & Wang, 2017; Hsu et al., 2013; Sayer et al., 2014) and locally (Bilal et al., 2019; Mhawish, Banerjee, Broday, Misra, & Tripathi, 2017; Misra, Jayaraman, & Ganguly, 2015; Y. Xie, Zhang, Xiong, Qu, & Che, 2011) with the results indicating similar levels of agreement with ground-based AOD measurements. Generally, higher performance is found with the DT algorithm over moderately-highly vegetated areas (e.g. cropland and forest) whilst the DB often had a better correlation with AERONET over the sites located in sparsely vegetated areas with higher surface reflectance (e.g. urban areas and arid, semi-arid regions). Similar results were reported by Tao et al. (2015) and Filonchyk and Hurynovich (2020) over China (and Eastern Europe) (Filonchyk & Hurynovich, 2020; Tao et al., 2015). In addition to the advantage of effective aerosol retrievals over bright surfaces by the DB algorithm, Hsu et al. (2006) revealed the capability of the DB algorithm in separating fine-mode anthropogenic pollution from dust plumes, even in a mixed aerosol environment (Hsu et al., 2006). The MODIS MAIAC aerosol product has also been compared to the lower spatial resolution MODIS DT and DB AOD retrievals with the results highlighting the greater spatiotemporal coverage of MAIAC and the better agreement with AERONET AODs, especially over mixed surface types (Qin et al., 2021). Jethva et al. (2019) reported a high correlation coefficient (0.90 and 0.93) between AERONET and MODIS DT and MAIAC products, respectively, over darker surfaces compared to the DB algorithm (r = 0.756) (Jethva, Torres, & Yoshida, 2019). The MAIAC algorithm also had the lowest RMSE (0.056) whilst over bright surfaces the DB and MAIAC algorithms have a robust agreement with AERONET (r = 0.72–0.83). Chen et al. (2020) also reported the highest correlation coefficient for the MODIS MAIAC aerosol product with AERONET AOD measurements and the lowest RMSE among the other MODIS aerosol products (e.g. DT and DB) (C. Chen et al., 2020). The MAIAC has the advantage of improved cloud/snow/ice masks, its higher spatial resolution enables the identification of hotspots of high AOD and it provides reliable performance over both dark and bright surfaces (Jethva et al., 2019; N. Liu et al., 2019; Mhawish et al., 2019; Tao et al., 2019).

2.4 Validation of Satellite Aerosol Products Over the Eastern Mediterranean and Black Sea

Depending on the geographical region, climate, and weather conditions, satellite aerosol products may perform differently. The best performer aerosol retrieval algorithm should be identified by validation of satellite AOD retrievals against AERONET AOD measurement and intercomparison of available aerosol products. In this section, a comprehensive assessment of MODIS and VIIRS AOD products over the eastern Mediterranean and Black Sea is conducted. We have seven satellite AOD products including the MODIS DB (10-km), MODIS DT at two spatial resolutions (10-km and 3-km), and MODIS MAIAC (1-km) AOD products. In addition to MODIS aerosol products, the assessment of VIIRS AOD products is performed. The VIIRS Aerosol product includes the AOD retrievals by enhanced DB and SOAR retrieval algorithms which produce AODs at spatial resolutions of 6-km. Ground-truth AOD measurements were obtained from three AERONET stations located in the study region including the IMS METU Erdemli (e.g., Erdemli) station and AERONET stations in Bulgaria (Galata) and Greece (Thessaloniki). The AERONET stations are selected based on 1) the wholeness of the AOD measurements between 2014-2018 and 2) the representation of three main surface types. As the surface type can be effective in the performance of the retrieval algorithm by changing the uncertainties of AOD retrievals due to surface reflectance estimations, optimal assessment of aerosol retrieval algorithms necessitates the reflection of multiple surface types. The different surface characteristics of urban/land, rural/coastal, and ocean are represented by Thessaloniki, Erdemli, and Galata Aironet stations, respectively. The performance of aerosol retrieval algorithms was intercompared and the best performer over each surface type is identified. Other than the intercomparison of AOD datasets over three AERONET sites, the aerosol retrieval algorithms were intercompared over locations in which the AERONET stations are not available. It will serve as an indicator of the consistency of aerosol retrieval algorithms at locations without ground-truth AOD measurements.

2.4.1 Data used

2.4.1.1 Satellite AOD products

We used daily MODIS aerosol products obtained from 2014 to 2018 with spatial resolutions of 10-km (MXD04_L2) and 3-km (MOD04_3K), which made up about 14,119 images of Terra (MOD04_L2) and 14,387 of the Aqua products (MYD04_L2 and MYD04_3K), where 8650, 8350, and 11502 of the images respectively covered the Thessaloniki, Erdemli, and Galata. For MODIS DT AOD retrievals, we use pixels with QA filters of QF > 1 in the ocean, QF = 3 for land, and QF ≥ 2 for MODIS DB AOD retrievals. In this study, daily MODIS MAIAC AOD Level 2 gridded data at 1-km resolution (MCD19A2) acquired between 2014 and 2018 are used. There are 11,205 Terra images and approximately 12,119 Aqua images in the MODIS AOD dataset. To perform further analysis, only the highest quality MAIAC AOD retrievals are retained. The number of MAIAC AOD retrievals decreases significantly (by 36% and 55% for Terra and Aqua respectively) after QA filtering due to stricter quality assurance cloud masks in the MAIAC AOD retrieval procedure. It is important to note that the MAIAC algorithm is only applied to tiles classified as land or that contain a combination of land and ocean pixels (i.e., no retrievals for 100% ocean tiles, (Alexei Lyapustin et al., 2018)). In addition, the AOD level 2 product from VIIRS DB is used (AERDB_L2_VIIRS_SNPP) (6-km at nadir) and consists of 8734 aerosol product images, of which around 2917, 2724, and 3093 cover Thessaloniki, Erdemli, and Galata AERONET stations, respectively. AOD retrievals from the VIIRS DB with a QA flag of 2 or 3 were used in this study.

AERONET AOD measurements

Other than Erdemli AERONET station which is the only AERONET station in Turkey having the complete set of AOD measurements between 2014 1n 2018, the AOD measurements from two AERONET stations namely the Thessaloniki and Galata are located in Greece and Bulgaria are utilized in this study. Table 2.1 lists the AERONET sites used in this study, and Figure 2.2 shows their geographical locations. AERONET's version 3.0 level 2.0 AOD measurements between 2014 and 2018 are used to validate MODIS and VIIRS aerosol products. Accordingly, the Thessaloniki, Galata, and Erdemli AERONET stations have measured AOD for 1131, 1118, and 994 days, respectively, that is, 38693, 35225, and 30150 AOD measurements.

Table 2.1 : Details of the AERONET Sites.

AERONET Site	Longitude/Latitude, deg	Elevation, m	Country	Surface type
Erdemli	34.255E / 36.565N	3	Turkey	Coastal
Galata	28.193E / 43.045N	31	Bulgaria	Ocean
Thessaloniki	22.960E / 40.630N	60	Greece	Land

Figure 2.2 : Image of the Eastern Mediterranean showing the locations (Red points) of AERONET stations in Turkey (Erdemli), Greece (Thessaloniki), and Bulgaria (Galata) with finer detail shown in the inset images.

The Erdemli station (Figure 2.3 (b)) is located in a rural site on the southeastern coast of Turkey which, according to the Corine land cover (CLC) 2018 map, is a complex cultivation pattern class and surrounded by semi-forested land cover. Also shown is the average annual albedo (2018) from the MCD43A3 product (visible white-sky surface albedo data; (Schaaf et al., 2002)), which indicates areas of high albedo are industrialized agricultural installations (e.g., greenhouses) and artificial surfaces in the villages with scattered buildings in the near vicinity. The Galata station (Figure 2.3(c)) is located in the Western Black Sea on the Bulgarian shelf 26-km east of the city of Varna. The station is surrounded by water and presents the lowest annual mean albedo which is marginally higher near the coastline due to the sediments in shallow water. Lastly, the Thessaloniki station (Figure 2.3 (a)) is located at the center of Thessaloniki which is surrounded by “Continuous and/or Discontinuous urban fabric” and “Industrial or commercial units”. The annual average albedo is therefore generally high but reduces over the surrounding forest hills to the north and east (Figure 2.3).

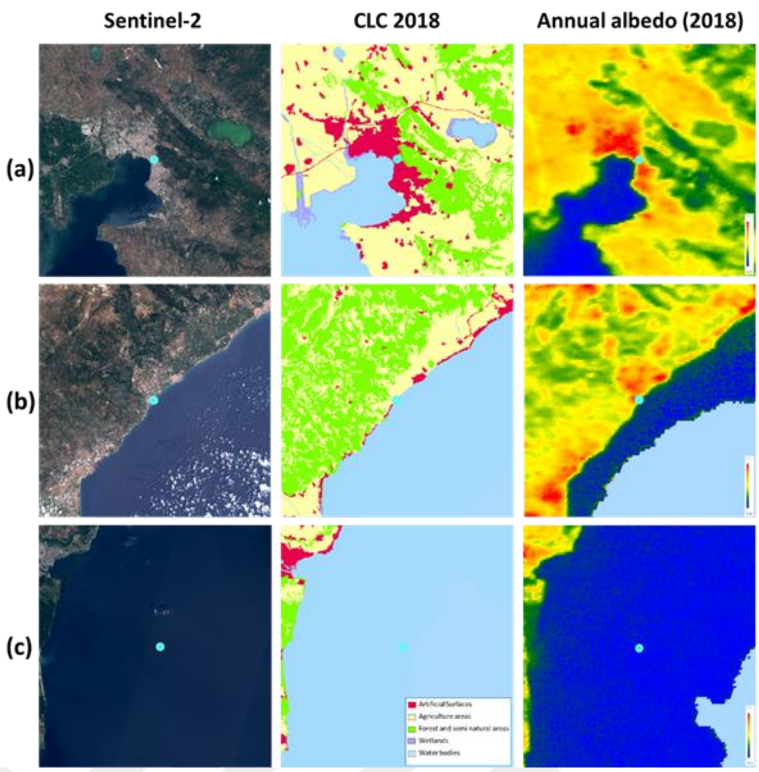

Figure 2.3 : A sentinel-2 true color image (2-3 July 2018), the Corrine LCU and annual average MDC43 albedo within 25km distance (covering the 5x5 pixels of AOD at 10km scale) of the in-situ AOD station (cyan points) for a) Thessaloniki, b) Erdemli, and c) Galata sites respectively.

2.4.2 Methodology

AOD measurements from AERONET and satellite AOD retrievals need to match in both space and time (Chu et al., 2002; Levy et al., 2010; L. A. Remer et al., 2005). To match in time, the average of AERONET AOD measurements is calculated within a specific time range of the satellite overpass of the AERONET station. By this means, the higher sampling rate of ground-based AOD measurement is utilized. Since AERONET measured AOD at 500 nm, AOD at 550 nm should be calculated by interpolation using the standard Ångström exponent (α) (Sayer, Hsu, Bettenhausen, & Jeong, 2013) to compare versus satellite AOD retrievals which are commonly measured at 550 nm wavelength.

To match in space, an average of pixels of satellite AOD retrievals within a sampling window centered on the AERONET station is calculated. This is required to consider the spatial variability imposed by atmospheric motion (Ichoku et al., 2002; W. Wang, Mao, Pan, Du, & Gong, 2017). In this study, the temporal window of ± 30 min and the spatial window of 5 × 5 pixels are selected for the collocation of satellite AOD retrievals and AERONET AOD measurements. The average of at least 2 out of possible 25 pixels in the spatial window samples is collocated with the average of at least 2 out of 4 possible AERONET AOD measurements in the ± 30 min temporal window samples. The steps of selecting optimal spatiotemporal window size and the impacts of using AODs of high-quality flags are discussed in section 3.1.

To quantitatively evaluate the accuracy of AOD products, Pearson's correlation coefficient (r) based on linear regression is selected to analyze the correlation between satellite AOD retrievals and AERONET AOD measurements. The uncertainty of the retrieval is quantified using the expected error (EE) envelope. The EE represents the totality of relative and absolute error. The EE over land is defined by equation 2.1 (Levy et al., 2010) and the EE over the ocean is defined by equation 2.2 (Levy et al., 2013). The percentage which has been defined as the least accepted one for having the normal set of satellite AOD retrievals is 67% of retrievals fall within the envelopes EE (e.g. within%) over land and ocean. The 67% of the set is about one standard deviation of the mean. The Root-Mean-Square Error (RMSE, equation 2.3) is used to report errors and the bias is estimated using equation 2.4.

$$EE(over\ land) = \pm(0.05 + 0.15(AOD)) \tag{2.1}$$

$$EE(over\ ocean) = +(0.04 + 0.1(AOD)), -(0.02 + 0.1(AOD)) \tag{2.2}$$

$$RMSE = \sqrt{\frac{1}{n}\sum_{i=1}^{n}(AOD_{satellite} - AOD_{AERONET})^2} \tag{2.3}$$

$$\text{Mean Bias (MB)} = \text{arithmetic mean } (AOD_{Satellite} - AOD_{AERNET}) \tag{2.4}$$

The AERONET AOD measurements can be classified into two categories of low and high observations. Low observations are AERONET AOD measurements lower than 0.2 and the AOD measurement higher than 0.5 are categorized as high observations. The MB of these two categories can be studied separately. The MB_{Low} and MB_{High} are the indicators of MB of these distinctive categories in this study.

2.4.2.1 Data pre-processing

Spatial collocation

To the assessment of selecting optimal window size, two window sizes are tried for the MODIS-AquaTerra MAIAC AOD retrievals at 1 km (hereafter referred to as the MAIAC_1) having the highest spatial resolution among other AOD products used in this study. Assuming that we have two aerosol products, the MAIAC at 1 km and the MODIS DT at 3 km, one sampling window with a radius of ±2.5 km and the other one with a radius of ±7.5 km, centered at AERONET stations are applied. A sampling window with a radius of ±2.5 km stands for using the same number of pixels (5 × 5 pixels of AOD at a 1km scale (5 × 5 km2) and one with a spatial radius of ±7.5 km represents using the same size of sampling window with AOD product of lower spatial resolution (15 × 15 km2 or 5 × 5 pixels of AOD at a 3km scale). Table 2.2 shows the overall validation results of “high quality“ MAIAC_1 (2014 - 2018) against AERONET AOD measurements applying different sampling window sizes.

A small number of collocated AOD retrievals (N) are available for a smaller sampling window (±2.5 km) (Table 2.2). The number of retrievals decreases of 4%–10% narrowing the sample window. Although the r values are almost the same, the RMSE is reduced on average to 0.0085 lower for the smaller window. According to slightly higher within% and lower RMSE in the case of using a smaller sampling window (Table 2.2), the average of AOD pixels in the sampling window roughly covered a 5 × 5-pixel group (average of 25 pixels) is used in this work-study. Applying a sampling window according to the spatial resolution of the aerosol product (multiple sampling windows rather than the fixed 50 × 50 km2 region which contains the 5 × 5 pixels of AOD product at the lowest spatial resolution (10 km)) will also support the utilization of finer resolution aerosol products (3km and 1km satellite AOD retrievals). Therefore, the capability of aerosol products at higher spatial resolution at identifying the detailed local aerosols can be assessed for further uses. A chosen sampling window of 5 × 5 pixels means the satellite AOD retrievals within a spatial radius (Sr) of ± 25 km for MODIS-Aqua/Terra AOD retrievals at 10 km, ± 15 km VIIRS AOD retrievals at 6 km, ± 7.5 km for MODIS-Aqua/Terra AOD at 3 km retrievals, and ± 2.5 km for AquaTerra MODIS AOD retrievals at 1 km.

Table 2.2 : Analysis of the impacts of different window sizes on validation of satellite AOD retrievals.

Station	Sr (km)	N	r	RMSE	Within %
Thessaloniki	± 7.5	1026	0.77	0.065	83.53
	± 2.5	953	0.77	0.062	85.63
Erdemli	± 7.5	947	0.79	0.080	82.15
	± 2.5	912	0.79	0.078	82.25
Galata	± 7.5	697	0.73	0.078	58.68
	± 2.5	625	0.79	0.063	62.40

Temporal collocation and quality flag filter

The quality of satellite AOD retrieval is represented by the quality flag (QF), ranging between 0 (low confidence) and 3 (high confidence). The use of the AOD retrievals with QF ≥ 1 over the ocean and QF = 3 over a land surface is strongly recommended (Levy et al., 2010; L. A. Remer et al., 2013; Sayer et al., 2013). To investigate the effects of the QF on the performances of aerosol algorithms, the accuracy of collocated VIIRS AOD retrievals and AERONET AOD measurements are calculated for before and after quality flag filtering. Table 2.3 shows the validation of all VIIRS AOD retrievals with any of the QFs (all retrievals) compared to those with high quality (QF= "High") (high quality (HQ) only) against AEORNET AOD retrievals.

Besides the assessment of the effects of quality flag filtering, to evaluate the impacts of the various temporal segment, results of evaluating VIIRS AOD retrievals against the average of AERONET AOD measurements within ±30 min of Suomi NPP overpass and an average of those measured during a day (daily average AERONET AOD measurements) are also inter-compared (Table 2.3).

Table 2.3 : Statistics of comparisons between VIIRS AOD retrievals and AERONET AOD measurements, before and after filtering by quality flags at two temporal segments.

	Daily Average of AERONET AOD measurements					AERONET AOD measurement within ±30 min				
Stations	Dataset	N	R	RMSE	Within %	Dataset	N	R	RMSE	Within %
Thessaloniki	all retrievals	1032	0.77	0.104	66.18	all retrievals	865	0.84	0.080	71.33
	HQ only	792	0.82	0.064	80.43	HQ only	724	0.84	0.061	82.04
Erdemli	all retrievals	1029	0.82	0.078	80.01	all retrievals	951	0.84	0.073	82.54
	HQ only	823	0.83	0.077	83.07	HQ only	732	0.86	0.069	85.75
Galata	all retrievals	961	0.73	0.102	54.01	all retrievals	609	0.79	0.086	50.57
	HQ only	846	0.82	0.080	68.68	HQ only	561	0.93	0.061	65.95

For daily AERONET measurements and high-quality VIIRS AOD retrievals (HQ only), the numbers of matchups decreased by 12% and 24%, but the percentage of retrievals falling within the EE increased by an average of 15% compared to “all retrievals (left portion of Table 2.3). For average AERONET AOD measurements within ±30 min and the HQ-only data, the number of matchups decreased by 8% and 23% while the percentage within the EE increased by 14% on average. The r is slightly when the AERONET data is averaged over the day or ±30 min and between the ‘HQ only’ and ‘all retrievals’ scenarios. The change of r caused by using only the high-quality data is obvious at Galata station; from 0.79 to 0.93 and 0.73 to 0.82 when the AERONET data is averaged over the day or ±30 min, respectively. Also, the quality flag filtering decreases the RMSE noticeably at all stations which is between 0.073 and 0.104 in the all-retrievals case and between 0.061 and 0.080 in high-quality retrievals selection (Table 2.3).

As shown in Table 2.3, data filtering based on quality flags has a greater impact on the evaluation of AOD retrievals over the ocean (Galata station) than over land and coastal areas (Thessaloniki and Erdemli stations). On average, the high-quality dataset exhibited better performance against AERONET AOD measurements than the "all retrievals" dataset.

Using the average of AERONET AOD measurements within ±30 min of satellite overpass instead of daily AERONET measurements for validation of VIIRS AOD retrievals decreases the number of AOD matchups for both datasets and the greatest decline is seen in Galata station. The r and the within% increased and the RMSE decreased by applying the temporal segment filter at all three stations for high-quality VIIRS AOD retrievals. For these reasons, “high-quality only” AOD retrievals within ± 30 min of satellite overpass are the recommended pair to be used in satellite AOD evaluations against AERONET AOD measurements (Table 2.3). The MAIAC AOD product is generated using data from both Terra and Aqua satellites. Consequently, AERONET AOD measurements are computed between 10:00 am and 2:00 pm since this overlaps the overpass times for the two satellites to validate the MAIAC AOD retrievals.

2.5 Results

2.5.1 Satellite AOD comparison against AERONET measurements

Figure 2.4 presents scatter plots of coincident satellite AOD retrievals and AERONET observations over Urban/land, ocean, and Rural/coastal surfaces between 2014 and 2018. The number of points varies between 346 and 727, 307 and 718, and 308 and 637 for land, coastal, and ocean scenes respectively over this period. The greatest part of the coincident observations is from the retrievals in summer (June-July-August (JJA)) (28-48%) and 16-30%, 9-32%, and 10-23% of them are from retrievals in Spring (March-April-May (MAM)), Autumn (September-October-November (SON)) and winter (December-January-February (DJF)), respectively

Figure 2.5 displays histograms showing the absolute difference between the satellite AOD and AERONET AOD as a function of the AERONET AOD (in bins 0.1 in width). The Thessaloniki, Erdemli, and Galata stations' data represent the Urban/Land, Rural/Coastal, and Ocean surface types, respectively. The slopes and intercepts of the regression lines showing the relationship between the satellite AOD retrievals and AOD measurements (Figure 2.4) are related to the errors in the surface reflectance estimation and/or assumptions made by the aerosol models used in the retrievals (Chu et al., 2002; Levy et al., 2013). At lower AODs errors are mainly related to surface reflectance estimation or sensor calibration whilst at higher AODs the offsets are mainly due to the errors in the assumptions of aerosol optical properties in the selected aerosol models (L. A. Remer et al., 2002; Sayer et al., 2014).

2.5.1.1 Urban/land site

The best-performing products over the Thessaloniki station with urban/land underlying surface type are the MODIS MAIAC and VIIRS DB AOD products with significant variance in correlation, N, RMSE, and within% evident between the other products. Although over the bright urban areas, the TOA sensitivity to aerosol loading is lower for relatively clear atmospheres dominated with low AODs (L. A. Remer et al., 2002), improvements made by the MAIAC algorithm in the surface reflectance characterization lead to lower biases at lower AODs. The MAIAC AOD retrievals over the urban/land site tend to be over-underestimated slightly at lower AODs with an

MB_{Low} of 0.005 and -0.013 for the Aqua and Terra MAIAC AOD products, respectively, compared to the DT aerosol products with MB_{Low} of 0.010 and 0.014 for the Aqua and Terra AOD products at 10-km resolution. The Aqua and Terra AOD products at a 3km scale have MB_{Low} of 0.071 and 0.075 respectively whereas the MB_{Low} for the VIIRS DB AOD product is 0.021.

The MODIS DT aerosol products tend to overestimate AOD over urban/land (Figures 2.4 and 2.5), which results from errors in surface reflectance estimation due to the spatial heterogeneity of the urban surface. Similar overestimations of the DT algorithm have been found over urban areas in East Asia, the greater Mediterranean region, Turkey, and China (A. K. Georgoulias et al., 2016; Tian, Liu, Li, & Wei, 2018; Tuna Tuygun et al., 2020; Wei & Sun, 2017). The 3-km DT AOD products are noisier than the 10-km scale which could be related to higher land surface variability at higher resolution and the influence of sub-pixel cloud contamination or other non-aerosol signals which are typically discarded at 10 km (Levy et al., 2013; L. A. Remer et al., 2013). The MODIS DT AOD products at 3km tend to have the poorest performance with the highest RMSE (>0.142) and lowest percentage of retrievals within the EE (<55%) over the urban/land site. A similar poor performance of the 3-km DT algorithm over urban land cover has also been observed in other studies (Bilal, Nazeer, Qiu, Ding, & Wei, 2018; Munchak et al., 2013; Nichol & Bilal, 2016), where the higher bias was related to the difficulties of estimating surface reflectance over heterogeneous urban areas using the DT retrieval procedure.

Predefined static aerosol models used through the MAIAC aerosol retrieval procedure which are based on the aerosol climatology data from several specific AERONET stations, can result in AOD retrieval errors, especially at higher AODs. The slopes lower than unity for the Terra and Aqua MAIAC AOD products (0.65 and 0.73, respectively) and the underestimation of the higher AODs (>0.5) (MB_{High} of -0.22 and -0.18 are found for Terra and Aqua MAIAC AOD, respectively) indicate the errors in the aerosol model assumptions. The assumed aerosol model over the Thessaloniki site (urban/land area) in MAIAC is “highly absorbing” with the aerosol properties from the east coast of the USA with high summertime humidity (Alexei Lyapustin et al., 2018). Over the Thessaloniki region, the aerosols comprise non-absorbing fine mode urban and industrial pollution mixed with occasional transported mineral dust from

North Africa, biomass burning emissions, and maritime aerosols from sea sprays (Kabatas, Unal, Pierce, Kindap, & Pozzoli, 2014; Ozdemir et al., 2020).

The VIIRS DB product with the slope nearest unity (0.97) performs well, particularly at high AODs with an MB_{High} of -0.03 compared to the MB_{High} for Aqua and Terra MAIAC AOD retrievals which are -0.18 and -0.22, respectively. Better performance of VIIRS DB at higher AODs might be due to the use of an enhanced radiative transfer model which provides improved accuracies at higher AODs through improved simulation of multiple scattering (Hsu et al., 2019). Although the retrieval procedure of the VIIRS DB and MODIS DB (C6.1) are similar, some improvements applied to VIIRS DB, such as improvements in discriminating the smoke plumes from urban/industrial aerosols and improvements in dust models, have not yet been applied to the MODIS C6.1 (Hsu et al., 2019).

Over the urban/land surface, the best-performing product is the Aqua MAIAC AOD (1km), which has a high correlation (r = 0.82), a low RMSE (0.048), and the highest percentage of retrievals within the EE (89%) although the number of coincident retrievals is lower (346) compared to the other products. The Terra MAIAC and VIIRS DB AOD products also show good correlations (r > 0.78) and within% EE (~ 82%) and the VIIRS DB aerosol product performs the best in terms of slope and intercept of linear regression. One advantage of Terra MAIAC and VIIRS DB over Aqua MAIAC is the higher number of matchups (541 and 724 for Terra MAIAC and VIIRS DB, respectively) which allows greater spatial coverage over the study region.

2.5.1.2 Rural/coastal site

Analysis of the AOD products against their respective AERONET AOD measurements over the Rural/Coastal site (Figure 2.4) indicates the VIIRS DB AOD product to be the best performing. Higher offsets over coastal areas are observable for most aerosol products, and the highest AODs (0.61 - 0.7 and > 0.71 bins) were found over the coastal site (Figure 2.5). AOD retrievals > 0.6 could be due to the whitecaps/foam contaminations of pixels and/or the hygroscopic growth of aerosol particles (K. Raghavendra Kumar et al., 2018; Mhawish et al., 2019). The uncertainties of gridding the data on coastlines can also lead to high offsets in which coastal regions with high sediment concentrations are usually omitted (Alexei Lyapustin et al., 2018). The assumption of nearly zero water-leaving radiance can also lead to significant bias over coastal sites with turbid waters (Jacob C. Anderson et al., 2013; Y. Wang, Wang, Levy, Xu, & Reid, 2017). Other perturbations that lead to noise in aerosol retrievals over coastal sites are wind speed and sunglint (J. C. Anderson et al., 2012; Myhre et al., 2005), artifacts in cloud/snow masks (A. Lyapustin, Korkin, et al., 2012; A. Lyapustin, Wang, et al., 2012; Alexei Lyapustin et al., 2018; Y. Shi et al., 2011), land/water masks (L. A. Remer et al., 2005), and the complex physical properties of aerosols over coastal areas (J. Zhang & Reid, 2006; Zieliński, 2004).

The high performance of the VIIRS product over the coastal site could be partly related to removing mixed land-water pixels which reduces the retrieval errors from mixed-surface types (Hsu et al., 2019). In addition, although shallow coastal water pixels are discarded by former retrieval algorithms, the VIIRS SOAR algorithm applies a threshold using VIIRS M-band 4 to detect moderate turbid or shallow water and applies a backup algorithm that has lower errors over complex coastal waters (Sayer, Hsu, Lee, Kim, et al., 2018). This approach also provides a higher number of retrievals over the coastal interface whilst the dynamic aerosol model selection by the VIIRS DB algorithm leads to lower biases (Jackson et al., 2013; Y. Wang et al., 2017).

The slopes closer to the unity of MODIS DT AODs compared to MAIAC and DB AODs over the Erdemli site highlight the advantages of the DT algorithm in mixed-type and coarse aerosol retrievals. The assumed static aerosol model by MAIAC may not account for the hygroscopic growth of aerosols within a humid coastal environment (Alexei Lyapustin et al., 2018). Although the assumed aerosol model by MAIAC addresses the contribution of dust particles from the Sahara and the Middle East in the region, it primarily represents an arid climate with a larger coarse fraction which seems inappropriate for a site dominated by fine-mode anthropogenic urban/industry aerosols, mixed with marine aerosols from the Mediterranean Sea (Tutsak & Koçak, 2019; X. Xu et al., 2020). The Aqua MODIS shows better performance over the coastal site than the Terra MODIS in terms of r, within%, and RMSE, which can be partly related to the lower marine near-surface wind speed close to offshore during the afternoon (Aqua overpass time) leading to clearer water (low turbidity) along the coast (Lapworth, 2005). As wind speed increases (e.g., during Terra overpass time), glint reflection spreads beyond the 40◦ masks, and the sea forms more white caps (Kleidman, Smirnov, Levy, Mattoo, & Tanre, 2012), which leads to larger biases in

AOD retrievals. The poorer performance of the Terra MODIS to Aqua MODIS may also be related to the Terra MODIS calibration uncertainties (Levy et al., 2018, 2010).

Over the coastal site, the best-performing product is the VIIRS DB, which shows the highest percentage of retrievals within EE (88%), the lowest RMSE of 0.059, and r of 0.88. Poor performance is observed for the MODIS DB algorithm with r ~ 0.45, N ~ 401, Within% ~ 47%, and RMSE ~0.121.

2.5.1.3 Ocean site

The 3-km MODIS DT statistically delivered the best results due to its robustness over the Galata ocean site located in the Black Sea region. The EE envelope over the ocean, represented by the green dashed lines in Figure 2.4, is narrower over the ocean than over land and coastal areas due to the higher accuracy of the ocean cloud mask and its surface characterization. Generally, aerosol products tend to overestimate AODs over the ocean due to cloud contamination (Y. Shi et al., 2011; J. Zhang & Reid, 2006, 2010) and similar overestimation is observed for aerosol products over Galata Station (Figure 2.4). The RMSEs between satellite and AERONET AOD are lower, and the slopes of satellite versus AERONET AODs are nearest to unity for AOD ocean retrievals compared to those over the land and coastal sites. This is related to the lower errors associated with the assumed aerosol model and surface reflectance estimates in aerosol retrieval (Choi et al., 2019; L. A. Remer et al., 2005).

The 3-km Terra-Aqua MODIS DT over the ocean shows the best performance in terms of r (0.92-0.91), Within% (78-80%), and RMSE (0.051-0.047)) whilst the 10 km Terra-Aqua MODIS DT provides the greatest spatial coverage (N = 637-624). The lower number of Ns for the MODIS DT product at 3km than at 10-km over the ocean surface could be related to the increased pixel rejection due to the sub-pixel cloud/shadow/snow contamination at 3km scale since the pixel selection is carried for the smaller blocks of pixels (400 pixels for the 10-km product and 36 pixels for the 3-km product). Removing contaminated pixels leads to higher R and within% and lower RMSEs for the MODIS DT at 3km over the ocean.

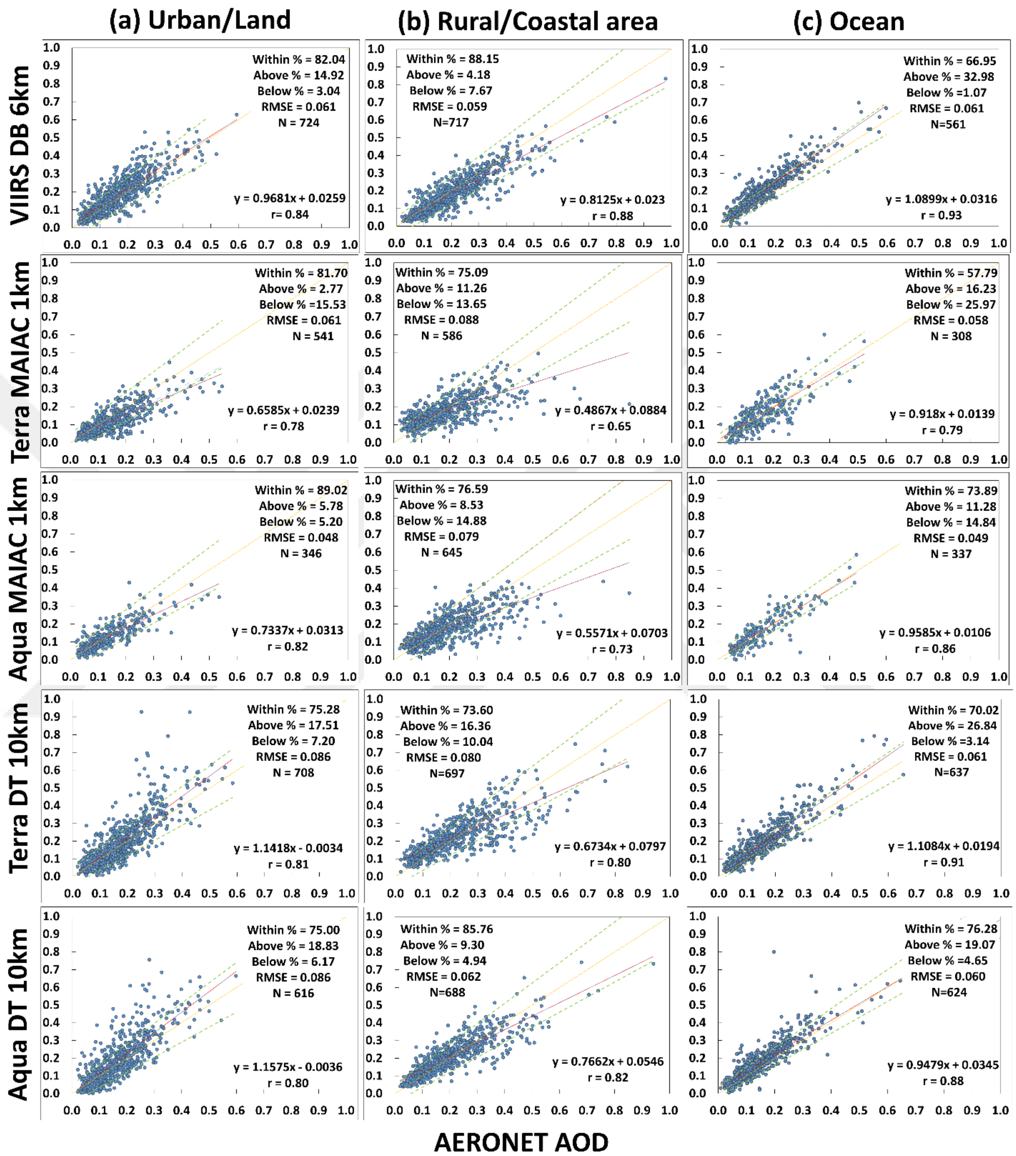

Figure 2.4 : Evaluation of AOD products from MODIS and VIIRS against AERONET AOD measurements between 2014 and 2018 over (a) Urban/Land; (b) Rural/Coastal area; (c) Ocean surface types.

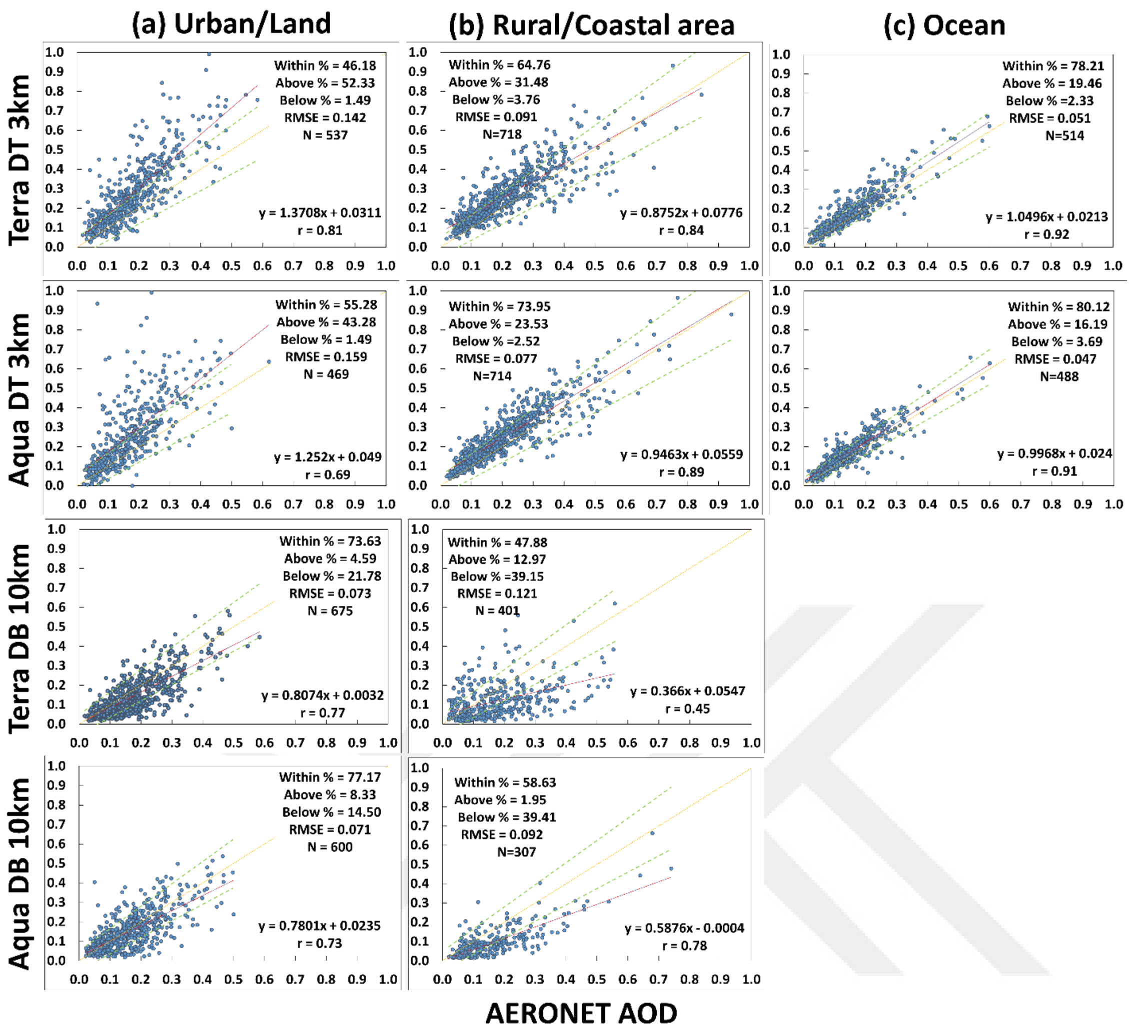

Figure 2.4 (continued): Evaluation of AOD products from MODIS and VIIRS against AERONET AOD measurements between 2014 and 2018 over (a) Urban/Land; (b) Rural/Coastal area; (c) Ocean surface types.

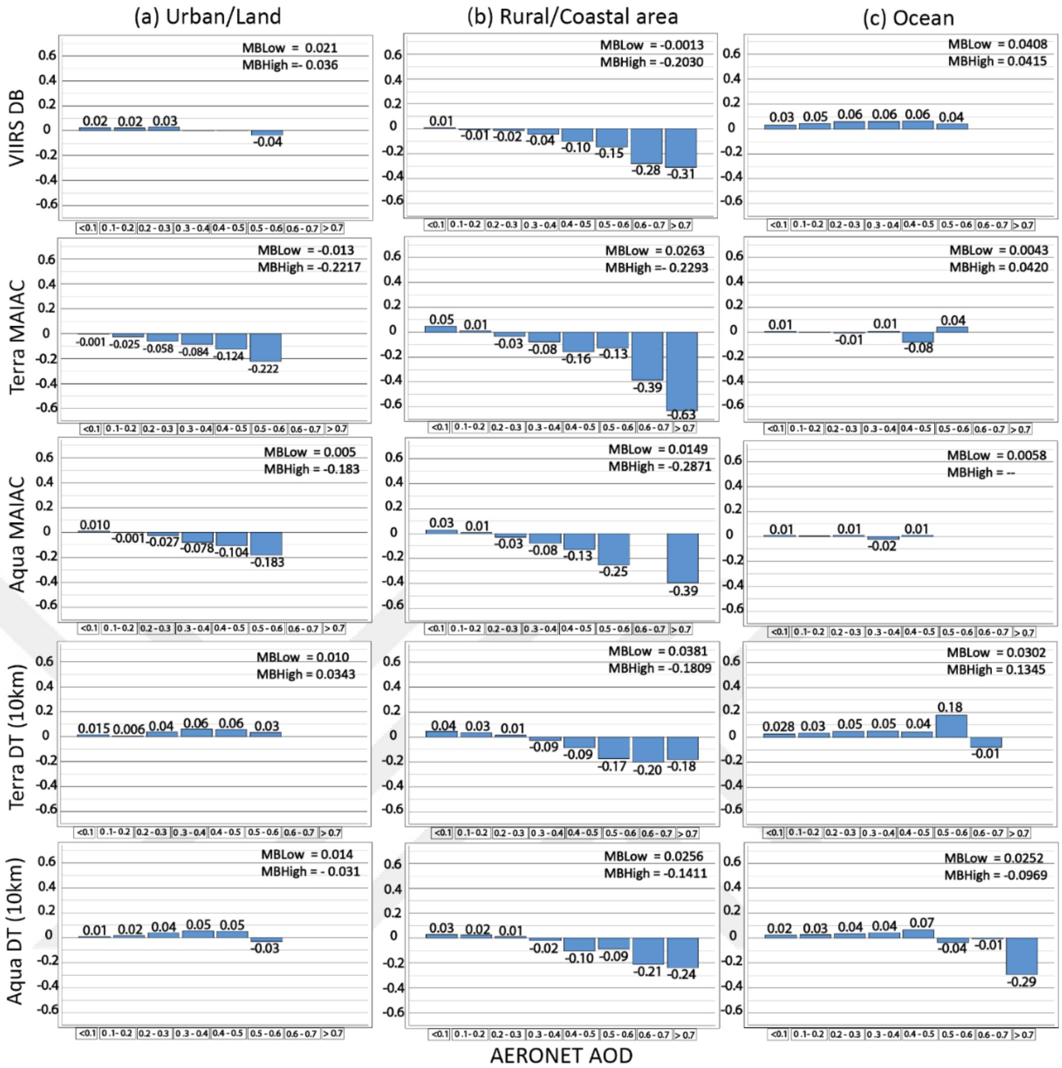

Figure 2.5 : The average difference between satellite and AERONET AOD measurements in bins with a width of 0.1, as a function of AERONET AOD over (a) Urban/Land; (b) Rural/Coastal area; (c) Ocean surface types. The labels indicate the average difference in each bin.

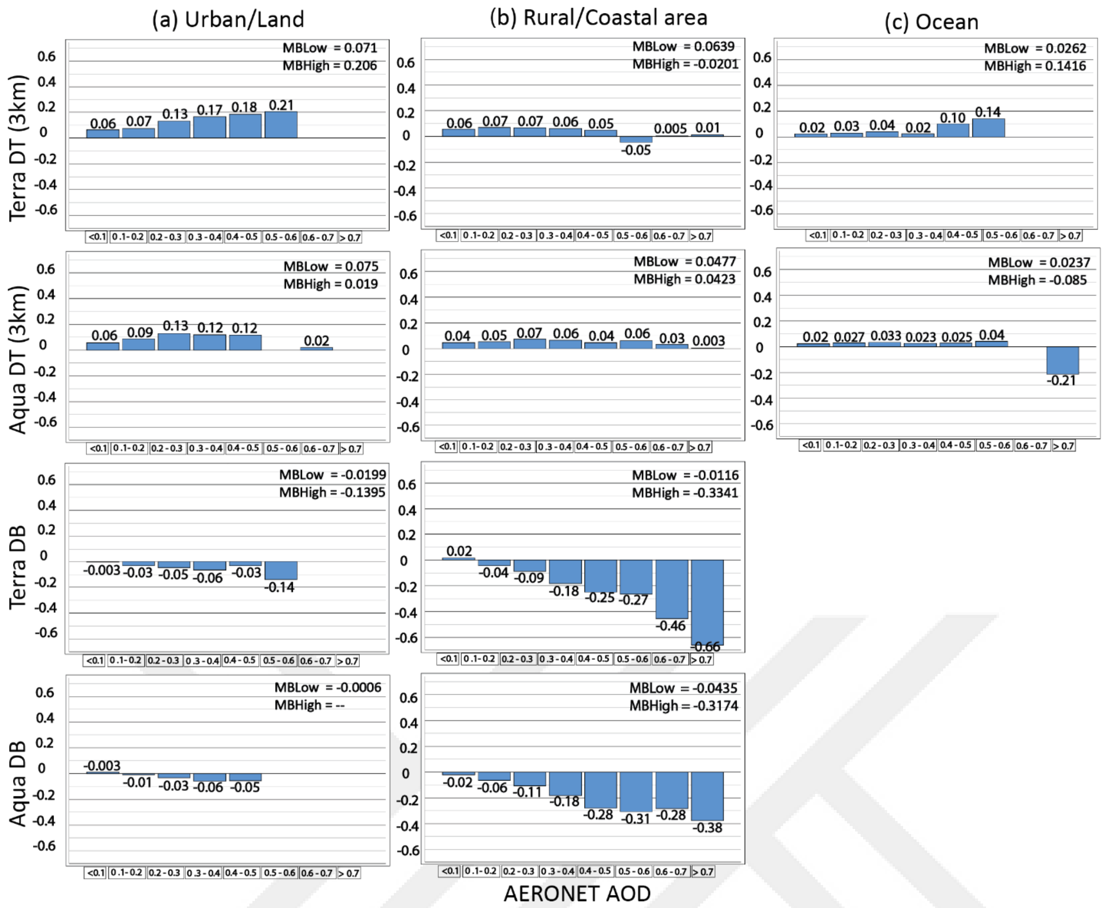

Figure 2.5 (continued): The average difference between satellite and AERONET AOD measurements in bins with a width of 0.1, as a function of AERONET AOD over (a) Urban/Land; (b) Rural/Coastal area; (c) Ocean surface types. The labels indicate the average difference in each bin.

In summary, all of the aerosol products perform well in terms of correlation with AERONET AOD measurements (r>0.65). Considering the percentage of retrievals within EE and RMSE values, the MODIS MAIAC and VIIRS DB aerosol products show better performance over urban/land surfaces whilst the Aqua-Terra MODIS DT retrievals at 10 and 3 km perform best over the ocean. Over the coastal region, all algorithms generally display greater variability and higher RMSE compared to retrievals over land and ocean surfaces; but the VIIRS DB-SOAR AOD product tends to perform best.

2.5.2 Coincident retrieval analysis

To assess the performance of the retrieval methods using AOD retrievals on the same day, an analysis is conducted using only those pixels where all aerosol products provide an AOD retrieval during 2014 – 2018. Since the VIIRS, MODIS Aqua, and

MODIS Terra have different overpass times, utilizing AERONET AOD measurements ±30min of the satellite overpass doesn't provide any temporally coincident matching datasets. Therefore, the coincident retrieval analysis compares the satellite AOD retrievals against the daily average of AERONET AOD ensuring an equal number of daily aerosol retrievals are compared with AERONET AOD measurements. The results of the comparison are shown in Table 2.4. The days in which all algorithms were able to retrieve AOD are likely to be clear sky days which removes the influence of cloud contamination on coincident AOD retrievals, with the errors in retrieved AODs related to the errors in surface reflectance estimation and aerosol model assumptions. This analysis, therefore, assesses the algorithms' ability to retrieve AOD under favorable surface and atmospheric conditions.

Comparison of 124 coincident satellite AOD retrievals with AERONET AOD measurements over urban/land surface indicates the 3-km Terra-Aqua MODIS AOD product has the lowest within% (52%-65%) and highest RMSE (0.099-0.146). Over the ocean, where the aerosol products have the highest performance in terms of r (> 0.84), analysis of 198 valid matchups indicates the Terra-Aqua MAIAC AOD product provides the lowest r (0.84-0.87) and within% (60%-72%). Over the coastal site, the Terra-Aqua MODIS DB AOD product provides the lowest correlation (r =0.60-0.69) and within% (49%-55%) and highest RMSEs (0.120-0.119). Slopes farthest from unity for the AOD retrievals over the coastal site suggest that the assumed aerosol models are not appropriate for AOD retrievals over the Erdemli region with the mixed aerosol type and high intercepts (compared to those over the land and ocean) suggesting errors in the land-water-sediment masks and surface reflectance estimations (Table 2.4).

Table 2.4 : Statistics of the coincident AOD retrievals analysis.

Surface type	Product	N	AERONET AOD Mean	Satellite AOD Mean	r	Slope	Intercept	RMSE	Within%	Above%	Below%
Urban /Land	Terra_MAIAC	124	0.139	0.113	0.76	0.57	0.03	0.064	83.87	4.03	12.10
	Aqua_MAIAC			0.119	0.86	0.75	0.014	0.049	87.10	2.42	10.48
	VIIRS_DB			0.146	0.90	0.96	0.011	0.041	91.94	7.26	0.81
	Terra_DT (10-km)			0.148	0.90	1.09	-0.00	0.048	94.35	5.65	0.00
	Aqua_DT (10-km)			0.130	0.86	1.17	-0.03	0.067	83.87	7.26	8.87
	Terra_DB			0.108	0.82	0.77	0.00	0.062	83.06	1.61	15.32
	Aqua_DB			0.123	0.82	0.82	0.00	0.057	87.90	4.84	7.26
	Terra_DT (3km)			0.211	0.88	1.31	0.02	0.099	52.42	47.58	0.00
	Aqua_DT (3km)			0.215	0.70	1.33	0.02	0.146	65.32	34.68	0.00
Ocean	Terra_MAIAC	198	0.157	0.154	0.84	0.91	0.01	0.047	60.10	13.64	26.26
	Aqua_MAIAC			0.152	0.87	0.89	0.01	0.040	72.73	4.55	22.73
	VIIRS_DB			0.157	0.92	1.03	0.02	0.045	80.30	17.68	2.02
	Terra_DT (10-km)			0.185	0.91	1.10	0.01	0.049	78.79	19.70	1.52
	Aqua_DT (10-km)			0.173	0.91	0.96	0.02	0.038	88.38	7.58	4.04
	Terra_DT (3km)			0.184	0.90	1.09	0.01	0.050	79.80	18.69	1.52
	Aqua_DT (3km)			0.175	0.88	0.95	0.02	0.044	80.30	12.63	7.07
Coastal/Rural	Terra_MAIAC	207	0.168	0.149	0.71	0.35	0.08	0.080	75.36	8.21	16.43
	Aqua_MAIAC			0.145	0.75	0.45	0.06	0.079	77.29	5.31	17.39
	VIIRS_DB			0.136	0.78	0.72	0.01	0.078	82.13	2.42	15.46
	Terra_DT (10-km)			0.174	0.83	0.59	0.07	0.064	82.13	11.11	6.76
	Aqua_DT (10-km)			0.162	0.87	0.68	0.04	0.057	91.79	1.45	6.76
	Terra_DB			0.080	0.69	0.38	0.01	0.120	49.76	0.97	49.28
	Aqua_DB			0.090	0.60	0.39	0.02	0.119	55.56	2.42	42.03
	Terra_DT (3km)			0.205	0.82	0.79	0.07	0.075	66.67	28.50	4.83
	Aqua_DT (3km)			0.189	0.85	0.86	0.04	0.066	86.96	10.63	2.42

2.5.2.1 Correlation between the aerosol products

Using the coincident retrievals, the correlation between the aerosol algorithms and AERONET AOD measurements is calculated and results are shown in Tables 2.5, 2.6, and 2.7, for the AOD retrievals over the urban/land, rural/coastal area, and ocean, respectively. Good correlations suggest that algorithms have verified similar variations in aerosol loading over the region. As can be seen in Tables 2.5, 2.6, and 2.7, the correlations are higher for the retrievals over the ocean which can be related to lower discrepancies of surface reflectance estimation and aerosol model assumptions in retrieval procedures (Table 2.7). Similar results were found by Choi et al. (2019) and Liu et al. (2019) (Choi et al., 2019; N. Liu et al., 2019) using MODIS and VIIRS AOD products. Over the land/urban surface, the 3-km Aqua MODIS DT shows the lowest correlation with other aerosol products while the remaining aerosol products show good agreement. The lower correlation of the 3-km Aqua MODIS DT suggests that this algorithm is not able to reflect the variation in aerosol loading over the region whilst the 10 km aerosol product shows better performance. This can be related to the removal of more pixels representing heterogeneous urban surfaces, in which surface reflectance estimation is difficult, at the MODIS DT product at 10-km since a larger retrieval box is used (Q. He, Zhang, Huang, & Tong, 2017; L. A. Remer et al., 2013).

Table 2.5 : Confusion matrix of correlations between aerosol products over the Urban/land. Cells with values >0.8 are shaded

Aerosol product	VIIRS_DB	Terra_MAIAC	Aqua_MAIAC	Terra_DT (10-km)	Aqua_DT (10-km)	Terra_DB	Aqua_DB	Terra_DT (3km)	Aqua_DT (3km)	AERONET
VIIRS_DB	1	0.78	0.86	0.89	0.89	0.81	0.87	0.89	0.73	0.91
Terra_MAIAC	0.78	1	0.69	0.79	0.76	0.73	0.68	0.74	0.59	0.76
Aqua_MAIAC	0.86	0.69	1	0.84	0.83	0.73	0.82	0.78	0.67	0.86
Terra_DT (10-km)	0.89	0.79	0.84	1	0.86	0.88	0.79	0.86	0.70	0.91
Aqua_DT (10-km)	0.89	0.76	0.83	0.86	1	0.70	0.91	0.83	0.71	0.86
Terra_DB	0.81	0.73	0.73	0.88	0.7	1	0.69	0.75	0.60	0.82
Aqua_DB	0.87	0.68	0.82	0.79	0.91	0.69	1	0.80	0.66	0.82
Terra_DT (3km)	0.89	0.74	0.78	0.86	0.83	0.75	0.80	1	0.68	0.89
Aqua_DT (3km)	0.73	0.59	0.67	0.70	0.71	0.60	0.66	0.68	1	0.71
AERONET	0.91	0.76	0.86	0.91	0.86	0.82	0.82	0.89	0.71	1

Generally, disagreement between the algorithms is higher over the coastal area which can be related to the higher uncertainties and increased difficulty in retrieving AOD over complex surfaces. Numerous studies have found AOD retrievals over coastal zones to have larger uncertainties which were attributed to turbid coastal waters contaminating the signal, the assumption of nearly-zero water-leaving radiance and a constant sea-surface wind speed, influences of sea salt and cloud, and surface inhomogeneity e.g.(Jacob C. Anderson et al., 2013; Chu et al., 2002; Filonchyk & Hurynovich, 2020; Mhawish et al., 2019; Y. Wang et al., 2017). Over the ocean, other than the MAIAC algorithm which has a lower correlation with other aerosol algorithms, other products typically have correlations r > 0.85.

Table 2.6 : Confusion matrix of correlations between aerosol products over the Rural/coastal area. Cells with values >0.8 are shaded

Aerosol product	VIIRS _DB	Terra_M AIAC	Aqua_M AIAC	Terra_DT (10-km)	Aqua_DT (10-km)	Terra _DB	Aqua _DB	Terra_DT (3km)	Aqua_DT (3km)	AERO NET
VIIRS_DB	1	0.78	0.86	0.89	0.89	0.81	0.87	0.89	0.73	0.91
Terra_MAI AC	0.78	1	0.69	0.79	0.76	0.73	0.68	0.74	0.59	0.76
Aqua_MAI AC	0.86	0.69	1	0.84	0.83	0.73	0.82	0.78	0.67	0.86
Terra_DT (10-km)	0.89	0.79	0.84	1	0.86	0.88	0.79	0.86	0.7	0.91
Aqua_DT (10-km)	0.89	0.76	0.83	0.86	1	0.70	0.91	0.83	0.71	0.86
Terra_DB	0.81	0.73	0.73	0.88	0.70	1	0.69	0.75	0.60	0.82
Aqua_DB	0.87	0.68	0.82	0.79	0.91	0.69	1	0.80	0.66	0.82
Terra_DT (3km)	0.89	0.74	0.78	0.86	0.83	0.75	0.8	1	0.68	0.89
Aqua_DT (3km)	0.73	0.59	0.67	0.70	0.71	0.6	0.66	0.68	1	0.71
AERONET	0.91	0.76	0.86	0.91	0.86	0.82	0.82	0.89	0.71	1

Table 2.7 : Confusion matrix of correlations between aerosol products over the ocean. Cells with values >0.8 are shaded

Aerosol product	VIIRS_S OAR	Terra_MA IAC	Aqua_MA IAC	Terra_DT (10-km)	Aqua_DT (10-km)	Terra_DT (3km)	Aqua_DT (3km)	AERON ET
VIIRS_SOA R	1	0.82	0.88	0.89	0.92	0.86	0.88	0.92
Terra_MAIA C	0.82	1	0.86	0.83	0.78	0.81	0.77	0.84
Aqua_MAIA C	0.88	0.86	1	0.80	0.86	0.78	0.83	0.87
Terra_DT (10-km)	0.89	0.83	0.80	1	0.88	0.98	0.87	0.91
Aqua_DT (10-km)	0.92	0.78	0.86	0.88	1	0.86	0.94	0.91
Terra_DT (3km)	0.86	0.81	0.78	0.98	0.86	1	0.85	0.90
Aqua_DT (3km)	0.88	0.77	0.83	0.87	0.94	0.85	1	0.88
AERONET	0.92	0.84	0.87	0.91	0.91	0.9	0.88	1

Since some of the retrievals rely on the aerosol model derived from AERONET climatology, the aerosol products may be correlated with one another over the AERONET sites. Therefore, the aerosol products are also inter-compared over different surface types far from the AERONET sites to evaluate their performance. The surface types were identified by visual interpretation of Google Earth and CLCs (2012-2018).

Tables 2.8-2.13 show the correlation coefficients among the aerosol products over densely vegetated surfaces (Table 2.8), bright surfaces (Salt Lake) (Table 2.9), moderately vegetated land (Table 2.10), urban area (Table 2.11), mountainous areas (Table 2.12), and suburban areas (Table 2.13). The number of coincident retrievals used in the analysis are 397, 122, 226, 205, 175, and 281 for densely vegetated surfaces, bright surfaces (Salt Lake), moderately vegetated areas, urban areas, mountainous regions, and suburban areas respectively. High correlation coefficients ($r > 0.78$) suggest the good performance of aerosol products over the other land surface sites, similar to the AERONET sites. It can be seen in Tables 2.8-2.13, that the correlation coefficients are higher for the retrievals over the vegetated areas than those over bright surfaces or those with lower vegetation cover. The lowest correlations ($r<0.5$) occur over a Salt Lake which has the brightest surface (Table 2.9) whilst all products perform well over surfaces with denser vegetation cover (Table 2.8). Overall, the MODIS DT 3-km and DB 10-km have a greater proportion of lower correlation coefficients with other aerosol products whilst the remaining aerosol products typically show good agreement with one another (Table 2.8-2.13).

Table 2.8 : Confusion matrix showing the correlation coefficients between aerosol products over the densely vegetated land. Cells with values >0.8 are shaded.

Aerosol product	VIIRS_DB	Terra_MAIAC	Aqua_MAIAC	Terra_DT (10-km)	Aqua_DT (10-km)	Terra_DB	Aqua_DB	Terra_DT (3km)	Aqua_DT (3km)
VIIRS_DB	1.00	0.87	0.92	0.80	0.89	0.89	0.92	0.85	0.86
Terra_MAIAC	0.87	1.00	0.93	0.92	0.87	0.94	0.90	0.93	0.83
Aqua_MAIAC	0.92	0.93	1.00	0.88	0.93	0.91	0.93	0.88	0.91
Terra_DT (10-km)	0.80	0.92	0.88	1.00	0.87	0.95	0.85	0.97	0.81
Aqua_DT (10-km)	0.89	0.87	0.93	0.87	1.00	0.91	0.95	0.89	0.92
Terra_DB	0.89	0.94	0.91	0.95	0.91	1.00	0.93	0.93	0.82
Aqua_DB	0.92	0.90	0.93	0.85	0.95	0.93	1.00	0.86	0.89
Terra_DT (3km)	0.85	0.93	0.88	0.97	0.89	0.93	0.86	1.00	0.85
Aqua_DT (3km)	0.86	0.83	0.91	0.81	0.92	0.82	0.89	0.85	1.00

Table 2.9 : Confusion matrix showing the correlation between aerosol products over the bright surfaces (Salt Lake). Cells with values >0.8 are shaded.

Aerosol products	VIIRS_DB	Terra_MAIAC	Aqua_MAIAC	Terra_DT (10-km)	Aqua_DT (10-km)	Terra_DB	Aqua_DB	Terra_DT (3km)	Aqua_DT (3km)
VIIRS_DB	1.00	0.65	0.74	0.52	0.75	0.51	0.40	0.56	0.67
Terra_MAIAC	0.65	1.00	0.81	0.87	0.77	0.86	0.54	0.85	0.72
Aqua_MAIAC	0.74	0.81	1.00	0.67	0.85	0.72	0.58	0.64	0.80
Terra_DT (10-km)	0.52	0.87	0.67	1.00	0.72	0.75	0.42	0.90	0.70
Aqua_DT (10-km)	0.75	0.77	0.85	0.72	1.00	0.77	0.69	0.68	0.88
Terra_DB	0.51	0.86	0.72	0.75	0.77	1.00	0.68	0.78	0.56
Aqua_DB	0.40	0.54	0.58	0.42	0.69	0.68	1.00	0.47	0.35
Terra_DT (3km)	0.56	0.85	0.64	0.90	0.68	0.78	0.47	1.00	0.67
Aqua_DT (3km)	0.67	0.72	0.80	0.70	0.88	0.56	0.35	0.67	1.00

Table 2.10 : Confusion matrix showing the correlation between aerosol products over moderately vegetated land surfaces. Cells with values >0.8 are shaded.

Aerosol product	VIIRS_DB	Terra_MAIAC	Aqua_MAIAC	Terra_DT (10-km)	Aqua_DT (10-km)	Terra_DB	Aqua_DB	Terra_DT (3km)	Aqua_DT (3km)
VIIRS_DB	1.00	0.74	0.83	0.71	0.81	0.62	0.75	0.64	0.81
Terra_MAIAC	0.74	1.00	0.85	0.89	0.84	0.92	0.71	0.85	0.78
Aqua_MAIAC	0.83	0.85	1.00	0.80	0.91	0.81	0.79	0.75	0.88
Terra_DT (10-km)	0.71	0.89	0.80	1.00	0.85	0.83	0.68	0.89	0.75
Aqua_DT (10-km)	0.81	0.84	0.91	0.85	1.00	0.73	0.83	0.77	0.88
Terra_DB	0.62	0.92	0.81	0.83	0.73	1.00	0.70	0.83	0.71
Aqua_DB	0.75	0.71	0.79	0.68	0.83	0.70	1.00	0.69	0.78
Terra_DT (3km)	0.64	0.85	0.75	0.89	0.77	0.83	0.69	1.00	0.69
Aqua_DT (3km)	0.81	0.78	0.88	0.75	0.88	0.71	0.78	0.69	1.00

Table 2.11 : Confusion matrix showing the correlations between aerosol products over the urban areas. Cells with values >0.8 are shaded.

	VIIRS_DB	Terra_MAIAC	Aqua_MAIAC	Terra_DT (10-km)	Aqua_DT (10-km)	Terra_DB	Aqua_DB	Terra_DT (3km)	Aqua_DT (3km)
VIIRS_DB	1.00	0.79	0.82	0.68	0.81	0.59	0.68	0.71	0.80
Terra_MAIAC	0.79	1.00	0.75	0.87	0.73	0.87	0.62	0.84	0.69
Aqua_MAIAC	0.82	0.75	1.00	0.75	0.86	0.70	0.71	0.74	0.82
Terra_DT (10-km)	0.68	0.87	0.75	1.00	0.72	0.87	0.43	0.86	0.74
Aqua_DT (10-km)	0.81	0.73	0.86	0.72	1.00	0.52	0.85	0.72	0.86
Terra_DB	0.59	0.87	0.70	0.87	0.52	1.00	0.69	0.82	0.58
Aqua_DB	0.68	0.62	0.71	0.43	0.85	0.69	1.00	0.70	0.78
Terra_DT (3km)	0.71	0.84	0.74	0.86	0.72	0.82	0.70	1.00	0.74
Aqua_DT (3km)	0.80	0.69	0.82	0.74	0.86	0.58	0.78	0.74	1.00

Table 2.12 : Confusion matrix showing the correlation between aerosol products over the mountainous areas. Cells with values >0.8 are shaded.

Aerosol product	VIIRS_DB	Terra_MAIAC	Aqua_MAIAC	Terra_DT (10-km)	Aqua_DT (10-km)	Terra_DB	Aqua_DB	Terra_DT (3km)	Aqua_DT (3km)
VIIRS_DB	1.00	0.80	0.81	0.75	0.83	0.59	0.83	0.72	0.71
Terra_MAIAC	0.80	1.00	0.76	0.86	0.77	0.78	0.71	0.86	0.62
Aqua_MAIAC	0.81	0.76	1.00	0.74	0.90	0.64	0.76	0.76	0.83
Terra_DT (10-km)	0.75	0.86	0.74	1.00	0.82	0.78	0.67	0.88	0.63
Aqua_DT (10-km)	0.83	0.77	0.90	0.82	1.00	0.57	0.92	0.75	0.88
Terra_DB	0.59	0.78	0.64	0.78	0.57	1.00	0.65	0.65	0.66
Aqua_DB	0.83	0.71	0.76	0.67	0.92	0.65	1.00	0.51	0.75
Terra_DT (3km)	0.72	0.86	0.76	0.88	0.75	0.65	0.51	1.00	0.74
Aqua_DT (3km)	0.71	0.62	0.83	0.63	0.88	0.66	0.75	0.74	1.00

Table 2.13 : Confusion matrix showing the correlation between aerosol products over the suburban areas. Cells with values >0.8 are shaded.

Aerosol product	VIIRS_DB	Terra_MAIAC	Aqua_MAIAC	Terra_DT (10-km)	Aqua_DT (10-km)	Terra_DB	Aqua_DB	Terra_DT (3km)	Aqua_DT (3km)
VIIRS_DB	1.00	0.81	0.84	0.77	0.73	0.83	0.83	0.70	0.83
Terra_MAIAC	0.81	1.00	0.82	0.77	0.73	0.82	0.77	0.71	0.75
Aqua_MAIAC	0.84	0.82	1.00	0.64	0.82	0.79	0.85	0.58	0.88
Terra_DT (10-km)	0.77	0.77	0.64	1.00	0.69	0.81	0.70	0.86	0.71
Aqua_DT (10-km)	0.73	0.73	0.82	0.69	1.00	0.72	0.83	0.73	0.88
Terra_DB	0.83	0.82	0.79	0.81	0.72	1.00	0.79	0.76	0.78
Aqua_DB	0.83	0.77	0.85	0.70	0.83	0.79	1.00	0.60	0.87
Terra_DT (3km)	0.70	0.71	0.58	0.86	0.73	0.76	0.60	1.00	0.63
Aqua_DT (3km)	0.83	0.75	0.88	0.71	0.88	0.78	0.87	0.63	1.00

2.6 Conclusion

This study inter-compares and validates several MODIS and VIIRS AOD products using AERONET AOD measurements over sites with different underlying surface types in the eastern Mediterranean over five years (2014 - 2018). The MODIS aerosol products, which utilize either the DT, DB, and MAIAC retrieval algorithms, are available at three spatial resolutions (10, 3, and 1 km) whilst the VIIRS aerosol product has a nominal 6-km resolution. The VIIRS AOD retrievals are retrieved using an enhanced DB method over land and by the SOAR method over the ocean.

Validation of aerosol products against AERONET AOD measurements reveals that most products have at least 67% of matchups falling within the EE envelope (Levy et al., 2013) except for the 3-km Terra-Aqua MODIS AOD product over land/urban site, the VIIRS SOAR, and the Terra MAIAC AOD product over the ocean and the Terra-Aqua MODIS DB and 3-km Terra MODIS AOD products over the coastal site. This highlights the overall reliability of the satellite AOD retrievals in the region although the results highlight the advantages and disadvantages of each product over different surface types. The results also show that the coverage provided by different algorithms can differ considerably on a regional basis. The VIIRS DB has 2.5% to 50% more AOD retrievals over the urban/land site than the MODIS DT, DB, and MAIAC products, whilst, over the coastal site, the VIIRS SOAR and MODIS DT at 3km products provide more high-quality AOD retrievals. Over the ocean, the Terra-Aqua MODIS DT at a 10 km scale is the product with the highest number of retrievals (N=637-624). Other studies have also found the number of retrievals to vary between AOD products over different surface types. For example, He et al. (2018) found a greater number of matchups over the urban/land site by VIIRS DB product compared to MODIS DT and DB products (L. He et al., 2018) whilst Remer et al. (2013) and Shen et al. (2018) found a greater number of matchups over ocean sites by MODIS DT 3km product compared to the 10-km product (L. A. Remer et al., 2013; X. Shen et al., 2018).

The Aqua MAIAC displays the highest performance against AERONET AOD measurements over urban/land surface type in terms of within% (89%) and RMSEs (0.048) which carries the advantage of finer spatial resolution (1 km) to capture the sub-grid aerosol characteristics. The Terra MAIAC and VIIRS DB, which provide a higher number of AOD retrievals compared to Aqua MAIAC, are the other two best performing AOD products over the land/urban site showing good performance in terms of within% (82%) and RMSE (0.061). The uncertainty in aerosol models has a great impact at high AODs (Chu et al., 2002; Hsu et al., 2019; Ichoku, Remer, & Eck, 2004; Y. R. Shi et al., 2019) and the VIIRS DB AOD product tends to perform better at higher AODs due to the approach used to select the aerosol model whereas, the MAIAC algorithm, for example, uses a static regional aerosol model. The results are encouraging with regard to applying satellite AOD products to analyze aerosol dynamics over the land surface, particularly in urbanized and industrialized areas with higher levels of local aerosol emissions.

Over the ocean surface, the MODIS DT at both 10-km and 3km outperforms other algorithms in terms of correlations (r between 0.86-0.92), within% EE (between 70% and 80%), and RMSEs (between 0.047 and 0.061) which shows the potential of the products for characterization of aerosols over water bodies (e.g. maritime transport emissions). Retrievals over the coastal area have the slopes farthest to unity (between 0.36 and 0.94) and higher intercepts (between -0.0004 and 0.088) attributable to complex surface type and mixed water/land pixels and biases from cloud/foam/sediment contaminations (Jacob C. Anderson et al., 2013). Further enhancements are required by refining the surface reflectance estimations (Limbacher & Kahn, 2019), improved water/land mask (Carroll et al., 2017; Y. Wang et al., 2017), and aerosol model that considers the hygroscopic properties of aerosol particles at high relative humidity along the coast (Ahmad et al., 2011; Qu, Wang, Zhang, Wang, & Sheng, 2015). Inter-comparison of the performance of the aerosol products over the coastal/rural site shows that the VIIRS DB-SOAR AOD product outperforms other products over the coastal site in terms of correlation with AERONET AOD measurements (r=0.88) and within% (88%).

As a final note, the study found that similar sensor characteristics and retrieval algorithms lead to comparable AOD retrievals by VIIRS and MODIS AOD products. The VIIRS DB-SOAR aerosol product shows a good correlation with MODIS AOD products over land and ocean surfaces (r between 0.74 and 0.89) which is encouraging for the continuation of global aerosol monitoring that MODIS instigated over two decades ago.

3. LONG-TERM INVESTIGATION OF AEROSOLS OVER THE MARMARA REGION BY SATELLITE DATA: ASSESSING SPATIOTEMPORAL VARIATIONS

It is important to study and investigate thoroughly the role aerosols play in regional climate change. Studying the geographical and temporal characteristics of aerosol loading over a region is made possible by satellite aerosol products with broad spatial coverage and long-term data sets. Real-time aerosol monitoring has been simpler as satellite technologies have improved, overcoming the shortcomings of the sparse ground-level measurement network. To measure and comprehend the links between the air environment and the physical and biological cover of the earth's surface, a synoptic and spatial picture provided by remote sensing is essential. NASA's continuous investment in developing better MODIS inversion algorithms has led to new aerosol data sets for global change research. Recent developments in the C6 MODIS MAIAC algorithm allow for AOD retrieval at the highest resolutions of 1 km over both dark and bright surfaces. This has enormous potential for use in aerosol and air quality investigations. By refining its assumption of the surface reflectance model and aerosol attributes at regional scales, the MAIAC algorithm has tremendous potential to enhance aerosol retrieval given the remarkable advantage in cloud and snow/ice screening, good spatiotemporal consistency, and pixel resolution (Tao et al., 2019). Ground-based validation with AERONET and cross-comparison with MODIS and VIIRS DT and DB retrievals in the preceding chapter of this study were used to ensure the performance of the MAIAC algorithm on three surface types including ocean, coastal site, and urban/land surface types in Turkey (Ettehadi Osgouei et al., 2022).

AOD trends and aerosol distribution in the Eastern Mediterranean region and Turkey, which includes the Marmara region, have been the subject of a few studies. These evaluations mostly rely on data with a coarser spatial resolution (10 km and/or $1° \times 1°$) than the MODIS MAIAC aerosol product (1km). To the extent of our knowledge, the study being referred to is the first to conduct research specifically on aerosol loading and long-term AOD trends over the Marmara region using aerosol products with a spatial resolution of 1km. As part of their study, Zeydan et al. (2023) assessed the spatiotemporal distribution of aerosol characteristics using level 3 MODIS Aqua-Terra AOD products with 1° × 1° spatial resolutions over Turkey from September 2002 to December 2021. They reported that AOD values ranged between 0.10 and 0.31 in Turkey (Zeydan, Tariq, Qayyum, Mehmood, & Ul-Haq, 2023). The highest AOD values were observed in the Southeastern Anatolia Region due to dust transport events from the Saharan Desert. Over Turkey, the average AODs for spring, summer, autumn, and winter were reported as 0.187, 0.183, 0.138, and 0.104, respectively (Zeydan et al., 2023). Floutsi et al. (2016) used MODIS Aqua with 1° × 1° spatial resolution to study the climatology and trends of AOD over the Mediterranean basin from 2002 to 2014 (Floutsi, Korras-Carraca, Matsoukas, Hatzianastassiou, & Biskos, 2016). According to their assessment, there is a south-to-north decline in AOD and an average decreasing trend of 0.0030/year. The researchers determined that anthropogenic and desert aerosols, respectively, are the main sources in the northern and southern parts of the region (Floutsi et al., 2016). Shaheen et al. (2020) utilized the merged AOD product of MODIS and MERRA-2 to assess the long-term AOD trend over the Eastern Mediterranean region and reported a significant upward trend between 1980 and 2018 over the region. They focused on AOD's yearly and seasonal trends. They found that throughout the summer and spring seasons, there was significant AOD loading in areas with natural mineral dust. In contrast, there was a relatively low loading during winter and autumn (Shaheen, Wu, & Aldabash, 2020). Aslanoğlu et al. (2022) found an increasing trend in the Eastern Mediterranean Basin between 2000 and 2015 (Aslanoğlu, Proestakis, Gkikas, Güllü, & Amiridis, 2022).

In this chapter, MODIS MAIAC data for 2000-2021 were analyzed to determine aerosol optical properties. I also determined how they varied spatially and temporally over the Marmara region. The validations and analyses conducted in this specific section can significantly assist policy and scientific organizations in addressing the growing need for precise and current information on atmospheric aerosols at the local level. The study's findings can be a useful tool for making decisions and developing policies about atmospheric aerosols. The analysis included a thorough description of aerosol loading during this time based on MODIS MAIAC retrievals. It highlighted how land use and cover affected aerosol properties in the area. Across the area, high aerosol hotspots and clear temporal variation were seen. Anthropogenic activities and agricultural practices contributed the most to AOD. The western part of the Marmara region saw a moderate decline in AOD-related cases over time, which was mostly ascribed to laws governing biomass and coal burning. Research demonstrated that throughout the growing cycle or farming season, a significant amount of large particles was released into the atmosphere. This caused the contribution of coarse particles to AOD to reach the maximum value recorded in the area over a year. Anthropogenic pollution has contributed to the high AOD levels on the eastern side of the Marmara region. However, the high AOD levels are not evenly distributed throughout the region and are concentrated in certain areas or spots.

(Aslanoğlu et al., 2022).

3.1 Study Area and Period

The most populous region in Turkey is the Marmara Region, situated in the northwest of the country (Figure 3.1). Although having the second-smallest area among Turkey's seven geographical regions, it has the most inhabitants. This is mostly because the area contains Istanbul, which, with a population of over 15 million, is not only the biggest metropolis in Turkey but also one of the biggest cities worldwide. Some other important cities are located in the Marmara region, including Bursa, Kocaeli, and Tekirdag. The area is a significant economic center as well, with commercial and industrial activity. In the Marmara region, aerosols are formed from a variety of natural and anthropogenic sources. Aerosols over the Marmara region include sea salt and sprays from the Mediterranean Sea, black sea, and along the Istanbul phosphorus line. In addition, aerosols from agricultural activities, forests, biomass burnings, anthropogenic aerosols from human and industrial activities, maritime transport, and seasonal Saharan dust transportation. The study encompasses the full period for which full months of MODIS MAIAC data were available at the time of writing, i.e. from 2000 until 2021.

Figure 3.1 : Study area. (Image from © Google Earth)

3.2 Data Used

We used daily MODIS MAIAC AOD Level 2 gridded data at 1-km resolution (MCD19A2) acquired between 2000 and 2021 are used. Each tile in the MODIS AOD product collection has a Sinusoidal (SIN) projection grid and covers an area of about 1200 km by 1200 km, or roughly 10° latitudes by 10° longitudes at the equator. The Marmara region is covered by 4 tiles of MODIS MAIAC AOD data (h19v04, h19v05, h20v04, and h20v05) (Figure 3.2). There are 2-3 daily observations for each tile acquired by either the Aqua or the Terra satellites. A total of 5627 images per year are averaged and mosaiced for conducting the annual aerosol profile of the Marmara region. The averaging operations are performed per pixel for the "Optical_Depth_055" band of the MCD19A2 V6 data product and "AOD_QA " and “AOD_QA Bitmask” bands of the MCD19A2 V6 data product were applied to mask out poor-quality pixels (Alexei Lyapustin et al., 2018). The Google Earth Engine (GEE) platform was used to compute the annual average values of AOD and to display the distribution of the averaged AOD over the study region. The tile-based MAIAC processing may result in a discontinuity in the AOD maps presented in this work at a line around 35° N (Alexei Lyapustin et al., 2018). Local aerosol models adjusted to AERONET climatology are used for aerosol retrieval and atmospheric correction. This leads to satisfactory AOD performance, according to a private communication from A. Lyapustin on October 20, 2021. However, the use of unique aerosol optical properties between the tiles makes the boundaries between the regions obvious if AOD levels are moderately or highly persistent. By the end of 2021, the MAIAC C6.1 re-processing is expected to minimize the gaps between tiles.

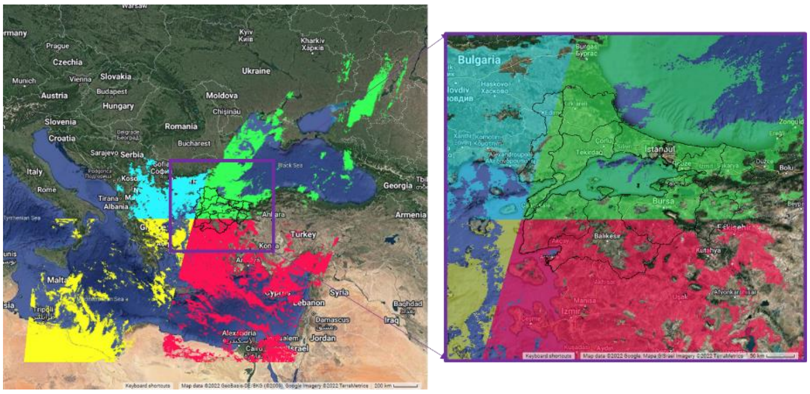

Figure 3.2 : Full view of tiles that are needed to cover the Marmara region with a focused view of the Marmara region indexed by the purple box. (Examples are MODIS MAIAC AOD data from 1st Jan 2011.)

The rainfall dataset is derived from the Climate Hazards Group InfraRed Precipitation with Station data (CHIRPS). It is a quasi-global rainfall dataset spanning more than 30 years available since 2013. To construct gridded rainfall time series for trend analysis and seasonal drought monitoring, CHIRPS combines in-situ station data and 0.05° resolution satellite imagery (Funk et al., 2015). The European Forest Fire Information System (EFFIS) fire database, which can be accessed at effis.jrc.ec.europa.eu, was utilized to examine fire effects on aerosol density and geographical spread.

For my study, I have utilized the CORINE Land Cover database, a readily available LCU dataset for European countries used by researchers for analyzing, simulating, and validating land changes (Feranec, Soukup, Hazeu, & Jaffrain, 2016; Yılmaz, 2010). The database provides multiple datasets describing LCU status in different years (1990, 2000, 2006, 2012, and 2018), making it a valuable input to my research.

3.3 Methodology

3.3.1 Preprocessing

To analyze spatiotemporal variations of AOD, observations in each month were averaged when at least one-third of monthly data or ten observations were available for the same location for a single month. In the AOD retrieval dataset, a QA band of 16 bits was utilized. To ensure the highest quality of data, only the best-quality bitmask derived from the QA band was selected. For the AOD data, an 8-bit QC bitmask was employed to choose pixels with good quality, which were free from errors in the cloud, cloud shadow, water sediments, snow/ice, and sunglint. The resulting cleaned data were then subjected to additional processing. The QA-masked AOD pixels are cleared from any massive AOD outliers which include the AODs lower than 0 and larger than 1 (Dadashi-Roudbari & Ahmadi, 2020; Filonchyk, Hurynovich, & Yan, 2020; Viana et al., 2014). Our focus in this context is specifically on AOD (aerosol optical depth) over land. We have masked out the AOD pixels over Seas and other water bodies. Additionally, due to the higher biases of satellite-derived AODs over coastal lines (as explained in Chapter 2), we have buffered the water bodies up to 500 meters to mask out the AOD pixels over the coastal site and clear out the overestimated AOD pixels.

3.3.2 Data analysis and interpretation methodology

To analyze the spatial and temporal distribution and to study the aspects of AOD that demonstrate variability, the data processing for this study mostly involved the collecting of aerosol data, projection definition, image cropping, data aggregation, and mean calculation. In this study, first, we projected the AOD data to the Universe Transverse Mercator (UTM) projection, and then the AOD data were clipped using Turkey's Civil Administration Boundaries provided by the Ministry of National Defense General Directorate of Mapping (www.harita.gov.tr) as a mask. Finally, the cut AOD data were aggregated and averaged. The obtained aerosol data were first screened to ensure their accuracy before the calculation of AOD, and the valid data (data were considered valid if the percentage of valid pixels in the image data was greater than 50%) were retained. Then, the annual, quarterly, and monthly aggregation, and mean values of the aerosol product data were calculated on the GEE platform. The monthly average AOD of the Marmara region analyzed in the study was obtained by accumulating the daily AOD and then averaging it. As well, the seasonal average AOD and annual average AOD were obtained by using all effective values of daily data. The monthly division criterion used was the natural month when analyzing the monthly changes in AOD. To analyze the annual variation in the data, the annual average was calculated by averaging the data from March to December and January to February of the following year. Additionally, the seasons were defined as follows: spring (March to May), summer (June to August), autumn (September to November), and winter (December to February of the following year). we can have a better idea of how trends change over a year by splitting the data into seasons and examining the variations in each season.

To examine how the AOD is distributed within the Marmara region, the AOD values, which vary over time, were spatially averaged for each province within the region. The analysis is then conducted at the provincial scale, which allows for a more detailed examination of the spatial patterns of AOD across the region. Essentially, this approach involves averaging the AOD values for each province within the Marmara region, which provides a better understanding of how AOD is distributed across the region at a more local level. This type of analysis can be useful for understanding the sources of aerosols and their impacts on air quality and human health within specific areas of the Marmara region. Variables that change over a year can be obtained.

To further analyze the distribution of AOD at smaller scales, temporal variations are considered in regions with high AOD values using a percentile-based approach(Sullivan, Levy, & Pryor, 2015; Xian et al., 2022). This involves calculating high AOD areas based on a threshold defined as the 85th percentile for each period, such as annually or seasonally. By using these thresholds, the temporal changes in high AOD areas can be evaluated and compared.

Essentially, the linear variation of AOD can be characterized as the long-term trend in a linear fashion, expressed either in absolute or percentage changes per decade. To quantify the spatial characteristics and dynamic changes in all grids, we utilized a simple regression analysis to evaluate the variation in a single pixel. By analyzing the slope of the regression line, we were able to determine the trend of AOD over the given period. If the slope was greater than 0, it indicated a gradual increase in AOD. On the other hand, if the slope was smaller than 0, it indicated a continuous decrease in AOD. If the slope was equal to 0, it indicated that the AOD remained constant over the given period. The long-term trend of the AOD is the slope of the linear regression for the time series of monthly or annually-averaged AOD. In our study, we followed the widely accepted decision criterion that a significant trend is identified at a 95% confidence level when LLT is greater than 2σ (Babu et al., 2013), where σ represents the standard deviation.

3.4 Results

3.4.1 AOD variations at different temporal scales

3.4.1.1 Daily scale

Figure 3.3 displays the temporal variation of daily variance of AOD over the Marmara region between 2000-2022. A high daily AOD variance tells us that the collected AOD pixel data of a day have higher variability, and the data is generally further from the mean. Higher variability happens on days in which the intense aerosol concentration is detected in the atmosphere. The dust transport event from the Saharan Desert to western Turkey that occurred on February 1, 2015, describes the high daily AOD variance (0.06) on this day. Following intense aerosol emissions like Saharan dust events (Hsu et al., 2019; Yu et al., 2019), volcanic plumes (Bègue et al., 2020; Sun et al., 2019), and wildfires (D. G. Kaskaoutis et al., 2011; Xingchuan Yang, Zhao, Yang, Yan, & Fan, 2021), the considerable daily AOD variances show the potential of transported intense aerosol loading over the region. The significant daily AOD variance is partly explained by the extreme emissions caused by regional events such as biomass burning activities, agricultural fires, and biofuel/coal combustion that led to an increase in smoke and fog in the atmosphere. In Figure 3.3 the daily variance higher than 0.03 are labeled. Between 2000 and 2002, there were more days with a daily variance larger than 0.02, which is a reference to the higher daily aerosol pollution.

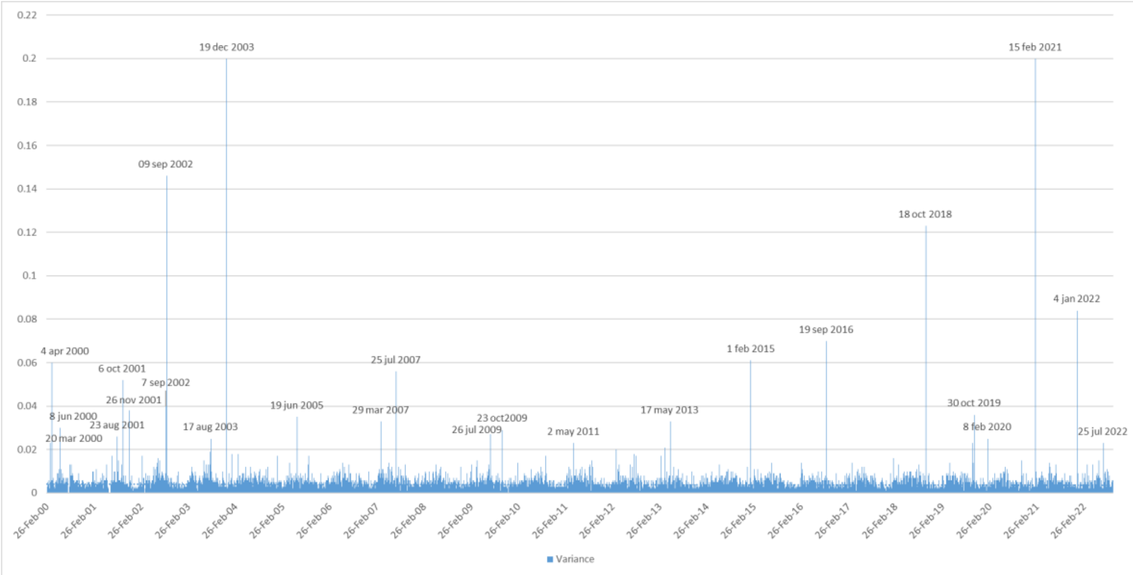

Figure 3.3 : The daily AOD variance over the region, 2000-2021.

3.4.1.2 Monthly scale

I investigate the monthly variabilities of aerosols over the Marmara region from 2000 to 2021. Figure 3.4 shows the monthly mean MODIS MAIAC AOD spatially averaged for the Marmara region, with one standard deviation shown by the dashed lines. The monthly mean AOD values are calculated using the daily AOD data between 2000 and 2021. The monthly mean AOD increases gradually from January to May and fluctuates between May and August and reaches its highest value in August. The monthly mean AOD decreases after August and reaches the lowest monthly mean at the end of the year during December.

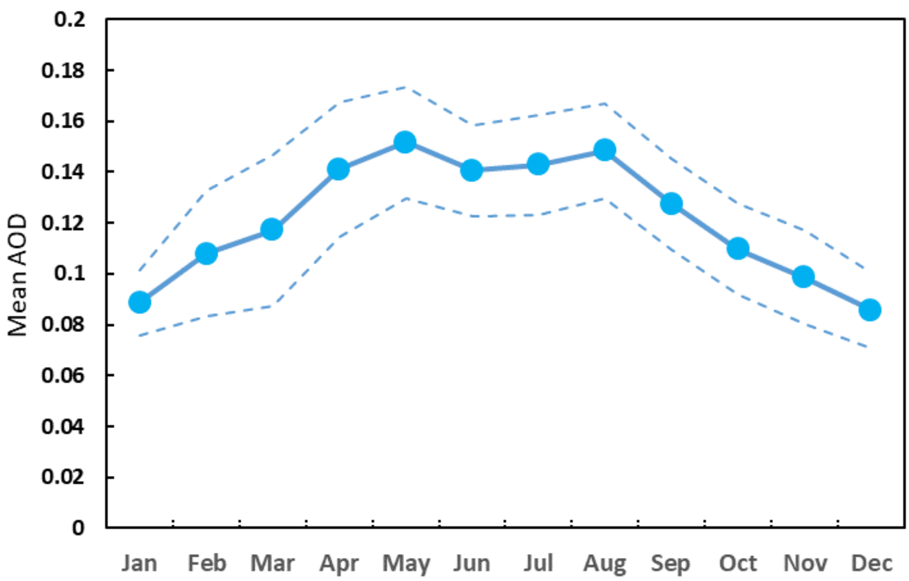

Figure 3.4 : Time series of monthly MODIS MAIAC AOD at 550 nm for the Marmara region during 2000–2021.

The monthly mean MODIS AOD varied from 0.087 (December) to 0.15 (August). The uppermost levels of MODIS-derived AOD broadly appeared from May to August ranging from 0.14 to 0.15. The highest AOD showed in August, with monthly means of 0.15±0.02. The standard deviation from the average AOD date between 2000-2021 represents the interannual variability of AOD over the Marmara region for 21 years (dashed lines in Figure 3.4). While transported dust from arid regions or emissions from severe wildfires create the highest interannual variabilities, persistent regional aerosol emissions have the lowest magnitudes of interannual variability in monthly AOD. Less spread in AOD values shows the relatively simple aerosol source in the period. AOD values vary from year to year in the Marmara region, with February, March, April, and May having the highest interannual fluctuation magnitudes between 2000 and 2021. Maximum intervariabilities in late-winter and early-spring could be thought of as the periods when the region receives transported dust aerosols. The transported dust could also become mixed with the regional anthropogenic emissions and intensify the aerosol concentration. The Marmara region is vulnerable to dust transport from the Sahara during spring, which is carried by the strong southwesterly flows. Winter is the second season after spring when the region gets dust storms (Baltaci, 2021). One of the highest AOD values over the Marmara region was recorded in February 2015 (AOD > 0.5) which is due to the transported Saharan dust happened.

The highest AOD values were recorded from April to August (Figure 3.4). The Marmara region's sowing and harvesting seasons last from April through mid-autumn (Republic Of Türkiye Ministry Of Agriculture And Forestry (Republic of Turkiye ministry of agriculture and forestry, n.d.)). The aerosol concentration can be increased in many different ways by agricultural activities. The Marmara region is a significant agricultural region in Turkey and because of its good soil properties, it offers the widest variety of agricultural products. Of all the cultivated land in Turkey, the Marmara region has the highest proportion of cropland (Yavuz, 2009). Though, it is vulnerable to aerosol emissions from agricultural practices. Tilling, land preparation actions, soil cultivation, and harvesting operations are the primary agricultural operations accountable for the formation and release of soil and dust emissions (J. Chen et al., 2017; Katra, 2020; S. Lee et al., 2006; Singh, Ravindra, Beig, & Mor, 2021). There are other types of particulate matter cause regional air pollution during agricultural practices such as spreading from highly fertilized fields and livestock manure, which combine with industrial emissions in the air to form solid particles (X. Li, Jin, & Kan, 2019; Maffia, Dinuccio, Amon, & Balsari, 2020; Udeigwe et al., 2015). The other farming activity which is a significant factor contributing to the higher AOD mean during summertime and more specifically during August is crop residue or stubble burning. The stubble is the roots and stalks of harvested cereals as a result of agricultural production. Farmers frequently burn stubble because it is seen as a good practice (Ozturk & Bascetincelik, 2006). Farmers utilize stubble burning to prepare a better seed bed and eradicate weeds and insects. Especially after harvesting wheat and corn, farmers often burn crop residue before planting another crop right away since the stubble on the soil surface reduces the efficiency of soil tillage and planting machinery. In locations with multi-season crop rotation, such as the double-cropping method, stubble burning has always been a part of the cultivation of rice, wheat, and sunflowers. However, the benefits of these explanations are so modest in comparison to the harm that they remain. Even though stubble burning has been outlawed in Turkey since 1993, it is nevertheless practiced in the majority of Turkey including the Marmara region. Turkey's cultivated land area in 2019 was about 15.4 million hectares, excluding fallow land. Each year, a stubble fire destroys 10 million tons of stalks and straw from the grain fields in Turkey, which make up over 40% of the country's total grain field (Temiz & Olgar, 2017). Aside from the detrimental effects on soil qualities and water resources, stubble burning is one of the biggest causes of air pollution.

Uncontrolled burning of stubble specifically during the warm seasons can cause unharvested crops in neighboring fields to burn and they can cause forest fires. Crop residue burning and increasing heat are the two major causes of forest fires. Out of the 11332.44 ha of land damaged by forest fires in Turkey just in 2019, 406.45 ha of the land was in the form of fires brought on by stubble burning (Yakupoglu, Dindaroğlu, Rodrigo-Comino, & Cerdà, 2022). Looking at the monthly AOD mean trend makes it clear that agricultural stubble burning emissions throughout the months of April to August caused an intensified aerosol concentration in the Marmara region (Figure 3.4).

By calculating the monthly averaged AOD for different provinces in the Marmara region, it is possible to identify potential unique aerosol patterns that may exist in a particular province or group of provinces and to understand the climatic or topographical factors that contribute to high aerosol concentrations. Figure 3.5 shows the monthly averaged AODs for the provinces of the Marmara region.

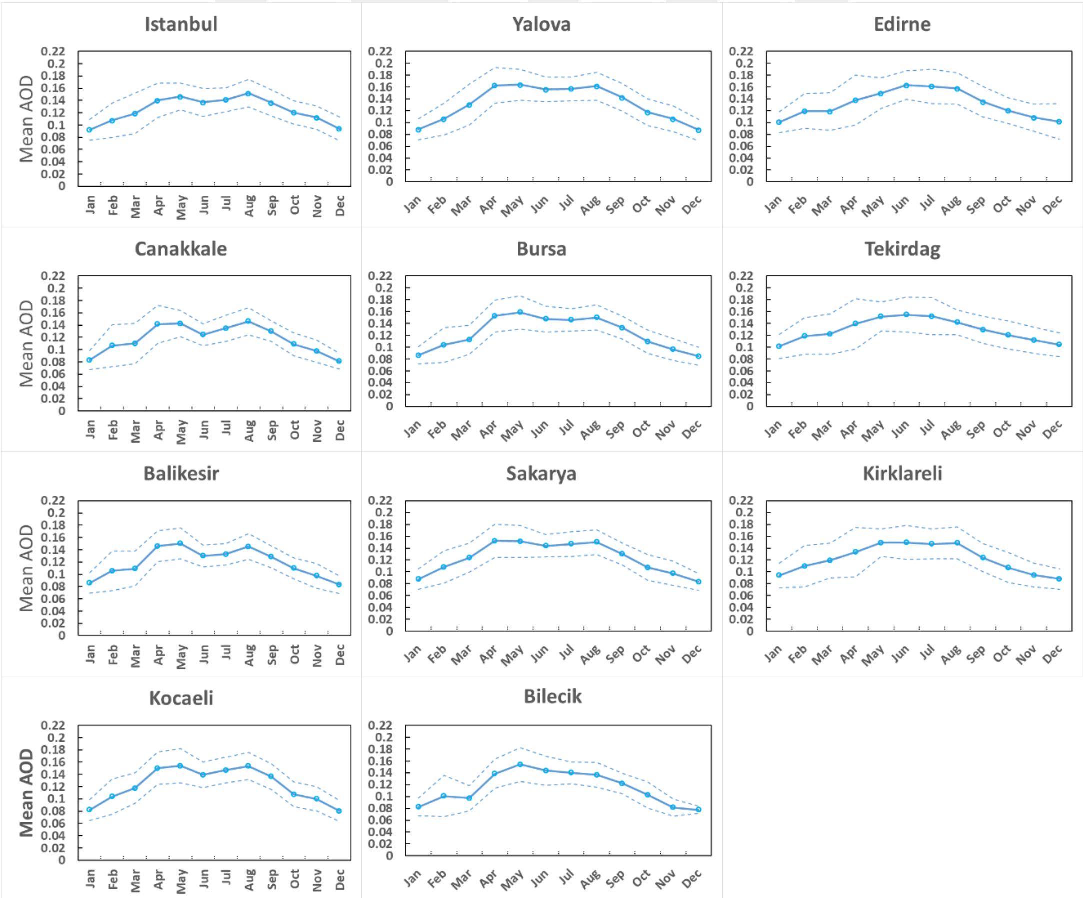

Figure 3.5 : Time series of monthly averaged MODIS MAIAC AOD for different provinces.

The relationship between precipitation and aerosol concentration is an important factor to consider in understanding AOD in the region. The monthly AOD variations are highly related to the dry and wet conditions controlled by natural climate variability. The Marmara region sees the most rain in December and January, which lowers the average aerosol concentration during the rainy season. Additionally, the region's pre-summer wet season falls in line with the low AOD in June (Figure 3.5). The smallest amount of rain in the Marmara region falls in August, at 1.0 mm. The 28 measuring weather stations in the Marmara region provided the data used to create all of the precipitation graphics within the “Worlddata.info” project (Figure 3.6). Each piece of information matches the average monthly values during the previous 20 years. The unit of measurement for precipitation is millimeters per square meter. Two millimeters per day means that two liters of water fall on a square meter in 24 hours.

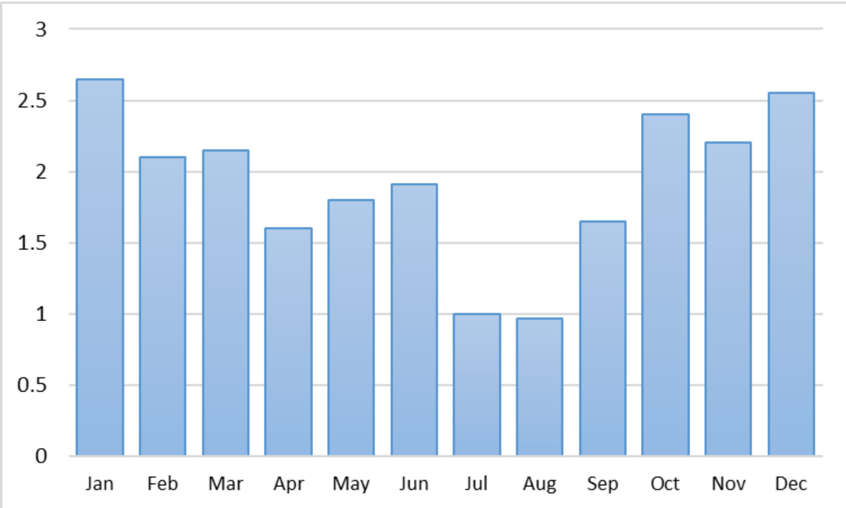

Figure 3.6 : Precipitation in mm/day (source: WorldData.info)

The Marmara Region receives a significant quantity of precipitation from northerly and northeasterly maritime trajectories, suggesting that the Black Sea has a significant impact on the region's rainfall regime. Although rainfall occurs during types with a southerly component (S, SW, and SE) in the western regions that are less impacted by the Black Sea, the geostrophic flow across the Marmara region is primarily of types NE and, with the NE pattern occurring every other day during pre-summer and summer months. The northern and eastern portions of the region are invaded by wet and somewhat cool air from the Black Sea due to the impact of the dominating NE trend (Akkoyunlu, Baltaci, & Tayanc, 2019; Baltaci, Gokturk, Kındap, Unal, & Karaca, 2015; Baltaci, Kındap, Unal, & Karaca, 2017).

Despite the similar summertime peak for provinces of the Marmara Region, one distinguishing optical feature shown in Figure 3.5 is that there are two peaks of monthly mean AOD spatially averaged for Balikesir, Canakkale, Sakarya, Istanbul, Bursa, Kocaeli, and Yalova appeared in April-May and August (0.70±0.02), while there is one peak for Edirne, Kirklareli, Bilecik, and Tekirdag appeared in May or June. Rainfalls in the western part of the Marmara region occur during circulation types with southerly directions (S, SW, and SE) which are relatively infrequent, especially during summer (Baltaci et al., 2015). The Thrace portion of the Marmara Region, as well as Bilecik, exhibit some signs of a continental climate and experience hot, dry summers. Since the soil is dry during this time of year and there hasn't been much rain, the local soil particles have been more thoroughly re-suspended. The Thrace region experiences high AOD in the summer due to persistently high temperatures and little precipitation, with little rain to wash out the region's high AOD in June (Figure 3.5).

3.4.1.3 Seasonal variation

The spatial distribution of aerosol loading over a region is not homogenous and may differ significantly in different seasons. The optical properties and intensities of the aerosol loadings can be monitored and investigated during each season. To quantify and investigate the optical properties of various aerosol types over the Marmara region, both natural and anthropogenic, seasonal monitoring of aerosol load and properties is suggested. The seasonal AOD profiles of the Marmara region are generated between 2000 and 2021 utilizing the daily MODIS MAIAC AOD data. The factors that influence aerosol distribution and magnitude are explored concerning the seasons' potent elements. Using seasonal AOD records, the interannual variation trends of aerosol loading across the Marmara region are analyzed, and the mechanisms influencing the significant differences between seasonal AOD values are investigated.

To generate the seasonal AOD profile for the Marmara region, I calculated the average AOD for each season between 2000-2021 (Figure 3.7). The average MODIS MAIAC AOD over the Marmara region was highest in summer, with an average value of 0.148, followed by spring and autumn, with average values of 0.136 and 0.116, respectively. The average AOD value decreased to 0.09 in winter, whereas the average AOD in summer was approximately 1.08-1.27 times that in spring and autumn and 1.65 times that in winter.

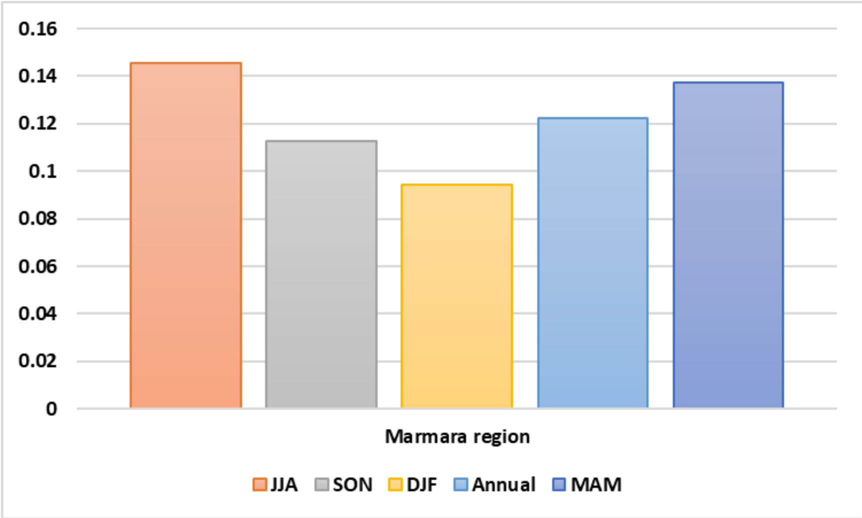

Figure 3.7 : Annual and Seasonal averaged MODIS MAIAC AOD over the Marmara region from 2000 to 2021.

I calculated the number of AOD pixels which were used to calculate the seasonal mean AODs between 2000 and 2021 across the region. The seasonal AOD numbers are the sum of the number of daily MODIS MAIAC AODs retrieved over the Marmara region. The total number of AOD pixels during winters, springs, summers, and autumns between 2000-2021 is 43,658,639, 65,846,053, 125,556,064, and 88,275,330, respectively. The total number of retrieved AOD pixels between 2000-2021 is highest for the summer.

lowest mean AODs in winter

One major reason for the scarcity of observations on aerosols during winters in which the AOD retrievals are at their lowest is due to challenges with conducting aerosol observations, detection, and retrieval brought on by snow cover. Snow cover affects surface albedo, and increased surface albedo causes certain pixels to lose data(Q.-X. Chen et al., 2022; Qin et al., 2021). The lack of observations on aerosols during the winter months in the Marmara region is also primarily due to the amount of cloudy and foggy days. Clouds cause the atmosphere to be heated for hours of the satellite overpass. While the number of missing retrievals increases in winter because of cloud cover, dense haze, and fog, the winter AOD changes are also related to meteorological factors over the Marmara region.

The aerosol concentration decreases in winter due to heavy rainfall that leads to wash out of aerosols from the atmosphere while greater winds during this season also contribute to a good dispersion of pollutants with increased horizontal mixing, which lowers particle concentration. In February, December, and January the strongest winds were recorded within the Marmara region (A. Deniz, Özdemir, Sezen, & Coskun, 2013). Extreme rainfall events occurred throughout the winter months in the Marmara region, which is surrounded by water bodies subject to the sea effect mechanism (Baltaci et al., 2017).

Low AOD levels have been linked to rainy seasons in multiple studies. Acharya and Sreekesh (2013) showed that the winter decline in AOD (0.3–0.2 at 0.47 μm and 0.22–0.16 at 0.66 μm) from 2001 to 2003 was possibly due to a reduction of aerosol load through precipitation from an extensive cloud cover remaining over the Indo-Gangetic plain that led to an undetected aerosol layer beneath the cloud while also they showed that the occurrence of local precipitation (India Meteorological Department 2007 and 2009 (especially over the Indo-Gangetic plains plain)) during the pre-monsoon season, on the other hand, might have reduced aerosol concentration, thereby leading to low optical depth between 2007 and 2009 (Acharya & Sreekesh, 2013). Luo et al. (2014) demonstrated that over China the washout from Asian summer monsoon rainfalls causes low AOD while dust storms in arid and semi-arid regions caused the AOD peaks in spring and early summer (Luo, Zheng, Zhao, & Chen, 2014). Khalid et al. (2021) declared that lower summer AOD values are caused by monsoon rains, which wash out the aerosols and thus reduce their concentration, primarily in Pakistan's east and southeast (Khalid et al., 2021). In the study by Chowdhury et al. (2016) the aerosol washout caused by monsoon rain in India was investigated in terms of rainfall duration, aerosol recovery time, aerosol type, and source strength. They declared that updraft plays an important role in post-precipitation aerosol build-up whereas, in dust-dominated northwest India, monsoon rainfall (whenever occurs) suppresses dust emission because of the increased soil moisture and therefore inhibits the recovery. The number of grids where washout outweighs recovery during the monsoon season for a 3-hour rainfall increases by 5.6% with an increase in rain rate from < 2 mm day–1 to > 4 mm day–1, while the corresponding increase for a 9-hour rainfall event is 2.8%. AOD reduces in ‘cloudy-sky’ conditions relative to ‘clear-sky’ conditions because aerosols are scavenged by cloud drops as the clouds grow vertically during the monsoon (Chowdhury, Dey, Ghosh, & Saud, 2016).

To examine the link between the rainfall and aerosol concentration over the Marmara region, I calculated the precipitation levels for the Marmara region using the CHIRPS rainfall dataset. There is a strong negative correlation, with Pearson's correlation of r = -0.70 between the mean monthly number of retrieved MODIS MAIAC AOD pixels and the monthly rainfall amounts across the Marmara region between 2000 and 2021. Figure 3.8 shows the temporal variation of the precipitation level and the number of retrieved AOD pixels and the higher rainfall amount correlates with the days of the lower number of retrieved AOD pixels which is due to the washouts of aerosols by heavy rainfalls.

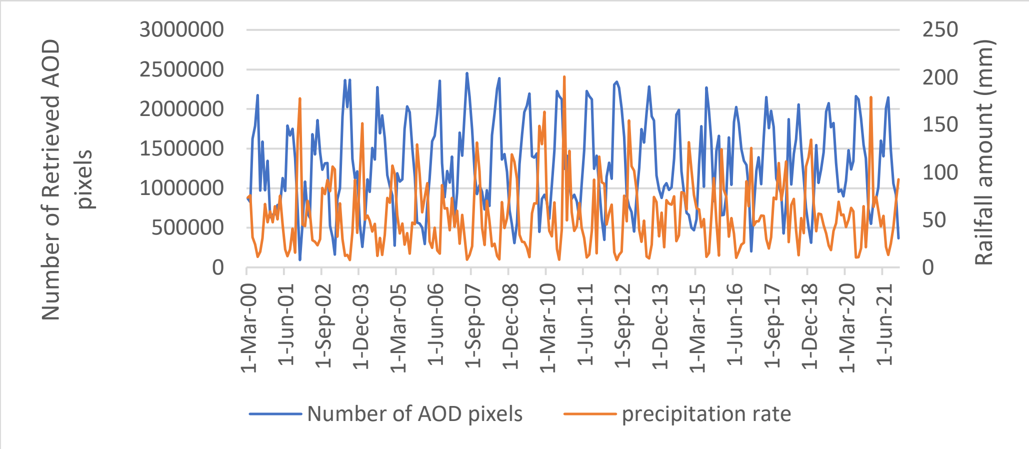

Figure 3.8 : Temporal variation of the precipitation level and the number of retrieved AOD pixels over the Marmara region during 2000-2021.

Highest mean AODs in summer

The biomass-burning and forest fires are among the factors has been approved to have an impact on the degradation of air quality. Lately, a vast forest fire tore through Turkey's Mediterranean region started in Manavgat, Antalya Province, on 28 July 2021. While the mean AOD value in the vicinity of Manavgat was between 0.2 and 0.5 during July and August 2021, the aerosol pollution emitted by forest fire increased the AOD value and the MODIS sensors observed AODs between 1.3 and 2 between the 28th of July and 8th of August. Although the highest aerosol emissions from forest fires are frequently misclassified as the cloud in the process of the AOD retrieval, the MODIS MAIAC-derived AOD data effectively represents the intense aerosol pollution in the Manavgat region. The daily AOD data acquired from MODIS MAIAC is capable of identifying the intense aerosol emission and they can be utilized for the investigation of extreme biomass burning and wildfire-induced aerosols.

The accumulation of increased aerosol concentrations in the study area throughout the summer is partly due to the forest fires. The Marmara region is among the sensitive regions of Turkey against forest fires (Demir, Küçükosmanoğlu, Hasdemir, Tolga

Ozturk, & Acar, 2009; Elvan, Birben, Özkan, Yıldırım, & Türker, 2021). The Marmara region's Balikesir and Canakkale provinces rank sixth and seventh, respectively, among the provinces with the highest rate of tree cover loss as a result of fires, with average annual losses of 175 ha and 144 ha, respectively, between 2001 and 2021 (Global forest watch,2022; https://www.globalforestwatch.org). The higher air temperature, less precipitation, and drier vegetative cover all contribute to an increase in fire activity during summer. A substantial amount of carbonaceous aerosols and other pollutants can be released into the atmosphere during the summer months (late June to mid-September) by forest burning. I calculated the number of forest fires that occurred in the Marmara region using the EFFIS fire database (effis.jrc.ec.europa.eu). Figure 3.9 displays the number of fires per month in the Marmara region (2000-2022). From 2000 to 2022, wildfires are most prevalent in July and August with a total of 24 and 35 forest fires, respectively.

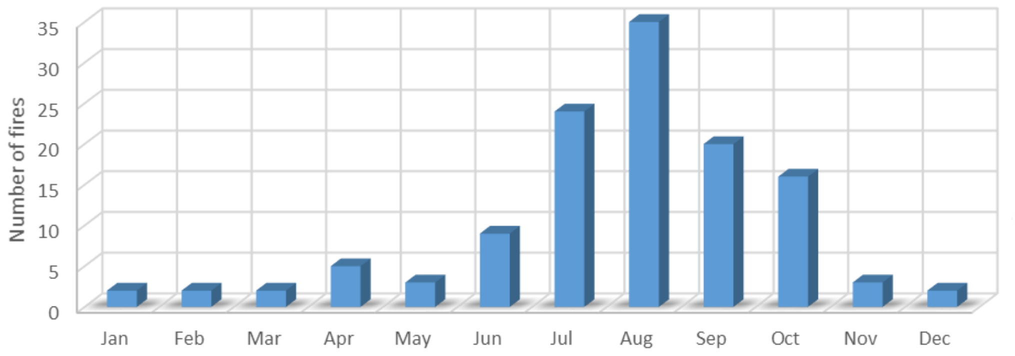

Figure 3.9 : Number of fires per month in the Marmara region (2000-2022).

The stagnant weather of summertime with weak wind speeds delays atmospheric diffusion ability and hence causes a higher concentration of aerosols at higher altitudes. In addition to the higher aerosol concentrations in the summer, the higher evaporation and greater specific humidity lead to higher recorded AOD values. By increasing the size and weight of aerosol particles through the condensation of water vapor on them as well as by promoting the nucleation-growth processes and development of additional aerosols, high humidity can increase AOD (Murari, Kumar, Barman, & Banerjee, 2015; Tao et al., 2017). This also explains the higher number of retrieved AOD pixels over the Marmara region at this time of year.

3.4.2 Spatio-temporal variation and impact factors analysis of AOD over the Marmara region

The spatial distribution of the AOD across the study area is presented in Figure 3.10, where the MODIS MAIAC AOD has been averaged over the years 2000–2021. Figure 3.10 also shows the digital elevation model (DEM) map of the Marmara region from the Multi-Error-Removed Improved-Terrain (MERIT) DEM which is a highly accurate global DEM at a resolution of about 90 m, created by removing significant error components from current DEMs (JAXA AW3D DEM, NASA SRTM3 DEM, and Viewfinder Panoramas DEM) (Yamazaki et al., 2017).

High values of AOD (AODs > 0.135) were found along the coastal area of the Marmara Sea, Aegean Sea, and black sea, while low ones were in the southwest and easternmost parts. Toward the southwest and easternmost, over Çanakkale, Bilecik, and Bursa, the AOD is lower than in the near-coastal areas with areas where the AOD varies between 0.05 and 0.1. The easternmost and southwest part of the Marmara region is the mountainous area, where the emission of anthropogenic aerosols remains at low levels.

87% of Turkey's total population resides in the coastal region of the Marmara Sea, and household activities there have an impact on the region's aerosol loading. In addition, the cities near the Marmara Sea, especially those in the North and East Marmara Sea region depend on industrial development economies and therefore have serious aerosol emissions. The region is subjected to increasing human interference in the form of industrial activities. Besides the pollution from various local land-based sources, from the heavily populated and industrialized Istanbul Metropolitan, Bursa, Yalova and Kocaeli, the region is also exposed to the emissions from maritime transport. Istanbul, Bursa, Yalova, Edirne and Tekirdag provinces have the highest annual AOD means (> 0.129) between 2000 and 2021.

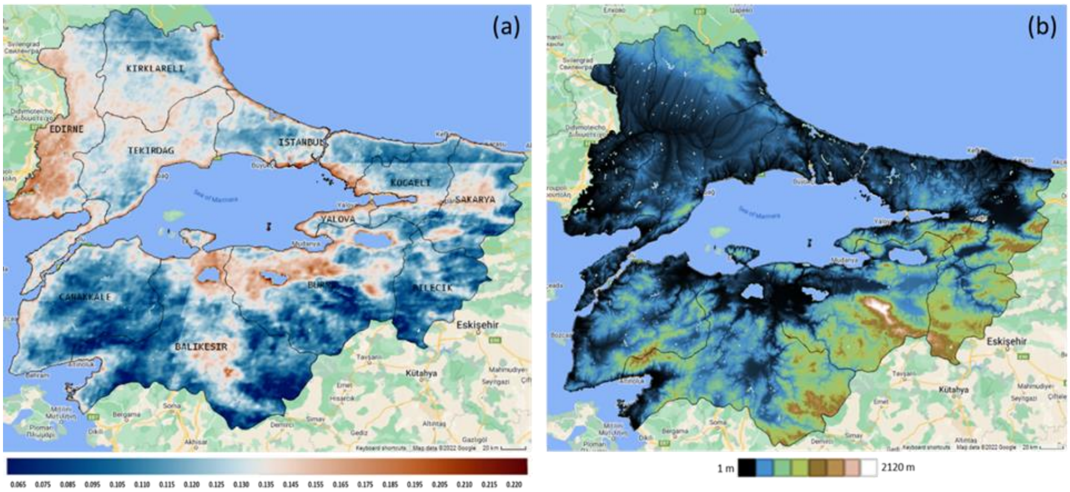

Figure 3.10 : The overlay of (a) the Average annual distribution of AOD from 2000 to 2021 and (b) an elevation map over a Google map.

The elevation map in Figure 3.10 (b) shows the mountains to the east of the high-AOD area which forms a natural barrier for the transport of aerosol between the densely populated and highly industrialized areas along the coast of the Marmara Sea and the easternmost part of the region. Bursa, Yalova, Sakarya, and Balikesir basins are blocked areas with high AOD because they are enclosed by high mountains that prevent the venting of aerosol and other pollutants. Fine anthropogenic particles can't cross these mountains, so it contributes to AOD in these spots. The Samanli mountains along the eastern coast of the Marmara Sea in Yalova together with the influence of maritime aerosols and emissions from shipping activities, result in high AOD values during a year in Yalova.

3.4.2.1 Monthly and seasonal variation of AOD distribution

To emphasize the spatial distribution of AOD, monthly averaged AOD maps are generated using the AOD data retrieved during the month between 2000 to 2021. Figure 3.11 shows the month-wise variation in AOD over the Marmara region in a period between 2000 and 2021. The spatially averaged AOD value of each month in 21 years ranged from 0.054 to 0.233. The spatial distribution of monthly mean AOD was comparable in all 21 years with higher AOD distributed over the entire study region from late-spring to early-autumn (April-September). The spatial distribution patterns of monthly average AOD for each year between 2000-2021 are shown in Appendix A.

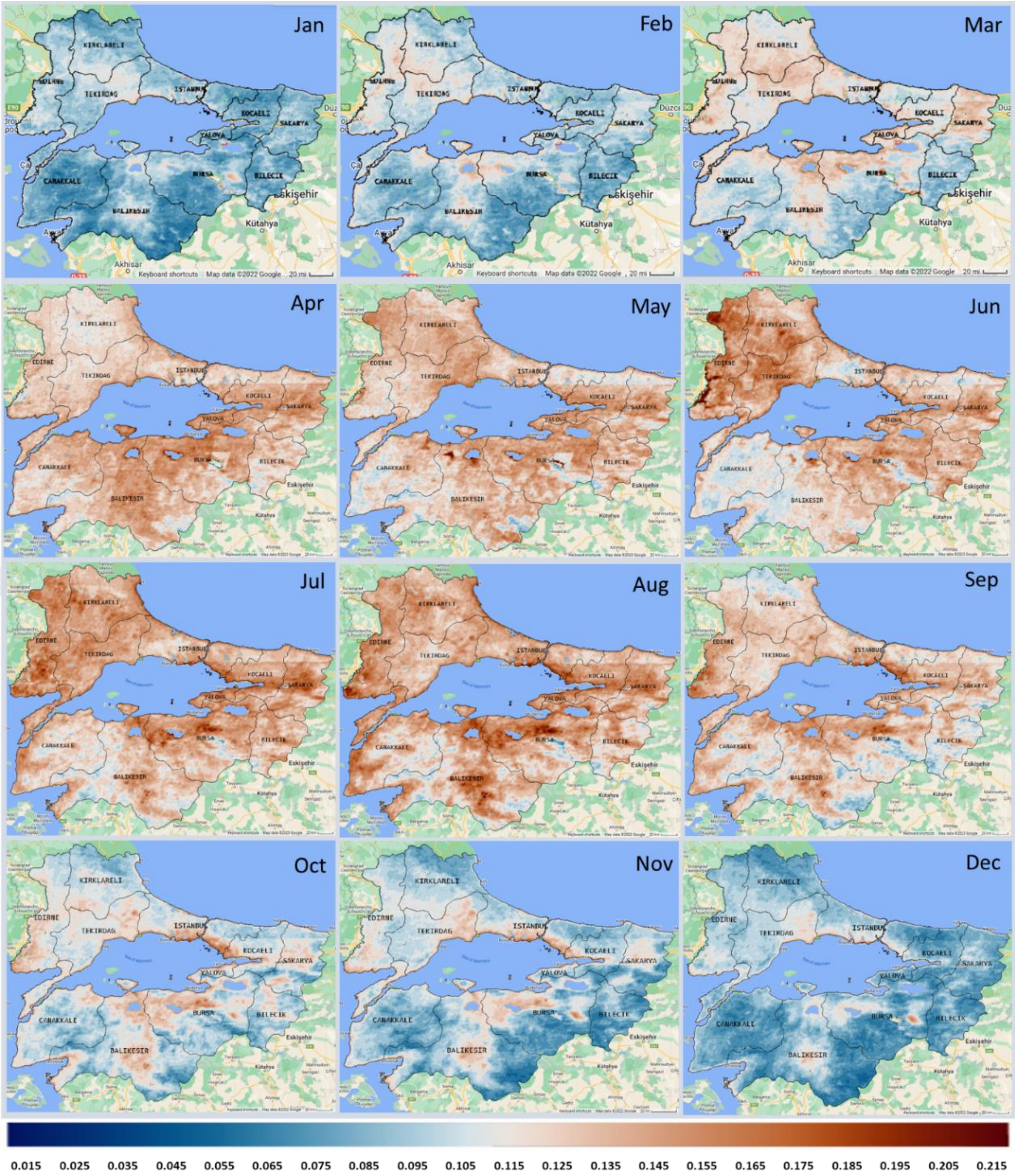

Figure 3.11 : Spatial distribution of mean MODIS MAIAC AOD in each month for the period 2000-2021 over the Marmara region.

Figure 3.12 depicts the seasonal average distribution of AOD value over the study region for the entire period of study. The annual mean AOD spatially averaged for the Marmara region was 0.12±0.02, with an AOD maximum in Summer (0.145±0.004). Summer was the season with the highest high-value area of the AOD, followed by spring and autumn, while winter had the lowest high-value area. The extent of the elevated AOD area varies with the season and is largest in the summer when it reaches west over the Thrace region.

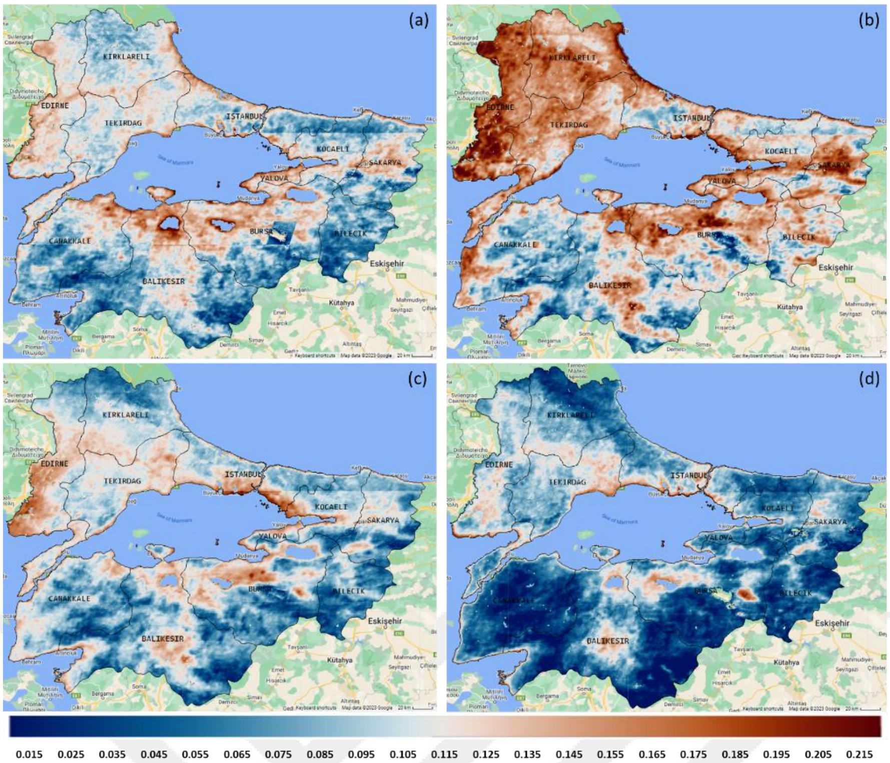

Figure 3.12 : Seasonal mean aerosol distributions for (a) spring (March-May), (b) Summer (June-August), (c) autumn (September-November) and (d) winter (December-Feb) for the period 2000-2021 over the Marmara region.

The differences in AOD value and temporal evolution are influenced by various factors, including anthropogenic emissions, climatic and meteorological effects, and long-distance transit, which can vary with the season. Figure 3.11 shows that there is higher AOD accumulation in the range of 0.13-0.15 during the April to September months, with larger high AOD areas observed in May and August due to an increase in aerosol water content favored by higher absolute humidity.

In contrast, lower AOD values are spread during the first three months of the year, and a substantial rise is observed from April until August. After summer ends, there is an apparent reduction in AOD, which is partly due to deposition favored by precipitation. The lower aerosol distribution in December and January could be attributed to missing AOD pixels caused by snow cover and changes in ground surface reflectance, as well as particulate removal from the atmosphere via precipitation scavenging. Winter weather patterns can increase air mixing and ventilation in some areas, which can aid in dispersing aerosol particles and lowering their concentration.

Despite these limitations, greater aerosol concentrations and AOD values were reported for winter months over predominantly urban areas, indicating the agglomeration of anthropogenic emissions in these areas. The highest high-value area of AOD during summer is greatly affected by seasonal weather, with a higher absolute humidity and temperature being present during the hotter months over the Marmara region. Figure 3.13 demonstrates the variance in absolute humidity and average daytime temperature in the Marmara region, where the highest moisture content occurred in July and August. The high moisture absorption effects and high temperature caused Secondary organic aerosol (SOA) conversion, which led to higher averaged AOD means.

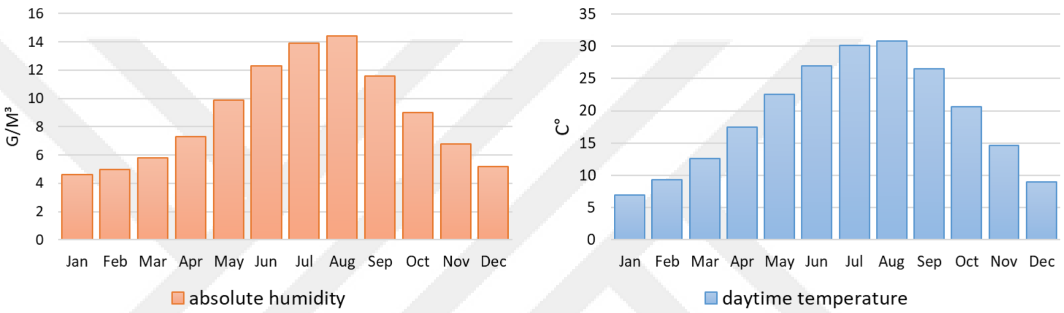

Figure 3.13 : Variance in absolute humidity and average daytime temperature in the Marmara region.

The spatial distributions and temporal variations of AOD are partly attributed to seasonal source emission variations. The emissions from non-residential sources of anthropogenic emissions, such as power generation, industry, and transportation, are observed throughout the year. Relatively high AOD is observed over urban and industrial areas during the spring, summer, and autumn, with values of about 0.11-0.18 and lower in the winter. The heating-specific emissions are the main source of anthropogenic emissions over the high AOD areas during the autumn and winter. The aerosols are highlighted over the urban centers where the population resides during autumn and winter, with higher AODs seen in autumn due to seasonal meteorological conditions. During winters, aerosols are reduced by higher aerosol washouts and dispersed by larger wind speeds over the Marmara region. Given the spatial variability in the evolution of AOD, an analysis is provided here with AODs averaged per province. Figure 3.14 displays the annual and seasonal mean trends for individual provinces of the Marmara region. Looking at the mean AODs for each of 13 provinces located in the Marmara region, the annual mean AOD for Edirne

(0.132 ± 0.023) and Yalova (0.132 ± 0.035) were slightly higher than those for other provinces (Figure 3.14). The seasonal maximum AOD appeared in the summertime for Edirne (0.1621±0.002) and Yalova (0.1603±0.004), which are similar to that in the summertime, but about 8%-18% higher than that for other provinces. In autumn Istanbul, Tekirdağ, and Kocaeli come after the Edirne-Yalova AOD maximal.

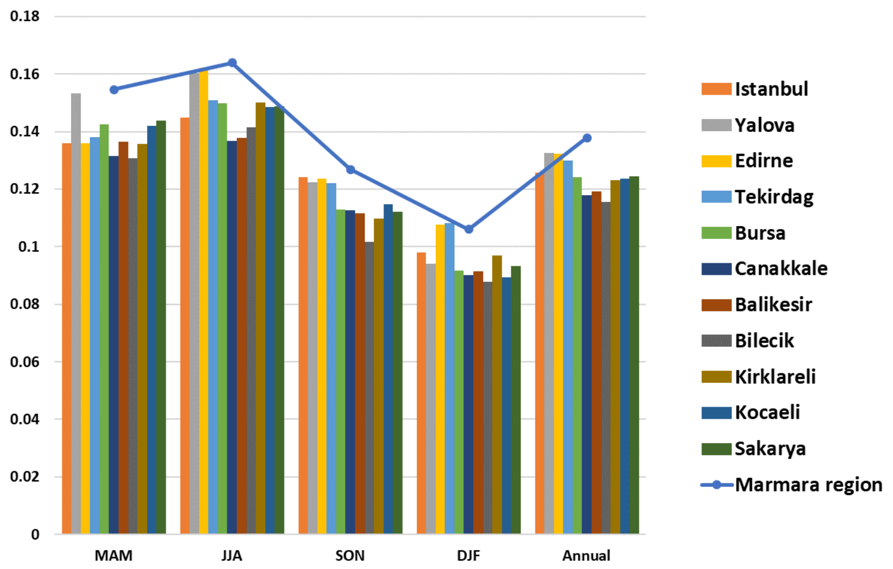

Figure 3.14 : Time series of seasonal averaged MODIS MAIAC AOD over the Marmara region in 11 provinces.

The extent of the elevated AOD area to the total area of a province determines the spatially averaged AOD mean for each sub-region of the study area. The average AOD over the province contains the AODs of highest to lowest AODs over the region. For instance, the Bursa may contain the highest and lowest AOD of the area at the same time. I masked the aerosol loading of low-value areas (LVA) (AOD < 0.135), calculated the mean AOD of just high-value areas (HVA) (AOD > 0.135) in the annual AOD mean between 2000-2021, and analyze the seasonal variations of AOD at province scale.

The thresholds for the annual and seasonal HVA and LVA were defined using the percentile thresholds. The HVA contains AOD pixels above the 85th percentile threshold. Figure 3.15 shows the spatial extent of HVA of 21-year mean AOD for the provinces in the Marmara region which are highlighted with red color.

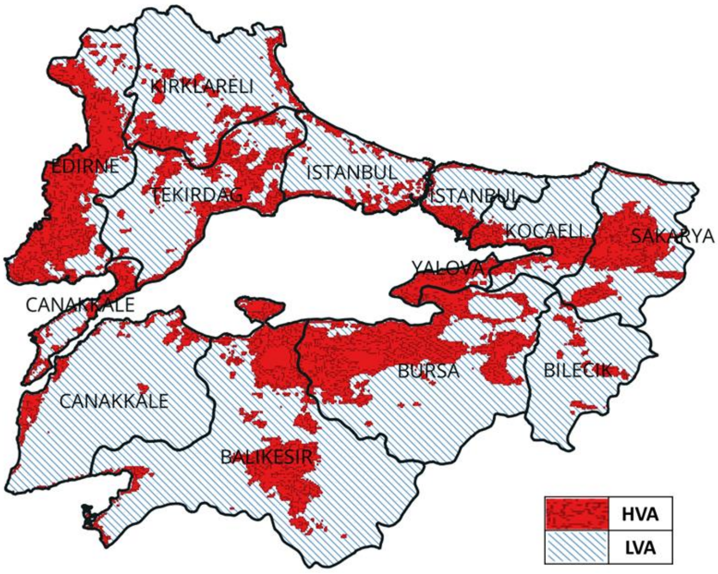

Figure 3.15 : Thematic map of HVA in the Marmara region.

Table 3.1 lists the percentage of HVAs in each province and the averaged AOD of HVAs. AOD values may vary across provinces due to differences in aerosol sources' intensity and density. Mean AOD is not determined by the size of the high AOD area alone. A province with fewer high AOD areas but a higher concentration and intensity of aerosol sources might have a higher mean AOD. The wind patterns and topography of an area can also influence mean AOD values. Several factors influence the relationship between a high AOD area and a mean AOD value.

Edirne and Yalova have the highest percentage of areas covered with high aerosol loadings (77% and 62%, respectively) but not the highest mean HVA AOD. The second-highest mean AOD value of HVA was recorded for Bursa and Yalova (0.144). With just 20% of the total area for the Asian side of Istanbul covered with high AODs, this region has the highest mean AOD value of HVA (0.147). Although the 62% of Edirne city include in HVA, the mean AOD of this portion is the sixth highest value comes after Bursa, Yalova, Balikesir, Kocaeli, Sakarya, and Istanbul. These results demonstrate that smaller areas with dense urbanization have higher mean AODs, whereas the aerosol emissions from burning biomass and agricultural activities are spread across broader areas with relatively lower AOD values.

Table 3.1 : Province-wise mean AOD over HVAs between 2000 and 2021.

Province	Mean AOD	HVA % (km^2)	Mean AOD of HVA
Yalova	0.140	76.67 (608)	0.143
Edirne	0.136	61.46 (3818)	0.140
Bursa	0.130	38.37 (4201)	0.144
Sakarya	0.129	37.02 (1802)	0.142
Tekirdag	0.133	29.70 (1864)	0.138
kocaeli	0.129	27.34 (931)	0.142
Balikesir	0.123	22.79 (3262)	0.143
Istanbul (Asian side)	0.127	20.68 (388)	0.147
Kirklareli	0.128	19.49 (1266)	0.137
Istanbul (European side)	0.130	17.74 (587)	0.141
Canakkale	0.124	11.47 (1100)	0.139
Bilecik	0.120	7.85 (326)	0.138

The extent of the elevated AOD area varies with the season. I highlighted the HVA and LVA for each season over the Marmara region (Figure 3.16). The HVA contains AOD pixels above the 85th percentile threshold of the seasonal means.

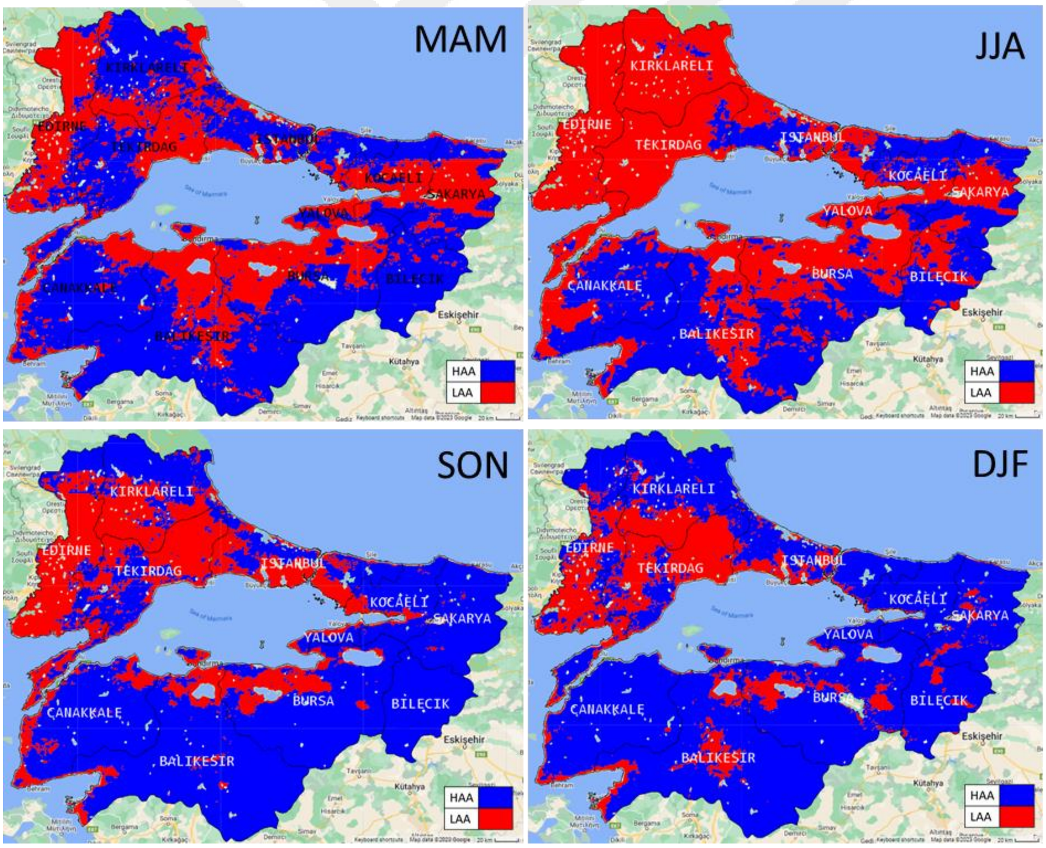

Figure 3.16 : Seasonal variation of HVA from 2000 to 2021. Spring- MAM, Summer- JJA, Autumn-SON, and winter-DJF.

The high AOD area is largest in the summer with about 54% of the total area and then spring (45%) and autumn (26%). Winter has the lowest HVA with 17% of the total area. The seasonal percentage rates of HVA are due to atmospheric conditions and aerosol sources. Larger HVA in summer is due to the increase of human activities, transportation, and mainly farming practices combined with intense solar radiation, which can lead to increased evaporation. Same as Summers, Springs in Marmara region is for the agricultural activities plus the pollen emissions which lead to larger HVAs. The increasing precipitation level in autumn and winters decrease HVAs which are largely concentrated in urbanized and industrialized spots. The Trakya region is exposed to larger HVAs in all seasons due to atmospheric conditions and aerosol sources. The coal burning for residential and industrialized activities combined with lower precipitation and warmer weather lead to larger HVAs during a year. Table 3.2 presents the seasonal mean AOD of HVA in each province between 2000 and 2021. Yalova has the highest average AOD (0.153) among the provinces in spring. Sakarya has the highest average AOD (0.162) in summer. The highest AOD mean of autumn and winter is seen over Kocaeli (0.143) and Istanbul (0.113) respectively.

Table 3.2 : Province-wise analysis of seasonal variations of averaged AOD in HVA.

Province	Mean AOD of HVA –MAM	Mean AOD of HVA -JJA	Mean AOD of HVA -SON	Mean AOD of HVA -DJF
Bursa	0.149	0.158	0.142	0.110
Bilecik	0.135	0.152	-	0.097
Sakarya	0.149	<u>0.162</u>	0.139	0.102
Kocaeli	0.145	0.158	<u>0.143</u>	0.105
Canakkale	0.138	0.150	0.128	0.106
Edirne	0.135	0.161	0.128	0.106
Tekirdag	0.139	0.150	0.125	0.107
Kirklareli	0.137	0.150	0.120	0.106
Istanbul	0.142	0.152	0.134	<u>0.113</u>
Balikesir	0.146	0.152	0.139	0.111
Yalova	<u>0.153</u>	0.160	0.139	0.109

3.4.3 Inter-annual spatial distribution and Evolution of AOD over the Marmara region - Time series of AOD averaged per province

Table 3.3 shows four statistical indicators of annual AOD values including the annual minimum, maximum, mean, and STD for the Marmara region. High annual mean AOD values (0.146, 0.141, 0.1368, and 0.1367, respectively) are found in 2002, 2003, 2008, and 2000. Among them, the aerosol loading in 2000 and 2002 have a greater variety of AOD values (STD = 0.02). However, lower annual mean AOD values are observed in recent years, 2020 and 2021. Although the global AOD values fluctuate in different years, aerosol values over the Marmara region generally remain stable (STD = 0.015), and the annual mean AOD value is around 0.128.

Table 3.3 : Statistical indicators of annual AOD values over the Marmara region between 2000 and 2021.

YEAR	MIN	MAX	MEAN	STD	YEAR	MIN	MAX	MEAN	STD
2000	0.049	0.217	0.137	0.020	2011	0.061	0.232	0.127	0.015
2001	0.062	0.208	0.126	0.016	2012	0.057	0.223	0.129	0.014
2002	0.044	0.286	0.143	0.020	2013	0.061	0.217	0.123	0.016
2003	0.061	0.229	0.139	0.019	2014	0.067	0.229	0.126	0.014
2004	0.059	0.209	0.126	0.017	2015	0.074	0.226	0.128	0.015
2005	0.073	0.245	0.131	0.014	2016	0.069	0.262	0.124	0.014
2006	0.071	0.229	0.128	0.015	2017	0.077	0.200	0.120	0.013
2007	0.075	0.232	0.133	0.014	2018	0.071	0.240	0.131	0.017
2008	0.061	0.228	0.137	0.014	2019	0.077	0.240	0.120	0.012
2009	0.067	0.224	0.131	0.016	2020	0.053	0.228	0.110	0.013
2010	0.072	0.247	0.130	0.014	2021	0.067	0.202	0.119	0.014
2011	0.061	0.232	0.127	0.015	2022	0.053	0.229	0.131	0.016

To present the multi-year variation of AOD, the mean value has been calculated in the Marmara region and shown in Figure 3.17. Between 2000 and 2021, AOD has a maximum value in 2002 with a value of 0.143 and is the smallest in 2020 with a value of 0.11. Between 2000 and 2010, AOD has two maxima in 2002 and 2008, respectively, with values of 0.146 and 0.137. From 2000–2021, AOD has a trend of decrease, with an annual decrease of 0.005/a. Only considering the period between 2018 and 2021, AOD has shown a significant decreasing trend, with an annual decrease of about 0.08/a. which is closely related to the reduction of regional pollutant emissions during two and a half years of COVID-19 pandemic restrictions.

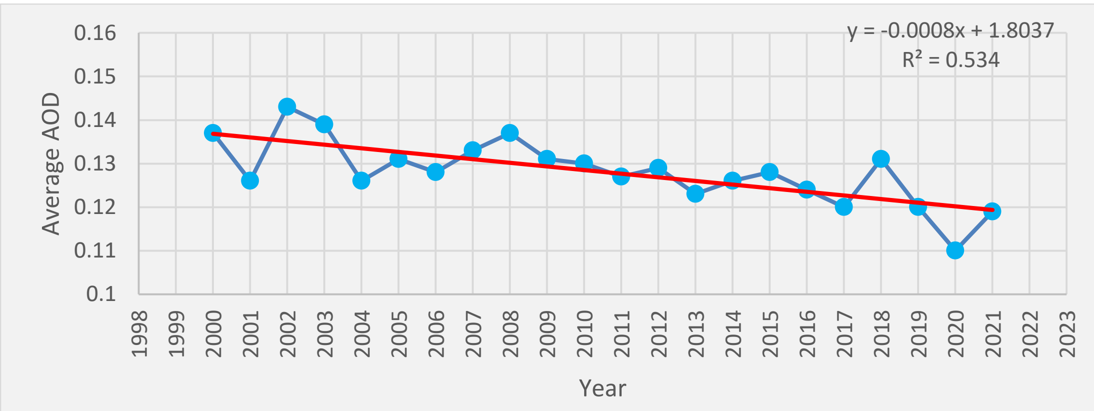

Figure 3.17 : Time series of the yearly averaged AOD over the Marmara region.

To track changes in the spatial distribution of AOD over time over the Marmara region, I used an image series where each frame (one for each year) comprises an average of high-quality MODIS MAIAC AOD data for that year. Figure 3.18 shows the spatial distribution of the annual mean MODIS MAIAC AOD over the Marmara region between 2000 and 2021.

While high-value areas of AOD occupy the urbanized and industrialized region of the study area, the low-value area of AOD in the easternmost part of the study area and its margins are relatively stable over time (Figure 3.18). The maps show the spatiotemporal variation of initially rising and, after a period of very high AOD, declining with significant changes in the emission patterns. There are differences between the AOD patterns in various regions of the area. The study area's first rise began in the western provinces and moved east a few years later. After 2003, the AOD steadily decreased in the western part (2004-2010) and this seems to have occurred first in Tekirdağ and Kirklareli provinces and then in Edirne (compare 2010–2016). AOD patterns over different areas have changed between 2000 and 2021, as indicated by annual averaged AOD maps. Istanbul and provinces in the eastern part of the Marmara region have been experiencing higher levels of AOD since 2014, with more concentrated spots of aerosols.

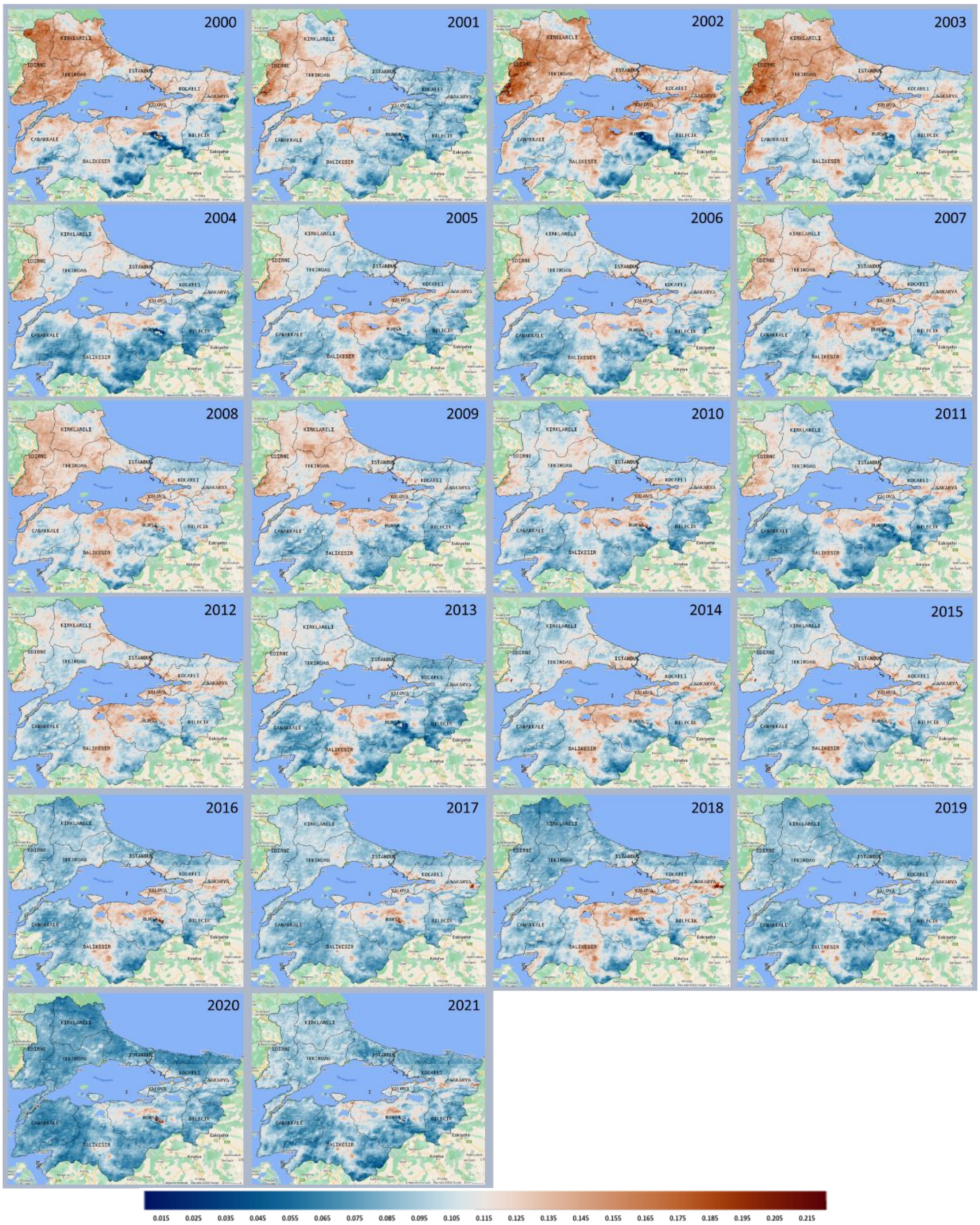

Figure 3.18 : Annual average AOD in the Marmara region from 2000 to 2021.

The Marmara region's high aerosol loadings between 2000 and 2003 were mainly caused by the consumption of low-quality fossil fuels, with residential and industrial coal combustion being significant contributors to atmospheric pollution. The Marmara region has been affected by the highest aerosol loadings between 2000 and 2003 which is mostly due to the consumption of low-quality fossil fuels. The severity of the level of AOD during these years highlighted the contributions of residential and industrial coal combustion to atmospheric pollution. After 2004, the effects of using natural gas instead of coal as a source of energy for heating, cooking, and electricity generation are vivid in the area. According to the THEP 2020-2024 report by the Republic of turkey ministry of Environment and Urbanization, (Thep, 2020) since 1997, sulfur dioxide concentrations in Istanbul have declined dramatically, particularly as a result of improved coal quality and the extensive usage of natural gas. Since 2004, these concentrations have been below the annual limit values outlined in European Union directives. In Turkey after Ankara city, in which natural gas was used for the first time in urban, domestic, and commercial in 1988, the government started to invest in gas in Istanbul and the first part of the project was completed in May 1993. Five cities along the route of the first main transmission line, entering from the Bulgarian border and extending to Ankara, including Istanbul, Izmit, Bursa, Eskisehir, and Ankara, were linked to the distribution line in 8 years. As of December 2001, natural gas is supplied to about 2.6 million customers in those cities. Although the use of natural gas has started to become widespread with an intense promotion since April 1994 in Istanbul, we can observe its effects on aerosol pollution across the Marmara region after 2003 when the gas became a major source of energy being used due to lower gas prices after the distribution companies start to operate widely.

Around 2003, the overall density of aerosols dropped while keeping its regional dispersion. Aerosol concentrations over the Edirne-Kirklareli-Tekirde and the European side of Istanbul, which are primarily covered by agricultural areas, typically dropped after 2009, both in value and spatial distribution. The reason for this decrease mostly points to the decrease in stubble burning in agriculture in the regions. The decrease of aerosol loading over the western side is trackable over the annual thematic maps showing the HVA and LVA of AOD (Figure 3.19).

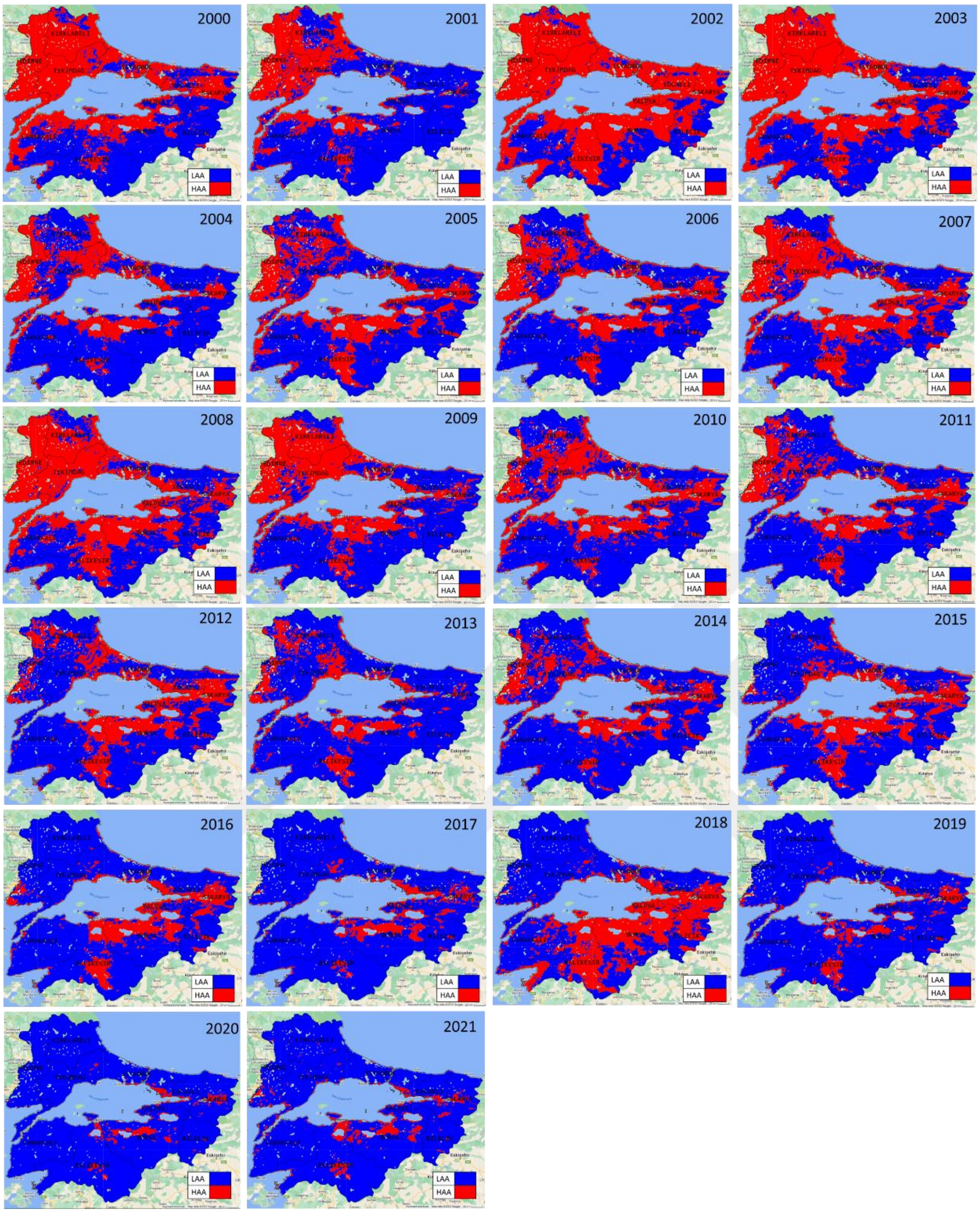

Figure 3.19 : Variation of HVA and LVA of annual AODs between 2000 and 2021 over the Marmara region.

After 2010, the aerosol distribution is more pronounced along urbanized and industrialized zones, but it is possible to detect a further increase in the aerosol value in the eastern part of the Marmara region. The most significant change in recent years is the drastic decrease in aerosol distribution and value in 2019 and 2020. The most likely reason for this decrease is the impact of COVID-19 restrictions and bans.

A six-year average AOD data layers were calculated and analyzed. The averaged AOD in the 6-year intervals reveals a significant AOD variability. Figure 3.20 presents the spatial distribution trend in annual mean AOD. With mean values of 0.134, 0.131, 0.124, and 0.120 for 2000–2005, 2006–2011, 2012–2017, and 2018–2022, respectively, the 6-year annual averaged AOD decreased by -0.03 (–3%) per 6-year. Between 2000 and 2005, the Marmara region's western portion saw the greatest accumulation of aerosols, while in subsequent years, the eastern side of the region saw higher aerosol distribution. The maximum annual AOD mean for the Marmara region was 0.134 between 2000 and 2005. A decrease in the usage of coal and biofuels for heating, cooking, and industrial boilers contributed to the progressive reduction in aerosol loading over the Marmara region. This was largely accomplished by increasing the usage of natural gas and partially by switching out low-quality, locally-produced lignite for high-quality, imported coal. Local lignite contributes more to air pollution due to its high sulfur and ash content, low calorific value, and low calorific content.

Istanbul and Bursa were among the cities located on the route of the natural gas pipeline that began to be constructed on 26.10.1986 and reached its last station in August 1988. Natural gas was supplied for use in the residential and commercial sectors in Istanbul and Bursa in January and December 1992, respectively. The extensive use of gas did not occur until the dates of 17 February 2004 in Istanbul and 18 September 2003 in Bursa, when the distribution of natural gas was handled by municipally held enterprises or private ones. Natural gas consumption has become widespread with the distribution networks built by private companies winning the license tenders in Edirne-Tekirdag-Kırklareli (25/01/2006) and Canakkale (20/04/2006) (EMRA (Energy Market Regulatory Authority), 2012). Comparing the mean AOD profiles of the first two 6-year intervals (2000-2005 and 2006-2011), the intensity of the aerosol loading over Edirne, Tekirdag, Kirklareli, and Canakkale was noticeably reduced from 2006 to 2011 (Figure 3.20).

The aerosol loading between 2012 and 2017 displays a similar pattern to that between 2006-2010 with lower aerosol loading over the Edirne-Tekirdag-Kirklareli subregion. During 2018 to 2021 the aerosol loading mostly accumulated over the most urbanized regions of the provinces. Bursa, Balikesir, Sakarya, the Eastern side of Istanbul, and Yalova are among the regions which experienced extreme air pollution during 2012-2022. The lower aerosol loading over the region, especially in Edirne, Kirklareli, Tekirdag, and Istanbul between 2018-2022 compared to the previous 6-year period is due to the decrease of human-induced air pollutants following the restrictions during the COVID-19 outbreaks. Although COVID-19 pandemic restrictions caused the decline of atmospheric pollution across the Marmara region, industrialized cities such as Bursa, Yalova, Kocaeli, Balikesir, and Sakarya in which industries continue operating through the restrictions.

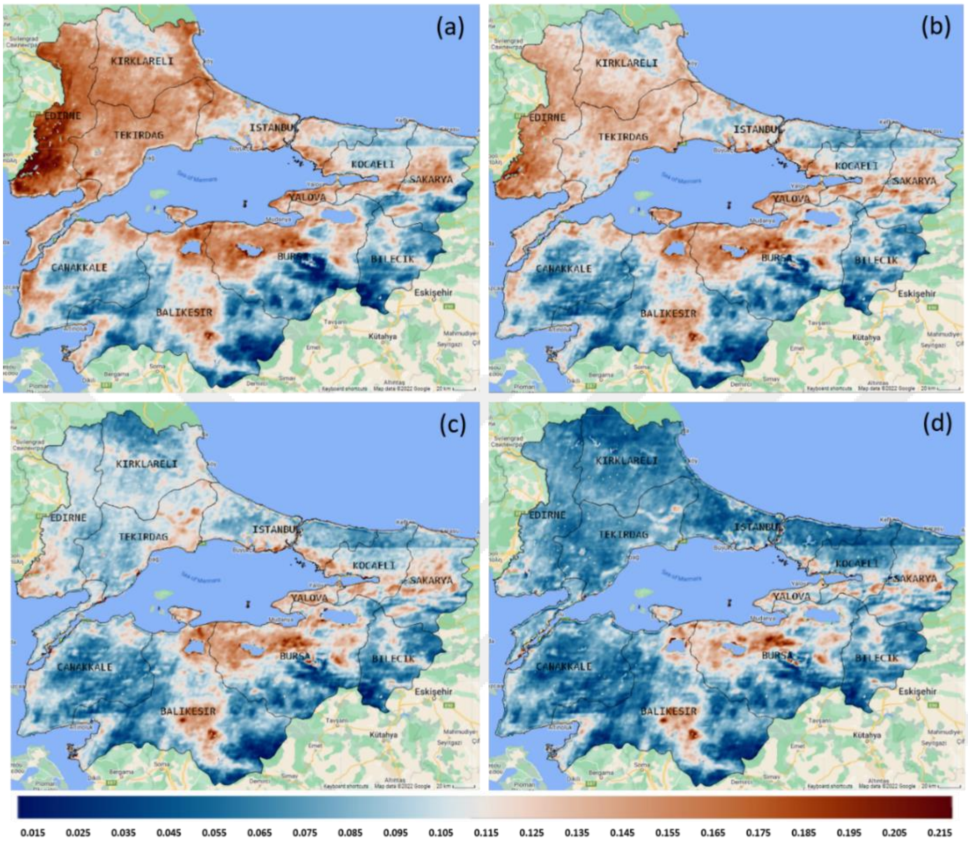

Figure 3.20 : Annual mean climatology of AOD observed by MODIS MAIAC over the Marmara region in 6-year intervals of (a) 2000-2005 (b)2006-2011 (c) 2012-2017 and (d)2018-2022.

To get a robust statistic on the trends, I estimated the long-term trend using MODIS MAIAC retrieved AOD for the Marmara region between 2000 and 2021 (Figure 3.21). The trend analysis data as seen in Figure 3.21 shows a high positive AOD trend (up to 0.05 AOD/decade) on the eastern side and a high negative AOD trend (up to 0.1 AOD/decade) on the western side of the Marmara region.

Significantly larger positive trends in AOD were observed in the mountain basins, which may be attributed to increased local emissions in nearby regions and the accumulation of particles in these basins. On the other hand, trends in AOD over the western side of the study area and Istanbul city are negative. These negative trends were found to be 2.5 times larger than the positive trend on the eastern side, indicating the stronger effects of agricultural burnings on the value and spatial distribution of AOD.

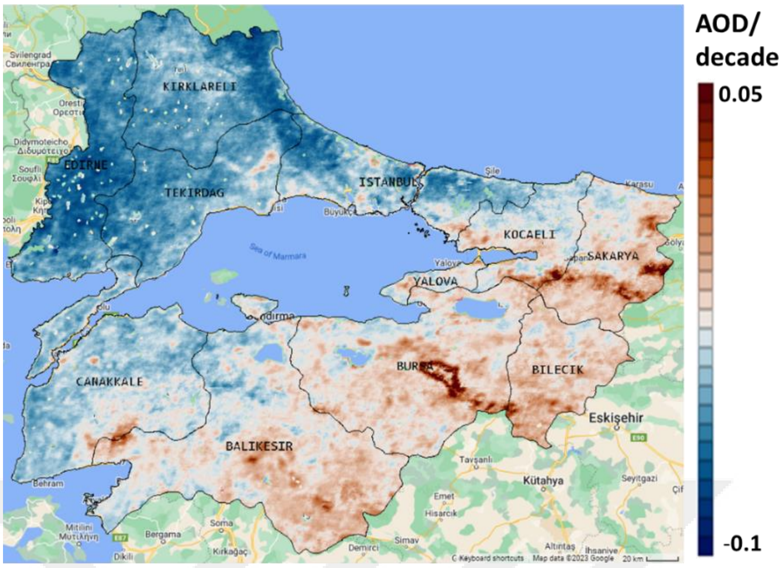

Figure 3.21 : The long-term trend observed in AOD by $\mathrm{MODIS}_{\mathrm{MAIAC}}$ (2000–2021),

3.4.3.1 AOD variations on a provincial scale

The annual mean AOD of the provinces from 2000 to 2021 is listed in Table 3.4. Aerosol hotspots with AOD values greater than 0.11 are highlighted (Table 3.4). Over the past 21 years, the number of years in which Yalova has been exposed to high aerosol loading (AOD>0.1) was the highest (N=11). The aerosol loading was higher over Edirne, Tekirdag, Kırklareli, Canakkale, Istanbul, and Kocaeli until 2005 and then between 2008 and 2011, while Bursa, Sakarya, and Balikesir were exposed to higher aerosol concentrations after 2016. Table 3.4 represents the transfer of the high AOD area of the western side of the Marmara region to the eastern side of it over the past 21 years. While the lower consumption of poor-quality coal in Edirne-Kirklareli-Tekirdag decreases the aerosol concentration on the western side of the Marmara region, the rapid urbanization and demand for denser constructions and industrial expansion in the eastern side of the Marmara region cause the remarkable increase in aerosol emissions.

Table 3.4 : Annual mean AOD of the provinces of the Marmara region.

	2000	2001	2002	2003	2004	2005	2006	2007	2008	2009	2010	2011	2012	2013	2014	2015	2016	2017	2018	2019	2020	2021
EDIRNE	0.128	0.132	0.167	0.107	0.126	0.135	0.1	0.095	0.141	0.112	0.095	0.157	0.094	0.086	0.102	0.097	0.096	0.101	0.1	0.115	0.088	0.09
TEKIRDAG	0.11	0.109	0.154	0.105	0.123	0.125	0.087	0.09	0.138	0.104	0.104	0.128	0.097	0.084	0.098	0.1	0.11	0.099	0.091	0.109	0.09	0.094
KİRKLARELI	0.106	0.108	0.137	0.094	0.109	0.123	0.082	0.073	0.129	0.103	0.083	0.119	0.089	0.071	0.084	0.09	0.086	0.095	0.086	0.105	0.078	0.086
CANAKKALE	0.116	0.101	0.129	0.112	0.116	0.131	0.088	0.095	0.142	0.106	0.108	0.131	0.102	0.083	0.107	0.109	0.1	0.104	0.108	0.119	0.089	0.105
ISTANBUL	0.123	0.091	0.14	0.118	0.117	0.126	0.088	0.097	0.132	0.111	0.097	0.117	0.1	0.09	0.103	0.103	0.098	0.106	0.112	0.104	0.098	0.104
KOCAELI	0.098	0.085	0.111	0.105	0.111	0.114	0.093	0.089	0.123	0.092	0.096	0.106	0.104	0.081	0.088	0.094	0.114	0.118	0.105	0.11	0.097	0.081
YALOVA	0.114	0.093	0.121	0.103	0.116	0.122	0.091	0.102	0.13	0.093	0.103	0.111	0.109	0.089	0.1	0.11	0.128	0.121	0.128	0.122	0.126	0.099
BURSA	0.094	0.084	0.097	0.1	0.099	0.104	0.089	0.106	0.121	0.087	0.085	0.102	0.105	0.08	0.095	0.101	0.111	0.111	0.114	0.118	0.113	0.095
SAKARYA	0.092	0.082	0.093	0.094	0.094	0.099	0.089	0.097	0.122	0.084	0.09	0.101	0.104	0.08	0.085	0.091	0.115	0.12	0.128	0.113	0.097	0.085
BALIKESIR	0.093	0.085	0.092	0.095	0.096	0.107	0.078	0.102	0.119	0.081	0.087	0.106	0.105	0.08	0.092	0.1	0.099	0.1	0.111	0.122	0.101	0.091
BILECIK	0.083	0.084	0.069	0.082	0.084	0.08	0.072	0.088	0.103	0.077	0.067	0.086	0.092	0.065	0.083	0.078	0.088	0.099	0.114	0.099	0.094	0.082

To intercompare the aerosol pollution of the provinces located in the Marmara region I classified the aerosol loading in four classes. I characterized the aerosol loading with levels using four classes of AOD values; the first level (AODs < 0.1) shows the lowest aerosol loading, the second (0.1 <AOD <0.2) and third (0.2 <AOD <0.3) levels show the moderate aerosol loading and the fourth level (AOD ≥ 0.3) shows the highest aerosol loading. The analysis was done at a daily scale and I used a daily mean MODIS MAIAC AOD data for each of the 11 provinces located in the Marmara region. I calculate the percentages of days in each level during the years between 2000 and 2020 for each province of the Marmara region and inter-compare the aerosol pollution levels at different provinces (Table 3.5).

As the AOD value is calculated by averaging the AOD pixels along the borders of a province, it includes areas with both high and low aerosol loading. It is not possible to determine the exact border of aerosol loading within each province using this method. However, provinces with the highest daily mean AOD values indicate that there is a considerable amount of aerosol loading in the region. Continually high AOD levels indicate a location that has experienced greater aerosol emissions from industrial activity in rural or peri-urban areas, household fuel consumption, biomass burning, or both. Long-range dust transport that accumulates in a place as a result of its geographical features, such as megacities that are encircled by mountains or seas, can also be linked to a region's ongoing aerosol pollution. These cities or districts can be categorized as areas that often experience higher levels of air pollution than others.

Table 3.5 : Validation of percentage statistics of aerosol pollution levels in the provinces of the Marmara region.

	Percentage Statistics (2000 - 2022)			
Province	Level 1 %	Level 2 %	Level 3 %	Level 4 %
Edirne	29.82	41.97	19.45	<u>8.76</u>
kırklarelı	32.43	40.12	19	8.44
Kocaeli	31.07	41.64	19.58	7.71
Tekirdag	30.79	42.1	19.47	7.64
Sakarya	29.83	41.47	21.06	7.64
Yalova	27.8	44.75	19.98	7.48
Istanbul	30.89	44.95	16.99	7.17
Bursa	29.52	43.24	20.33	6.9
Bilecik	<u>34.25</u>	40.9	18.6	6.25
Çanakkale	32.72	44.63	16.71	5.95
Balikesir	32.68	46.58	16.12	4.62

From 2000 to 2021 the highest number of days with lower aerosol pollution is seen in Bilecik (≈ 35%) while Edirne experienced the highest percentage of days with the highest aerosol pollution level (≈ 9%). The higher aerosol concentration in Edirne province during 2000-2021 also affected the neighboring districts, Kırklareli and Tekirdag. The highest aerosol loadings in most of the cases over the Tekirdag and Kırklareli were accumulated near the Edirne-Kırklareli or Tekirdag-Kırklareli border regions. Intense aerosol pollution in Edirne is the result of coal combustion which is used for heating purposes. In 2019, 35730,125 tons of coal a year were used for heating purposes during the cold season in that zone. 65% of the total amount of used fuel is the low-quality domestic lignite while the rest is the imported coal.

I calculated the percentage of days with four levels of aerosol pollution for each province of the Marmara region for the period between 2000 and 2021. Over 21 years, patterns in the percentage of days spent at each level for each province were examined. The detailed information on statistical results for each province is shown in Tables B.1-B.10 in Appendix B. For Edirne, Kirklareli, and Tekirdag provinces in the western Marmara area, the percentage of days with high aerosol pollution (level 4) is highest (7% - 16%) which primarily occurred from 2000 to 2011. In 2018, the percentage of days with level 4 aerosol pollution was highest in the Marmara region's provinces which are located in the eastern part of the Marmara region, including Bursa, Bilecik, Kocaeli, Yalova, the eastern part of Istanbul, and Sakarya (Appendix B).

Although the patterns of aerosol pollution levels vary throughout years and provinces, according to statistics from 2000 to 2021, 2020 is the year in which all the provinces in the Marmara region had the largest percentage of days (between 35% and 49%) with AOD values below 0.1 (level 1). The COVID-19 pandemic restriction reduces human-caused air pollution in 2019–2020, which consequently has an impact on the AOD levels in the Marmara region as well.

To observe the temporal changes of AOD over the Marmara region and compare temporal changes at each province of the Marmara region, I calculated the time series of the annual mean AOD of the provinces for years between 2000 and 2021 (Figure 3.22).

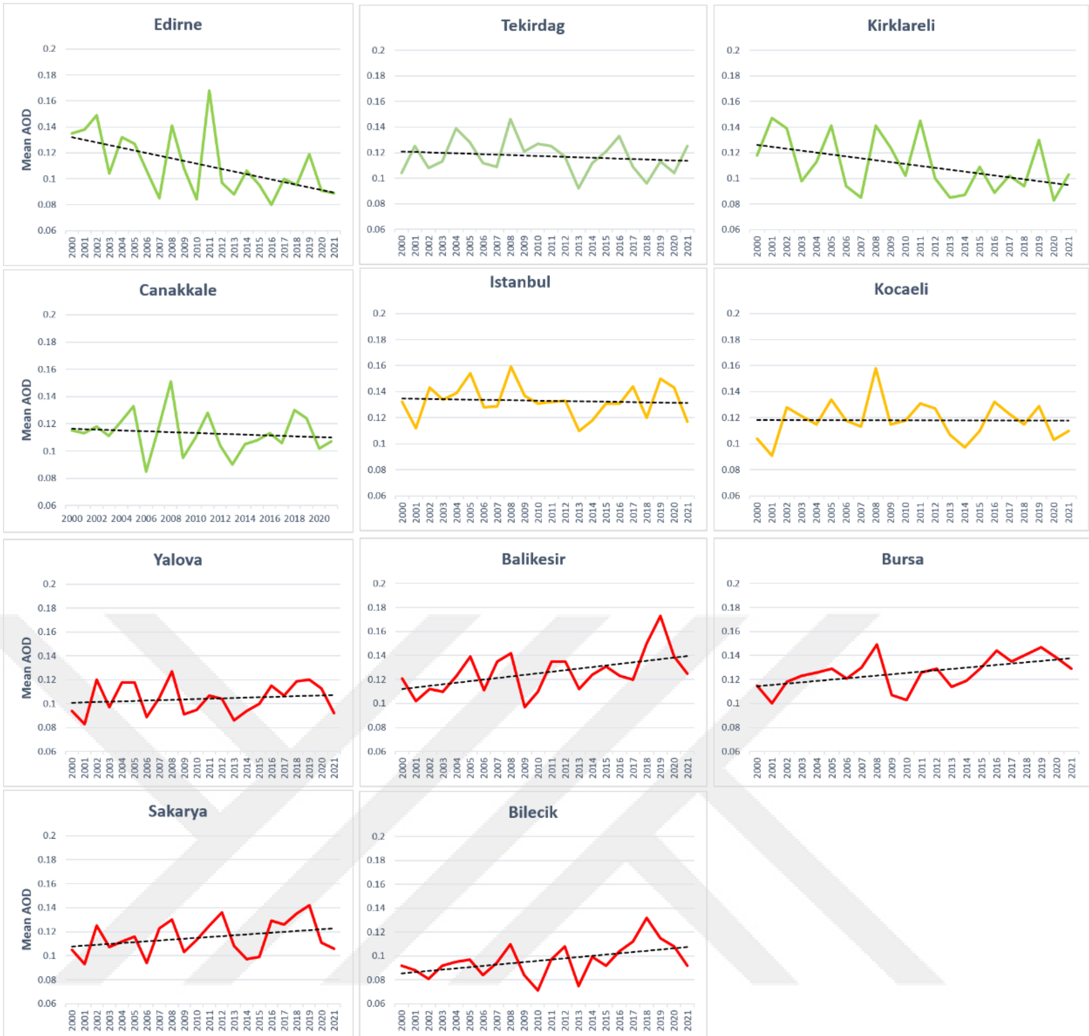

Figure 3.22 : Time series and trend lines for annual AOD over the provinces of the Marmara region.

There are upward trends in annual mean AODs over the majority of the provinces in the Marmara region's eastern side including Bursa, Balikesir, Sakarya, Yalova, and Bilecik while the trends are downwards at the provinces located in the western part of the Marmara region including Tekirdag, Kirklareli, Canakkale, and Edirne. The average AOD between 2000-2021 in Edirne is the highest (0.112) among the provinces located in the Marmara region and the AOD trend of it was the lowest negative trend over the past 21 years (slope = -0.002), which is associated with the biggest drop in AOD. In the last 21 years, Balikesir has experienced the highest positive trend (slope = 0.0013) and the greatest increase in AOD. The annual AOD means for Istanbul (slope = -0.0002) and Kocaeli (slope = -0.00002) show a slight downward trend.

The fact that Kocaeli and Istanbul both exhibit a minor decline in AOD means suggests that the air quality in both locations may have marginally improved over time, however, other elements (such as modifications to weather patterns or emission laws) may also be influencing the trend. This is while the Istanbul metropolitan city is the most populated in Turkey with increasing industrial activities. Due to the specific topographical features of the Marmara region and metrological properties with the dominant northerly wind system transport the pollutant from Istanbul and Kocaeli to Yalova and Bursa and the districts of Canakkale (i.e. Biga, Lapseki) and Balikesir (i.e. Erdek and Banirma) bordering the Marmara Sea which is majorly surrounded by mountain ranges. The industrialized metropolitan city of Istanbul has a population of over 15 million people (TUIK, 2021a) and more than 4.5 million registered vehicles (TUIK, 2021b). Istanbul's location on a peninsula bordered by the Sea of Marmara and the Bosphorus Strait, together with the city's varied topography and prevailing sea wind, can aid to reduce some of the air pollution brought on by the city's dense population and heavy traffic.

3.4.4 Effects of land use/cover types on AOD

Certain types of land cover or land use can contribute to atmospheric aerosol concentration and significant AOD value spots. The 2018 CLC map and the regions with high annual AOD distribution are displayed in Figure 3.23. High aerosol dispersion is observed over large metropolitan clusters and artificial surfaces, which are significant geographical producers of anthropogenic aerosols (regions 1 to 6). Rural and agricultural areas (regions 7 and 8) make up the other two high aerosol-loading areas.

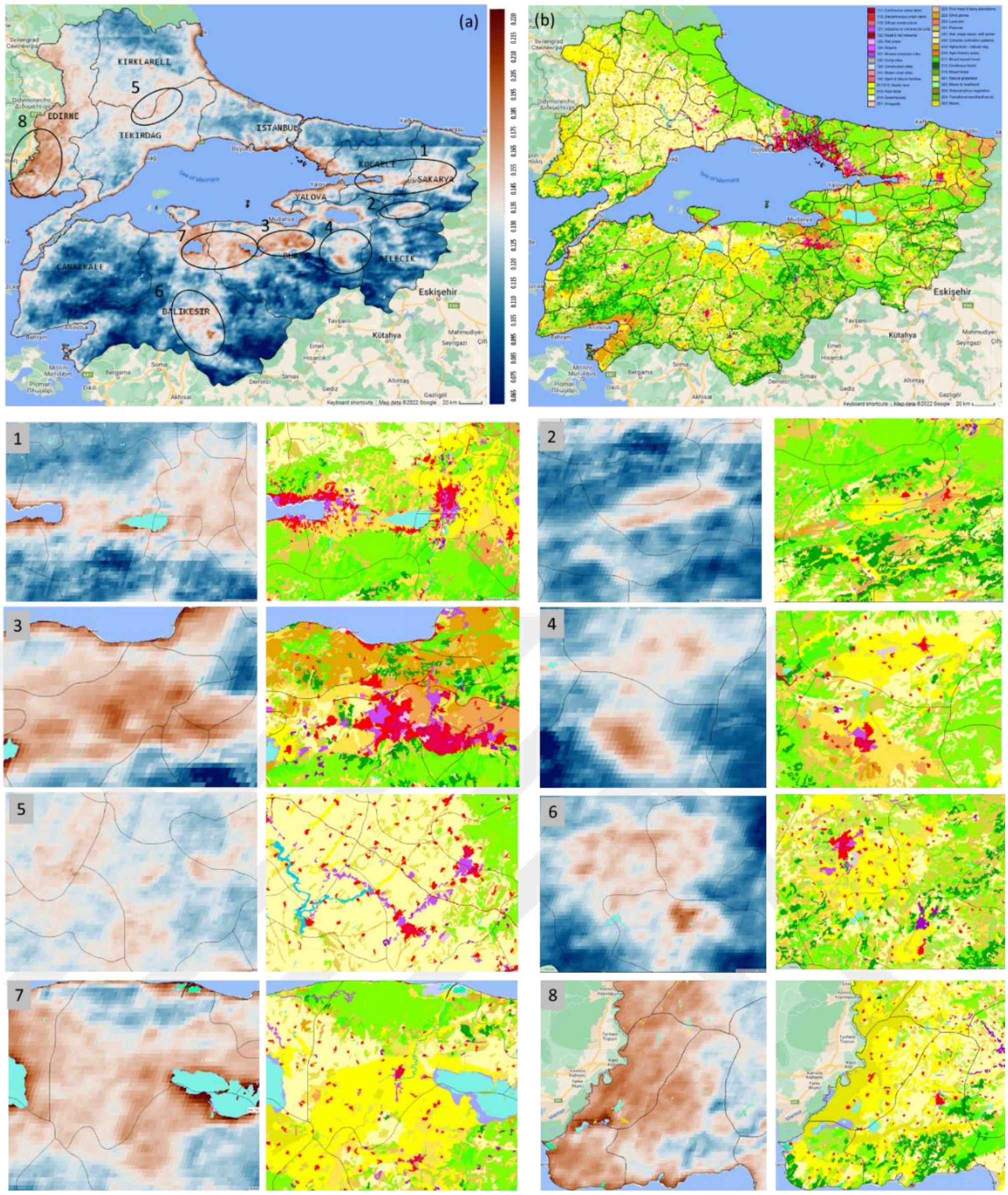

Figure 3.23 : The overlay of (a) the Average annual distribution of AOD from 2001 to 2021 and high AOD spots shown in the black ellipses (b) CORINE 2018 land cover map over a Google map and the zoom-in views of the eight indexed regions.

The Istanbul-Kocaeli region is one of the most populated and industrial regions of the Marmara region. According to the CLC 2018, Istanbul owns 33% of the Marmara region's urban fabric and 36% of its industrial and commercial units. Kocaeli is the province that owns the second-highest industrial and commercial units in the Marmara region (14%). The Yalova is close to Istanbul and Kocaeli, connecting with water and land transport lines also includes significant population and economic activities of Turkey. Except for the hilly sections in the Armutlu distinct near the east sides of the distinct, the region is characterized by a considerable portion of flat land on the city's coastal sides. According to the CLC 2018, the artificial surfaces of Yalova City have the third highest percentage of the province’s total land, 6%, among 11 provinces of the Marmara region after Istanbul (22%) and Kocaeli (9%). Having the hilly section on the east side results in an increase in aerosol concentration in the plain areas adjacent to the mountains. This prevents the dominant northerly wind to blow aerosol pollutants away in Yalova. Yalova has the highest AOD in this region with an annual mean value larger than 0.14 (Table 3.1).

In addition to the high AOD zones over the heavily populated and industrialized areas of the Marmara region, which are mainly along the coasts and straits where the polluted continental aerosols combine with marine aerosols and sea salt and where also the humid weather facilitates the hygroscopic growth of aerosols, six other regions with relatively higher AOD values (larger than 0.13) were found in the study area. These regions are also dominated by urban agglomerations centered in the provinces and their vicinity which are all economic and industrial centers. Anthropogenic activities contribute considerably to aerosols in these regions.

Edirne's AOD value was the second largest with an annual mean of 0.136 (Table 3.1), which largely resulted from agricultural activities. Over 77% of Edirne's total land area is used for agriculture. Larger than 87% of agricultural land is under temporary crops (i.e. arable land) which contributes highly to aerosol emissions. Arable land contributes to aerosol pollution by emitting soil and dust during planting and harvesting, as well as by burning crop residue or stubble after harvest and preparing the soil for fresh crop planting. Similar to Edirne, a large portion of Tekirdag's total land area is used for agricultural purposes (about 77%) with 84% under temporary crops. Tekirdag's annual mean AOD (2000-2021) is the third highest (0.132). The high aerosol distribution over the Tekirdag province is majorly due to the emission from agricultural activities.

Besides aerosol emissions from Edirne's agricultural activities, soot aerosols from domestic solid low-quality coals and biomass fuel combustion in rural households contribute to the annual mean AOD over the province. According to the report of the Turkiye energy market regulatory authority (EPDK) in 2013, 28,514 residential subscribers had access to clean fuels for heating and cooking in Edirne. Bilecik is the next province with the least residential subscribers (33,432). This is while Istanbul and Bursa had the highest number of residential subscribers 3,498,203, and 685,015, respectively. According to data from the Turkish Statistical Institute, Turkey's average household size was 3.8 in 2013. According to this ratio, just 28% of the Edirne population had access to clean gas back in 2013 which is the lowest among the provinces of the Marmara region This is while more than 94% of Istanbul’s and Bursa’s population had access to natural gas. The average household size in Turkey was seen to decrease to 3.23 people in 2021 (TUIK) and according to the EPDK report of 2021, the percentage of Edirne’s population having access to natural gas rose to 65% in 2021. Although the rate has been increasing since 2013 and is projected to double by 2021 with the highest rate of 15 % (i.e. the average rate of growth between 2013 and 2021), the rate is still the second-lowest after Balikesir (58%).

Bilecik is the least populated province in the Marmara region and Edirne has approximately twice the total population of Bilecik. The overall number of residential gas subscribers in Bilecik and Edirne between 2013 and 2021 was at its lowest levels. However, it wasn't until 2018 that Edirne's number overtook Bilecik's. The government's ban on burning crop residue and the rise in natural gas combustion overall both reduce aerosols over Edirne. Canakkale and Bilecik provinces were characterized by low annual aerosol distribution, due to their vegetation coverage and low percentage of artificial surfaces throughout the provinces. According to the CLC map 2018 Bilecik and Canakkale have the lowest artificial percentages of 1.65% and 1.87%, respectively across the Marmara region while have the two highest forest and semi-natural area percentages of 58% and 54%, respectively.

Figure 3.24 shows the annual mean AOD values of three primary CORINE land use cover types (i.e. artificial surfaces, forest, and semi-natural areas, and agricultural areas) in the years between 2000-2021. The annual AOD mean trends are similar for the three main land covers, with the highest AOD values observed over artificial surfaces and the lowest over forest and semi-natural areas. Despite the lower magnitudes of AODs over forested areas, the similarity of aerosol trends suggests that urban and industrial emissions affect air quality over wider areas through wind transport of aerosols. Although pollution centers experience higher aerosol concentrations, wind and circulation patterns can disperse aerosol loading to broader regions.

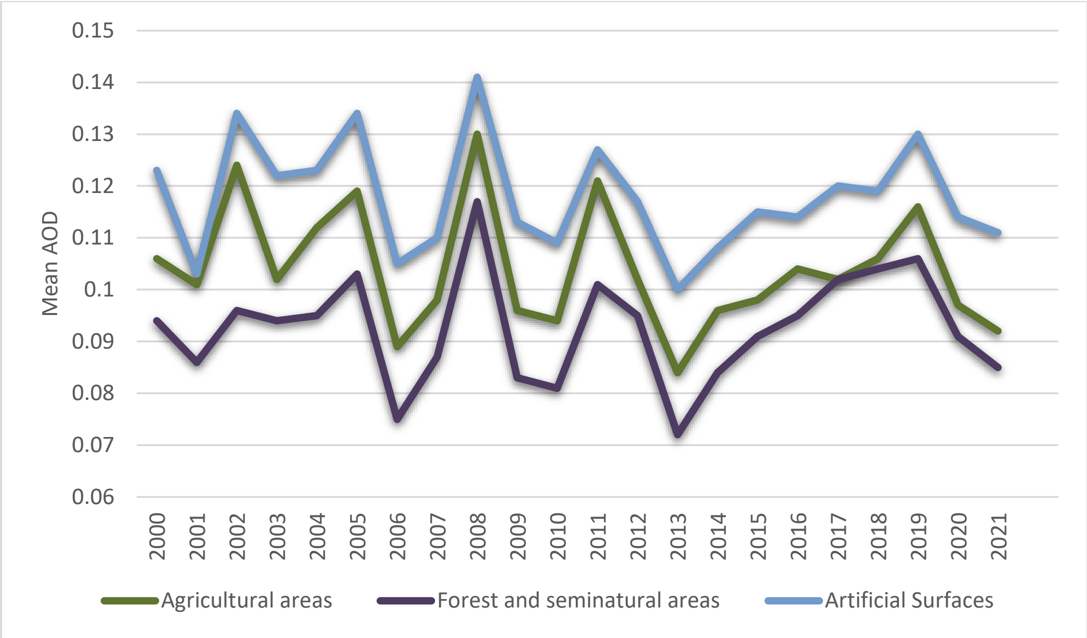

Figure 3.24 : Temporal variation in the annual mean AOD over three main land covers of the Marmara region.

I calculated and examined the AOD over various artificial surfaces in the Marmara region to provide information on the distribution of aerosol concentration across various types of artificial surfaces and to highlight the main sources of air pollution and their effects on the aerosol concentration of the region. Figure 3.25 represents the annual mean AOD of the aerosol loading over the sub-classes of the artificial surfaces across the Marmara region including continuous urban fabric, discontinuous urban fabric, Industrial, commercial and transport units, and mine, dump, and construction sites. The trends are similar for the sub-classes. The highest AOD mean is recorded over the industrial, commercial, and transport units. The aerosol emissions of industrial activities and vehicle exhaust emissions in transportation activities have the highest impact on the aerosol concentration of the region. The emissions from human activities in the continuous urban fabric of the region have the second highest impact on the aerosol concentration of the region. Despite having a larger spatial extent that is 2.5 times bigger, the urban area still has lower AOD values compared to the industrial zone of the Marmara region. This difference can be attributed to the varying intensity and density of aerosol sources in each area. The mean AOD value cannot be solely determined by the size of the high AOD area. A region with fewer high AOD areas but a greater concentration and intensity of aerosol sources may have a higher mean AOD value.

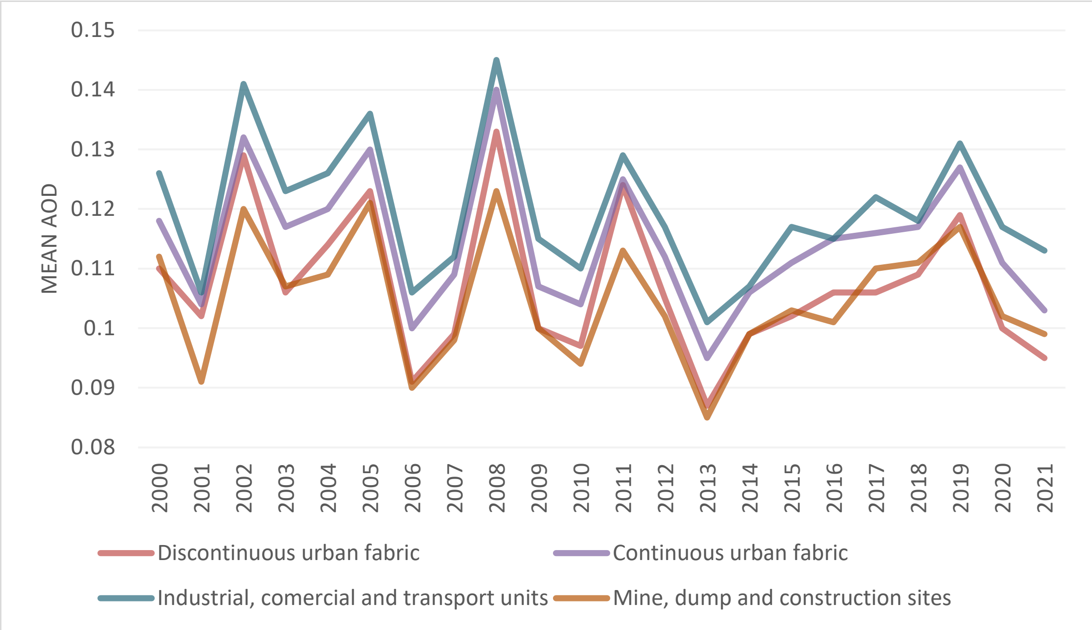

Figure 3.25 : Temporal variation in the annual mean AOD over the subclasses of the artificial surface land cover class of the Marmara region.

3.5 Conclusion

The spatial distribution of aerosol loading over the Marmara region is not uniform and varies significantly between seasons. To investigate the optical properties of different aerosol types, including natural and anthropogenic, seasonal monitoring of aerosol load and properties is recommended. The chapter presents the seasonal AOD profiles of the Marmara region, generated using daily MODIS MAIAC AOD data between 2000 and 2021, at a scale of 1 km. The study finds that the average AOD value is highest in summer and lowest in winter, primarily due to heavy rainfall and increased horizontal mixing of pollutants. The article concludes that low AOD levels are linked to rainy seasons, while dust storms cause AOD peaks in arid and semi-arid regions. Overall, the findings suggest that monitoring the spatial and seasonal variations of aerosol loading is essential to understanding the mechanisms influencing significant differences between seasonal AOD values.

The temporal variations of atmospheric aerosols and the factors that affect them over the Marmara region have been discussed. The study provides useful insights into the temporal variations of atmospheric aerosols and the factors that affect them over the Marmara region, which could help in improving air quality and human health in the region. Through the analysis of month-wise variation of AOD over the Marmara region between 2000 and 2021, it is shown that higher AOD was distributed over the entire study region from late-spring to early-autumn (April-September), with the highest values observed in May and August due to the increase in aerosol water content favored by higher absolute humidity. Lower AOD values were observed during the first three months of the year and a substantial rise was detected from April until August. The results also showed an apparent reduction in AOD after summer ends, partly due to deposition favored by precipitation. The study also found that lower aerosol distribution in December and January could be partly attributed to missing AOD pixels caused by snow cover and changes in ground surface reflectance, as well as particulate removal from the atmosphere via precipitation scavenging. Despite the limitations, the study reported greater aerosol concentrations and AOD values for winter months in predominantly urban areas, indicating agglomeration of anthropogenic emissions in these areas.

The chapter also includes the calculation of statistical indicators such as annual minimum, maximum, mean, and standard deviation for AOD values between 2000 and 2021. The analysis showed that high annual mean AOD values were observed in 2000, 2002, 2003, and 2008, whereas lower annual mean AOD values were observed in recent years, 2020 and 2021. The aerosol loading in 2000 and 2002 showed a greater variety of AOD values, while the AOD values over the Marmara region remained stable with an annual mean of 0.128 and a standard deviation of 0.015. The analysis of multi-year variation of AOD indicated a decreasing trend in AOD between 2000 and 2021, with an annual decrease of 0.005/a. However, AOD has shown a significant decreasing trend of about 0.08/a between 2018 and 2021, which is related to the reduction of regional pollutant emissions during COVID-19 pandemic restrictions. The inter-annual variability of seasonal AOD showed a decreasing trend in summers and springs and increasing trends in falls and winters. The article also presents the spatial distribution of annual mean MODIS MAIAC AOD over the Marmara region between 2000 and 2021.

The last part of the chapter discusses the spatial distributions of atmospheric aerosols in the Marmara region and the effects of land use and cover types on AOD. The AOD trends over different land covers, including artificial surfaces, forest, and semi-natural areas, and agricultural areas, are similar, with the highest values observed over artificial surfaces and the lowest over forest and semi-natural areas. The industrial, commercial, and transport units and continuous urban fabric of the region have the highest impact on the aerosol concentration of the region. Certain types of land cover or land use can contribute to the concentration of atmospheric aerosols and high AOD value spots. Six regions with relatively higher AOD values were found in the study area, all of which are occupied with urban agglomerations centered in the provinces and their vicinity which are all the economic and industrial centers. Anthropogenic activities contributed considerably to the aerosols in the air over these regions. The AOD values of Edirne and Yalova were also discussed, with the former having high values due to agricultural activities and the latter due to the hilly section that causes the aerosol concentration over the plain areas adjacent to the mountains. The passage also notes that despite the lower magnitudes of AODs over forested areas, the similarity of aerosol trends suggests that urban and industrial emissions affect air quality over wider areas through wind transport of aerosols.

Human activities in urban areas and industrial zones, and agricultural practices are two of the most significant factors contributing to aerosol loading and high AODs in the Marmara region. Anthropogenic emissions from urban and industrial activities, such as transportation, power generation, and manufacturing, contribute significantly to the aerosol loading in the atmosphere. These emissions contain particles and gases that can undergo chemical reactions in the atmosphere to form aerosols. In addition, agricultural practices, such as tilling, harvesting, and livestock management, can also release dust particles into the air, further contributing to aerosol loading. It is important to distinguish between built-up areas and bare lands to accurately assess and manage the sources of aerosol emissions. Bare land can refer to any area of land that does not have vegetation cover, including agricultural land during the time of no vegetation, as well as other barren lands such as deserts, dunes, and rocky areas. The type of bare land depends on the region and the prevailing climate conditions. Urban and industrial areas may require different mitigation strategies than agricultural areas or natural dust sources, for example. Therefore, understanding the sources and distribution of aerosols is crucial for effective air quality management.

In the next chapter of this study, the importance of distinguishing between built-up areas (i.e. urbanized or industrialized regions) and bare lands (i.e. agricultural or barren lands) in terms of aerosol loading and atmospheric pollution will be discussed. The chapter will propose a new strategy for separating these two types of land cover to better understand and address the sources of aerosols in the atmosphere. This strategy may involve the use of remote sensing techniques or other data analysis methods to identify and quantify the extent of built-up areas and bare lands in a region. By separating these land cover types, it may be possible to better understand the impact of human activities and natural processes on aerosol concentrations in the atmosphere and to develop more effective strategies for mitigating the negative effects of aerosol pollution on human health and the environment. Organizations trying to better understand and manage atmospheric aerosols can benefit from the research by receiving insightful information and assistance.

4. DETERMINATION OF THE COMPLEX AND MORPHOLOGICALLY HETEROGENEOUS LCU PATTERNS: SEPARATING BUILT-UP AREAS FROM BARE LAND

Throughout history, the increase in population densities and the expansion of urban areas, especially in metropolitan cities, have changed the form of the Earth's surface (Yuan, Sawaya, Loeffelholz, & Bauer, 2005). The rate of LCU changes has increased in recent decades. Population growth leads to increases in water and energy consumption and causes land surface changes, which result in regional to global climate change and environmental degradation (Sertel, Robock, & Ormeci, 2010).

LCU changes that have occurred due to urbanization, deforestation, desertification, natural disasters, and intense agricultural practices, have greatly influenced climatic characteristics at the regional and global scale. Such changes generally result in increases in near-surface temperatures

and formation of heat islands, which trigger other climatic phenomena (Luyssaert et al., 2014; Mahmood et al., 2014). Thus, there is a need for accurate, up-to-date, and periodical LCU maps to develop efficient decision-making mechanisms to cope with climate change and effectively manage and plan cities (Huidong Li, Wolter, Wang, & Sodoudi, 2018). With the advances in satellite technologies, traditional methods have been mostly replaced by remotely-sensed data analysis to monitor LCU change (Aburas, Ho, Ramli, & Ash'aari, 2016; Sertel & Akay, 2015). The availability of free global and historical satellite imagery provides a valuable opportunity for mapping and monitoring LCU, constantly and effectively (Rawat & Kumar, 2015). The separate or combined use of optical and synthetic aperture radar (SAR) data provides valuable information about the physical characteristics of the land surface; different analysis methods have been developed to determine different object types. Among these methods, image classification has become the most popular method for mapping LCU and its changes (Srivastava, Han, Rico-Ramirez, Bray, & Islam, 2012). Lu and Weng, (2007), reviewed the classification algorithms and accuracy of several image classification studies. They reported that the classification accuracy was affected by several factors and these factors can be grouped as (i) the Use of advanced classification algorithms, such as Support Vector Machine (SVM), Random Forest (RF), and regression tree (CART); (ii) selection of multiple remote sensing features, such as multi-spectral, multi-temporal, or multi-sensor data fusion; and (iii) integration of additional data, such as topographic maps or soil maps (D. Lu & Weng, 2007). The use of non-parametric classification algorithms, such as machine learning algorithms, decision trees, and knowledge-based classifiers has increased (D. Lu & Weng, 2007). Among these, SVMs, which use a set of related learning algorithms for classification, showed superior performance, compared to traditional classification techniques such as maximum likelihood, minimum distance, or parallelepiped classifiers (Bruzzone & Persello, 2009; Dalponte, Bruzzone, & Gianelle, 2008; Mountrakis, Im, & Ogole, 2011). SVM also provided better performance when applied to multi-index images than the Neural Network (NN) classifier and CART (Shao & Lunetta, 2012). In a recent article, Maulik and Chakraborty (2017) summarized the recently developed advanced SVM-based classification approaches used in remote sensing studies. They concluded that SVM-based classification methods perform better in terms of accuracy, speed, and memory requirements, and can operate effectively and accurately in cases where training samples are limited, which is generally the case for satellite image classification problems. They also noted the constraints that should be considered in SVM, such as the need to appropriately define the kernel function, the representation efficiency of the training sample, and the consistency of statistical distributions between classes (Maulik & Chakraborty, 2017). In most satellite image classification scenarios, higher accuracies (over 85%) are attained when the major land cover (LC) classes, such as vegetation, water, and urban classes are the concern (Jia et al., 2014). Achieving high accuracies becomes challenging when the higher-level class definitions are the concern, due to the spectral and spatial similarities. According to a survey done by Li et al. (2014), the classification accuracies achieved by supervised algorithms vary greatly, due to the number of training samples and proprieties of selected features for classification. These findings indicate a feature selection problem that occurs regardless of the classification algorithm (C. Li, Wang, Wang, Hu, & Gong, 2014). An increased number of features, such as the image bands, generally improves the accuracy; however, it increases the number of training samples required (Y. Huang et al., 2017). Considering the limited training sample availability in most conditions and the nonlinear response of the LCU classes across several bands, which is known as the “Hughes effect” (Hughes, 1968), there is a need for a method to select a subset of relevant features from the original dataset to improve the classification process and achieve a dimension reduction (Yi Zhou, Zhang, Wang, & Wang, 2018). One alternative to overcome the above-mentioned problem is to perform linear transformation methods (such as principal components analysis (PCA) and independent component analysis (ICA)), or nonlinear algorithms (such as locality adaptive discriminant analysis (LADA) and multiple marginal fisher analysis (MMFA)), to remove the correlations and higher-order dependencies in the image bands and use the produced components as input data for classification, to simplify and improve the process. The linear methods have been widely applied to multispectral data, however, nonlinear methods are generally applied to hyperspectral test data or natural image-based applications, such as face recognition (H. Huang, Liu, & Pan, 2012; Q. Wang, Meng, & Li, 2017).

Spectral indices derived from satellite images can be used as an alternative data source for LCU characterization (Ceccato, Gobron, Flasse, Pinty, & Tarantola, 2002; C. He, Shi, Xie, & Zhao, 2010). The characteristics of the reflected energy in different regions of the spectrum for a specific land property can be utilized to produce various indices. Using the spectral indices for LCU mapping is an operational approach as it enables LCU mapping at a higher degree of accuracy, which is highly comparable to those from a complex interpretation of quantity (Hanqiu Xu, 2007; Xiaojun Yang & Liu, 2005). Zha et al. (2003), for the first time, introduced an automated index-based method for mapping the built-up regions. Nevertheless, there is a significant drawback that should be considered when using spectral indices for LCU mapping (Zha, Gao, & Ni, 2003). Some land features, such as water bodies and vegetation cover have very specific spectral reflectance characteristics, which facilitate the separation from other features, using spectral indices. However, it is challenging to detect built-up areas and effectively separate them from bare lands using a single index, due to similarities in the spectral characteristics. Confusion over, and misclassification of, built-up areas and bare lands is a problem, which can be partially addressed by the available built-up, index-based analyses (As-Syakur, Adnyana, Arthana, & Nuarsa, 2012; Hui Li et al., 2017; Zha et al., 2003). Urbanized areas are composed of heterogeneous surfaces, including different artificial materials and natural areas, and therefore, exhibit a complex landscape characteristic, making it difficult to map all LCU classes using a single index. The main objective of this research work was to propose a multi-index-based SVM classification approach, for mapping seven different LCU classes, in complex urban areas. The research focused on separating the built-up areas and bare lands, in addition to providing an accurate and reliable LCU map, in three densely urbanized metropolitan cities of Turkey, using the Sentinel-2A imagery. The method design comprised using a few sets of specific indices, each group of which highlighted a generalized LCU category—built-up regions, vegetation covers, and water bodies. For the built-up category, the existing built-up indices and the normalized difference tillage index (NDTI) were used as the first components of the multi-index dataset, and their performances were evaluated. For the vegetation cover determination, NDVI, the soil adjusted vegetation index (SAVI), and the red-edge-based normalized difference vegetation index (NDVIre) were evaluated as the second component. The normalized difference water index (NDWI) and modified normalized difference water index (MNDWI) were used to highlight the water bodies as the third component. Several combinations of spectral indices and the original satellite images were classified using the same training sample set and supervised SVM algorithm, as it has a non-parametric, machine-learning-based structure and because of its reported performance in supervised, pixel-based algorithms, mentioned above (Bruzzone & Persello, 2009; Dalponte et al., 2008; Mountrakis et al., 2011). Accuracy assessment was performed using stratified random points to evaluate the performance of the multi-index approach and its possible advantages over the traditional classification of the original spectral bands. The proposed approach was developed with the Sentinel-2A image of the metropolitan city of Istanbul and applied to two independent regions located in the metropolitan cities of Ankara and Konya, in Turkey, to validate the common usage and effectiveness.

4.1 Study Area

Istanbul is the most populated and the largest city in Turkey, located at a latitude of 41◦00044.0600 N and a longitude of 28◦58033.6600 E, in the Northern Hemisphere, joining the two continents of Asia and Europe. Istanbul is also one of the largest metropolitan cities in Europe, covering approximately 5.500 km2, with a population of over 15 million in 2017, corresponding to 18% of the country. The significant population growth that occurred due to the industrial development and unplanned urbanization, during the second half of the twentieth century, resulted in critical transformations of the structure and morphology of the city. The densely urbanized regions of Istanbul are located in its southern half. In the last decade, the construction of new transportation infrastructures, such as the Yavuz Sultan Selim Bridge, the Northern Black Sea Highway, and a third airport, have affected the ecosystem and caused a dramatic increase in built-up areas, in the northern half of the city. Istanbul presents a complex pattern of various feature classes, including forests, water bodies, croplands, bare land, and heterogeneous urban areas, making it a suitable candidate for this research work.

The intensive urbanization in Istanbul and the change in LCU have attracted the attention of many researchers and several studies have been conducted to determine the LCU and its changes, using satellite images (Canaz, Aliefendioğlu, & Tanrıvermiş, 2017; Coskun, Alganci, & Usta, 2008; Kaya, 2007). These studies have reported an intensive increase in urbanization—for different periods—that has destroyed the natural landscape, by applying the traditional, pixel-based spectral image classification methods.

The two test regions, Ankara and Konya, are located in the middle of the country. Ankara is the capital of Turkey and is the second most crowded city after Istanbul. Konya is also an important city in Turkey, with a high level of industrial activity, which is ranked seventh in the urbanization rate. Both of these regions include high- and low-density residential areas and industrial areas that are located between and surrounded by extensive bare land, which makes them good candidates to test the challenging bare-land–urban-area separation process. The locations of the main study area and test regions have been presented in Figure 4.1.

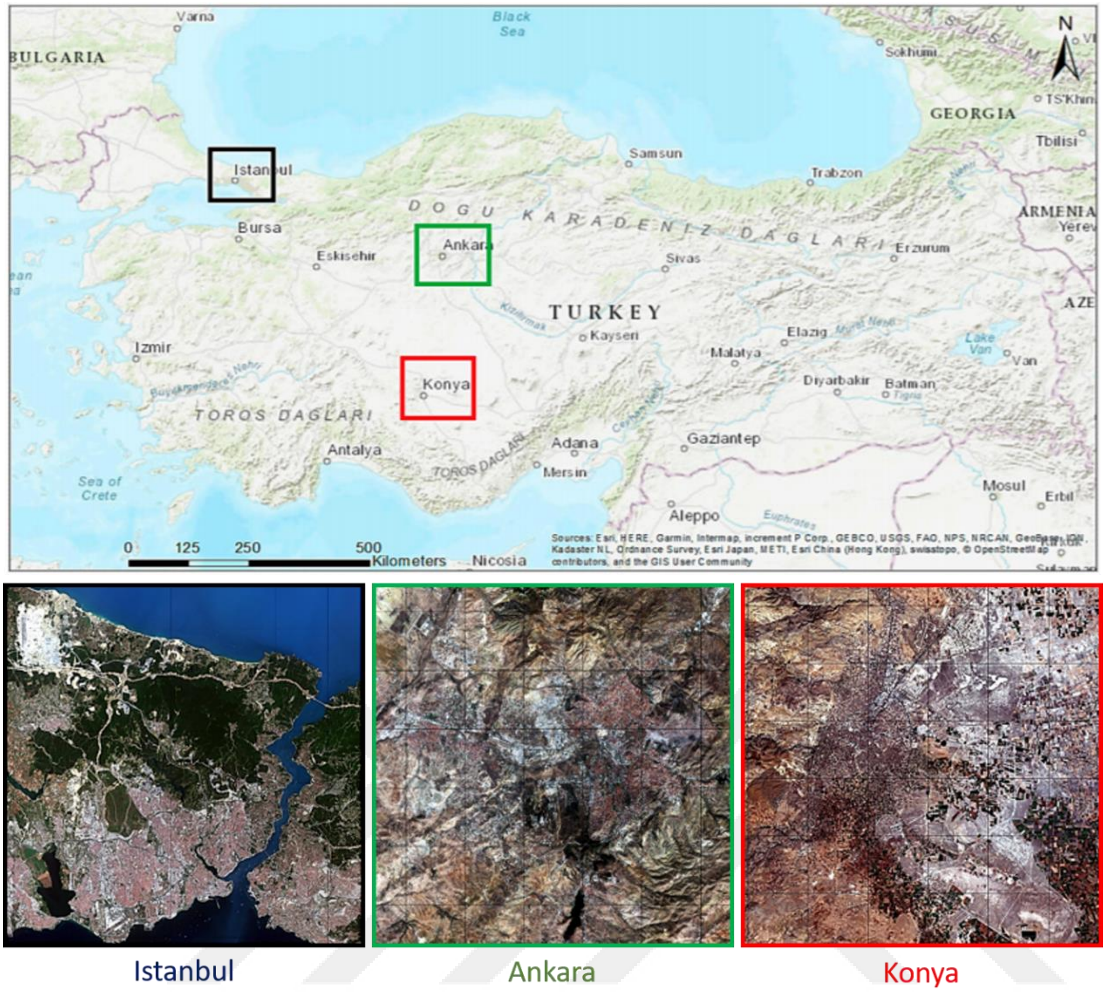

Figure 4.1 : Location map of the main study area and the test regions (Country map from ESRI©, California, USA, closer look from the natural colour composite of the Sentinel-2A).

4.2 Data Used

In this research, 1C-level-processed, cloudless Sentinel-2A images were used to perform the analysis and evaluation. The acquisition dates of the images were 29 June 2017, 3 November 2017, and 19 September 2018 for the Istanbul, Ankara, and Konya regions, respectively. The European Space Agency (ESA) developed the operational Sentinel-2 mission within the frame of the European Union Copernicus program. The Sentinel-2 mission is based on a constellation of two satellites, Sentinel-2A, and Sentinel-2B, flying in the same orbit but phased at 180◦, to observe the land surface, thoroughly, with a short revisit period, and to meet the requirements of applications, such as land management, agriculture and forestry, and disaster control. Sentinel-2A was launched on 23 June 2015 and was followed by Sentinel-2B on 7 March 2017; both maintain a sun-synchronous orbit at 786 km altitude. The temporal resolution is five days from the two-satellite constellations, at the equator. The multispectral imager covers 13 spectral bands with a swath width of 290 km and a spatial resolution of 10 m (four visible and near-infrared bands (NIR)), 20 m (six red-edge and SWIR bands), and 60 m (three atmospheric correction bands). Sentinel-2 image products are available to the community at the Level-1C (top-of-atmosphere reflectance in cartographic geometry) and Level-2A (bottom-of-atmosphere reflectance in cartographic geometry) processing levels. The granules or tiles of Sentinel-2A images for these two levels are provided as 100 km×100 km sized ortho-images in the UTM/WGS84 projection, which can be downloaded from the ESA website, free of charge. Sentinel-2 data provide a viable complementary source to the pre-existing moderate-resolution images, with an increased spectral resolution, and provide a continuity of SPOT and LANDSAT-type image data, by contributing to the current multispectral observations of LCU (Immitzer, Vuolo, & Atzberger, 2016).

4.3 Methodology

4.3.1 Pre-processing of the Satellite Images and Extraction of Spectral Signatures

The satellite images used in this research were acquired in clear sky conditions, with minimum atmospheric disruptions. A single image was used for each region; therefore, an atmospheric correction pre-processing step was not necessary. The spatial resolution of the Sentinel-2 image bands varied through the wavelength portions. Thus, there was a need for uniform spatial resolution for analyses such as point-based spectral profile generation, spectral index generation, and multispectral image classification. Zheng et al. (2017), had performed a comparative analysis to evaluate the effects of downscaling to 10 m resolution and upscaling to 20 m resolution on land-cover and land-use classification with Sentinel-2 images. They asserted that the upscaled 20 m resolution images provided the lowest classification accuracies, due to a loss of spatial details and an increase in the number of mixed pixels, by combining four adjacent pixels. Their results revealed that downscaling to a 10 m resolution with the nearest neighbor resampling algorithm improved the classification, and they recommend this approach for unifying the spatial resolution (Zheng et al., 2017). Atkinson (2013), had asserted that downscaling to a fine resolution is more suitable for an LCU classification by completely utilizing the detailed information from high spatial resolution bands (Atkinson, 2013). Based on the above findings, the 20 m and 60 m resolution bands of the Sentinel-2A imagery were resampled to 10 m, by using the nearest neighbor method, to maintain the spatial resolution integrity. This resampling algorithm has been widely used, due to its easy implementation and spectral information conservation. In the next step, spectral profiles of different land object types, including broadleaf forest, deciduous forest, farmland, urban green cover, built-up, industrial region, sparse built-up region, seawater, lake water, asphalt, and bare land, were extracted to examine and compare the separation capacity of the Sentinel-2A image bands (Figure 4.2). During the classification process, samples from broadleaf and deciduous forest were assigned to the forest class, samples from urban green cover and farmland were assigned to the vegetation class, and samples from lake and sea were assigned to the water class, to obtain the seven land cover types used in this research.

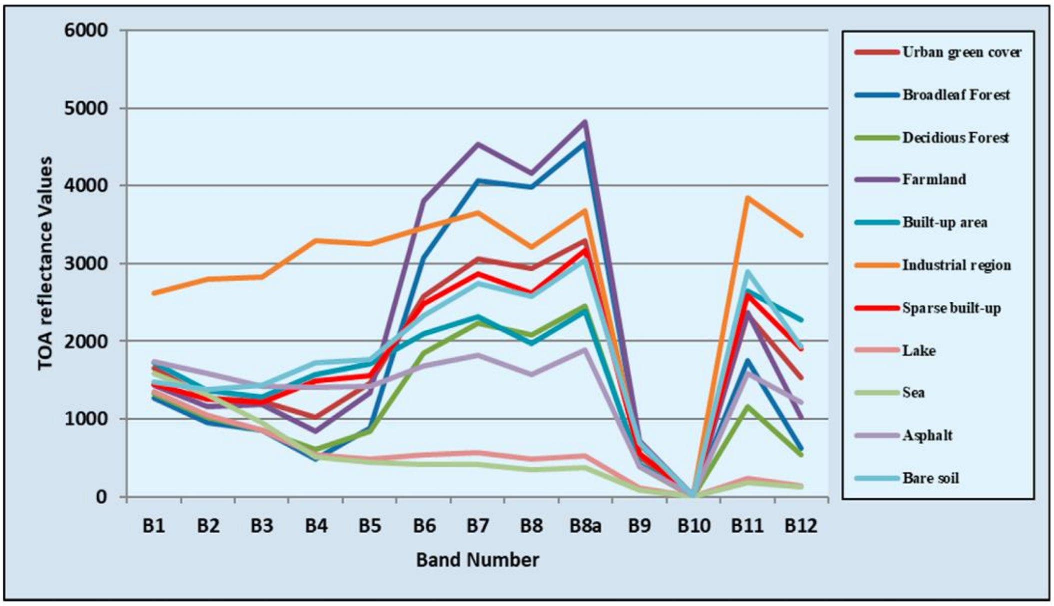

Figure 4.2 : Spectral reflectance curves of different LCU types, according to the Sentinel-2A image bands (top of atmosphere reflectance values derived from 12-bit resolution satellite image).

As Figure 4.2 illustrates, bare land had a similar reflectance to built-up areas and it was difficult to identify these two categories using a single index. It was simple to determine water bodies from other land cover types, due to their unique spectral signature. The gradual decrease of reflectance from band 1 to band 12 was specific to water bodies. A significant reflectance increment in the red-edge bands (B5, B6, B7) and NIR bands (B8, B8a), compared with the red band (B4) was specific to vegetation cover and could be utilized to detect vegetated regions. Additionally, the reflectance curve analyses proved that B1, B9, and B10 (60 m native resolution) could not be used to separate the land cover classes. These observations could be explained by the characteristics of these bands. B1 (coastal aerosol), strongly influenced by the atmosphere and by B9 and B10, which were water vapor and cirrus, did not provide spectral information about the Earth’s surface. Thus, these bands were removed from the data and further analyses were performed with the remaining 10 bands. The spectral evaluation showed that the main challenge was to separate the bare land and the built-up areas, which was the principal objective of this research. Therefore, it aimed to evaluate the existing built-up indices as a first step and proposed an alternative index for those cases that had a lower efficiency. The next step was to suggest a strategy to improve the overall LCU classification results, using the multi-index data composed of three spectral indices, which were sensitive to a built-up area/bare land, vegetation cover, and waterbodies, respectively.

4.3.2 Generating Multi-Index Images

The suitable index combination selection was performed by an experimental analysis of the various combinations of indices as components of the multi-index dataset. For the built-up component, the existing built-up indices and NDTI were examined. Detailed evaluations of the existing built-up indices and the NDTI are provided in Section 4.3 and Section 4.4.

For the vegetation cover component, the red-edge-based normalized difference vegetation index (NDVIre), and two well-known vegetation indices, the soil-adjusted vegetation index (SAVI), and NDVI were examined. Hansen and Schjoerring (2003) first evaluated the NDVIre by analyzing hyperspectral reflectance data (Hansen & Schjoerring, 2003). Delegido et al. (2011) and Frampton et al. (2013) first tested its applicability on the designed Sentinel-2 wavelength portions, before the launch of the satellite mission, using data from several ESA field campaigns over agricultural sites. The results of both studies demonstrated that the application of this index to the Sentinel-2 red B4 (665 nm) and the new red-edge B5 (705 nm) bands, provided high correlations during the estimation of the leaf area index and the chlorophyll content (Delegido, Verrelst, Alonso, & Moreno, 2011; Frampton, Dash, Watmough, & Milton, 2013). Pu and Landry (2012) and Zhu et al. (2017) introduced the operational use of this index for the Worldview-2 satellite imagery. To the best of our knowledge, this research is a novel evaluation of the NDVIre on operational Sentinel-2A imagery (Pu & Landry, 2012; Zhu et al., 2017).

Lastly, for the water body component, the normalized difference water index (NDWI) and modified normalized difference water index (MNDWI) were examined (McFEETERS, 1996; Hanqiu Xu, 2006). Table 4.1 summarizes the spectral indices that were used to produce the multi-index images, according to the three main LCU categories.

Table 4.1 : Spectral indices used in this research were categorized according to three main LCU classes.

Built-up Areas	Vegetation Cover	Water Bodies
Built-up indices (Table 4.2)	NDVIre	MNDWI
NDTI	NDVI	NDWI
	SAVI	

The formulas related to the above spectral indices were as shown by equations 4.1 to 4.6:

$$\text{NDTI}= ((\text{SWIR 1}-\text{SWIR 2}))/((\text{SWIR 1}+\text{SWIR 2})) \tag{4.1}$$

$$\text{NDVIre}= ((\text{RedEdge 1}-\text{Red}))/((\text{RedEdge 1}+\text{Red})) \tag{4.2}$$

$$\text{NDVI}=((\text{NIR}-\text{Red}))/((\text{NIR}+\text{Red})) \tag{4.3}$$

$$\text{SAVI}=((\text{NIR}-\text{Red}))/((\text{NIR}+\text{Red}+0.5))\times 1.5 \tag{4.4}$$

$$\text{NDWI}=((\text{Green}-\text{NIR}))/((\text{Green}+\text{NIR})) \tag{4.5}$$

$$\text{MNDWI}=((\text{Green}-\text{SWIR 1}))/((\text{Green}+\text{SWIR 1})) \tag{4.6}$$

4.3.3 Experimental Comparison of the Existing Built-Up Indices

The main concern for LCU classification in urban areas is the separation of bare land and built-up areas, due to their similar spectral characteristics. Extracting the bare land is a challenging task, due to the complexity of soil components and soil spectra. As Ben-Dor et al. (2002) stated, the chemical constituent directly influences the spectral signature of bare lands, which can be strong or weak (Ben-Dor, Patkin, Banin, & Karnieli, 2002). In addition, many of these spectral signatures overlap one another, which makes it difficult to determine soil cover. Accordingly, the spectral characteristics of soil cover, with different components and water content, can vary across different environments and seasons, which makes it difficult to differentiate bare land.

Several indices using different combinations of spectral bands were proposed for mapping built-up areas. Table 4.2 provides a summary of previously introduced built-up indices used in this research (Bouzekri, Lasbet, & Lachehab, 2015; C. He et al., 2010; Jieli, Manchun, Yongxue, Chenglei, & Wei, 2010; Kawamura, Jayamanna, & Tsujiko, 1996; Roy, Miyatake, & Rikimaru, 2009; Stathakis, Perakis, & Savin, 2012; H. Xu, 2008; Zha et al., 2003).

Table 4.2 : Existing built-up indices.

Index Name	Index ID	Used bands	Formula	Application	Reference
Normalized difference built-up index	NDBI	SWIR and NIR	$\frac{\mathrm{SWIR} - \mathrm{NIR}}{\mathrm{SWIR} + \mathrm{NIR}}$	Automatically mapping urban areas	(Zha et al., 2003)
Built-up index	BUI	SWIR, NIR and Red	$\mathrm{NDBI} - \mathrm{NDVI}$	Mapping urban built-up areas	(C. He et al., 2010)
Built-up Area Extraction Index	BAEI	Red, Green and SWIR	$\frac{\mathrm{Red} + \mathrm{L}}{\mathrm{Green} + \mathrm{SWIR}}$ L=0.3	Extraction of built-up area	(Bouzekri et al., 2015)
New built-up index	NBI	Red, NIR and SWIR	$\frac{\mathrm{SWIR}\ \times \mathrm{Red}}{\mathrm{NIR}}$	Automating the process of mapping residential areas	(Jieli et al., 2010)
Vegetation Index Built-up Index	VIBI	Red, NIR and SWIR	$\frac{\mathrm{NDVI}}{\mathrm{NDVI} + \mathrm{NDBI}}$	Segmenting urban areas	(Stathakis et al., 2012)
Index-based Built-up Index	IBI	Red, Green, NIR and SWIR	$\frac{\mathrm{NDBI} - (\mathrm{SAVI} + \mathrm{MNDWI})/2}{\mathrm{NDBI} + (\mathrm{SAVI} + \mathrm{MNDWI})/2}$	Enhancing the built-up land feature while effectively suppressing background noise	(H. Xu, 2008)
Urban Index	UI	NIR and SWIR	$(\frac{\mathrm{SWIR} - \mathrm{NIR}}{\mathrm{SWIR} - \mathrm{NIR}} + 1.0) \times 100$	Evaluating urbanization	(Kawamura et al., 1996)
Bare Soil Index	BSI	Red, Blue, NIR and SWIR	$\frac{(\mathrm{SWIR} + \mathrm{R}) - (\mathrm{NIR} + \mathrm{B})}{(\mathrm{SWIR} + \mathrm{R}) + (\mathrm{NIR} + \mathrm{B})}$	Enhancing bare soil areas, fallow lands	(Roy et al., 2009)

As illustrated in Figure 4.3, the built-up indices listed in Table 4.2 can highlight the urban areas and separate them from the water bodies and vegetation cover. However, detailed inspection revealed that these indices could not separate the bare land from the built-up areas, in most cases. The region marked by a blue circle corresponds to the built-up area covered by buildings and impervious surfaces and the region marked by a red circle shows an empty farmland covered by bare soil. There was no major contrast between these two regions in the index images, indicating a low separability between the two land cover classes. The NBI image provided a slight contrast difference between the urban area and the soil cover, compared to the other indices, but not enough for an accurate separation (Figure 4.3 (e)). The BSI, which is mostly used for determining bare land, in the literature, was not successful in separating the bare land from the built-up areas. Visual interpretation results of the BSI image showed that the urban area and the bare land were highly mixed. The urban areas, composed of buildings with brown roofs, showed a similar spectral response to that of bare land, which made them possible candidates for getting mixed up (Figure 4.3 (i)). The initial visual analysis indicated the necessity for an index that could highlight the built-up area and separate it from the soil cover.

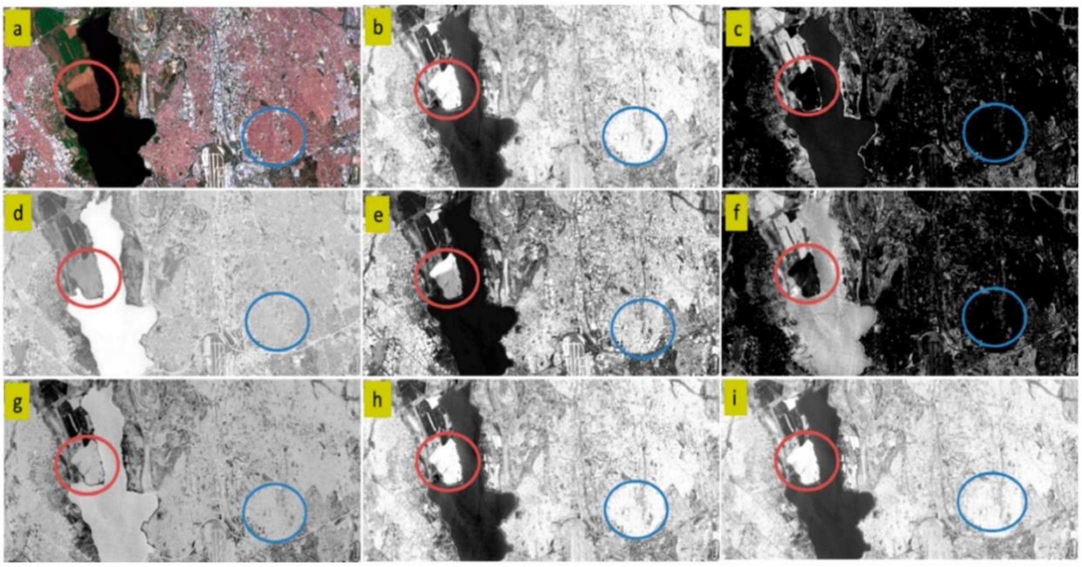

Figure 4.3 : Images of (a) Sentinel-2A RGB; (b) normalized difference built-up index (NDBI); (c) built-up index (BUI); (d) built-up area extraction index (BAEI); (e) new built-up index (NBI); (f) vegetation index built-up index (VIBI); (g) index-based built-up index (IBI); (h) urban index (UI); and (i) bare soil index (BSI).

4.3.4 Normalized Difference Tillage Index (NDTI)

To propose an index that can highlight built-up areas and separate them from bare land, the spectral profiles of these two land features were analyzed at several sample locations. It showed that the reflectance difference between the SWIR bands (bands 11 and 12) was higher for the pixels selected from the bare land than for the pixels selected from the built-up areas. This indicated the possible efficiency of these two SWIR bands for differentiating built-up areas from bare land. The applicability of the NDTI on SWIR bands of the Sentinel-2A images for the built-up area and bare land extraction was investigated. This index was first proposed by van Deventer et al. (1997) for soil practices, tillage management, and crop residue mapping (van Deventer, Ward, Gowda, & Lyon, 1997), and was successfully applied by several studies for agricultural practices and soil management (Daughtry, Serbin, Reeves, Doraiswamy, & Hunt, 2010; Eskandari, Navid, & Rangzan, 2016; van Deventer et al., 1997). To our knowledge, this is the first time that the NDTI has been used as a component to discriminate and separate built-up areas and bare land.

The NDTI data provided in Figure 4.4 and the existing built-up indices provided in Figure 4.3 shows that the NDTI can highlight the urban areas and increases the contrast between the bare land (red circle) and built-up area (blue circle). This visual inspection indicates the possible efficiency of the NDTI, compared to the existing built-up indices.

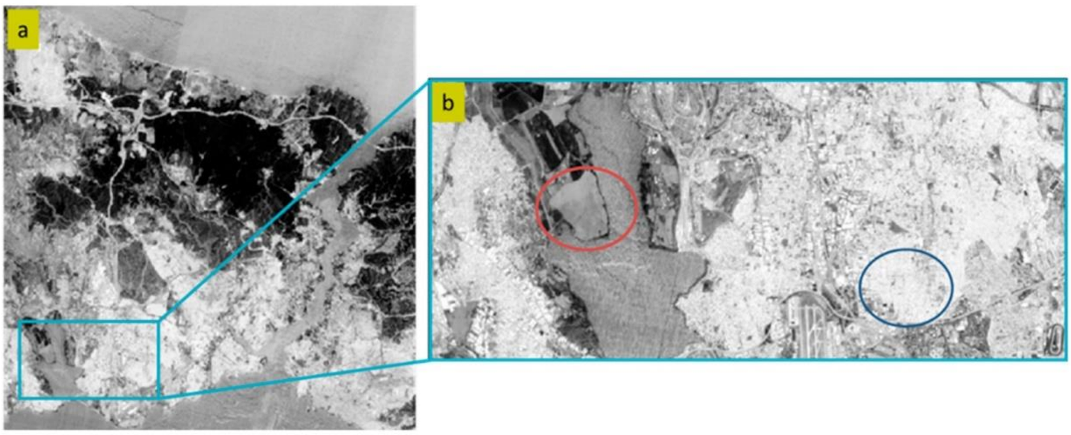

Figure 4.4 : Images of (a) the Normalized Difference Tillage Index (NDTI) and (b) a subset of NDTI exemplify the contrast between bare land and built-up regions.

As a second analysis, 80 random points (40 for each class) were selected and the mean index values were calculated to statistically evaluate the capability of the NDTI in separating the bare land from the built-up areas. As illustrated in Figure 4.5, the NDTI provides distinctive values for bare land and built-up area classes, whereas the existing built-up indices provide similar values.

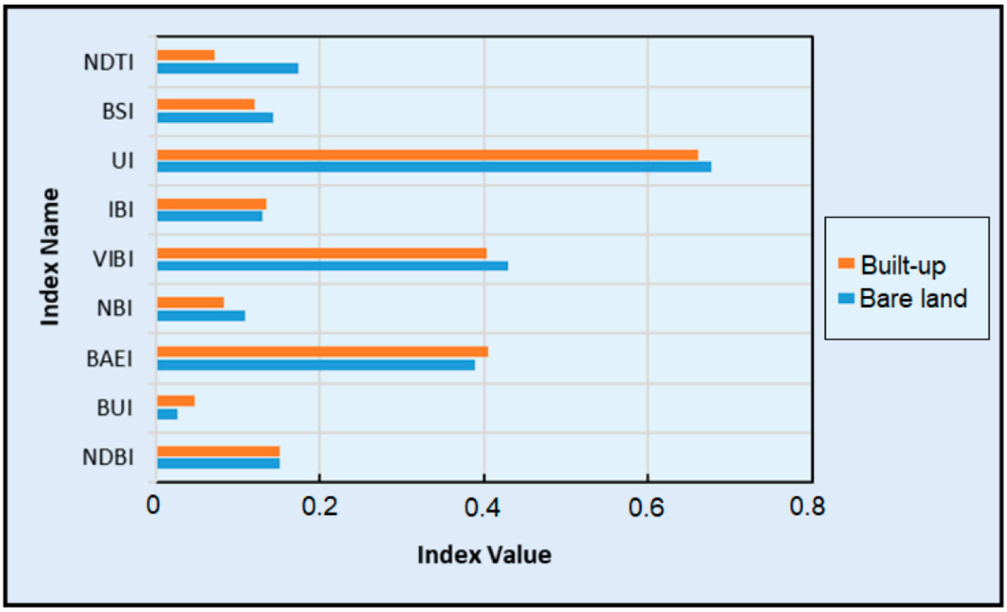

Figure 4.5 : Comparison of the average index values of points on bare land and built-up classes.

While the NDTI increases the contrast between bare land and built-up areas, it decreases the contrast between water bodies and other land covers (Figure 4.4). This drawback is overcome by the multi-index approach proposed in this research.

Figure 4.6 (a) shows an RGB composite multi-index image produced from the NDTI, the NDVIre, and the MNDWI. This multi-index image provides good discrimination between the three major LC categories—vegetation cover in red, water bodies in blue, and the built-up areas in green. The spectral signature analysis shows that the multi-index dataset represents a more linear and simplified response for the main LC categories than the original image bands, which indicates a better separation capability (Figure 4.6 (b,c)).

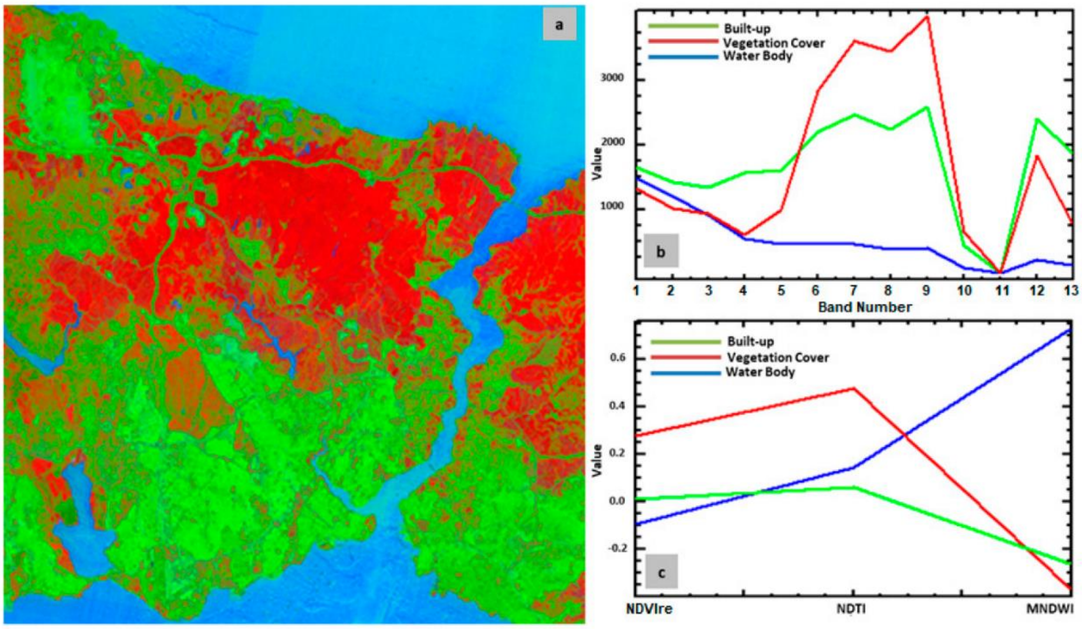

Figure 4.6 : (a) RGB composite of the NDTI, NDVIre, and MNDWI. (b) Spectral signatures are represented by the mean of the three major categories of land cover for the thirteen bands of the Sentinel-2A image. (c) Simplified spectral signatures represented by the mean of the three major categories of land cover for the multi-index image.

4.3.5 Classification and Accuracy Assessment

To examine the capability of the multi-index approach in extracting the built-up area and determining the other LCU classes, the SVM classification method with radial basis function (RBF) kernel was applied to the multi-index images. The SVM was initially developed as a binary classifier, thus, a pairwise classification approach was implemented for multiclass classification requirements, by creating a binary classifier for each possible pair of classes (Wu, Lin, & Weng, 2003). The classification process was performed using the ENVI software, which requires a set of parameter definitions. The gamma is the most critical parameter and was the only parameter changed in this research (determined by the division of 1 by the number of data layers). The penalty parameter reduces misclassification in the training step when set to 100. The classification probability threshold should be set to zero to guarantee that each pixel is assigned to a class. A pyramid level of zero allows for the classification to be performed directly on the original image pixels, instead of a first-pass classification on low-resolution pyramid layers.

The built-up index data listed in Table 4.2 and the NDTI were separately layer-stacked with vegetation and water index data and were classified using the same training samples, defined by the region of interest (ROI). In addition, the ten-band Sentinel-2A image was classified and compared with the multi-index image classification results to analyze and illustrate the improvements in the classification accuracy, using the index images. Lastly, the NDTI-based multi-index dataset was layer-stacked with the ten-band original image, and this thirteen-band combination was also classified for further comparison.

To evaluate the accuracy of the classification results, the overall accuracies with the user's, the producer's, and the overall accuracy metrics and Kappa statics were derived from the confusion matrix (Foody, 2002). The accuracy assessment of the classification results was performed with stratified random points, and the original Sentinel-2A image and Google Earth© imagery as the reference data. A random point distribution was designed, according to the heterogeneity potential and areal coverage of the classes. The training sample distribution and number of points used in the accuracy assessment are provided for each class and region in Table 4.3.

Table 4.3 : Training sample and accuracy assessment point distribution for the study regions.

Class Name/ Region	Training Sample						Number of Accuracy Assessment Points		
	Istanbul		Ankara		Konya		Istanbul	Ankara	Konya
	Poly.	Pix.	Poly.	Pix.	Poly.	Pix.	Point	Point	Point
Bare Land	215	1874	67	12198	72	42070	250	185	250
Asphalt	47	473	25	360	19	1033	60	40	50
Water	18	1587	2	4543	1	636	40	15	10
Industry	26	198	4	72	12	731	70	30	50
Built-up	333	1326	295	629	84	1373	250	185	250
Forest	173	5184	8	565	6	85	70	25	20
Veg. Cover	81	4458	4	118	17	2206	70	45	25
Total	893	15100	405	18485	211	48134	810	525	655

4.4 Results and Discussion

4.4.1 Results for the Main Study Region

The classification results and accuracy assessment metrics showed that the NDTI, in combination with NDVIre and the MNDWI, provided the highest accuracy, in comparison to other combinations including the existing built-up indices and the original image classification (Table 4.4 and Table 4.5). Visual analysis of the resulting images in Figure 4.7 shows that the NDTI solves the mixing problem of the built-up and the bare land, which is obvious in other built-up indices. In addition, the problems related to overestimation of built-up regions and underestimation of bare land improved significantly, using this combination. The second highest accuracy was achieved with the combination of NDBI, NDVIre, and MNDWI, for all multi-index combinations. This result was following NDBI's reported performance in built-up area detection (Ettehadi Osgouei & Kaya, 2017). However, this combination provided lower overall accuracies and a low rate of bare land detection, compared to the NDTI-based combination and original image classification results. These results strengthened the findings regarding the built-up indices described in Section 4.3.

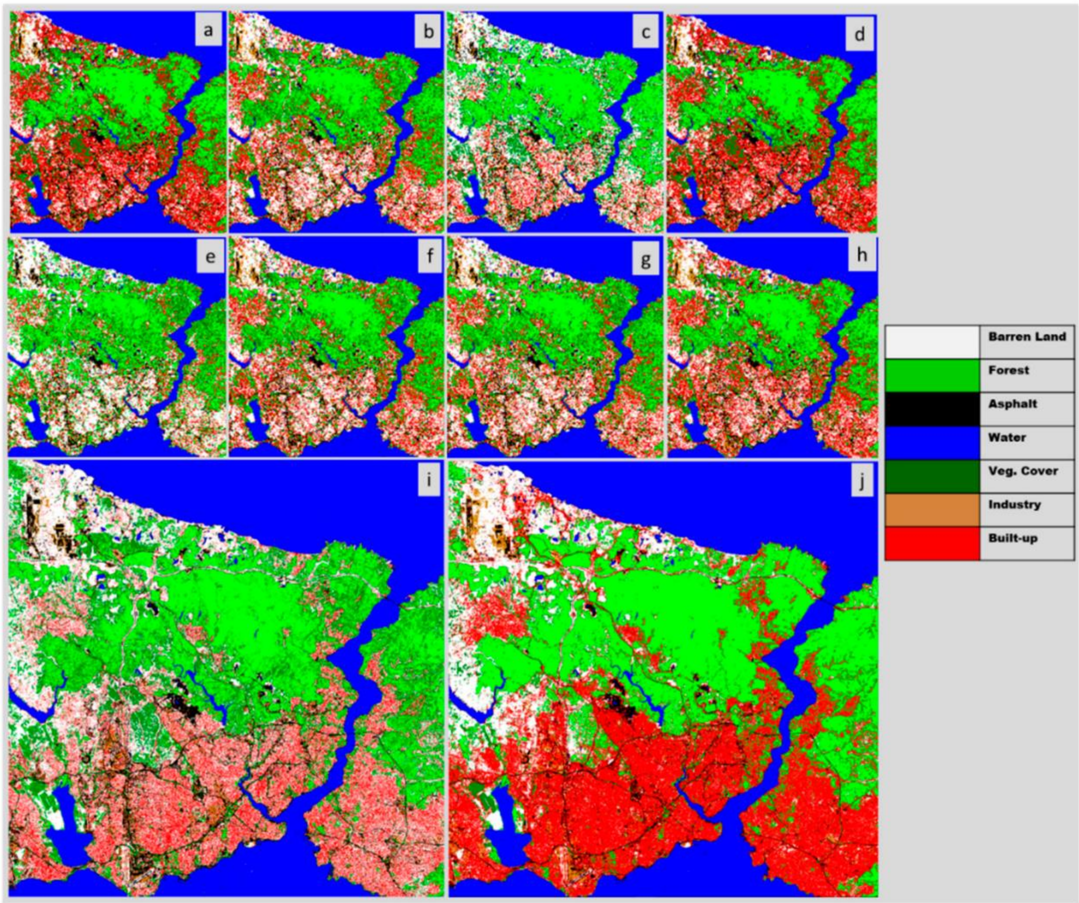

Figure 4.7 : Classification results of (a) NDBI; (b) BUI; (c) BAEI; (d) NBI; (e) VIBI; (f) IBI; (g) UI; (h) BSI; (i) NDTI-based multi-index sets; and (j) original spectral bands.

Table 4.4 : Classification accuracy values of different approaches.

	(Sentinel-2A image(10Bands))		(NDBI+NDVIre+MNDWI)		(NDTI+NDVIre+MNDWI)	
Land cover classes	Producer's accuracy (%)	User's accuracy (%)	Producer's accuracy (%)	User's accuracy (%)	Producer's accuracy (%)	User's accuracy (%)
Bare lands	90.78	55.49	53.32	61.13	92.90	92.11
Asphalt	93.75	100	72.50	96.67	85.71	100
Water	100	97.50	100.00	97.50	100.00	97.50
Industry	96.77	85.71	92.68	54.29	98.28	81.43
Built-Up	62.77	95.20	40.79	34.32	93.28	92.25
Forest	62.89	100	81.90	86.00	94.23	98.00
Veg. Cover	78.57	45.71	81.82	77.14	93.33	100

Table 4.5 : Comparison of the overall accuracy and Kappa statistics.

Data type	Overall accuracy	Kappa
Sentinel-2A image(10Bands)	0.75	0.67
Multi-index (NDBI+NDVIre+MNDWI)	0.60	0.47
Multi-index (NDTI+NDVIre+MNDWI)	0.93	0.91

According to the per-class accuracy results presented in Table 4.4, the multi-index image of the NDBI, the NDVIre, and the MNDWI, provided lower accuracies than the ten-band original Sentinel-2A image for most land cover classes, except for improvements in the vegetation cover class. This improvement can be explained by the use of the NDVIre index, which includes the red-edge band of the Sentinel-2A, for vegetation monitoring. However, this combination could not provide a reliable separation between the built-up area and the bare land. The multi-index image of the NDTI, the NDVIre, and the MNDWI provided better accuracies for most of the land cover classes, especially the built-up and the bare land classes. Similarly, the red-edge band included in the NDVIre provided superior information about vegetation cover class. The overall accuracy and kappa metric presented in Table 4.5 indicated that the NDTI-based combination improved the accuracy metrics with consistent ranges for each LCU class, compared to the classified Sentinel-2A image and classified multi-index image of the NDBI, the NDVIre, and the MNDWI.

As an additional experiment, three indices, including the NDTI, the NDVIre, and the MNDWI were stacked with the original Sentinel-2A ten bands, and the resultant image with thirteen layers (ten original bands and three index images) was classified using the same ROIs; however, the classification result did not show a satisfying performance. Notably, the NDTI-based multi-index approach could not completely solve the problem of mixed pixels of bare land and built-up area, but showed an evident improvement, compared to other built-up indices and original image classifications.

The sub-regions from the classification results of Istanbul are provided in the following figures (Figure 4.8, Figure 4.9 , and Figure 4.10) to demonstrate the improvements of the proposed NDTI-based method, over other classification results. The accuracy metrics show the ten-band original image classification and NDBI-based multi-index set classification provided similar accuracies, whereas the NDTI-based multi-index set outperformed them with a 30% overall accuracy improvement and better consistency of the producer's and the user's accuracy. These results supported the accuracy assessment results of the whole study region.

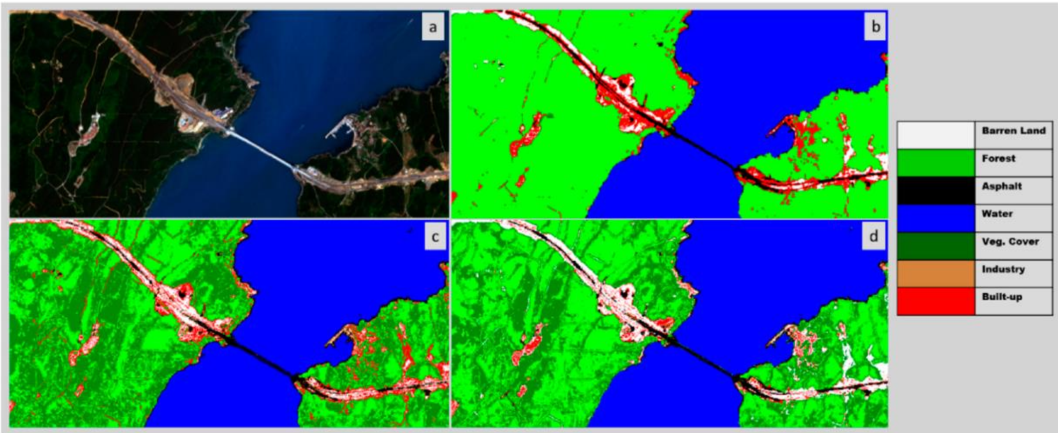

Figure 4.8 : (a) RGB image of the Sentinel-2A; (b) the classified Sentinel-2A; (c) the classified multi-index (NDBI, NDVIre, and MNDWI); and (d) classified multi-index (NDTI, NDVIre, and MNDWI) images.

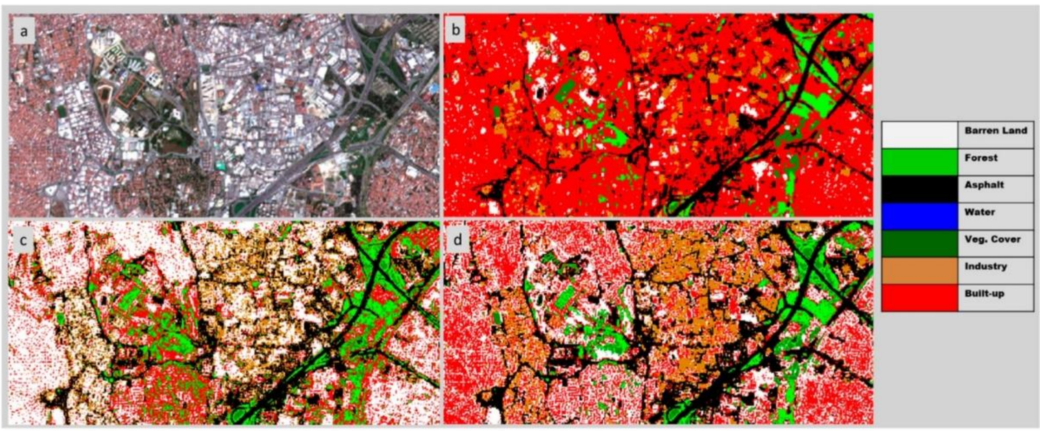

Figure 4.9 : (a) RGB image of the Sentinel-2A; (b)the classified Sentinel-2A; (c) the classified multi-index (NDBI, NDVIre, and MNDWI), and (d) the classified multi-index images.

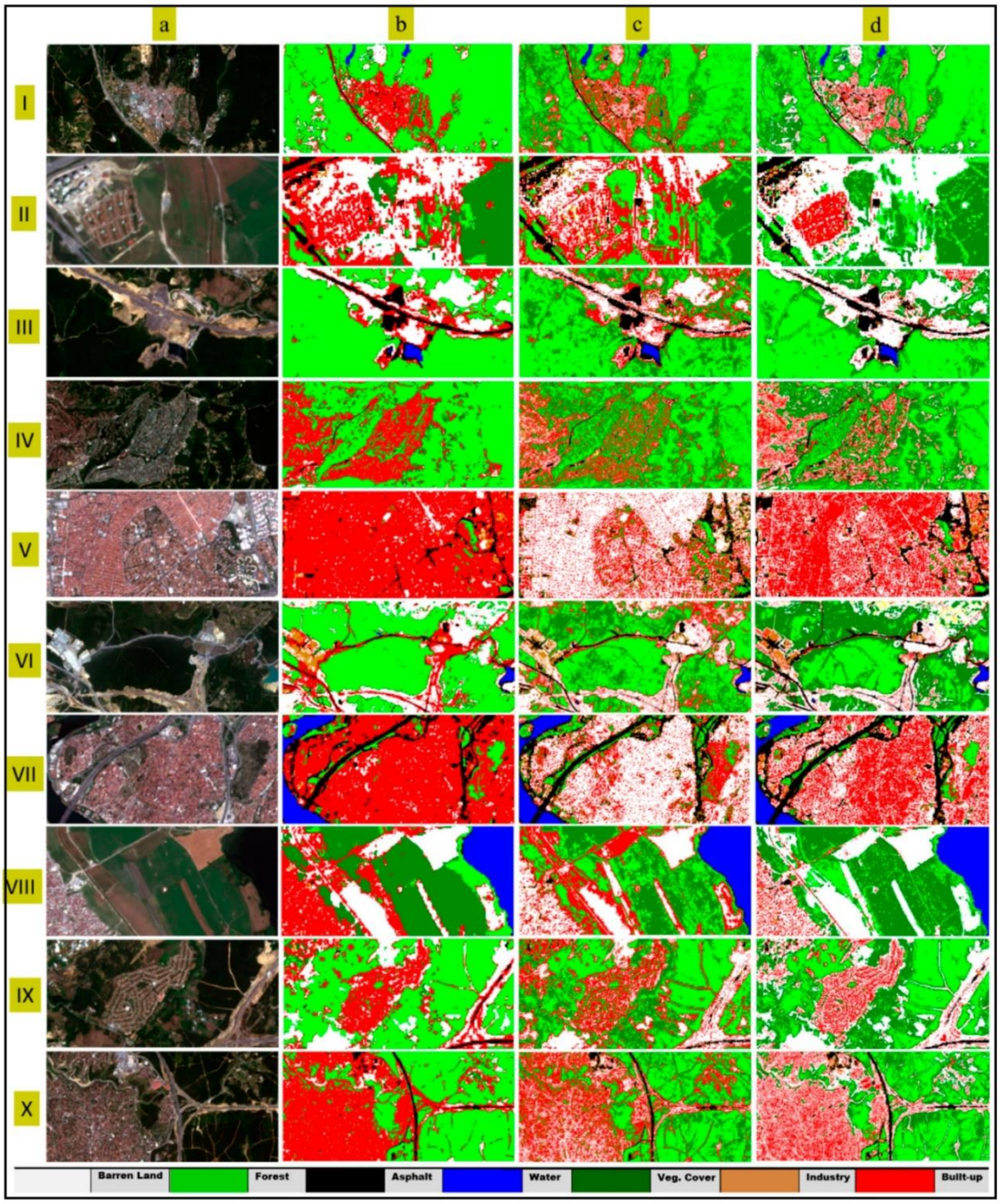

Figure 4.10 : (a) RGB image of the Sentinel-2A; (b) classified Sentinel-2A; (c) classified multi-index (NDBI, NDVIre, MNDWI); and (d) classified multi-index (NDTI, NDVIre, MNDWI) images. Regions illustrated: (I) Eyup-Gokturk; (II) Avcilar; (III) Gumusdere; (IV) Beykoz; (V) Bahcelievler; (VI) Eyup-Akpinar, (VII) Beyoglu; (VIII) Esenyurt; (IX) Sariyer-Uskumrukoy; and (X) Umraniye districts.

Figure 4.8 represents regions covered by water, asphalt road, bare land, vegetation covers, and built-up area land cover classes. All classified images accurately classified water bodies and asphalt road, but there was a misclassification of the bare lands as built-up regions in the multi-index images, using the NDBI (Figure 4.8 (c)) and a misclassification issue and overestimation of the built-up area in the classified

Sentinel-2A image (Figure 4.8 (b)). The multi-index image of the NDTI, the NDVIre, and the MNDWI provided better results than the other two (Figure 4.8 (d)). The NDTI-based image classification determined the built-up areas, more accurately, and separated the bare land near roads, which were classified as built-up areas in the classified Sentinel-2A image (Figure 4.8 (b)). The multi-index combinations, including the NDVIre, determined vegetation cover better and improved the separation of different vegetation types in the study area. Different vegetation types can be recognized more obviously in both multi-index images (Figure 8c,d) than in the classified Sentinel-2A image (Figure 4.8 (b)).

In Figure 4.9, more complicated and heterogeneous parts of Istanbul were investigated. The area is covered with dense residential and industrial built-up patches and includes highways and urban green areas. According to visual inspection, the original ten-band image classification suffered from overestimation of residential areas and misclassification of industrial areas and bare land (Figure 4.9 (b)). Additionally, the NDBI-based multi-index image could not separate the industrial areas from residential areas and there was a misclassification problem of the residential areas, due to the overestimation of bare land. These problems were also observed in other built-up, index-based combinations (Figure 4.9 (c)). The NDTI, in combination with the NDVI and the MNDWI determined the industrial regions more precisely. In such a heterogeneous region, a multi-index image of NDTI, NDVIre, and MNDWI provided superior information about all land cover classes, compared to the other classification results (Figure 4.9(d)).

Generally, the multi-index image of the NDTI, NDVIre, and the MNDWI successfully separated bare land from the built-up areas, while categorizing other land cover classes, such as vegetation cover and water body precisely (Figure 4.10 (d)). Classification of the NDTI-based multi-index set provided a superior understanding of the built-up area patterns and building footprints, especially for the organized types of residential construction (Figure 4.10 (II,IV,IX)) and avoided an overestimation of the built-up areas in the classified Sentinel-2A image (10 bands) (Figure 4.10 (b)). The other multi-index image generated using the NDBI, the NDVIre, and the MNDWI, using the NDBI as the nominee of the existing built-up indices had an excessive misclassification issue. It classified bare land cover as the built-up class and vice versa (Figure 4.10 (c)). Farmlands with no vegetation cover and low water content and especially those that were compacted because of the field operations, heavy equipment, and tillage implements were mostly misclassified as built-up regions with the NDBI-based set. This misclassification problem was mostly overcome using the proposed NDTI-based multi-index image (Figure 4.10 (VIII)). Bare land cover near asphalt roads, which also contained a lower water content, were among the land cover classes that were highly misclassified as built-up areas, and this problem was significantly improved by using the NDTI-based multi-index image (Figure 4.10 (III,VI,X,IX)). Although, the classification results of the NDTI-based multi-index image underestimated the density of the built-up area in some dense built-up regions, the proposed multi-index image classification method provided reliable information about both bare land and built-up classes, while accurately categorizing water and vegetation land cover classes.

4.4.2 Validation on Independent Test Regions

The efficiency and applicability of the proposed approach was tested in two metropolitan cities of Turkey, Ankara, and Konya. These regions were good candidates for evaluating the performance of the multi-index method because they include residential and industrial areas surrounded by extensive bare land, which suited the main objective of this research. Additionally, the image acquisition dates represented different seasonal conditions. The SVM classification was performed on these regions for the three datasets, which were the original ten-band Sentinel-2A image, the NDBI, NDVIre, MNDWI dataset, and the NDTI, NDVIre, MNDWI dataset. The training sample distribution and the number accuracy assessment points are presented in Table 4.3.

The classification results of the Ankara region are presented in Figure 4.11 and the accuracy assessment values are provided in Table 4.6 and Table 4.7. The results showed that the accuracy improvement using the NDTI-based multi-index image was evident. This combination provided higher accuracies for bare land, industry, and built-up classes, indicating a better separation among them. Additionally, the consistency between the producer’s and the user’s accuracy was higher than that of the other datasets. The overall accuracy was improved by, approximately, 30–40%. The two sub-regions presented in Figure 4.11 shows that the classification result of the ten–band multispectral image (Regions 1b and 2b) was dominated by the built-up and the industrial lands, and it misclassified the bare land surrounding them, especially in low-density urban areas. There were incorrectly classified regions near the green areas, due to this effect, which occurred in the north-west and east of both sub-regions. The NDBI-based, multi-index set was less affected by this over classification, but it suffered while trying to distinguish between industry and built-up classes and false classification occurred due to labelling an extensive amount of the built-up areas as industrial land (Regions 1c and 2c – Figure 4.11).

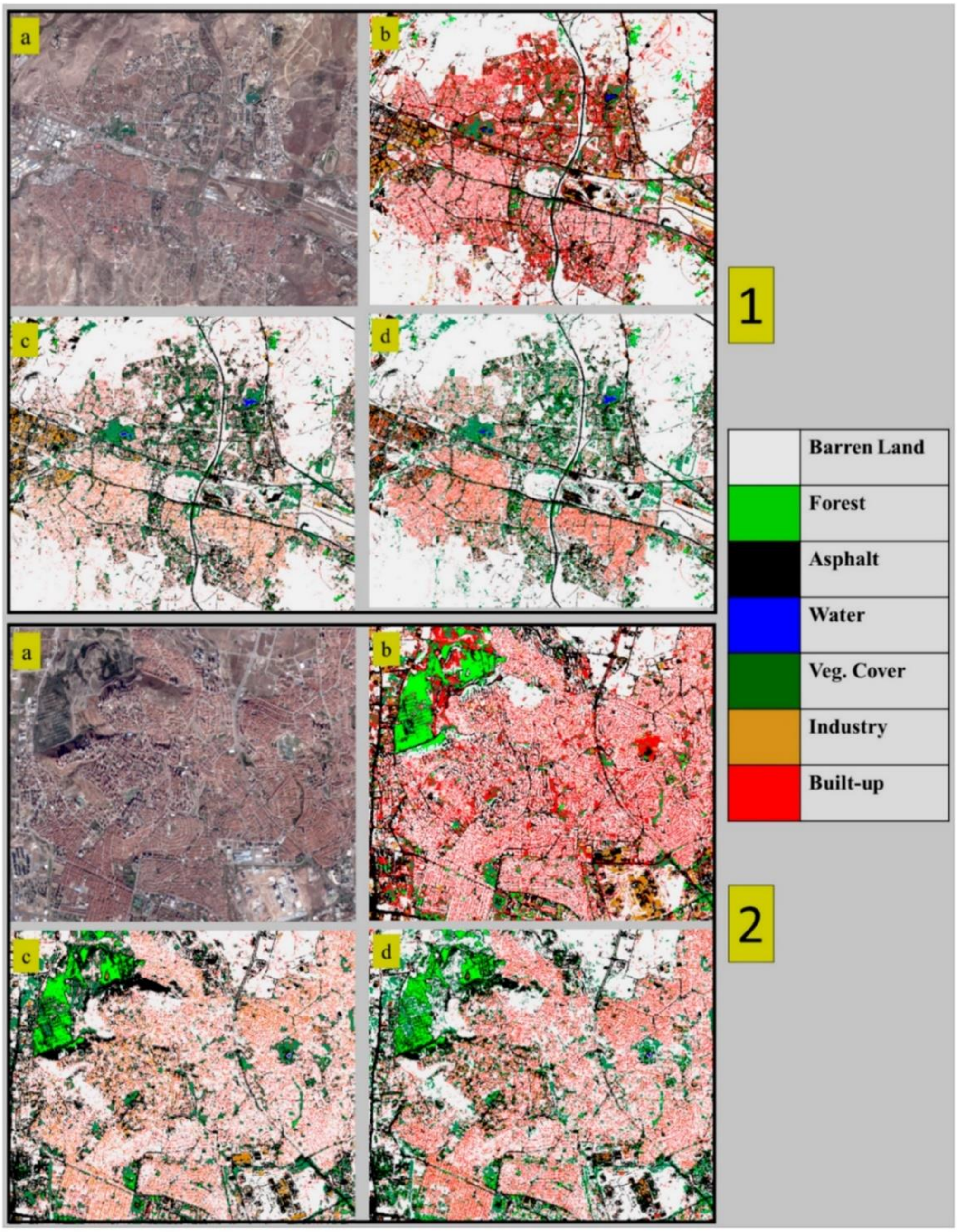

Figure 4.11 : (a) RGB image of Ankara from Sentinel-2A, (b) the classified Sentinel-2A, (c) the classified multi-index (NDBI, NDVIre, and MNDWI) and (d) the classified multi-index (NDTI, NDVIre, and MNDWI) images.

Table 4.6 : Classification accuracies of the different approaches for the Ankara region.

	(Sentinel-2A Image (10 Bands))		(NDBI+NDVIre+MNDWI)		(NDTI+NDVIre+MNDWI)	
Land Cover Class	Producer's Accuracy (%)	User's Accuracy (%)	Producer's Accuracy (%)	User's Accuracy (%)	Producer's Accuracy (%)	User's Accuracy (%)
Bare land	59.52	22.73	43.18	34.55	89.77	90.80
Asphalt	97.50	66.10	92.50	84.09	100	97.56
Water	100	100	100	100	100	100
Industry	26.67	53.33	70.00	100	83.33	100.00
Built-Up	84.34	43.48	20.48	48.57	92.77	92.77
Forest	94.44	65.39	88.89	72.73	100	81.82
Veg. Cover	36.36	100	93.18	57.75	97.72	95.56

Table 4.7 : Comparison of the overall accuracy and Kappa statistics for the Ankara region.

Data Type	Overall Accuracy	Kappa
Sentinel-2A image (10 Bands)	0.51	0.42
Multi-index (NDBI+NDVIre+MNDWI)	0.58	0.48
Multi-index (NDTI+NDVIre+MNDWI)	0.92	0.90

The classification results of the Konya region are presented in Figure 4.12 and the accuracy assessment values are provided in Table 4.8 and Table 4.9. The accuracy improvement and consistency between the producer's and the user's accuracy with the NDTI-based dataset was similar to that in the Ankara region, and the other datasets suffered from low accuracies for the bare land, built-up, and the industry classes. The evaluation in Figure 4.12 shows that the ten-band multispectral imagery classification over-classified built-up lands and could not detect the industrial areas, which could be seen clearly in Region 2b. For the NDBI-based dataset, the bare land in the western part of Regions 1 and 2 were over-classified as built-up land (Regions 1c and 2c). Moreover, there were improvements in the accuracy metrics of the asphalt, forest, and vegetation classes, when applying the proposed method (Regions 1d and 2d).

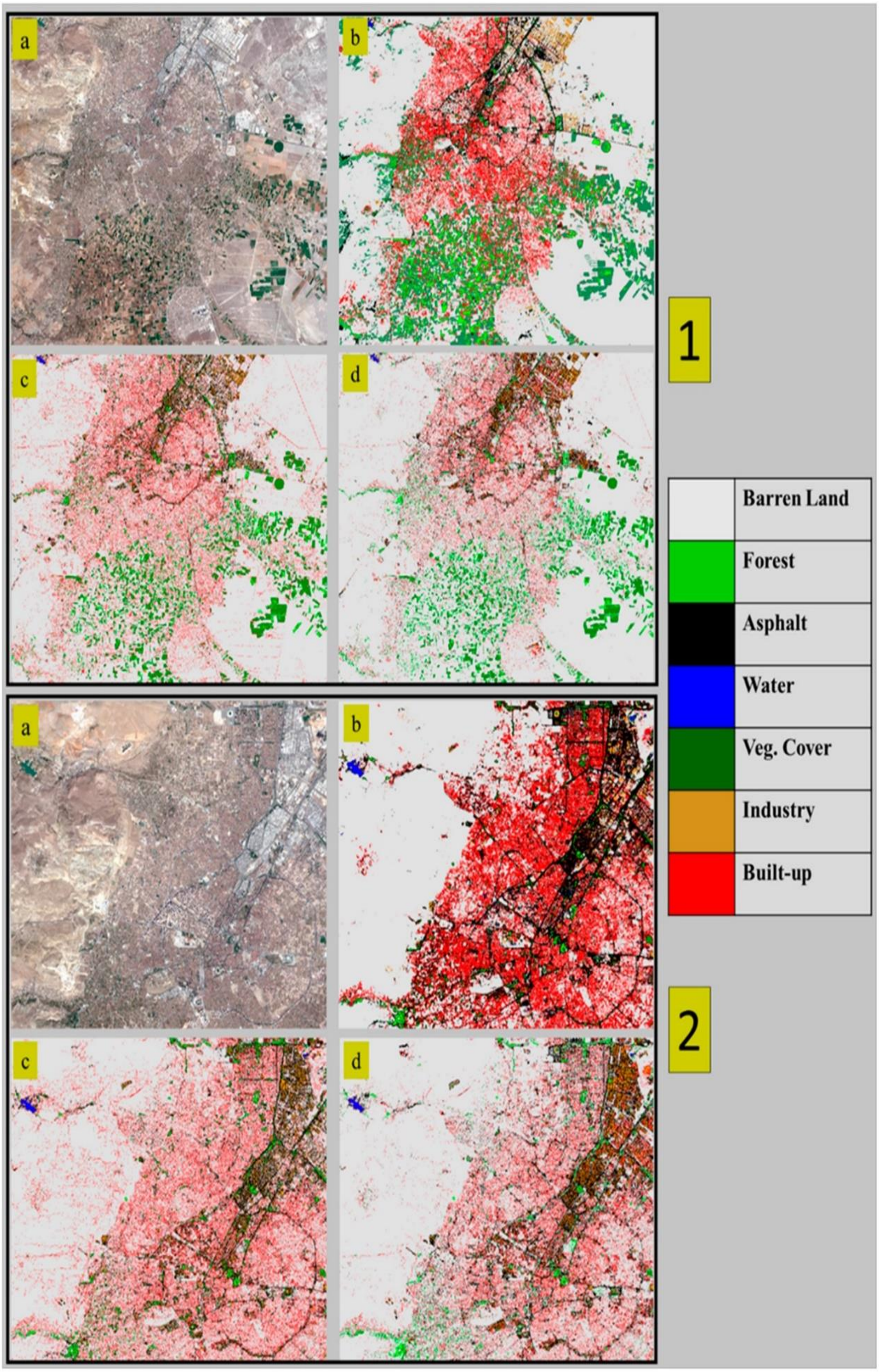

Figure 4.12 : (a) RGB image of Konya from Sentinel-2A, (b) the classified Sentinel-2A, (c) the classified multi-index (NDBI, NDVIre, and MNDWI), and (d) the classified multi-index (NDTI, NDVIre, and MNDWI) images.

Table 4.8 : Classification accuracies of different approaches for the Konya region.

	(Sentinel-2A Image (10 Bands))		(NDBI+NDVIre+MNDWI)		(NDTI+NDVIre+MNDWI)	
Land Cover Class	Producer's Accuracy (%)	User's Accuracy (%)	Producer's Accuracy (%)	User's Accuracy (%)	Producer's Accuracy (%)	User's Accuracy (%)
Bare land	21.13	77.77	34.95	40.56	91.05	77.24
Asphalt	96.42	47.36	46.42	37.14	96.42	75.00
Water	100	100	100	100	100	100
Industry	68.18	96.77	61.36	96.42	84.09	100
Built-Up	77.77	50.90	53.70	42.02	70.37	89.41
Forest	45.00	69.23	35.00	70.00	95.00	86.36
Veg. Cover	78.26	54.54	82.60	65.51	86.95	95.23

Table 4.9 : Comparison of the overall accuracy and Kappa statistics for the Konya region.

Data Type	Overall Accuracy	Kappa
Sentinel-2A image (10 Bands)	0.57	0.45
Multi-index (NDBI+NDVIre+MNDWI)	0.49	0.33
Multi-index (NDTI+NDVIre+MNDWI)	0.84	0.79

The analysis of the two independent test regions showed similar characteristics and supported the effectiveness of the NDTI-based multi-index set in different land and seasonal conditions. Notably, the roofs of buildings in industrial areas were made of aluminium-based materials and concrete, whereas the roofs of the other buildings in the built-up areas were made of tiles in the main and in the test regions. The difference in the roof material resulted in different spectral responses and enabled separation in the original spectral bands and the multi-index data for these classes. Thus, the mixing problem was mainly between bare land and the built-up areas and between bare land and industry. Further analysis was required to evaluate the performance of the proposed approach in regions where the industrial and built-up areas were composed of similar roof materials.

The results from the study and the test regions demonstrated that although built-up indices have been shown to highlight built-up areas, their performance was limited in heterogeneous landscapes, where urban areas and bare lands were mixed. A shortwave infrared-based index improved the separation of urban areas and bare lands, as shown in this research work. In addition, the newly added red-edge spectral bands of Sentinel-2A enhanced the vegetation cover detection and mapping.

4.5 Conclusions

Separating bare land from the impervious surfaces and built-up areas has been the main problem in mapping urbanized areas. In this research work, a novel multi-index approach has been proposed for the LCU classification of Sentinel-2A satellite images, focusing on separating the urban and bare land, in addition to other land cover categories. To improve the classification accuracy and solve the misclassification and overestimation problems, a methodology was developed using spectral indices that categorized the three major land cover classes, water bodies, vegetation cover, and built-up areas. The multi-index images created with different index combinations were classified using the machine-learning-based SVM algorithm. The multi-index classification results were compared with the SVM classification result of the ten-band Sentinel-2A image. The results of this research showed that NDTI in combination with NDVIre and MNDWI improved the separation between the built-up regions and bare land, and significantly improved the misclassification of bare lands as built-up regions. In addition, the NDTI, which was calculated by the difference of the SWIR bands, divided by its sum of them, could be applied to the Landsat 5, 7, and 8 images, as well as the Landsat missions that included the SWIR bands with a similar wavelength range of the Sentinel-2 mission. This applicability enabled a further analysis using combined historic archival Landsat missions and higher spatial and spectral resolution Sentinel-2A images, to detect LCU changes through decades. Although classification of the ten-band Sentinel-2A imagery provided acceptable results related to the built-up area and bare land classes, the multi-index image of the NDTI, the NDVIre, and the MNDWI provided more interpretable and illustratable results for the built-up regions, in terms of shape, intensity, and pattern. The proposed combination also provided satisfactory results and accuracy improvements for the other LCU classes, with 85% or better accuracy in the three study regions, compared to other datasets. These findings indicate the possible effectiveness of the proposed multi-index set as a dimension reduction method in multi-temporal analysis. Further studies are planned to integrate multi-temporal and multi-polarization SAR data, such as Sentinel 1 (to process chain), in order to take advantage of the SAR data in the separation of bare lands and built-up areas.

5. CONCLUSION AND DISCUSSIONS

Satellite data have substantial potential for environmental studies. One of the most important environmental concepts is air pollution. Evaluation of free-of-charge satellite data for monitoring and controlling atmospheric aerosol emissions is necessary. Satellite observations of aerosol properties provide a valuable source for researchers and decision-makers trying to understand how aerosols change in the long and short term and how they affect the environment. The dataset presents a significant opportunity to investigate the factors that influence aerosol pollution and the impact of aerosols on climate change and society.

The ultimate goal of this research is to gain a better understanding of air pollution and develop effective strategies to observe and monitor it. The research will involve gathering and analyzing appropriate data using specific techniques over an extended period to assess aerosol concentration changes. This research study aims the evaluation the potential of satellite aerosol data to analyze the aerosol pollution of one of the most polluted regions of Turkey, the Marmara region, which has been exposed to various air pollutants emitted from urbanization and industrialization activities, marine activities, dust transportation, and agricultural practices.

The first step in using satellite aerosol dataset is the evaluation of satellite-derived aerosol information against accurate ground-based aerosol observations. The AERONET stations located worldwide can serve as a benchmark for this evaluation. The first part was dedicated to the evaluation of various satellite aerosol products against the AOD measurements from the nearest AERONET sites to evaluate the accuracy of aerosol products from satellite sensors over the study region and choose the most effective satellite sensor and aerosol retrieval algorithm for the study area, which may then be utilized for additional analysis such as assessing the spatiotemporal distribution of aerosol concentrations and their effects on air quality, climate, and human health.

For this, I compared and validated multiple satellite aerosol products, including MODIS DT, DB, MAIAC, and VIIRS SOAR/DB AOD. The validation was performed by the comparison of satellite-derived AOD against AERONET AOD measurements over different surface types in the eastern Mediterranean from 2014-2018. The results show that most products are reliable with at least 67% of matchups falling within the

EE envelope, but their performance varies depending on the surface type and algorithm used. MODIS MAIAC at 1-km performs best over urban/land surface types in terms of within% (89%) and RMSEs (0.048), while MODIS DT at both 10-km and 3km performs best over ocean surfaces in terms of correlations (r between 0.86-0.92), within% EE (between 70% and 80%), and RMSEs (between 0.047 and 0.061). Although various factors lead to errors in AOD retrievals over the coastal region, the VIIRS DB-SOAR outperforms other products over the coastal site in terms of correlation with AERONET AOD measurements (r=0.88) and within% (88%). Complex surface type and mixed water/land pixels and biases from cloud/foam/sediment contaminations are among the factors that can introduce noise and bias into AOD retrievals over the coastal region. The chapter also emphasized the importance of considering factors when interpreting AOD data over coastal zones. Additionally, the chapter considered the potential for the continuation of global aerosol monitoring that MODIS instigated over two decades ago by VIIRS AOD products. The validations show that this continuity is possible due to the similar sensor characteristics and retrieval algorithms of the two products. According to the validations performed in the first chapter of the study, MODIS MAIAC AOD becomes the most appropriate aerosol dataset in terms of performance against AERONET AOD measurements which also has the highest spatial resolution of 1 km.

In the second chapter, I focus on understanding the spatial and temporal variation of AOD over the Marmara region. This is essential to revealing the impact of aerosols on climate and the environment. Once I collected and analyzed the appropriate data, I used various statistical and visualization techniques to identify patterns and trends in AOD levels over time and space. The analysis was based on the MAIAC AOD 1 km product from 2000 to 2021 and I analyzed AOD's distribution patterns and trends in different time series across the Marmara region.

The inter-annual and intra-annual (daily, monthly, and seasonal) variations of AOD have been thoroughly studied. Through the analysis of month-wise AOD variation over the Marmara region between 2000 and 2021, it is shown that higher AOD was distributed over the entire study region from late spring to early autumn (April-September), with the highest values observed in May and August. Aerosol intensification during this time of year is largely attributed to increased agricultural practices. Conversely, lower precipitation levels and higher temperatures lead to drier soils, causing an increase in elevated soil and dust from bare land.

The prevailing meteorological conditions can play a significant role in determining the seasonal patterns of AOD. As a result, it is crucial to comprehend the connections between meteorological factors and AOD levels in order to properly interpret satellite measurements and create methods for minimizing the effects of aerosols on both human health and the environment. During the summer months, higher temperatures can cause the formation of secondary aerosols, which can contribute to an increase in AOD values. In addition, higher absolute humidity levels during the summer can boost the water content of aerosol particles, leading to an increase in AOD. In wintertime, aerosol concentrations are primarily observed in narrow areas, mostly in the center of cities, towns, and in the industrialized zones of the Marmara region. Despite increasing precipitation levels during wintertime causing aerosol washout, aerosol concentrations remain high in these areas due to consistent intense aerosol emissions during the coldest time of the year. This is attributed to the increased use of heating systems and wood-burning stoves.

The inter-annual AOD variability examinations show that the mean AOD value in the Marmara region between 2000 and 2021 has decreased with an annual decrease of 0.005/a, showing a significant decrease between 2018 and 2021, with an annual decrease of about 0.08/a, which can be attributed to the reduction of regional pollutant emissions during the COVID-19 pandemic. The factors that influence the decreasing-increasing trends of AOD and meteorological and geographical factors that can affect the magnitude and spatial distribution of AOD have been discussed. By analyzing the MODIS MAIAC aerosol product within the period of 2000 to 2021, it is believed that human activities are the main source of aerosols in the eastern part of the Marmara region whereas agricultural practices are the main contributors in the western part. Edirne is a province that has experienced the highest decrease in AOD levels, which can be primarily attributed to the implementation of bans on biomass-residue burning and the use of high-quality coal, as well as the increased usage of natural gas in households and industrial activities. The Balikesir province, located in the eastern part of the region, has experienced the highest increasing trend of AOD. This increase in AOD can be attributed to the rise in industrial activities and urban expansion in the province.

The spatial distribution of the AOD was also examined using the percentile thresholds to define the monthly and annual high AOD areas in which the zones with AOD values greater than the specified threholds are considered. The study found that while larger areas in the western portion of the Marmara region had higher AOD values, the mean AOD values were actually highest in smaller areas on the eastern side which can named as hot sport od aerosols. Additionally, the study found that the western side of Istanbul had the highest mean AOD values despite having the smaller high AOD value area, indicating that there are intense anthropogenic aerosol emission sources, likely due to industrial activities and intensified coastal filling works on the Anatolian side coasts of Istanbul.

The impacts of LCU on AOD have been analyzed utilizing the CLC maps. The two most critical land cover/uses that influence the atmospheric aerosol loading over the Marmara region were detected. The key factors affecting the aerosol loading over the Marmara region are the industrial and urban activities as well as agricultural practices and elevated dust and sand from bare soils in the Marmara region. Agricultural land and urbanized/industrialized zones are the LCUs which are mostly contributed to the atmosphere in the Marmara region. The last part is devoted to proposing a strategy of segregating developed regions from undeveloped bare lands and agricultural bare soil with no vegetation within intricate and diverse urban landscapes. This is of critical importance because urbanized and industrialized zones as well as bare soil areas contribute to the atmospheric aerosol burden. The chapter proposes a novel multi-index approach to mapping urbanized areas by using spectral indices to categorize land cover categories such as water bodies, vegetation cover, built-up areas, and bare land. The multi-index images are classified using the SVM algorithm and compared with the SVM classification of the ten-band Sentinel-2A image. The results show that the proposed multi-index set of NDTI, NDVIre, and MNDWI provides more accurate and interpretable results for the built-up regions compared to other datasets, with 85% or better accuracy in the three study regions. The proposed method also enables further analysis using combined historic archival Landsat missions and higher spatial and spectral resolution Sentinel-2A images to detect LCU changes through decades. The article suggests integrating multi-temporal and multi-polarization SAR data in future studies to further improve the separation of bare land and built-up areas.

As a conclusion, the prior knowledge gained from the comparison of satellite aerosol products with ground-based aerosol observation and the intercomparison of various aerosol retrieval algorithms can guide the creation of future aerosol datasets, which could lead to more accurate and dependable results from climate research and environmental studies. This study also offers significant observations on the extended patterns of AOD, the possible sources of the aerosols, and the seasonal and long-term variability of AOD in the Marmara region of Turkey. The results obtained from this research can be used to inform air quality management strategies in the region and it can assist in enhancing our comprehension of the elements that affect air contamination at the local scale. Moreover, the study outcomes can contribute to making policy decisions aimed at emphasizing the importance of continued monitoring and control of air pollution in urban areas.

The valuable information on the AOD in the Marmara region of Turkey can help in developing strategies to mitigate air pollution and its impacts on climate change as well as demonstrating how satellite AOD data can be used to analyze the spatial and temporal patterns of aerosol loading over a region and to investigate the effective factors on aerosol concentration. The suggested approach in this reaserch study can be applied to other regions to better understand the impacts of aerosols on regional climate and air quality and mitigate the adverse effects of aerosols on human health and the environment. Based on the needs of the research and the features of the study region, the approach entails a number of processes to choose the optimum satellite aerosol product. Using appropriate methodologies for data analysis and interpretation is part of it, as is being aware of the benefits and drawbacks of certain goods. This strategy enables researchers to provide reliable study results and make well-informed conclusions.

Although the findings of this study shed light on the use and validation of the satellite-derived aerosol dataset in a study area, there are still several important questions that require further analysis, consideration, and discussion. I used AOD measurements at three closest AERONET stations to validate the satellite-derived AOD data. To reinforce the cross-validation of these datasets, adding more extensive ground-based sites in various climate zones, land-cover types, and aerosol conditions can help to improve the accuracy and reliability of the data. This can provide a more comprehensive and diverse range of data, which can help to identify any potential biases or errors in the data and ultimately improve our understanding of the distribution and characteristics of aerosols in the atmosphere.

Land cover and land use mapping, as well as air pollution, are two critical environmental issues that are currently facing our planet. Remotely sensed satellite data can be a valuable resource for addressing these issues, as it allows us to gather information about the Earth's surface and atmosphere from a distance, without the need for direct contact or physical presence. This study worked on these two issues and brought forward the advantages as well as challenges of using satellite data. Although the satellite-derived aerosol dataset has been gradually upgraded for a better analysis of the atmospheric aerosol, the best aerosol product provided by MODIS is at a spatial resolution of 1km. The detailed validation of the impacts of aerosol pollution on human health and climate change be conducted with AOD datasets at a finer resolution. The detailed strategy proposed for the mapping of urbanized areas in the last part of the study can be evaluated for monitoring air pollution at a finer scale in case of having an aerosol dataset at a finer resolution.

REFERENCES

Aburas, M. M., Ho, Y. M., Ramli, M. F., & Ash'aari, Z. H. (2016). The simulation and prediction of spatio-temporal urban growth trends using cellular automata models: A review. *International Journal of Applied Earth Observation and Geoinformation*, *52*, 380–389. doi:10.1016/j.jag.2016.07.007

Acharya, P., Barik, G., Gayen, B. K., Bar, S., Maiti, A., Sarkar, A., … Sreekesh, S. (2021). Revisiting the levels of Aerosol Optical Depth in south-southeast Asia, Europe and USA amid the COVID-19 pandemic using satellite observations. *Environmental Research*, *193*, 110514.

Acharya, P., & Sreekesh, S. (2013). Seasonal variability in aerosol optical depth over India: a spatio-temporal analysis using the MODIS aerosol product. *International Journal of Remote Sensing*, *34*(13), 4832–4849. doi:10.1080/01431161.2013.782114

Agacayak, T., Kindap, T., Unal, A., Pozzoli, L., Mallet, M., & Solmon, F. (2015). A case study for Saharan dust transport over Turkey via RegCM4.1 model. *Atmospheric Research*, *153*, 392–403. doi:10.1016/j.atmosres.2014.09.012

Ahmad, Z., Franz, B., Mcclain, C., Kwiatkowska, E., Werdell, J., Shettle, E., & Holben, B. (2011). New aerosol models for the retrieval of aerosol optical thickness and normalized water-leaving radiances from the SeaWiFS and MODIS sensors over coastal regions and open oceans: publisher's note. *Applied Optics*, *50*, 626. doi:10.1364/AO.50.000626

Air pollution report. (2020). *Air pollution report* (p. 158). Retrieved from https://www.cmo.org.tr/resimler/ekler/a9992ac36b8068a_ek.pdf

Akkoyunlu, B. O., Baltaci, H., & Tayanc, M. (2019). Atmospheric conditions of extreme precipitation events in western Turkey for the period 2006–2015. *Natural Hazards and Earth System Sciences*, *19*(1), 107–119. doi:10.5194/nhess-19-107-2019

Alam, K., Trautmann, T., & Blaschke, T. (2011). Aerosol optical properties and radiative forcing over mega-city Karachi. *Atmospheric Research*, *101*(3), 773–782.

Ali, M. A., Nichol, J. E., Bilal, M., Qiu, Z., Mazhar, U., Wahiduzzaman, M., … Islam, M. N. (2020). Classification of aerosols over Saudi Arabia from 2004–2016. *Atmospheric Environment*, *241*, 117785.

Al-Saadi, J., Szykman, J., Pierce, R. B., Kittaka, C., Neil, D., Chu, D. A., … Fishman, J. (2005). Improving National Air Quality Forecasts with Satellite Aerosol Observations. *Bulletin of the American Meteorological Society*, *86*(9), 1249–1262. doi:10.1175/BAMS-86-9-1249

Anderson, J. C., Wang, J., Zeng, J., Petrenko, M., Leptoukh, G. G., & Ichoku, C. (2012). Accuracy assessment of Aqua-MODIS aerosol optical depth over coastal regions: importance of quality flag and sea surface wind speed. *Atmospheric Measurement Techniques Discussions*, *5*(4), 5205–5243. doi:10.5194/amtd-5-5205-2012

Anderson, Jacob C., Wang, J., Zeng, J., Leptoukh, G., Petrenko, M., Ichoku, C., & Hu, C. (2013). Long-term statistical assessment of Aqua-MODIS aerosol optical depth over coastal regions: bias characteristics and uncertainty sources. *Tellus B: Chemical and Physical Meteorology*, *65*(1), 20805. doi:10.3402/tellusb.v65i0.20805

Anoruo, C. M. (2021). Sub-seasonal aerosol characterization at the Middle East regions of AERONET site. *Urban Climate*, *37*, 100827. doi:https://doi.org/10.1016/j.uclim.2021.100827

Arkian, F., & Nicholson, S. (2018). Long-term variations of aerosol optical depth and aerosol radiative forcing over Iran based on satellite and AERONET data. *Environmental Monitoring and Assessment*, *190*(1), 1–15.

Arola, A., Eck, T. F., Kokkola, H., Pitkänen, M. R. A., & Romakkaniemi, S. (2017). Assessment of cloud-related fine-mode AOD enhancements based on AERONET SDA product. *Atmospheric Chemistry and Physics*, *17*(9), 5991–6001. doi:10.5194/acp-17-5991-2017

Arslan, O., & Akyürek, Ö. (2018). Spatial Modelling of Air Pollution from PM10 and SO2 concentrations during Winter Season in Marmara Region (2013-2014). *International Journal of Environment and Geoinformatics*, *5*(1), 1–16. doi:10.30897/ijegeo.412391

Artaxo, P., V. Rizzo, L., F. Brito, J., J. Barbosa, H. M., Arana, A., T. Sena, E., … O. Andreae, M. (2013). Atmospheric aerosols in Amazonia and land use change: from natural biogenic to biomass burning conditions. *Faraday Discussions*, *165*(0), 203–235. doi:10.1039/C3FD00052D

Aslanoğlu, S. Y., Proestakis, E., Gkikas, A., Güllü, G., & Amiridis, V. (2022). Dust Climatology of Turkey as a Part of the Eastern Mediterranean Basin via 9-Year CALIPSO-Derived Product. *Atmosphere*, *13*(5), 733. doi:10.3390/atmos13050733

Asongu, S. A., Agboola, M. O., Alola, A. A., & Bekun, F. V. (2020). The criticality of growth, urbanization, electricity and fossil fuel consumption to environment sustainability in Africa. *Science of The Total Environment*, *712*, 136376. doi:10.1016/j.scitotenv.2019.136376

As-Syakur, A. R., Adnyana, I. W. S., Arthana, I. W., & Nuarsa, I. W. (2012). Enhanced built-up and bareness index (EBBI) for mapping built-up and bare land in an urban area. *Remote Sensing*, *4*(10), 2957–2970.

Atkinson, P. M. (2013). Downscaling in remote sensing. *International Journal of Applied Earth Observation and Geoinformation*, *22*, 106–114. doi:10.1016/j.jag.2012.04.012

Attwood, A. R., Washenfelder, R. A., Brock, C. A., Hu, W., Baumann, K., Campuzano-Jost, P., … Brown, S. S. (2014). Trends in sulfate and organic aerosol mass in the Southeast U.S.: Impact on aerosol optical depth and radiative forcing. *Geophysical Research Letters*, *41*(21), 7701–7709. doi:10.1002/2014GL061669

Babu, S. S., Manoj, M. R., Moorthy, K. K., Gogoi, M. M., Nair, V. S., Kompalli, S. K., … Singh, D. (2013). Trends in aerosol optical depth over Indian region: Potential causes and impact indicators. *Journal of Geophysical Research: Atmospheres*, *118*(20), 11,794-11,806. doi:10.1002/2013JD020507

Badarinath, K., Kharol, S. K., Kaskaoutis, D., Sharma, A. R., Ramaswamy, V., & Kambezidis, H. (2010). Long-range transport of dust aerosols over the Arabian Sea and Indian region—A case study using satellite data and ground-based measurements. *Global and Planetary Change*, *72*(3), 164–181.

Bae, C., Kim, B.-U., Kim, H. C., Yoo, C., & Kim, S. (2020). Long-Range Transport Influence on Key Chemical Components of PM2.5 in the Seoul Metropolitan Area, South Korea, during the Years 2012–2016. *Atmosphere*, *11*(1), 48. doi:10.3390/atmos11010048

Baltaci, H. (2021). Meteorological characteristics of dust storm events in Turkey | Elsevier Enhanced Reader. doi:10.1016/j.aeolia.2021.100673

Baltaci, H., Arslan, H., & Akkoyunlu, B. O. (2022). High PM10 source regions and their influence on respiratory diseases in Canakkale, Turkey. *International Journal of Environmental Science and Technology*, *19*(2), 797–806. doi:10.1007/s13762-020-02914-7

Baltaci, H., Gokturk, O. M., Kındap, T., Unal, A., & Karaca, M. (2015). Atmospheric circulation types in Marmara Region (NW Turkey) and their influence on precipitation. *International Journal of Climatology*, *35*(8), 1810–1820. doi:10.1002/joc.4122

Baltaci, H., Kındap, T., Unal, A., & Karaca, M. (2017). The influence of atmospheric circulation types on regional patterns of precipitation in Marmara (NW Turkey). *Theoretical and Applied Climatology*, *127*(3), 563–572. doi:10.1007/s00704-015-1653-1

Basart, S., Pérez, C., Cuevas, E., Baldasano, J. M., & Gobbi, G. P. (2009). Aerosol characterization in Northern Africa, Northeastern Atlantic, Mediterranean Basin and Middle East from direct-sun AERONET observations. *Atmospheric Chemistry and Physics*, *9*(21), 8265–8282. doi:10.5194/acp-9-8265-2009

Bègue, N., Shikwambana, L., Bencherif, H., Pallotta, J., Sivakumar, V., Wolfram, E., … Formenti, P. (2020). Statistical analysis of the long-range transport of the 2015 Calbuco volcanic plume from ground-based and space-borne observations. *Annales Geophysicae*, *38*(2), 395–420. doi:10.5194/angeo-38-395-2020

Bekkar, B., Pacheco, S., Basu, R., & DeNicola, N. (2020). Association of Air Pollution and Heat Exposure With Preterm Birth, Low Birth Weight, and Stillbirth in the US. *JAMA Network Open*, *3*(6), e208243. doi:10.1001/jamanetworkopen.2020.8243

Bencharif-Madani, F., Ali-Khodja, H., Kemmouche, A., Terrouche, A., Lokorai, K., Naidja, L., & Bouziane, M. (2019). Mass concentrations, seasonal variations, chemical compositions and element sources of PM10 at an urban site in Constantine, northeast Algeria. *Journal of Geochemical Exploration*, *206*, 106356. doi:10.1016/j.gexplo.2019.106356

Ben-Dor, E., Patkin, K., Banin, A., & Karnieli, A. (2002). Mapping of several soil properties using DAIS-7915 hyperspectral scanner data - a case study over clayey soils in Israel. *International Journal of Remote Sensing*, *23*(6), 1043–1062. doi:10.1080/01431160010006962

Bibi, H., Alam, K., & Bibi, S. (2016). In-depth discrimination of aerosol types using multiple clustering techniques over four locations in Indo-Gangetic plains. *Atmospheric Research*, *181*, 106–114.

Bibi, H., Alam, K., Chishtie, F., Bibi, S., Shahid, I., & Blaschke, T. (2015). Intercomparison of MODIS, MISR, OMI, and CALIPSO aerosol optical depth retrievals for four locations on the Indo-Gangetic plains and validation against AERONET data. *Atmospheric Environment*, *111*, 113–126. doi:10.1016/j.atmosenv.2015.04.013

Bilal, M., Mhawish, A., Nichol, J. E., Qiu, Z., Nazeer, M., Ali, Md. A., … Ke, S. (2021). Air pollution scenario over Pakistan: Characterization and ranking of extremely polluted cities using long-term concentrations of aerosols and trace gases. *Remote Sensing of Environment*, *264*, 112617. doi:10.1016/j.rse.2021.112617

Bilal, M., Nazeer, M., & Nichol, J. E. (2017). Validation of MODIS and VIIRS derived aerosol optical depth over complex coastal waters. *Atmospheric Research*, *186*, 43–50. doi:10.1016/j.atmosres.2016.11.009

Bilal, M., Nazeer, M., Nichol, J., Qiu, Z., Wang, L., Bleiweiss, M. P., … Lolli, S. (2019). Evaluation of Terra-MODIS C6 and C6.1 Aerosol Products against Beijing, XiangHe, and Xinglong AERONET Sites in China during 2004-2014. *Remote Sensing*, *11*(5), 486. doi:10.3390/rs11050486

Bilal, M., Nazeer, M., Qiu, Z., Ding, X., & Wei, J. (2018). Global Validation of MODIS C6 and C6.1 Merged Aerosol Products over Diverse Vegetated Surfaces. *Remote Sensing*, *10*(3), 475. doi:10.3390/rs10030475

Bilal, M., Nichol, J. E., & Nazeer, M. (2016). Validation of Aqua-MODIS C051 and C006 Operational Aerosol Products Using AERONET Measurements Over Pakistan. *IEEE Journal of Selected Topics in Applied Earth Observations and Remote Sensing*, *9*(5), 2074–2080. doi:10.1109/JSTARS.2015.2481460

Bilal, M., Nichol, J. E., & Wang, L. (2017). New customized methods for improvement of the MODIS C6 Dark Target and Deep Blue merged aerosol product. *Remote Sensing of Environment*, *197*, 115–124. doi:10.1016/j.rse.2017.05.028

Bouzekri, S., Lasbet, A. A., & Lachehab, A. (2015). A New Spectral Index for Extraction of Built-Up Area Using Landsat-8 Data. *Journal of the Indian Society of Remote Sensing*, *43*(4), 867–873. doi:10.1007/s12524-015-0460-6

Bright, J. M., & Gueymard, C. A. (2019). Climate-specific and global validation of MODIS Aqua and Terra aerosol optical depth at 452 AERONET stations. *Solar Energy*, *183*, 594–605. doi:10.1016/j.solener.2019.03.043

Bruzzone, L., & Persello, C. (2009). A Novel Context-Sensitive Semisupervised SVM Classifier Robust to Mislabeled Training Samples. *IEEE Transactions on Geoscience and Remote Sensing*, *47*(7), 2142–2154. doi:10.1109/TGRS.2008.2011983

Bucak, U., Arslan, T., Demirel, H., & Balın, A. (2021). Analysis of Strategies to Reduce Air Pollution from Vessels: A Case for the Strait of Istanbul. *Journal of ETA Maritime Science*, *9*(1), 22–30.

Canaz, S., Aliefendioğlu, Y., & Tanrıvermiş, H. (2017). Change detection using Landsat images and an analysis of the linkages between the change and property tax values in the Istanbul Province of Turkey. *Journal of Environmental Management*, *200*, 446–455.

Cao, C., Xiong, J., Blonski, S., Liu, Q., Uprety, S., Shao, X., … Weng, F. (2013). Suomi NPP VIIRS sensor data record verification, validation, and long-term performance monitoring. *Journal of Geophysical Research: Atmospheres*, *118*(20), 11,664-11,678. doi:10.1002/2013JD020418

Capraz, O., & Deniz, A. (2021). Assessment of hospitalizations from asthma, chronic obstructive pulmonary disease and acute bronchitis in relation to air pollution in İstanbul, Turkey. *Sustainable Cities and Society*, *72*, 103040. doi:10.1016/j.scs.2021.103040

Carroll, M. L., DiMiceli, C. M., Townshend, J. R. G., Sohlberg, R. A., Elders, A. I., Devadiga, S., … Levy, R. (2017). Development of an operational land water mask for MODIS Collection 6, and influence on downstream data products. *International Journal of Digital Earth*, *10*(2), 207–218. doi:10.1080/17538947.2016.1232756

Carroll, M. L., Townshend, J. R. G., DiMiceli, C. M., Loboda, T., & Sohlberg, R. A. (2011). Shrinking lakes of the Arctic: Spatial relationships and trajectory of change. *Geophysical Research Letters*, *38*(20). doi:10.1029/2011GL049427

Ceccato, P., Gobron, N., Flasse, S., Pinty, B., & Tarantola, S. (2002). Designing a spectral index to estimate vegetation water content from remote sensing data: Part 1: Theoretical approach. *Remote Sensing of Environment*, *82*(2–3), 188–197.

Che, H., Qi, B., Zhao, H., Xia, X., Eck, T. F., Goloub, P., … Zhang, X. (2018). Aerosol optical properties and direct radiative forcing based on measurements from the China Aerosol Remote Sensing Network (CARSNET) in eastern China. *Atmospheric Chemistry and Physics*, *18*(1), 405–425. doi:10.5194/acp-18-405-2018

Che, H., Xia, X., Zhao, H., Dubovik, O., Holben, B. N., Goloub, P., … Zhang, X. (2019). Spatial distribution of aerosol microphysical and optical properties and direct radiative effect from the China Aerosol Remote Sensing Network. *Atmospheric Chemistry and Physics*, *19*(18), 11843–11864. doi:10.5194/acp-19-11843-2019

Chen, B., Song, Y., Jiang, T., Chen, Z., Huang, B., & Xu, B. (2018). Real-Time Estimation of Population Exposure to PM2.5 Using Mobile- and Station-Based Big Data. *International Journal of Environmental Research and Public Health, 15*(4), 573. doi:10.3390/ijerph15040573

Chen, C., Dubovik, O., Fuertes, D., Litvinov, P., Lapyonok, T., Lopatin, A., … Federspiel, C. (2020). Validation of GRASP algorithm product from POLDER/PARASOL data and assessment of multi-angular polarimetry potential for aerosol monitoring. *Earth System Science Data*, *12*(4), 3573–3620. doi:10.5194/essd-12-3573-2020

Chen, H., Xia, X., Wang, P., & Zhang, W. (2007). Ground-based measurements of aerosol optical properties and radiative forcing in North China. *China Particuology, 5*(3), 202–205.

Chen, J., Li, C., Ristovski, Z., Milic, A., Gu, Y., Islam, M. S., … Dumka, U. C. (2017). A review of biomass burning: Emissions and impacts on air quality, health and climate in China. *Science of The Total Environment, 579*, 1000–1034. doi:10.1016/j.scitotenv.2016.11.025

Chen, Q.-X., Han, X.-L., Gu, Y., Yuan, Y., Jiang, J. H., Yang, X.-B., … Tan, H.-P. (2022). Evaluation of MODIS, MISR, and VIIRS daily level-3 aerosol optical depth products over land. *Atmospheric Research*, *265*, 105810. doi:10.1016/j.atmosres.2021.105810

Cheng, L., Li, L., Chen, L., Hu, S., Yuan, L., Liu, Y., … Zhang, T. (2019). Spatiotemporal Variability and Influencing Factors of Aerosol Optical Depth over the Pan Yangtze River Delta during the 2014–2017 Period. *International Journal of Environmental Research and Public Health*, *16*(19), 3522. doi:10.3390/ijerph16193522

Chianese, E., Tirimberio, G., & Riccio, A. (2019). PM2.5 and PM10 in the urban area of Naples: chemical composition, chemical properties and influence of air masses origin. *Journal of Atmospheric Chemistry*, *76*(2), 151–169. doi:10.1007/s10874-019-09392-3

Chin, M., Diehl, T., Dubovik, O., Eck, T. F., Holben, B. N., Sinyuk, A., & Streets, D. G. (2009). *Light absorption by pollution, dust, and biomass burning aerosols: a global model study and evaluation with AERONET measurements*. In *Annales Geophysicae* (Vol. 27, pp. 3439–3464). Copernicus GmbH.

Choi, M., Lim, H., Kim, J., Lee, S., Eck, T. F., Holben, B. N., … Liu, H. (2019). Validation, comparison, and integration of GOCI, AHI, MODIS, MISR, and VIIRS aerosol optical depth over East Asia during the 2016 KORUS-AQ campaign. *Atmospheric Measurement Techniques*, *12*(8), 4619–4641. doi:10.5194/amt-12-4619-2019

Chowdhury, S., Dey, S., Ghosh, S., & Saud, T. (2016). Satellite-Based Estimates of Aerosol Washout and Recovery over India during Monsoon. *Aerosol and Air Quality Research*, *16*(5), 1302–1314. doi:10.4209/aaqr.2015.01.0018

Chu, D. A., Kaufman, Y. J., Ichoku, C., Remer, L. A., Tanré, D., & Holben, B. N. (2002). Validation of MODIS aerosol optical depth retrieval over land. *Geophysical Research Letters*, *29*(12), MOD2-1-MOD2-4. doi:10.1029/2001GL013205

Chudnovsky, A. A., Koutrakis, P., Kostinski, A., Proctor, S. P., & Garshick, E. (2017). Spatial and temporal variability in desert dust and anthropogenic pollution in Iraq, 1997–2010. *Journal of the Air & Waste Management Association*, *67*(1), 17–26.

Collins, W. D., Rasch, P. J., Eaton, B. E., Khattatov, B. V., Lamarque, J., & Zender, C. S. (2001). Simulating aerosols using a chemical transport model with assimilation of satellite aerosol retrievals: Methodology for INDOEX. *Journal of Geophysical Research: Atmospheres*, *106*(D7), 7313–7336.

Coskun, H. G., Alganci, U., & Usta, G. (2008). Analysis of land use change and urbanization in the Kucukcekmece water basin (Istanbul, Turkey) with temporal satellite data using remote sensing and GIS. *Sensors*, *8*(11), 7213–7223.

Dadashi-Roudbari, A., & Ahmadi, M. (2020). Evaluating temporal and spatial variability and trend of aerosol optical depth (550 nm) over Iran using data from MODIS on board the Terra and Aqua satellites. *Arabian Journal of Geosciences*, *13*, 1–23.

Dalponte, M., Bruzzone, L., & Gianelle, D. (2008). Fusion of Hyperspectral and LIDAR Remote Sensing Data for Classification of Complex Forest Areas. *IEEE Transactions on Geoscience and Remote Sensing*, *46*(5), 1416–1427. doi:10.1109/TGRS.2008.916480

Daughtry, C. S. T., Serbin, G., Reeves, J. B., Doraiswamy, P. C., & Hunt, E. R. (2010). Spectral Reflectance of Wheat Residue during Decomposition and Remotely Sensed Estimates of Residue Cover. *Remote Sensing*, *2*(2), 416–431. doi:10.3390/rs2020416

de Leeuw, G., Holzer-Popp, T., Bevan, S., Davies, W. H., Descloitres, J., Grainger, R. G., … Pinnock, S. (2015). Evaluation of seven European aerosol optical depth retrieval algorithms for climate analysis. *Remote Sensing of Environment*, *162*, 295–315. doi:10.1016/j.rse.2013.04.023

de Reus, M., Krejci, R., Williams, J., Fischer, H., Scheele, R., & Ström, J. (2001). Vertical and horizontal distributions of the aerosol number concentration and size distribution over the northern Indian Ocean. *Journal of Geophysical Research: Atmospheres*, *106*(D22), 28629–28641. doi:10.1029/2001JD900017

Delegido, J., Verrelst, J., Alonso, L., & Moreno, J. (2011). Evaluation of Sentinel-2 Red-Edge Bands for Empirical Estimation of Green LAI and Chlorophyll Content. *Sensors*, *11*(7), 7063–7081. doi:10.3390/s110707063

Demir, M., Küçükosmanoğlu, A., Hasdemir, M., Tolga, & Acar, H. (2009). Assessment of forest roads and firebreaks in Turkey. *African Journal of Biotechnology*, *8*, 4553–4561. Retrieved from ResearchGate

Deniz, A., Özdemir, E. T., Sezen, İ., & Coskun, M. (2013). Investigations of storms in the region of Marmara in Turkey. *Theoretical and Applied Climatology*, *112*(1–2), 61–71. doi:10.1007/s00704-012-0715-x

Deniz, C., & Durmusoglu, Y. (2008). Estimating shipping emissions in the region of the Sea of Marmara, Turkey. *Science of the Total Environment*, *390*(1), 255–261.

Denjean, C., Cassola, F., Mazzino, A., Triquet, S., Chevaillier, S., Grand, N., … Formenti, P. (2016). Size distribution and optical properties of mineral dust aerosols transported in the western Mediterranean. *Atmospheric Chemistry and Physics*, *16*(2), 1081–1104. doi:10.5194/acp-16-1081-2016

Deuzé, J., Bréon, F., Devaux, C., Goloub, P., Herman, M., Lafrance, B., … Perry, G. (2001). Remote sensing of aerosols over land surfaces from POLDER-ADEOS-1 polarized measurements. *Journal of Geophysical Research: Atmospheres*, *106*(D5), 4913–4926.

Dubovik, O., Holben, B., Eck, T. F., Smirnov, A., Kaufman, Y. J., King, M. D., … Slutsker, I. (2002). Variability of Absorption and Optical Properties of Key Aerosol Types Observed in Worldwide Locations. *Journal of the Atmospheric Sciences*, *59*(3), 590–608. doi:10.1175/1520-0469(2002)059<0590:VOAAOP>2.0.CO;2

Dubovik, O., & King, M. D. (2000). A flexible inversion algorithm for retrieval of aerosol optical properties from Sun and sky radiance measurements. *Journal of Geophysical Research: Atmospheres*, *105*(D16), 20673–20696. doi:10.1029/2000JD900282

Duyzer, J., van den Hout, D., Zandveld, P., & van Ratingen, S. (2015). Representativeness of air quality monitoring networks. *Atmospheric Environment*, *104*, 88–101. doi:10.1016/j.atmosenv.2014.12.067

Eck, T. F., Holben, B. N., Dubovik, O., Smirnov, A., Goloub, P., Chen, H. B., … Slutsker, I. (2005). Columnar aerosol optical properties at AERONET sites in central eastern Asia and aerosol transport to the tropical mid-Pacific. *Journal of Geophysical Research: Atmospheres*, *110*(D6). doi:10.1029/2004JD005274

Eck, T. F., Holben, B. N., Reid, J. S., Arola, A., Ferrare, R. A., Hostetler, C. A., … Sinyuk, A. (2014). Observations of rapid aerosol optical depth enhancements in the vicinity of polluted cumulus clouds. *Atmospheric Chemistry and Physics*, *14*(21), 11633–11656. doi:10.5194/acp-14-11633-2014

Elvan, O. D., Birben, Ü., Özkan, U. Y., Yıldırım, H. T., & Türker, Y. Ö. (2021). Forest fire and law: an analysis of Turkish forest fire legislation based on Food and Agriculture Organization criteria. *Fire Ecology*, *17*(1), 12. doi:10.1186/s42408-021-00102-7

EMRA (Energy Market Regulatory Authority). (2012). *Natural gas market 2011 sector report*.

Eskandari, I., Navid, H., & Rangzan, K. (2016). Evaluating spectral indices for determining conservation and conventional tillage systems in a vetch-wheat rotation. *International Soil and Water Conservation Research*, *4*(2), 93–98. doi:10.1016/j.iswcr.2016.04.002

Ettehadi Osgouei, P., & Kaya, S. (2017). Analysis of land cover/use changes using Landsat 5 TM data and indices. *Environmental Monitoring and Assessment*, *189*(4), 1–11.

Ettehadi Osgouei, P., Kaya, S., Sertel, E., & Alganci, U. (2019). Separating built-up areas from bare land in mediterranean cities using Sentinel-2A imagery. *Remote Sensing*, *11*(3), 345.

Ettehadi Osgouei, P., Roberts, G., Kaya, S., Bilal, M., Dash, J., & Sertel, E. (2022). Evaluation and comparison of MODIS and VIIRS aerosol optical depth (AOD) products over regions in the Eastern Mediterranean and the Black Sea. *Atmospheric Environment*, *268*, 118784. doi:10.1016/j.atmosenv.2021.118784

Fan, H., Zhao, C., & Yang, Y. (2020). A comprehensive analysis of the spatio-temporal variation of urban air pollution in China during 2014–2018. *Atmospheric Environment*, *220*, 117066. doi:10.1016/j.atmosenv.2019.117066

Fan, J., Wang, Y., Rosenfeld, D., & Liu, X. (2016). Review of Aerosol–Cloud Interactions: Mechanisms, Significance, and Challenges. *Journal of the Atmospheric Sciences*, *73*(11), 4221–4252. doi:10.1175/JAS-D-16-0037.1

Fan, Y., Sun, X., Huang, H., Ti, R., & Liu, X. (2021). The primary aerosol models and distribution characteristics over China based on the AERONET data. *Journal of Quantitative Spectroscopy and Radiative Transfer*, *275*, 107888. doi:10.1016/j.jqsrt.2021.107888

Farahat, A., El-Askary, H., Adetokunbo, P., & Fuad, A.-T. (2016). Analysis of aerosol absorption properties and transport over North Africa and the Middle East using AERONET data. *Annales Geophysicae*, *34*(11), 1031–1044. doi:10.5194/angeo-34-1031-2016

Feranec, J., Soukup, T., Hazeu, G., & Jaffrain, G. (2016). *European landscape dynamics: CORINE land cover data*. CRC Press.

Fernández, A. J., Molero, F., Salvador, P., Revuelta, A., Becerril-Valle, M., Gómez-Moreno, F. J., … Pujadas, M. (2017). Aerosol optical, microphysical and radiative forcing properties during variable intensity African dust events in the Iberian Peninsula. *Atmospheric Research*, *196*, 129–141. doi:10.1016/j.atmosres.2017.06.019

Filonchyk, M., & Hurynovich, V. (2020). Validation of MODIS Aerosol Products with AERONET Measurements of Different Land Cover Types in Areas over Eastern Europe and China. *Journal of Geovisualization and Spatial Analysis*, *4*(1), 10. doi:10.1007/s41651-020-00052-9

Filonchyk, M., Hurynovich, V., & Yan, H. (2020). Trends in aerosol optical properties over Eastern Europe based on MODIS-Aqua. *Geoscience Frontiers*, *11*(6), 2169–2181.

Floutsi, A. A., Korras-Carraca, M. B., Matsoukas, C., Hatzianastassiou, N., & Biskos, G. (2016). Climatology and trends of aerosol optical depth over the Mediterranean basin during the last 12years (2002–2014) based on Collection 006 MODIS-Aqua data. *Science of The Total Environment*, *551–552*, 292–303. doi:10.1016/j.scitotenv.2016.01.192

Foody, G. M. (2002). Status of land cover classification accuracy assessment. *Remote Sensing of Environment*, *80*(1), 185–201. doi:10.1016/S0034-4257(01)00295-4

Fotiadi, A., Hatzianastassiou, N., Drakakis, E., Matsoukas, C., Pavlakis, K. G., Hatzidimitriou, D., … Vardavas, I. (2006). Aerosol physical and optical properties in the Eastern Mediterranean Basin, Crete, from Aerosol Robotic Network data. *Atmospheric Chemistry and Physics*, *6*(12), 5399–5413. doi:10.5194/acp-6-5399-2006

Frampton, W. J., Dash, J., Watmough, G., & Milton, E. J. (2013). Evaluating the capabilities of Sentinel-2 for quantitative estimation of biophysical variables in vegetation. *ISPRS Journal of Photogrammetry and Remote Sensing*, *82*, 83–92. doi:10.1016/j.isprsjprs.2013.04.007

Funk, C., Peterson, P., Landsfeld, M., Pedreros, D., Verdin, J., Shukla, S., … Michaelsen, J. (2015). The climate hazards infrared precipitation with stations—a new environmental record for monitoring extremes. *Scientific Data*, *2*(1), 150066. doi:10.1038/sdata.2015.66

Galindo, N., Yubero, E., Clemente, Á., Nicolás, J. F., Varea, M., & Crespo, J. (2020). PM events and changes in the chemical composition of urban aerosols: A case study in the western Mediterranean. *Chemosphere*, *244*, 125520. doi:10.1016/j.chemosphere.2019.125520

García, O. E., Díaz, J. P., Expósito, F. J., Díaz, A. M., Dubovik, O., Derimian, Y., … Roger, J.-C. (2012). Shortwave radiative forcing and efficiency of key aerosol types using AERONET data. *Atmospheric Chemistry and Physics*, *12*(11), 5129–5145. doi:10.5194/acp-12-5129-2012

Georgoulias, A. K., Alexandri, G., Kourtidis, K. A., Lelieveld, J., Zanis, P., & Amiridis, V. (2016). Differences between the MODIS Collection 6 and 5.1 aerosol datasets over the greater Mediterranean region. *Atmospheric Environment*, *147*, 310–319. doi:10.1016/j.atmosenv.2016.10.014

Georgoulias, Aristeidis K., Alexandri, G., Kourtidis, K. A., Lelieveld, J., Zanis, P., Pöschl, U., … Tsikerdekis, A. (2016). Spatiotemporal variability and contribution of different aerosol types to the aerosol optical depth over the Eastern Mediterranean. *Atmospheric Chemistry and Physics*, *16*(21), 13853–13884. doi:10.5194/acp-16-13853-2016

Gharibzadeh, M., Alam, K., Bidokhti, A. A., Abedini, Y., & Masoumi, A. (2017). Radiative Effects and Optical Properties of Aerosol during Two Dust Events in 2013 over Zanjan, Iran. *Aerosol and Air Quality Research*, *17*(3), 888–898. doi:10.4209/aaqr.2016.04.0161

Giles, D. M., Holben, B. N., Eck, T. F., Sinyuk, A., Smirnov, A., Slutsker, I., … Schafer, J. S. (2012). An analysis of AERONET aerosol absorption properties and classifications representative of aerosol source regions. *Journal of Geophysical Research: Atmospheres*, *117*(D17). doi:10.1029/2012JD018127

Giles, D. M., Sinyuk, A., Sorokin, M. G., Schafer, J. S., Smirnov, A., Slutsker, I., … Campbell, J. R. (2019). Advancements in the Aerosol Robotic Network (AERONET) Version 3 database–automated near-real-time quality control algorithm with improved cloud screening for Sun photometer aerosol optical depth (AOD) measurements. *Atmospheric Measurement Techniques*, *12*(1), 169–209.

Gobbi, G. P., Kaufman, Y. J., Koren, I., & Eck, T. F. (2007). Classification of aerosol properties derived from AERONET direct sun data. *Atmospheric Chemistry and Physics*, *7*(2), 453–458. doi:10.5194/acp-7-453-2007

Gorai, A. K., Tchounwou, P. B., & Tuluri, F. (2016). Association between Ambient Air Pollution and Asthma Prevalence in Different Population Groups Residing in Eastern Texas, USA. *International Journal of Environmental Research and Public Health*, *13*(4), 378. doi:10.3390/ijerph13040378

Gordon, H. R., & Wang, M. (1994). Retrieval of water-leaving radiance and aerosol optical thickness over the oceans with SeaWiFS: a preliminary algorithm. *Applied Optics*, *33*(3), 443–452.

Grover, B. D., Kleinman, M., Eatough, N. L., Eatough, D. J., Hopke, P. K., Long, R. W., … Ambs, J. L. (2005). Measurement of total PM2.5 mass (nonvolatile plus semivolatile) with the Filter Dynamic Measurement System tapered element oscillating microbalance monitor. *Journal of Geophysical Research: Atmospheres*, *110*(D7). doi:10.1029/2004JD004995

Gueymard, C. A., & Yang, D. (2020). Worldwide validation of CAMS and MERRA-2 reanalysis aerosol optical depth products using 15 years of AERONET observations. *Atmospheric Environment*, *225*, 117216.

Guirado, C., Cuevas, E., Cachorro, V. E., Toledano, C., Alonso-Pérez, S., Bustos, J. J., … de Frutos, A. M. (2014). Aerosol characterization at the Saharan AERONET site Tamanrasset. *Atmospheric Chemistry and Physics*, *14*(21), 11753–11773. doi:10.5194/acp-14-11753-2014

Guo, J.-P., Zhang, X.-Y., Wu, Y.-R., Zhaxi, Y., Che, H.-Z., La, B., … Li, X.-W. (2011). Spatio-temporal variation trends of satellite-based aerosol optical depth in China during 1980–2008. *Atmospheric Environment*, *45*(37), 6802–6811. doi:10.1016/j.atmosenv.2011.03.068

Gupta, P., Levy, R., Mattoo, S., Remer, L. A., & Munchak, L. A. (2016). A surface reflectance scheme for retrieving aerosol optical depth over urban surfaces in MODIS Dark Target retrieval algorithm. *Atmospheric Measurement Techniques*, *9*(7), 3293–3308. doi:10.5194/amt-9-3293-2016

Gupta, P., Remer, L. A., Levy, R., & Mattoo, S. (2018). Validation of MODIS 3 km land aerosol optical depth from NASA's EOS Terra and Aqua missions. *Atmospheric Measurement Techniques*, *11*(5), 3145–3159. doi:10.5194/amt-11-3145-2018

Haider, A., Bashir, A., & Husnain, M. I. ul. (2020). Impact of agricultural land use and economic growth on nitrous oxide emissions: Evidence from developed and developing countries. *Science of The Total Environment*, *741*, 140421. doi:10.1016/j.scitotenv.2020.140421

Hansen, P. M., & Schjoerring, J. K. (2003). Reflectance measurement of canopy biomass and nitrogen status in wheat crops using normalized difference vegetation indices and partial least squares regression. *Remote Sensing of Environment*, *86*(4), 542–553. doi:10.1016/S0034-4257(03)00131-7

He, C., Shi, P., Xie, D., & Zhao, Y. (2010). Improving the normalized difference built-up index to map urban built-up areas using a semiautomatic segmentation approach. *Remote Sensing Letters*, *1*(4), 213–221.

He, H., Wang, Y., Ma, Q., Ma, J., Chu, B., Ji, D., … Hao, J. (2014). Mineral dust and NOx promote the conversion of SO2 to sulfate in heavy pollution days. *Scientific Reports*, *4*(1), 4172. doi:10.1038/srep04172

He, J., Gong, S., Yu, Y., Yu, L., Wu, L., Mao, H., … Li, R. (2017). Air pollution characteristics and their relation to meteorological conditions during 2014–2015 in major Chinese cities. *Environmental Pollution*, *223*, 484–496. doi:10.1016/j.envpol.2017.01.050

He, L., Wang, L., Lin, A., Zhang, M., Bilal, M., & Wei, J. (2018). Performance of the NPP-VIIRS and aqua-MODIS Aerosol Optical Depth Products over the Yangtze River Basin. *Remote Sensing*, *10*(1), 117. doi:10.3390/rs10010117

He, Q., Zhang, M., & Huang, B. (2016). Spatio-temporal variation and impact factors analysis of satellite-based aerosol optical depth over China from 2002 to 2015. *Atmospheric Environment*, *129*, 79–90. doi:10.1016/j.atmosenv.2016.01.002

He, Q., Zhang, M., Huang, B., & Tong, X. (2017). MODIS 3 km and 10 km aerosol optical depth for China: Evaluation and comparison. *Atmospheric Environment*, *153*, 150–162. doi:10.1016/j.atmosenv.2017.01.023

Herman, J. R., Bhartia, P. K., Torres, O., Hsu, C., Seftor, C., & Celarier, E. (1997). Global distribution of UV-absorbing aerosols from Nimbus 7/TOMS data. *Journal of Geophysical Research: Atmospheres*, *102*(D14), 16911–16922. doi:10.1029/96JD03680

Hoff, R. M., & Christopher, S. A. (2009). Remote Sensing of Particulate Pollution from Space: Have We Reached the Promised Land? *Journal of the Air & Waste Management Association*, *59*(6), 645–675. doi:10.3155/1047-3289.59.6.645

Holben, B. N., Eck, T. F., Slutsker, I., Tanré, D., Buis, J. P., Setzer, A., … Smirnov, A. (1998). AERONET—A Federated Instrument Network and Data Archive for Aerosol Characterization. *Remote Sensing of Environment*, *66*(1), 1–16. doi:10.1016/S0034-4257(98)00031-5

Hsu, N. C., Jeong, M.-J., Bettenhausen, C., Sayer, A. M., Hansell, R., Seftor, C. S., … Tsay, S.-C. (2013). Enhanced Deep Blue aerosol retrieval algorithm: The second generation. *Journal of Geophysical Research: Atmospheres*, *118*(16), 9296–9315. doi:10.1002/jgrd.50712

Hsu, N. C., Lee, J., Sayer, A. M., Kim, W., Bettenhausen, C., & Tsay, S.-C. (2019). VIIRS Deep Blue Aerosol Products Over Land: Extending the EOS Long-Term Aerosol Data Records. *Journal of Geophysical Research: Atmospheres*, *124*(7), 4026–4053. doi:10.1029/2018JD029688

Hsu, N. C., Tsay, S.-C., King, M. D., & Herman, J. R. (2004). Aerosol properties over bright-reflecting source regions. *IEEE Transactions on Geoscience and Remote Sensing*, *42*(3), 557–569. doi:10.1109/TGRS.2004.824067

Hsu, N. C., Tsay, S.-C., King, M. D., & Herman, J. R. (2006). Deep Blue Retrievals of Asian Aerosol Properties During ACE-Asia. *IEEE Transactions on Geoscience and Remote Sensing*, *44*(11), 3180–3195. doi:10.1109/TGRS.2006.879540

Huang, H., Liu, J., & Pan, Y. (2012). Semi-Supervised Marginal Fisher Analysis for Hyperspectral Image Classification. *ISPRS Annals of the Photogrammetry, Remote Sensing and Spatial Information Sciences*, *I–3*, 377–382. doi:10.5194/isprsannals-I-3-377-2012

Huang, J., Kondragunta, S., Laszlo, I., Liu, H., Remer, L. A., Zhang, H., … Petrenko, M. (2016). Validation and expected error estimation of Suomi-NPP VIIRS aerosol optical thickness and Ångström exponent with AERONET. *Journal of Geophysical Research: Atmospheres*, *121*(12), 7139–7160. doi:10.1002/2016JD024834

Huang, K., Fu, J. S., Hsu, N. C., Gao, Y., Dong, X., Tsay, S.-C., & Lam, Y. F. (2013). Impact assessment of biomass burning on air quality in Southeast and East Asia during BASE-ASIA. *Atmospheric Environment*, *78*, 291–302. doi:10.1016/j.atmosenv.2012.03.048

Huang, Y., Zhao, C., Yang, H., Song, X., Chen, J., & Li, Z. (2017). Feature Selection Solution with High Dimensionality and Low-Sample Size for Land Cover Classification in Object-Based Image Analysis. *Remote Sensing*, *9*(9), 939. doi:10.3390/rs9090939

Hughes, G. (1968). On the mean accuracy of statistical pattern recognizers. *IEEE Transactions on Information Theory*, *14*(1), 55–63. doi:10.1109/TIT.1968.1054102

Husar, R. B., Prospero, J. M., & Stowe, L. L. (1997). Characterization of tropospheric aerosols over the oceans with the NOAA advanced very high resolution radiometer optical thickness operational product. *Journal of Geophysical Research: Atmospheres*, *102*(D14), 16889–16909.

Ichoku, C., Chu, D. A., Mattoo, S., Kaufman, Y. J., Remer, L. A., Tanré, D., … Holben, B. N. (2002). A spatio-temporal approach for global validation and analysis of MODIS aerosol products. *Geophysical Research Letters*, *29*(12), MOD1-1-MOD1-4. doi:10.1029/2001GL013206

Ichoku, C., Remer, L., & Eck, T. (2004). Quantitative evaluation and intercomparison of morning and afternoon MODIS aerosol measurements from Terra and Aqua Satellites. Retrieved from ResearchGate

Immitzer, M., Vuolo, F., & Atzberger, C. (2016). First experience with Sentinel-2 data for crop and tree species classifications in central Europe. *Remote Sensing*, *8*(3), 166.

IQAir, A. (2018). *AIR QUALITY REPORT 2018*. Retrieved from file:///C:/Users/Asus/Documents/world-air-quality-report-2018-en.pdf

IQAir, A. (2020). *World Air Quality Report*. Retrieved from https://www.greenpeace.org/static/planet4-romania-stateless/2021/03/d8050eab-2020-world_air_quality_report.pdf

Jackson, J. M., Liu, H., Laszlo, I., Kondragunta, S., Remer, L. A., Huang, J., & Huang, H.-C. (2013). Suomi-NPP VIIRS aerosol algorithms and data products. *Journal of Geophysical Research: Atmospheres*, *118*(22), 12,673-12,689. doi:10.1002/2013JD020449

Jethva, H., Torres, O., & Yoshida, Y. (2019). Accuracy assessment of MODIS land aerosol optical thickness algorithms using AERONET measurements over North America. *Atmospheric Measurement Techniques*, *12*(8), 4291–4307. doi:10.5194/amt-12-4291-2019

Jia, K., Wei, X., Gu, X., Yao, Y., Xie, X., & Li, B. (2014). Land cover classification using Landsat 8 Operational Land Imager data in Beijing, China. *Geocarto International*, *29*(8), 941–951. doi:10.1080/10106049.2014.894586

Jieli, C., Manchun, L., Yongxue, L., Chenglei, S., & Wei, H. (2010). *Extract residential areas automatically by New Built-up Index*. In *2010 18th International Conference on Geoinformatics* (pp. 1–5). doi:10.1109/GEOINFORMATICS.2010.5567823

Jo, S., Kim, Y.-J., Park, K. W., Hwang, Y. S., Lee, S. H., Kim, B. J., & Chung, S. J. (2021). Association of NO2 and Other Air Pollution Exposures With the Risk of Parkinson Disease. *JAMA Neurology*, *78*(7), 800–808. doi:10.1001/jamaneurol.2021.1335

Kabatas, B., Unal, A., Pierce, R. B., Kindap, T., & Pozzoli, L. (2014). The contribution of Saharan dust in PM10 concentration levels in Anatolian Peninsula of Turkey. *Science of The Total Environment*, *488–489*, 413–421. doi:10.1016/j.scitotenv.2013.12.045

Kahn, R. A., Gaitley, B. J., Martonchik, J. V., Diner, D. J., Crean, K. A., & Holben, B. (2005). Multiangle Imaging Spectroradiometer (MISR) global aerosol optical depth validation based on 2 years of coincident Aerosol Robotic Network (AERONET) observations. *Journal of Geophysical Research: Atmospheres*, *110*(D10). doi:10.1029/2004JD004706

Kahya, C., Balcik, F., Oztaner, Y. B., Ozcomak, D., & Seker, D. (2017). Spatio-temporal analysis of PM2.5 over Marmara region, Turkey. *Resenius Environmental Bulletin*, *26*, 310–317. Retrieved from ResearchGate

Kambezidis, H. D., & Kaskaoutis, D. G. (2008). Aerosol climatology over four AERONET sites: An overview. *Atmospheric Environment*, *42*(8), 1892–1906. doi:10.1016/j.atmosenv.2007.11.013

Karagulian, F., Barbiere, M., Kotsev, A., Spinelle, L., Gerboles, M., Lagler, F., … Borowiak, A. (2019). Review of the Performance of Low-Cost Sensors for Air Quality Monitoring. *Atmosphere*, *10*(9), 506. doi:10.3390/atmos10090506

Kaskaoutis, D. G., Kharol, S. K., Sifakis, N., Nastos, P. T., Sharma, A. R., Badarinath, K. V. S., & Kambezidis, H. D. (2011). Satellite monitoring of the biomass-burning aerosols during the wildfires of August 2007 in Greece: Climate implications. *Atmospheric Environment*, *45*(3), 716–726. doi:10.1016/j.atmosenv.2010.09.043

Kaskaoutis, D. G., Sinha, P. R., Vinoj, V., Kosmopoulos, P. G., Tripathi, S. N., Misra, A., … Singh, R. P. (2013). Aerosol properties and radiative forcing over Kanpur during severe aerosol loading conditions. *Atmospheric Environment*, *79*, 7–19. doi:10.1016/j.atmosenv.2013.06.020

Kaskaoutis, Dimitris G., Grivas, G., Liakakou, E., Kalivitis, N., Kouvarakis, G., Stavroulas, I., … Gerasopoulos, E. (2021). Assessment of the COVID-19 lockdown effects on spectral aerosol scattering and absorption properties in Athens, Greece. *Atmosphere*, *12*(2), 231.

Kasparoglu, S., Incecik, S., & Topcu, S. (2018). Spatial and temporal variation of O3, NO and NO2 concentrations at rural and urban sites in Marmara Region of Turkey. *Atmospheric Pollution Research*, *9*(6), 1009–1020.

Katra, I. (2020). Soil Erosion by Wind and Dust Emission in Semi-Arid Soils Due to Agricultural Activities. *Agronomy*, *10*(1), 89. doi:10.3390/agronomy10010089

Kaufman, Y. J., Tanré, D., Gordon, H. R., Nakajima, T., Lenoble, J., Frouin, R., … Teillet, P. M. (1997). Passive remote sensing of tropospheric aerosol and atmospheric correction for the aerosol effect. *Journal of Geophysical Research: Atmospheres*, *102*(D14), 16815–16830. doi:10.1029/97JD01496

Kaufman, Y. J., Tanré, D., Remer, L. A., Vermote, E. F., Chu, A., & Holben, B. N. (1997). Operational remote sensing of tropospheric aerosol over land from EOS moderate resolution imaging spectroradiometer. *Journal of Geophysical Research: Atmospheres*, *102*(D14), 17051–17067. doi:10.1029/96JD03988

Kaufman, Y.J., Remer, L. A., Tanre, D., Li, R.-R., Kleidman, R., Mattoo, S., … Koren, I. (2005). A critical examination of the residual cloud contamination and diurnal sampling effects on MODIS estimates of aerosol over ocean. *IEEE Transactions on Geoscience and Remote Sensing*, *43*(12), 2886–2897. doi:10.1109/TGRS.2005.858430

Kaufman, Yoram J., Tanré, D., & Boucher, O. (2002). A satellite view of aerosols in the climate system. *Nature*, *419*(6903), 215–223. doi:10.1038/nature01091

Kawamura, M., Jayamanna, S., & Tsujiko, Y. (1996). Relation between Social and Environmental Conditions in Colombo Sri Lanka and the Urban Index Estimated by Satellite Remote Sensing Data. *International Archives of Photogrammetry and Remote Sensing*, *31*, 321–326.

Kaya, S. (2007). Multitemporal analysis of rapid urban growth in Istanbul using remotely sensed data. *Environmental Engineering Science*, *24*(2), 228–233.

Khalid, B., Khalid, A., Muslim, S., Habib, A., Khan, K., Alvim, D. S., … Chen, B. (2021). Estimation of aerosol optical depth in relation to meteorological parameters over eastern and western routes of China Pakistan economic corridor. *Journal of Environmental Sciences*, *99*, 28–39. doi:10.1016/j.jes.2020.04.045

Khan, R., Kumar, K. R., Zhao, T., & Ali, G. (2020). The contribution of different aerosol types to direct radiative forcing over distinct environments of Pakistan inferred from the AERONET data. *Environmental Research Letters*, *15*(11), 114062. doi:10.1088/1748-9326/aba2a6

Kim, D., Chin, M., Yu, H., Eck, T. F., Sinyuk, A., Smirnov, A., & Holben, B. N. (2011). Dust optical properties over North Africa and Arabian Peninsula derived from the AERONET dataset. *Atmospheric Chemistry and Physics*, *11*(20), 10733–10741.

King, M. D., Kaufman, Y. J., Tanré, D., & Nakajima, T. (1999). Remote Sensing of Tropospheric Aerosols from Space: Past, Present, and Future. *Bulletin of the American Meteorological Society*, *80*(11), 2229–2260. doi:10.1175/1520-0477(1999)080<2229:RSOTAF>2.0.CO;2

Kleidman, R. G., Smirnov, A., Levy, R., Mattoo, S., & Tanre, D. (2012). Evaluation and Wind Speed Dependence of MODIS Aerosol Retrievals Over Open Ocean. *IEEE Transactions on Geoscience and Remote Sensing*, *50*(2), 429–435. doi:10.1109/TGRS.2011.2162073

Koven, C. D., & Fung, I. (2006). Inferring dust composition from wavelength-dependent absorption in Aerosol Robotic Network (AERONET) data. *Journal of Geophysical Research: Atmospheres*, *111*(D14).

Kubilay, N., Cokacar, T., & Oguz, T. (2003). Optical properties of mineral dust outbreaks over the northeastern Mediterranean. *Journal of Geophysical Research: Atmospheres*, *108*(D21).

Kulshrestha, A., Satsangi, P. G., Masih, J., & Taneja, A. (2009). Metal concentration of PM2.5 and PM10 particles and seasonal variations in urban and rural environment of Agra, India. *Science of The Total Environment*, *407*(24), 6196–6204. doi:10.1016/j.scitotenv.2009.08.050

Kumar, K. Raghavendra, Kang, N., & Yin, Y. (2018). Classification of key aerosol types and their frequency distributions based on satellite remote sensing data at an industrially polluted city in the Yangtze River Delta, China. *International Journal of Climatology*, *38*(1), 320–336. doi:10.1002/joc.5178

Kumar, Kanike Raghavendra, Sivakumar, V., Reddy, R. R., Gopal, K. R., & Adesina, A. J. (2014). Identification and classification of different aerosol types over a subtropical rural site in Mpumalanga, South Africa: Seasonal variations as retrieved from the AERONET Sunphotometer. *Aerosol and Air Quality Research*, *14*(1), 108–123.

Lapworth, A. (2005). The diurnal variation of the marine surface wind in an offshore flow. *Quarterly Journal of the Royal Meteorological Society*, *131*(610), 2367–2387. doi:10.1256/qj.04.161

Lee, Jaehwa, Kim, J., Song, C. H., Kim, S. B., Chun, Y., Sohn, B. J., & Holben, B. N. (2010). Characteristics of aerosol types from AERONET sunphotometer measurements. *Atmospheric Environment*, *44*(26), 3110–3117. doi:https://doi.org/10.1016/j.atmosenv.2010.05.035

Lee, Jeffrey, Gill, T. E., Mulligan, K. R., Dominguez Acosta, M., & Perez, A. E. (2009). Land use/land cover and point sources of the 15 December 2003 dust storm in southwestern North America. *Geomorphology*, *105*(1), 18–27. doi:10.1016/j.geomorph.2007.12.016

Lee, S., Adhikari, A., Grinshpun, S. A., McKay, R., Shukla, R., & Reponen, T. (2006). Personal Exposure to Airborne Dust and Microorganisms in Agricultural Environments. *Journal of Occupational and Environmental Hygiene*, *3*(3), 118–130. doi:10.1080/15459620500524607

Levy, R., Mattoo, S., Munchak, L. A., Remer, L. A., Sayer, A. M., Patadia, F., & Hsu, N. C. (2013). The Collection 6 MODIS aerosol products over land and ocean. *Atmospheric Measurement Techniques*, *6*(11), 2989–3034. doi:10.5194/amt-6-2989-2013

Levy, R., Mattoo, S., Sawyer, V., Shi, Y., Colarco, P. R., Lyapustin, A. I., … Remer, L. A. (2018). Exploring systematic offsets between aerosol products from the two MODIS sensors. *Atmospheric Measurement Techniques*, *11*(7), 4073–4092. doi:10.5194/amt-11-4073-2018

Levy, R., Remer, L. A., & Dubovik, O. (2007). Global aerosol optical properties and application to Moderate Resolution Imaging Spectroradiometer aerosol retrieval over land. *Journal of Geophysical Research: Atmospheres*, *112*(D13). doi:10.1029/2006JD007815

Levy, R., Remer, L. A., Kleidman, R. G., Mattoo, S., Ichoku, C., Kahn, R., & Eck, T. F. (2010). Global evaluation of the Collection 5 MODIS dark-target aerosol products over land. *Atmospheric Chemistry and Physics*, *10*(21), 10399–10420. doi:10.5194/acp-10-10399-2010

Levy, R., Remer, L. A., Mattoo, S., Vermote, E. F., & Kaufman, Y. J. (2007). Second-generation operational algorithm: Retrieval of aerosol properties over land from inversion of Moderate Resolution Imaging Spectroradiometer spectral reflectance. *Journal of Geophysical Research: Atmospheres*, *112*(D13). doi:10.1029/2006JD007811

Li, C., Wang, J., Wang, L., Hu, L., & Gong, P. (2014). Comparison of Classification Algorithms and Training Sample Sizes in Urban Land Classification with Landsat Thematic Mapper Imagery. *Remote Sensing*, *6*(2), 964–983. doi:10.3390/rs6020964

Li, Hui, Wang, C., Zhong, C., Su, A., Xiong, C., Wang, J., & Liu, J. (2017). Mapping urban bare land automatically from Landsat imagery with a simple index. *Remote Sensing*, *9*(3), 249.

Li, Huidong, Wolter, M., Wang, X., & Sodoudi, S. (2018). Impact of land cover data on the simulation of urban heat island for Berlin using WRF coupled with bulk approach of Noah-LSM. *Theoretical and Applied Climatology*, *134*(1), 67–81. doi:10.1007/s00704-017-2253-z

Li, J., Carlson, B. E., Dubovik, O., & Lacis, A. A. (2014). Recent trends in aerosol optical properties derived from AERONET measurements. *Atmospheric Chemistry and Physics*, *14*(22), 12271–12289. doi:10.5194/acp-14-12271-2014

Li, L., & Wang, Y. (2014). What drives the aerosol distribution in Guangdong - the most developed province in Southern China? *Scientific Reports*, *4*(1), 5972. doi:10.1038/srep05972

Li, R.-R., Kaufman, Y., Gao, B.-C., & Davis, C. (2003). Remote sensing of suspended sediments and shallow coastal waters. *Geoscience and Remote Sensing, IEEE Transactions On*, *41*, 559–566. doi:10.1109/TGRS.2003.810227

Li, X., Jin, L., & Kan, H. (2019). Air pollution: a global problem needs local fixes. *Nature*, *570*(7762), 437–439. doi:10.1038/d41586-019-01960-7

Limbacher, J. A., & Kahn, R. A. (2019). Updated MISR over-water research aerosol retrieval algorithm – Part 2: A multi-angle aerosol retrieval algorithm for shallow, turbid, oligotrophic, and eutrophic waters. *Atmospheric Measurement Techniques*, *12*(1), 675–689. doi:10.5194/amt-12-675-2019

Lin, C., Labzovskii, L. D., Leung Mak, H. W., Fung, J. C. H., Lau, A. K. H., Kenea, S. T., … Ma, J. (2020). Observation of PM2.5 using a combination of satellite remote sensing and low-cost sensor network in Siberian urban areas with limited reference monitoring. *Atmospheric Environment*, *227*, 117410. doi:10.1016/j.atmosenv.2020.117410

Liu, H., Remer, L. A., Huang, J., Huang, H.-C., Kondragunta, S., Laszlo, I., … Jackson, J. M. (2014). Preliminary evaluation of S-NPP VIIRS aerosol optical thickness. *Journal of Geophysical Research: Atmospheres*, *119*(7), 3942–3962. doi:10.1002/2013JD020360

Liu, N., Zou, B., Feng, H., Wang, W., Tang, Y., & Liang, Y. (2019). Evaluation and comparison of multiangle implementation of the atmospheric correction algorithm, Dark Target, and Deep Blue aerosol products over China. *Atmospheric Chemistry and Physics*, *19*(12), 8243–8268. doi:10.5194/acp-19-8243-2019

Logothetis, S.-A., Salamalikis, V., & Kazantzidis, A. (2020). Aerosol classification in Europe, Middle East, North Africa and arabian Peninsula based on AERONET version 3. *Atmospheric Research*, *239*, 104893.

Lu, D., & Weng, Q. (2007). A survey of image classification methods and techniques for improving classification performance. *International Journal of Remote Sensing*, *28*(5), 823–870. doi:10.1080/01431160600746456

Lu, Y., Yuan, J., Lu, X., Su, C., Zhang, Y., Wang, C., … Sweijd, N. (2018). Major threats of pollution and climate change to global coastal ecosystems and enhanced management for sustainability. *Environmental Pollution*, *239*, 670–680. doi:10.1016/j.envpol.2018.04.016

Luo, Y., Zheng, X., Zhao, T., & Chen, J. (2014). A climatology of aerosol optical depth over China from recent 10 years of MODIS remote sensing data. *International Journal of Climatology*, *34*(3), 863–870. doi:10.1002/joc.3728

Luyssaert, S., Jammet, M., Stoy, P. C., Estel, S., Pongratz, J., Ceschia, E., … Dolman, A. J. (2014). Land management and land-cover change have impacts of similar magnitude on surface temperature. *Nature Climate Change*, *4*(5), 389–393. doi:10.1038/nclimate2196

Lyamani, H., Olmo, F., & Alados-Arboledas, L. (2005). Saharan dust outbreak over southeastern Spain as detected by sun photometer. *Atmospheric Environment*, *39*(38), 7276–7284.

Lyapustin, A., Korkin, S., Wang, Y., Quayle, B., & Laszlo, I. (2012). Discrimination of biomass burning smoke and clouds in MAIAC algorithm. *Atmospheric Chemistry and Physics*, *12*(20), 9679–9686. doi:10.5194/acp-12-9679-2012

Lyapustin, A., Wang, Y., Laszlo, I., Kahn, R., Korkin, S., Remer, L., … Reid, J. S. (2011). Multiangle implementation of atmospheric correction (MAIAC): 2. Aerosol algorithm. *Journal of Geophysical Research: Atmospheres*, *116*(D3). doi:10.1029/2010JD014986

Lyapustin, A., Wang, Y., Laszlo, I., & Korkin, S. (2012). Improved cloud and snow screening in MAIAC aerosol retrievals using spectral and spatial analysis. *Atmospheric Measurement Techniques*, *5*(4), 843–850. doi:10.5194/amt-5-843-2012

Lyapustin, A., Wang, Y., Xiong, X., Meister, G., Platnick, S., Levy, R., … Angal, A. (2014). Scientific impact of MODIS C5 calibration degradation and C6+ improvements. *Atmospheric Measurement Techniques*, *7*(12), 4353–4365. doi:10.5194/amt-7-4353-2014

Lyapustin, Alexei, Martonchik, J., Wang, Y., Laszlo, I., & Korkin, S. (2011a). Multiangle implementation of atmospheric correction (MAIAC): 1. Radiative transfer basis and look-up tables. *Journal of Geophysical Research: Atmospheres*, *116*(D3). doi:10.1029/2010JD014985

Lyapustin, Alexei, Wang, Y., Korkin, S., & Huang, D. (2018). MODIS Collection 6 MAIAC algorithm. *Atmospheric Measurement Techniques*, *11*(10), 5741–5765. doi:10.5194/amt-11-5741-2018

Ma, X., Xiao, Z., He, L., Shi, Z., Cao, Y., Tian, Z., … Liu, J. (2019). Chemical Composition and Source Apportionment of PM2.5 in Urban Areas of Xiangtan, Central South China. *International Journal of Environmental Research and Public Health*, *16*(4), 539. doi:10.3390/ijerph16040539

Maffia, J., Dinuccio, E., Amon, B., & Balsari, P. (2020). PM emissions from open field crop management: Emission factors, assessment methods and mitigation measures – A review. *Atmospheric Environment*, *226*, 117381. doi:10.1016/j.atmosenv.2020.117381

Maghrabi, A. H., & Alotaibi, R. N. (2018). Long-term variations of AOD from an AERONET station in the central Arabian Peninsula. *Theoretical and Applied Climatology*, *134*(3–4), 1015–1026. doi:10.1007/s00704-017-2328-x

Mahmood, R., Pielke Sr., R. A., Hubbard, K. G., Niyogi, D., Dirmeyer, P. A., McAlpine, C., … Fall, S. (2014). Land cover changes and their biogeophysical effects on climate. *International Journal of Climatology*, *34*(4), 929–953. doi:10.1002/joc.3736

Manisalidis, I., Stavropoulou, E., Stavropoulos, A., & Bezirtzoglou, E. (2020). Environmental and Health Impacts of Air Pollution: A Review. *Frontiers in Public Health*, *8*. Retrieved from Frontiers

Mao, Q., Zhang, H., Chen, Q., Huang, C., & Yuan, Y. (2019). Satellite-based assessment of direct aerosol radiative forcing using a look-up table established through AERONET observations. *Infrared Physics & Technology*, *102*, 103017.

Martin, F., Fileni, L., Palomino, I., Vivanco, M. G., & Garrido, J. L. (2014). Analysis of the spatial representativeness of rural background monitoring stations in Spain. *Atmospheric Pollution Research*, *5*(4), 779–788. doi:10.5094/APR.2014.087

Martins, J. V., Tanré, D., Remer, L., Kaufman, Y., Mattoo, S., & Levy, R. (2002). MODIS Cloud screening for remote sensing of aerosols over oceans using spatial variability. *Geophysical Research Letters*, *29*(12), MOD4-1-MOD4-4. doi:10.1029/2001GL013252

Maulik, U., & Chakraborty, D. (2017). Remote Sensing Image Classification: A survey of support-vector-machine-based advanced techniques. *IEEE Geoscience and Remote Sensing Magazine*, *5*(1), 33–52. doi:10.1109/MGRS.2016.2641240

McFEETERS, S. K. (1996). The use of the Normalized Difference Water Index (NDWI) in the delineation of open water features. *International Journal of Remote Sensing*, *17*(7), 1425–1432. doi:10.1080/01431169608948714

McPhetres, A., & Aggarwal, S. (2018). An Evaluation of MODIS-Retrieved Aerosol Optical Depth over AERONET Sites in Alaska. *Remote Sensing*, *10*(9), 1384. doi:10.3390/rs10091384

Mentese, S., Bakar, C., Mirici, N. A., Oymak, S., & Otkun, M. T. (2018). Associations between respiratory health and ambient air quality in Canakkale, Turkey: a long-term cohort study. *Environmental Science and Pollution Research*, *25*(13), 12915–12931. doi:10.1007/s11356-018-1307-9

Mhawish, A., Banerjee, T., Broday, D. M., Misra, A., & Tripathi, S. N. (2017). Evaluation of MODIS Collection 6 aerosol retrieval algorithms over Indo-Gangetic Plain: Implications of aerosols types and mass loading. *Remote Sensing of Environment*, *201*, 297–313. doi:10.1016/j.rse.2017.09.016

Mhawish, A., Banerjee, T., Sorek-Hamer, M., Lyapustin, A., Broday, D. M., & Chatfield, R. (2019). Comparison and evaluation of MODIS Multi-angle Implementation of Atmospheric Correction (MAIAC) aerosol product over South Asia. *Remote Sensing of Environment*, *224*, 12–28. doi:10.1016/j.rse.2019.01.033

Misra, A., Jayaraman, A., & Ganguly, D. (2015). Validation of Version 5.1 MODIS Aerosol Optical Depth (Deep Blue Algorithm and Dark Target Approach) over a Semi-Arid Location in Western India. *Aerosol and Air Quality Research*, *15*(1), 252–262. doi:10.4209/aaqr.2014.01.0004

Moulin, C., Lambert, C. E., Dayan, U., Masson, V., Ramonet, M., Bousquet, P., … Marticorena, B. (1998). Satellite climatology of African dust transport in the Mediterranean atmosphere. *Journal of Geophysical Research: Atmospheres*, *103*(D11), 13137–13144.

Mountrakis, G., Im, J., & Ogole, C. (2011). Support vector machines in remote sensing: A review. *ISPRS Journal of Photogrammetry and Remote Sensing*, *66*(3), 247–259. doi:10.1016/j.isprsjprs.2010.11.001

Munchak, L. A., Levy, R., Mattoo, S., Remer, L. A., Holben, B. N., Schafer, J. S., … Ferrare, R. A. (2013). MODIS 3 km aerosol product: applications over land in an urban/suburban region. *Atmospheric Measurement Techniques*, *6*(7), 1747–1759. doi:10.5194/amt-6-1747-2013

Murari, V., Kumar, M., Barman, S. C., & Banerjee, T. (2015). Temporal variability of MODIS aerosol optical depth and chemical characterization of airborne particulates in Varanasi, India. *Environmental Science and Pollution Research*, *22*(2), 1329–1343. doi:10.1007/s11356-014-3418-2

Myhre, G., Stordal, F., Johnsrud, M., Diner, D. J., Geogdzhayev, I. V., Haywood, J. M., … Wang, M. (2005). Intercomparison of satellite retrieved aerosol optical depth over ocean during the period September 1997 to December 2000. *Atmos. Chem. Phys.*, 23. Retrieved from Zotero

Nahar, N., Mahiuddin, S., & Hossain, Z. (2021). The Severity of Environmental Pollution in the Developing Countries and Its Remedial Measures. *Earth*, *2*(1), 124–139. doi:10.3390/earth2010008

Ng, D., Li, R., Raghavan, S., & Liong, S.-Y. (2017). Investigating the relationship between Aerosol Optical Depth and Precipitation over Southeast Asia with Relative Humidity as an influencing factor. *Scientific Reports*, *7*. doi:10.1038/s41598-017-10858-1

Ngo, N. S., Asseko, S. V. J., Ebanega, M. O., Allo'o Allo'o, S. M., & Hystad, P. (2019). The relationship among PM2.5, traffic emissions, and socioeconomic status: Evidence from Gabon using low-cost, portable air quality monitors. *Transportation Research Part D: Transport and Environment*, *68*, 2–9. doi:10.1016/j.trd.2018.01.029

Nichol, J. E., & Bilal, M. (2016). Validation of MODIS 3 km Resolution Aerosol Optical Depth Retrievals Over Asia. *Remote Sensing*, *8*(4), 328. doi:10.3390/rs8040328

Nowak, D. J., Hirabayashi, S., Doyle, M., McGovern, M., & Pasher, J. (2018). Air pollution removal by urban forests in Canada and its effect on air quality and human health. *Urban Forestry & Urban Greening*, *29*, 40–48. doi:10.1016/j.ufug.2017.10.019

Omar, A. H., Won, J.-G., Winker, D. M., Yoon, S.-C., Dubovik, O., & McCormick, M. P. (2005). Development of global aerosol models using cluster analysis of Aerosol Robotic Network (AERONET) measurements. *Journal of Geophysical Research: Atmospheres*, *110*(D10). doi:10.1029/2004JD004874

Ozdemir, E., Tuna Tuygun, G., & Elbir, T. (2020). Application of aerosol classification methods based on AERONET version 3 product over eastern Mediterranean and Black Sea. *Atmospheric Pollution Research*, *11*(12), 2226–2243. doi:10.1016/j.apr.2020.06.008

Ozturk, H. H., & Bascetincelik, A. (2006). Energy Exploitation of Agricultural Biomass Potential in Turkey. *Energy Exploration & Exploitation*, *24*(4), 313–330. doi:10.1260/014459806779398802

Pérez-Ramírez, D., Andrade-Flores, M., Eck, T. F., Stein, A. F., O'Neill, N. T., Lyamani, H., … Alados-Arboledas, L. (2017). Multi year aerosol characterization in the tropical Andes and in adjacent Amazonia using AERONET measurements. *Atmospheric Environment*, *166*, 412–432. doi:10.1016/j.atmosenv.2017.07.037

Popoola, O. A. M., Carruthers, D., Lad, C., Bright, V. B., Mead, M. I., Stettler, M. E. J., … Jones, R. L. (2018). Use of networks of low cost air quality sensors to quantify air quality in urban settings. *Atmospheric Environment*, *194*, 58–70. doi:10.1016/j.atmosenv.2018.09.030

Popov, O., Iatsyshyn, A., Kovach, V., Artemchuk, V., Kameneva, I., Taraduda, D., … Yatsyshyn, T. (2020). Risk Assessment for the Population of Kyiv, Ukraine as a Result of Atmospheric Air Pollution. *Journal of Health and Pollution*, *10*(25), 200303. doi:10.5696/2156-9614-10.25.200303

Prasad, A. K., & Singh, R. P. (2007). Changes in aerosol parameters during major dust storm events (2001–2005) over the Indo-Gangetic Plains using AERONET and MODIS data. *Journal of Geophysical Research: Atmospheres*, *112*(D9). doi:10.1029/2006JD007778

Prasad, A. K., Singh, S., Chauhan, S., Srivastava, M. K., Singh, R. P., & Singh, R. (2007). Aerosol radiative forcing over the Indo-Gangetic plains during major dust storms. *Atmospheric Environment*, *41*(29), 6289–6301.

Pu, R., & Landry, S. (2012). A comparative analysis of high spatial resolution IKONOS and WorldView-2 imagery for mapping urban tree species. *Remote Sensing of Environment*, *124*, 516–533. doi:10.1016/j.rse.2012.06.011

Qin, W., Fang, H., Wang, L., Wei, J., Zhang, M., Su, X., … Liang, X. (2021). MODIS high-resolution MAIAC aerosol product: Global validation and analysis. *Atmospheric Environment*, *264*, 118684. doi:10.1016/j.atmosenv.2021.118684

Qu, W. J., Wang, J., Zhang, X. Y., Wang, D., & Sheng, L. F. (2015). Influence of relative humidity on aerosol composition: Impacts on light extinction and visibility impairment at two sites in coastal area of China. *Atmospheric Research*, *153*, 500–511. doi:10.1016/j.atmosres.2014.10.009

Quaas, J., Boucher, O., Bellouin, N., & Kinne, S. (2008). Satellite-based estimate of the direct and indirect aerosol climate forcing. *Journal of Geophysical Research: Atmospheres*, *113*(D5). doi:10.1029/2007JD008962

Rajagopalan, S., Al-Kindi, S. G., & Brook, R. D. (2018). Air Pollution and Cardiovascular Disease. *Journal of the American College of Cardiology*, *72*(17), 2054–2070. doi:10.1016/j.jacc.2018.07.099

Ranjan, A. K., Patra, A., & Gorai, A. (2020). Effect of lockdown due to SARS COVID-19 on aerosol optical depth (AOD) over urban and mining regions in India. *Science of the Total Environment*, *745*, 141024.

Rawat, J. S., & Kumar, M. (2015). Monitoring land use/cover change using remote sensing and GIS techniques: A case study of Hawalbagh block, district Almora, Uttarakhand, India. *The Egyptian Journal of Remote Sensing and Space Science*, *18*(1), 77–84. doi:10.1016/j.ejrs.2015.02.002

Remer, L. A., Kaufman, Y. J., Tanré, D., Mattoo, S., Chu, D. A., Martins, J. V., … Holben, B. N. (2005). The MODIS Aerosol Algorithm, Products, and Validation. *Journal of the Atmospheric Sciences*, *62*(4), 947–973. doi:10.1175/JAS3385.1

Remer, L. A., Mattoo, S., Levy, R., & Munchak, L. A. (2013). MODIS 3 km aerosol product: algorithm and global perspective. *Atmospheric Measurement Techniques*, *6*(7), 1829–1844. doi:10.5194/amt-6-1829-2013

Remer, L. A., Tanré, D., Kaufman, Y. J., Ichoku, C., Mattoo, S., Levy, R., … Ahmad, Z. (2002). Validation of MODIS aerosol retrieval over ocean. *Geophysical Research Letters*, *29*(12), MOD3-1-MOD3-4. doi:10.1029/2001GL013204

Remer, L., Mattoo, S., Levy, R., Heidinger, A., Pierce, R., & Chin, M. (2012). Retrieving aerosol in a cloudy environment: Aerosol product availability as a function of spatial resolution. *Atmospheric Measurement Techniques*, *5*, 1823–1840. doi:10.5194/amt-5-1823-2012

Remer, Lorraine A., & Kaufman, Y. J. (1998). Dynamic aerosol model: Urban/industrial aerosol. *Journal of Geophysical Research: Atmospheres*, *103*(D12), 13859–13871. doi:10.1029/98JD00994

Remer, Lorraine A., Kleidman, R. G., Levy, R., Kaufman, Y. J., Tanré, D., Mattoo, S., … Holben, B. N. (2008). Global aerosol climatology from the MODIS satellite sensors. *Journal of Geophysical Research: Atmospheres*, *113*(D14). doi:10.1029/2007JD009661

Republic of Turkiye ministry of agriculture and forestry. (n.d.). Retrieved 30 March 2023, from https://www.tarimorman.gov.tr/Sayfalar/EN/AnaSayfa.aspx

Riojas-Rodríguez, H., da Silva, A. S., Texcalac-Sangrador, J. L., & Moreno-Banda, G. L. (2016). Air pollution management and control in Latin America and the Caribbean: implications for climate change. *Revista Panamericana de Salud Pública*, *40*, 150–159. Retrieved from SciELO

Roy, P. S., Miyatake, S., & Rikimaru, A. (2009, September 15). Biophysical spectral response modeling approach for forest density stratification. Retrieved 22 July 2018, from http://www.gisdelopment.net/aars/acrs/1997/tTM5/tTM5008a.shtml

Russell, P. B., Bergstrom, R. W., Shinozuka, Y., Clarke, A. D., DeCarlo, P. F., Jimenez, J. L., … Strawa, A. (2010). Absorption Angstrom Exponent in AERONET and related data as an indicator of aerosol composition. *Atmospheric Chemistry and Physics*, *10*(3), 1155–1169. doi:10.5194/acp-10-1155-2010

Ryu, S. Y., Kwon, B. G., Kim, Y. J., Kim, H. H., & Chun, K. J. (2007). Characteristics of biomass burning aerosol and its impact on regional air quality in the summer of 2003 at Gwangju, Korea. *Atmospheric Research*, *84*(4), 362–373. doi:10.1016/j.atmosres.2006.09.007

Saint Akadiri, S., Alola, A. A., Akadiri, A. C., & Alola, U. V. (2019). Renewable energy consumption in EU-28 countries: Policy toward pollution mitigation and economic sustainability. *Energy Policy*, *132*, 803–810. doi:10.1016/j.enpol.2019.06.040

Samek, L., Stegowski, Z., Styszko, K., Furman, L., Zimnoch, M., Skiba, A., … Konduracka, E. (2020). Seasonal variations of chemical composition of PM2.5 fraction in the urban area of Krakow, Poland: PMF source attribution. *Air Quality, Atmosphere & Health*, *13*(1), 89–96. doi:10.1007/s11869-019-00773-x

Sayer, A. M., Hsu, N. C., Bettenhausen, C., & Jeong, M.-J. (2013). Validation and uncertainty estimates for MODIS Collection 6 "Deep Blue" aerosol data. *Journal of Geophysical Research: Atmospheres, 118*(14), 7864–7872. doi:10.1002/jgrd.50600

Sayer, A. M., Hsu, N. C., Bettenhausen, C., Jeong, M.-J., Holben, B. N., & Zhang, J. (2012). Global and regional evaluation of over-land spectral aerosol optical depth retrievals from SeaWiFS. *Atmospheric Measurement Techniques*, *5*(7), 1761–1778. doi:10.5194/amt-5-1761-2012

Sayer, A. M., Hsu, N. C., Lee, J., Bettenhausen, C., Kim, W. V., & Smirnov, A. (2018). Satellite Ocean Aerosol Retrieval (SOAR) Algorithm Extension to S-NPP VIIRS as Part of the "Deep Blue" Aerosol Project. *Journal of Geophysical Research: Atmospheres, 123*(1), 380–400. doi:10.1002/2017JD027412

Sayer, A. M., Hsu, N. C., Lee, J., Kim, W. V., Dubovik, O., Dutcher, S. T., … Winker, D. M. (2018). Validation of SOAR VIIRS Over-Water Aerosol Retrievals and Context Within the Global Satellite Aerosol Data Record. *Journal of Geophysical Research: Atmospheres, 123*(23), 13,496-13,526. doi:10.1029/2018JD029465

Sayer, A. M., Hsu, N. C., Lee, J., Kim, W. V., & Dutcher, S. T. (2019). Validation, Stability, and Consistency of MODIS Collection 6.1 and VIIRS Version 1 Deep Blue Aerosol Data Over Land. *Journal of Geophysical Research: Atmospheres, 124*(8), 4658–4688. doi:10.1029/2018JD029598

Sayer, A. M., Munchak, L., Hsu, N., Levy, R., Bettenhausen, C., & Jeong, M.-J. (2014). MODIS Collection 6 aerosol products: Comparison between Aqua's e-Deep Blue, Dark Target, and 'merged' datasets, and usage recommendations. *Journal of Geophysical Research: Atmospheres, 119*. doi:10.1002/2014JD022453

Saygın, M., Gonca, T., Öztürk, Ö., Has, M., Çalışkan, S., Has, Z. G., & Akkaya, A. (2017). To Investigate the Effects of Air Pollution (PM10 and SO2) on the Respiratory Diseases Asthma and Chronic Obstructive Pulmonary Disease. *Turkish Thoracic Journal*, *18*(2), 33–39. doi:10.5152/TurkThoracJ.2017.16016

Schaaf, C. B., Gao, F., Strahler, A. H., Lucht, W., Li, X., Tsang, T., … Roy, D. (2002). First operational BRDF, albedo nadir reflectance products from MODIS. *Remote Sensing of Environment*, *83*(1), 135–148. doi:10.1016/S0034-4257(02)00091-3

Schafer, J. S., Eck, T. F., Holben, B. N., Artaxo, P., & Duarte, A. F. (2008). Characterization of the optical properties of atmospheric aerosols in Amazônia from long-term AERONET monitoring (1993–1995 and 1999–2006). *Journal of Geophysical Research: Atmospheres*, *113*(D4). doi:10.1029/2007JD009319

Science, G. (2014). Aerosol Characteristics and Radiative Forcing during Pre-Monsoon and Post-Monsoon Seasons in an Urban Environment. *Aerosol and Air Quality Research*, *14*(1), 99–107. doi:10.4209/aaqr.2013.05.0154

Seinfeld, J. H., Bretherton, C., Carslaw, K. S., Coe, H., DeMott, P. J., Dunlea, E. J., … Kahn, R. (2016). Improving our fundamental understanding of the role of aerosol− cloud interactions in the climate system. *Proceedings of the National Academy of Sciences*, *113*(21), 5781–5790.

Sertel, E., & Akay, S. S. (2015). High resolution mapping of urban areas using SPOT-5 images and ancillary data. *International Journal of Environment and Geoinformatics*, *2*(2), 63–76. doi:10.30897/ijegeo.303545

Sertel, E., Robock, A., & Ormeci, C. (2010). Impacts of land cover data quality on regional climate simulations. *International Journal of Climatology*, *30*(13), 1942–1953. doi:10.1002/joc.2036

Sezer Turalıoğlu, F., Nuhoğlu, A., & Bayraktar, H. (2005). Impacts of some meteorological parameters on SO2 and TSP concentrations in Erzurum, Turkey. *Chemosphere*, *59*(11), 1633–1642. doi:10.1016/j.chemosphere.2005.02.003

Shaheen, A., Wu, R., & Aldabash, M. (2020). Long-term AOD trend assessment over the Eastern Mediterranean region: A comparative study including a new merged aerosol product. *Atmospheric Environment*, *238*, 117736. doi:10.1016/j.atmosenv.2020.117736

Shahsavari, A., & Akbari, M. (2018). Potential of solar energy in developing countries for reducing energy-related emissions. *Renewable and Sustainable Energy Reviews*, *90*, 275–291. doi:10.1016/j.rser.2018.03.065

Shao, Y., & Lunetta, R. S. (2012). Comparison of support vector machine, neural network, and CART algorithms for the land-cover classification using limited training data points. *ISPRS Journal of Photogrammetry and Remote Sensing*, *70*, 78–87. doi:10.1016/j.isprsjprs.2012.04.001

Shen, L., Wang, H., Zhao, T., Liu, J., Bai, Y., Kong, S., & Shu, Z. (2020). Characterizing regional aerosol pollution in central China based on 19 years of MODIS data: Spatiotemporal variation and aerosol type discrimination. *Environmental Pollution*, *263*, 114556. doi:10.1016/j.envpol.2020.114556

Shen, X., Bilal, M., Qiu, Z., Sun, D., Wang, S., & Zhu, W. (2018). Validation of MODIS C6 Dark Target Aerosol Products at 3 km and 10 km Spatial Resolutions Over the China Seas and the Eastern Indian Ocean. *Remote Sensing*, *10*(4), 573. doi:10.3390/rs10040573

Shi, H., Xiao, Z., Zhan, X., Ma, H., & Tian, X. (2019). Evaluation of MODIS and two reanalysis aerosol optical depth products over AERONET sites. *Atmospheric Research*, *220*, 75–80.

Shi, Y. R., Levy, R., Eck, T. F., Fisher, B., Mattoo, S., Remer, L. A., … Zhang, J. (2019). Characterizing the 2015 Indonesia fire event using modified MODIS aerosol retrievals. *Atmospheric Chemistry and Physics*, *19*(1), 259–274. doi:10.5194/acp-19-259-2019

Shi, Y., Zhang, J., Reid, J. S., Holben, B., Hyer, E. J., & Curtis, C. (2011). An analysis of the collection 5 MODIS over-ocean aerosol optical depth product for its implication in aerosol assimilation. *Atmospheric Chemistry and Physics*, *11*(2), 557–565. doi:10.5194/acp-11-557-2011

Shi, Yuan, Bilal, M., Ho, H. C., & Omar, A. (2020). Urbanization and regional air pollution across South Asian developing countries – A nationwide land use regression for ambient PM2.5 assessment in Pakistan. *Environmental Pollution*, *266*, 115145. doi:10.1016/j.envpol.2020.115145

Shin, S.-K., Tesche, M., Kim, K., Kezoudi, M., Tatarov, B., Müller, D., & Noh, Y. (2018). On the spectral depolarisation and lidar ratio of mineral dust provided in the AERONET version 3 inversion product. *Atmospheric Chemistry and Physics*, *18*(17), 12735–12746.

Shin, S.-K., Tesche, M., Noh, Y., & Müller, D. (2019). Aerosol-type classification based on AERONET version 3 inversion products. *Atmospheric Measurement Techniques*, *12*(7), 3789–3803. doi:10.5194/amt-12-3789-2019

Shrestha, A. M., Shrestha, U. B., Sharma, R., Bhattarai, S., Tran, H. N. T., & Rupakheti, M. (2020). Lockdown caused by COVID-19 pandemic reduces air pollution in cities worldwide. Retrieved from eartharxiv.org

Sicard, P., Augustaitis, A., Belyazid, S., Calfapietra, C., de Marco, A., Fenn, M., … Paoletti, E. (2016). Global topics and novel approaches in the study of air pollution, climate change and forest ecosystems. *Environmental Pollution (Barking, Essex: 1987)*, *213*, 977–987. doi:10.1016/j.envpol.2016.01.075

Silver, B., Reddington, C. L., Arnold, S. R., & Spracklen, D. V. (2018). Substantial changes in air pollution across China during 2015–2017. *Environmental Research Letters*, *13*(11), 114012. doi:10.1088/1748-9326/aae718

Singh, T., Ravindra, K., Beig, G., & Mor, S. (2021). Influence of agricultural activities on atmospheric pollution during post-monsoon harvesting seasons at a rural location of Indo-Gangetic Plain. *Science of The Total Environment*, *796*, 148903. doi:10.1016/j.scitotenv.2021.148903

Sinyuk, A., Holben, B. N., Eck, T. F., Giles, D. M., Slutsker, I., Korkin, S., … Lyapustin, A. (2020). The AERONET Version 3 aerosol retrieval algorithm, associated uncertainties and comparisons to Version 2. *Atmospheric Measurement Techniques*, *13*(6), 3375–3411. doi:10.5194/amt-13-3375-2020

Smirnov, A., Holben, B. N., Kaufman, Y. J., Dubovik, O., Eck, T. F., Slutsker, I., … Halthore, R. N. (2002). Optical Properties of Atmospheric Aerosol in Maritime Environments. *Journal of the Atmospheric Sciences*, *59*(3), 501–523. doi:10.1175/1520-0469(2002)059<0501:OPOAAI>2.0.CO;2

Song, Q., Zhang, Z., Yu, H., Kato, S., Yang, P., Colarco, P., … Ryder, C. L. (2018). Net radiative effects of dust in the tropical North Atlantic based on integrated satellite observations and in situ measurements. *Atmospheric Chemistry and Physics*, *18*(15), 11303–11322.

Srivastava, P. K., Han, D., Rico-Ramirez, M. A., Bray, M., & Islam, T. (2012). Selection of classification techniques for land use/land cover change investigation. *Advances in Space Research*, *50*(9), 1250–1265. doi:10.1016/j.asr.2012.06.032

Stathakis, D., Perakis, K., & Savin, I. (2012). Efficient segmentation of urban areas by the VIBI. *International Journal of Remote Sensing*, *33*(20), 6361–6377. doi:10.1080/01431161.2012.687842

Stefan, S., Voinea, S., & Iorga, G. (2020). Study of the aerosol optical characteristics over the Romanian Black Sea Coast using AERONET data. *Atmospheric Pollution Research*, *11*(7), 1165–1178. doi:https://doi.org/10.1016/j.apr.2020.04.007

Su, L., & Toon, O. B. (2011). Saharan and Asian dust: similarities and differences determined by CALIPSO, AERONET, and a coupled climate-aerosol microphysical model. *Atmospheric Chemistry and Physics*, *11*(7), 3263–3280.

Sullivan, R. C., Levy, R., & Pryor, S. C. (2015). Spatiotemporal coherence of mean and extreme aerosol particle events over eastern North America as observed from satellite. *Atmospheric Environment*, *112*, 126–135. doi:10.1016/j.atmosenv.2015.04.026

Sun, E., Xu, X., Che, H., Tang, Z., Gui, K., An, L., … Shi, G. (2019). Variation in MERRA-2 aerosol optical depth and absorption aerosol optical depth over China from 1980 to 2017. *Journal of Atmospheric and Solar-Terrestrial Physics*, *186*, 8–19. doi:10.1016/j.jastp.2019.01.019

Tanré, D., Kaufman, Y., Herman, M., & Mattoo, S. (1997). Remote sensing of aerosol properties over oceans using the MODIS/EOS spectral radiances. *Journal of Geophysical Research: Atmospheres*, *102*(D14), 16971–16988.

Tao, M., Chen, L., Wang, Z., Tao, J., Che, H., Wang, X., & Wang, Y. (2015). Comparison and evaluation of the MODIS Collection 6 aerosol data in China. *Journal of Geophysical Research: Atmospheres*, *120*(14), 6992–7005. doi:10.1002/2015JD023360

Tao, M., Gui, L., Li, R., Wang, L., Liang, S., Li, Q., … Chen, L. (2021). Tracking prevailing dust aerosol over the air pollution in central China with integrated satellite and ground observations. *Atmospheric Environment*, *253*, 118369. doi:10.1016/j.atmosenv.2021.118369

Tao, M., Wang, J., Li, R., Wang, L., Wang, L., Wang, Z., … Chen, L. (2019). Performance of MODIS high-resolution MAIAC aerosol algorithm in China: Characterization and limitation. *Atmospheric Environment*, *213*, 159–169. doi:10.1016/j.atmosenv.2019.06.004

Tao, M., Wang, Z., Tao, J., Chen, L., Wang, J., Hou, C., … Zhu, H. (2017). How Do Aerosol Properties Affect the Temporal Variation of MODIS AOD Bias in Eastern China? *Remote Sensing*, *9*(8), 800. doi:10.3390/rs9080800

Temiz, H., & Olgar, K. (2017). Doğal ve Yapay Liflerden Üretilen Panellerin Yalıtım Özelliklerinin Araştırılması. *Karaelmas Fen ve Mühendislik Dergisi*, *7*(2), 608–618. Retrieved from dergipark.org.tr

Thep, 2020-2024. (2020). *Clean air action plan for Istanbul* (p. 438).

Tian, X., Liu, Q., Li, X., & Wei, J. (2018). Validation and Comparison of MODIS C6.1 and C6 Aerosol Products over Beijing, China. *Remote Sensing*, *10*(12), 2021. doi:10.3390/rs10122021

Toledano, C., Cachorro, V. E., Berjon, A., de Frutos, A. M., Sorribas, M., de la Morena, B. A., & Goloub, P. (2007). Aerosol optical depth and Ångström exponent climatology at El Arenosillo AERONET site (Huelva, Spain). *Quarterly Journal of the Royal Meteorological Society*, *133*(624), 795–807. doi:10.1002/qj.54

Toledano, C., Cachorro, V. E., de Frutos, A. M., Sorribas, M., Prats, N., & de la Morena, B. A. (2007). Inventory of African desert dust events over the southwestern Iberian Peninsula in 2000–2005 with an AERONET Cimel Sun photometer. *Journal of Geophysical Research: Atmospheres*, *112*(D21). doi:10.1029/2006JD008307

Tripathi, S. N., Dey, S., Chandel, A., Srivastava, S., Singh, R. P., & Holben, B. N. (2005). Comparison of MODIS and AERONET derived aerosol optical depth over the Ganga Basin, India. *Annales Geophysicae*, *23*(4), 1093–1101. doi:10.5194/angeo-23-1093-2005

TUIK. (2021a). *Turkish Statistical Institute, Population and Housing Census 2020*. Retrieved from https://data.tuik.gov.tr/Bulten/DownloadIstatistikselTablo?p=D/iyuDY0YaNRJp8DX69ESortYsYRQss36XKkV5ynlsLTp4WYhvc8Woz6qEb2bTRj

TUIK. (2021b). *Turkish Statistical Institute, The number of road motor vehicles by province, 2020*. Retrieved from https://tuikweb.tuik.gov.tr/HbGetir.do?id=33658&tb_id=2

Tuna Tuygun, G., & Elbir, T. (2020). Long-term temporal analysis of the columnar and surface aerosol relationship with planetary boundary layer height at a southern coastal site of Turkey. *Atmospheric Pollution Research*, *11*(12), 2259–2269. doi:10.1016/j.apr.2020.09.008

Tuna Tuygun, G., Ozdemir, E., & Elbir, T. (2020). Evaluation of MODIS C6 and C6.1 Dark Target AOD products over Turkey based on NDVI and aerosol type. *Atmospheric Pollution Research*, *11*(12), 2335–2349. doi:10.1016/j.apr.2020.07.003

Tutsak, E., & Koçak, M. (2019). Long-term measurements of aerosol optical and physical properties over the Eastern Mediterranean: hygroscopic nature and source regions. *Atmospheric Environment*, *207*, 1–15.

Tutsak, E., & Koçak, M. (2020). Optical and microphysical properties of the columnar Aerosol burden over the Eastern Mediterranean: Discrimination of Aerosol types. *Atmospheric Environment*, *229*, 117463.

Udeigwe, T. K., Teboh, J. M., Eze, P. N., Hashem Stietiya, M., Kumar, V., Hendrix, J., … Kandakji, T. (2015). Implications of leading crop production practices on environmental quality and human health. *Journal of Environmental Management*, *151*, 267–279. doi:10.1016/j.jenvman.2014.11.024

Ülker, D., Bayırhan, İ., Mersin, K., & Gazioğlu, C. (2021). A comparative CO2 emissions analysis and mitigation strategies of short-sea shipping and road transport in the Marmara Region. *Carbon Management*, *12*(1), 1–12. doi:10.1080/17583004.2020.1852853

van Deventer, A. P., Ward, A. D., Gowda, P. H., & Lyon, J. G. (1997). Using Thematic Mapper Data to Identify Contrasting Soil Plains and Tillage Practices. Retrieved from Zotero

Veefkind, J. P., de Leeuw, G., & Durkee, P. A. (1998). Retrieval of aerosol optical depth over land using two-angle view satellite radiometry during TARFOX. *Geophysical Research Letters*, *25*(16), 3135–3138.

Velasco-Merino, C., Mateos, D., Toledano, C., Prospero, J. M., Molinie, J., Euphrasie-Clotilde, L., … de Frutos, A. M. (2018). Impact of long-range transport over the Atlantic Ocean on Saharan dust optical and microphysical properties based on AERONET data. *Atmospheric Chemistry and Physics*, *18*(13), 9411–9424. doi:10.5194/acp-18-9411-2018

Verma, S., Payra, S., Gautam, R., Prakash, D., Soni, M., Holben, B., & Bell, S. (2013). Dust events and their influence on aerosol optical properties over Jaipur in Northwestern India. *Environmental Monitoring and Assessment*, *185*(9), 7327–7342. doi:10.1007/s10661-013-3103-9

Viana, M., Fann, N., Tobías, A., Querol, X., Rojas-Rueda, D., Plaza, A., … Fernández, C. (2015). Environmental and Health Benefits from Designating the Marmara Sea and the Turkish Straits as an Emission Control Area (ECA). *Environmental Science & Technology*, *49*(6), 3304–3313. doi:10.1021/es5049946

Viana, M., Hammingh, P., Colette, A., Querol, X., Degraeuwe, B., de Vlieger, I., & Van Aardenne, J. (2014). Impact of maritime transport emissions on coastal air quality in Europe. *Atmospheric Environment*, *90*, 96–105.

Wang, C., Wang, C., Myint, S. W., & Wang, Z.-H. (2017). Landscape determinants of spatio-temporal patterns of aerosol optical depth in the two most polluted metropolitans in the United States. *Science of The Total Environment*, *609*, 1556–1565. doi:10.1016/j.scitotenv.2017.07.273

Wang, H., Lyu, X., Guo, H., Wang, Y., Zou, S., Ling, Z., … Pan, W. (2018). Ozone pollution around a coastal region of South China Sea: interaction between marine and continental air. *Atmospheric Chemistry and Physics*, *18*(6), 4277–4295.

Wang, L., Yu, Y., Huang, K., Zhang, Z., & Li, X. (2020). The inharmonious mechanism of CO2, NOx, SO2, and PM2.5 electric vehicle emission reductions in Northern China. *Journal of Environmental Management*, *274*, 111236. doi:10.1016/j.jenvman.2020.111236

Wang, Q., Meng, Z., & Li, X. (2017). Locality Adaptive Discriminant Analysis for Spectral–Spatial Classification of Hyperspectral Images. *IEEE Geoscience and Remote Sensing Letters*, *14*(11), 2077–2081. doi:10.1109/LGRS.2017.2751559

Wang, S., Gao, S., Li, S., & Feng, K. (2020). Strategizing the relation between urbanization and air pollution: Empirical evidence from global countries. *Journal of Cleaner Production*, *243*, 118615. doi:10.1016/j.jclepro.2019.118615

Wang, W., Mao, F., Pan, Z., Du, L., & Gong, W. (2017). Validation of VIIRS AOD through a Comparison with a Sun Photometer and MODIS AODs over Wuhan. *Remote Sensing*, *9*(5), 403. doi:10.3390/rs9050403

Wang, X., Lei, Y., Yan, L., Liu, T., Zhang, Q., & He, K. (2019). A unit-based emission inventory of SO2, NOx and PM for the Chinese iron and steel industry from 2010 to 2015. *Science of The Total Environment*, *676*, 18–30. doi:10.1016/j.scitotenv.2019.04.241

Wang, Y., Wang, J., Levy, R., Xu, X., & Reid, J. S. (2017). MODIS Retrieval of Aerosol Optical Depth over Turbid Coastal Water. *Remote Sensing*, *9*(6), 595. doi:10.3390/rs9060595

Wei, J., Li, Z., Peng, Y., & Sun, L. (2019). MODIS Collection 6.1 aerosol optical depth products over land and ocean: validation and comparison. *Atmospheric Environment*, *201*, 428–440. doi:10.1016/j.atmosenv.2018.12.004

Wei, J., Li, Z., Sun, L., Peng, Y., Liu, L., He, L., … Cribb, M. (2020). MODIS Collection 6.1 3 km resolution aerosol optical depth product: global evaluation and uncertainty analysis. *Atmospheric Environment*, *240*, 117768. doi:https://doi.org/10.1016/j.atmosenv.2020.117768

Wei, J., Peng, Y., Mahmood, R., Sun, L., & Guo, J. (2019). Intercomparison in spatial distributions and temporal trends derived from multi-source satellite aerosol products. *Atmospheric Chemistry and Physics*, *19*(10), 7183–7207. doi:10.5194/acp-19-7183-2019

Wei, J., & Sun, L. (2017). Comparison and Evaluation of Different MODIS Aerosol Optical Depth Products Over the Beijing-Tianjin-Hebei Region in China. *IEEE Journal of Selected Topics in Applied Earth Observations and Remote Sensing*, *10*(3), 835–844. doi:10.1109/JSTARS.2016.2595624

Wu, T., Lin, C., & Weng, R. (2003). *Probability Estimates for Multi-Class Classification by Pairwise Coupling*. In *Advances in Neural Information Processing Systems* (Vol. 16). MIT Press. Retrieved from Neural Information Processing Systems

Xia, L., & Gao, Y. (2010). Chemical composition and size distributions of coastal aerosols observed on the US East Coast. *Marine Chemistry*, *119*(1), 77–90. doi:10.1016/j.marchem.2010.01.002

Xia, X., Chen, H., Goloub, P., Zhang, W., Chatenet, B., & Wang, P. (2007). A compilation of aerosol optical properties and calculation of direct radiative forcing over an urban region in northern China. *Journal of Geophysical Research: Atmospheres*, *112*(D12).

Xian, P., Zhang, J., O'Neill, N. T., Reid, J. S., Toth, T. D., Sorenson, B., … Ranjbar, K. (2022). Arctic spring and summertime aerosol optical depth baseline from long-term observations and model reanalyses–Part 2: Statistics of extreme AOD events, and implications for the impact of regional biomass burning processes. *Atmospheric Chemistry and Physics*, *22*(15), 9949–9967.

Xiao, Q., Zhang, H., Choi, M., Li, S., Kondragunta, S., Kim, J., … Liu, Y. (2016). Evaluation of VIIRS, GOCI, and MODIS Collection 6 AOD retrievals against ground sunphotometer observations over East Asia. *Atmospheric Chemistry and Physics*, *16*(3), 1255–1269. doi:10.5194/acp-16-1255-2016

Xie, Q., & Sun, Q. (2021). Monitoring the Spatial Variation of Aerosol Optical Depth and Its Correlation with Land Use/Land Cover in Wuhan, China: A Perspective of Urban Planning. *International Journal of Environmental Research and Public Health*, *18*(3), 1132.

Xie, Y., Zhang, Y., Xiong, X., Qu, J. J., & Che, H. (2011). Validation of MODIS aerosol optical depth product over China using CARSNET measurements. *Atmospheric Environment*, *45*(33), 5970–5978. doi:10.1016/j.atmosenv.2011.08.002

Xu, H. (2008). A new index for delineating built-up land features in satellite imagery. *International Journal of Remote Sensing*, *29*(14), 4269–4276. doi:10.1080/01431160802039957

Xu, Hanqiu. (2006). Modification of normalised difference water index (NDWI) to enhance open water features in remotely sensed imagery. *International Journal of Remote Sensing*, *27*(14), 3025–3033. doi:10.1080/01431160600589179

Xu, Hanqiu. (2007). Extraction of urban built-up land features from Landsat imagery using a thematicoriented index combination technique. *Photogrammetric Engineering & Remote Sensing*, *73*(12), 1381–1391.

Xu, J., Jiang, H., Zhang, X., Lu, X., & Peng, W. (2014). Study on spatial-temporal variation of aerosol optical depth over the Yangtze Delta and the impact of land-use/cover. *International Journal of Remote Sensing*, *35*(5), 1741–1755. doi:10.1080/01431161.2014.882033

Xu, X., Xie, L., Yang, X., Wu, H., Cai, L., & Qi, P. (2020). Aerosol optical properties at seven AERONET sites over Middle East and Eastern Mediterranean Sea. *Atmospheric Environment*, *243*, 117884. doi:10.1016/j.atmosenv.2020.117884

Yakupoglu, T., Dindaroğlu, T., Rodrigo-Comino, J., & Cerdà, A. (2022). Stubble burning and wildfires in Turkey considering the Sustainable Development Goals of the United Nations. *EURASIAN JOURNAL OF SOIL SCIENCE (EJSS)*, *11*, 66–76. doi:10.18393/ejss.993611

Yamazaki, D., Ikeshima, D., Tawatari, R., Yamaguchi, T., O'Loughlin, F., Neal, J. C., … Bates, P. D. (2017). A high-accuracy map of global terrain elevations. *Geophysical Research Letters*, *44*(11), 5844–5853. doi:10.1002/2017GL072874

Yang, B.-Y., Fan, S., Thiering, E., Seissler, J., Nowak, D., Dong, G.-H., & Heinrich, J. (2020). Ambient air pollution and diabetes: A systematic review and meta-analysis. *Environmental Research*, *180*, 108817. doi:10.1016/j.envres.2019.108817

Yang, W., Pudasainee, D., Gupta, R., Li, W., Wang, B., & Sun, L. (2021). An overview of inorganic particulate matter emission from coal/biomass/MSW combustion: Sampling and measurement, formation, distribution, inorganic composition and influencing factors. *Fuel Processing Technology*, *213*, 106657. doi:10.1016/j.fuproc.2020.106657

Yang, Xiaojun, & Liu, Z. (2005). Use of satellite-derived landscape imperviousness index to characterize urban spatial growth. *Computers, Environment and Urban Systems*, *29*(5), 524–540.

Yang, Xingchuan, Zhao, C., Yang, Y., Yan, X., & Fan, H. (2021). Statistical aerosol properties associated with fire events from 2002 to 2019 and a case analysis in 2019 over Australia. *Atmospheric Chemistry and Physics*, *21*(5), 3833–3853. doi:10.5194/acp-21-3833-2021

Yatkin, S., Gerboles, M., Belis, C. A., Karagulian, F., Lagler, F., Barbiere, M., & Borowiak, A. (2020). Representativeness of an air quality monitoring station for PM2.5 and source apportionment over a small urban domain. *Atmospheric Pollution Research*, *11*(2), 225–233. doi:10.1016/j.apr.2019.10.004

Yavuz, G. G. (2009). Türkiye ve Avrupa Birliği'nde Tarımsal Üretim Karşılaştırması, 8. Retrieved from Zotero

Yılmaz, R. (2010). Monitoring land use/land cover changes using CORINE land cover data: a case study of Silivri coastal zone in Metropolitan Istanbul. *Environmental Monitoring and Assessment*, *165*, 603–615.

Yousefi, R., Wang, F., Ge, Q., & Shaheen, A. (2020). Long-term aerosol optical depth trend over Iran and identification of dominant aerosol types. *Science of The Total Environment*, *722*, 137906. doi:10.1016/j.scitotenv.2020.137906

Yu, H., Tan, Q., Chin, M., Remer, L. A., Kahn, R. A., Bian, H., … Chédin, A. (2019). Estimates of African Dust Deposition Along the Trans-Atlantic Transit Using the Decadelong Record of Aerosol Measurements from CALIOP, MODIS, MISR, and IASI. *Journal of Geophysical Research: Atmospheres*, *124*(14), 7975–7996. doi:10.1029/2019JD030574

Yuan, F., Sawaya, K. E., Loeffelholz, B. C., & Bauer, M. E. (2005). Land cover classification and change analysis of the Twin Cities (Minnesota) Metropolitan Area by multitemporal Landsat remote sensing. *Remote Sensing of Environment*, *98*(2), 317–328. doi:10.1016/j.rse.2005.08.006

Yun, X., Shen, G., Shen, H., Meng, W., Chen, Y., Xu, H., … Tao, S. (2020). Residential solid fuel emissions contribute significantly to air pollution and associated health impacts in China. *Science Advances*, *6*(44), eaba7621. doi:10.1126/sciadv.aba7621

Yurtseven, E., Vehid, S., Bosat, M., Koksal, S., & Yurtseven, C. N. (2018). Assessment of Ambient Air Pollution in Istanbul during 2003–2013. *Iranian Journal of Public Health*, *47*(8), 1137–1144. Retrieved from PubMed Central

Zeydan, Ö., Tariq, S., Qayyum, F., Mehmood, U., & Ul-Haq, Z. (2023). Investigating the long-term trends in aerosol optical depth and its association with meteorological parameters and enhanced vegetation index over Turkey. *Environmental Science and Pollution Research*, *30*(8), 20337–20356. doi:10.1007/s11356-022-23553-0

Zha, Y., Gao, J., & Ni, S. (2003). Use of normalized difference built-up index in automatically mapping urban areas from TM imagery. *International Journal of Remote Sensing*, *24*(3), 583–594.

Zhang, H., Wang, Y., Hu, J., Ying, Q., & Hu, X.-M. (2015). Relationships between meteorological parameters and criteria air pollutants in three megacities in China. *Environmental Research*, *140*, 242–254. doi:10.1016/j.envres.2015.04.004

Zhang, J., & Reid, J. S. (2006). MODIS aerosol product analysis for data assimilation: Assessment of over-ocean level 2 aerosol optical thickness retrievals. *Journal of Geophysical Research: Atmospheres*, *111*(D22). doi:10.1029/2005JD006898

Zhang, J., & Reid, J. S. (2010). A decadal regional and global trend analysis of the aerosol optical depth using a data-assimilation grade over-water MODIS and Level 2 MISR aerosol products. *Atmospheric Chemistry and Physics*, *10*(22), 10949–10963. doi:10.5194/acp-10-10949-2010

Zhang, J., Reid, J. S., & Holben, B. N. (2005). An analysis of potential cloud artifacts in MODIS over ocean aerosol optical thickness products. *Geophysical Research Letters*, *32*(15). doi:10.1029/2005GL023254

Zhang, L., & Li, J. (2019). Variability of major aerosol types in China classified using AERONET measurements. *Remote Sensing*, *11*(20), 2334.

Zhang, Q., Jiang, X., Tong, D., Davis, S. J., Zhao, H., Geng, G., … Guan, D. (2017). Transboundary health impacts of transported global air pollution and international trade. *Nature*, *543*(7647), 705–709. doi:10.1038/nature21712

Zheng, H., Du, P., Chen, J., Xia, J., Li, E., Xu, Z., … Yokoya, N. (2017). Performance evaluation of downscaling Sentinel-2 imagery for land use and land cover classification by spectral-spatial features. *Remote Sensing*, *9*(12), 1274.

Zhou, Yi, Zhang, R., Wang, S., & Wang, F. (2018). Feature Selection Method Based on High-Resolution Remote Sensing Images and the Effect of Sensitive Features on Classification Accuracy. *Sensors*, *18*(7), 2013. doi:10.3390/s18072013

Zhou, Yunhong, Xiao, H., Guan, H., Zheng, N., Zhang, Z., Tian, J., … Xiao, H. (2020). Chemical composition and seasonal variations of PM2.5 in an urban environment in Kunming, SW China: Importance of prevailing westerlies in cold season. *Atmospheric Environment*, *237*, 117704. doi:10.1016/j.atmosenv.2020.117704

Zhu, Y., Liu, K., Liu, L., Myint, S. W., Wang, S., Liu, H., & He, Z. (2017). Exploring the Potential of WorldView-2 Red-Edge Band-Based Vegetation Indices for Estimation of Mangrove Leaf Area Index with Machine Learning Algorithms. *Remote Sensing*, *9*(10), 1060. doi:10.3390/rs9101060

Zieliński, T. (2004). Studies of Aerosol Physical Properties in Coastal Areas. *Aerosol Science and Technology*, *38*(5), 513–524. doi:10.1080/02786820490466738

Zoogman, P., Liu, X., Suleiman, R. M., Pennington, W. F., Flittner, D. E., Al-Saadi, J. A., … Chance, K. (2017). Tropospheric emissions: Monitoring of pollution (TEMPO). *Journal of Quantitative Spectroscopy and Radiative Transfer*, *186*, 17–39. doi:10.1016/j.jqsrt.2016.05.008

APPENDICES

APPENDIX A: Monthly averaged AOD Maps

APPENDIX B: Tables of annual variation of aerosol pollution levels

APPENDIX A

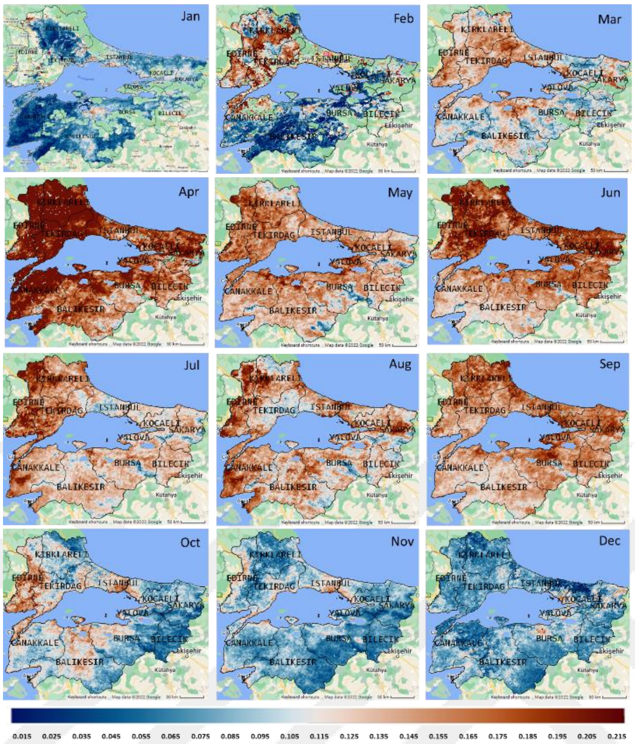

Figure A.1 : Monthly averaged MODIS MAIAC AOD for 2000.

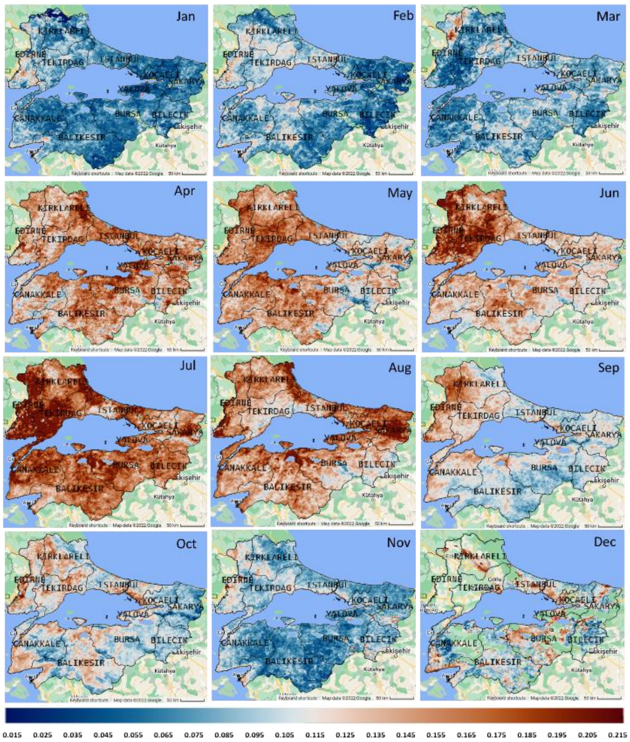

Figure A.2 : Monthly averaged MODIS MAIAC AOD for 2001.

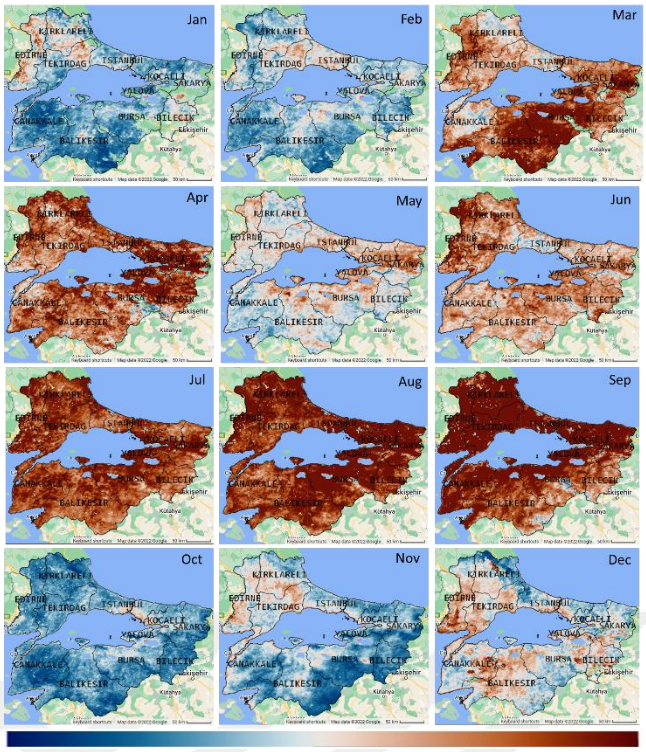

Figure A.3 : Monthly averaged MODIS MAIAC AOD for 2002.

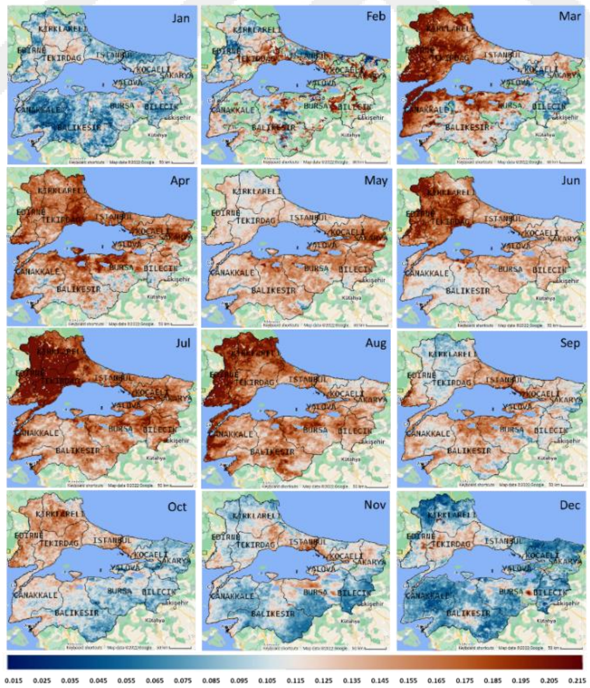

Figure A.4 : Monthly averaged MODIS MAIAC AOD for 2003.

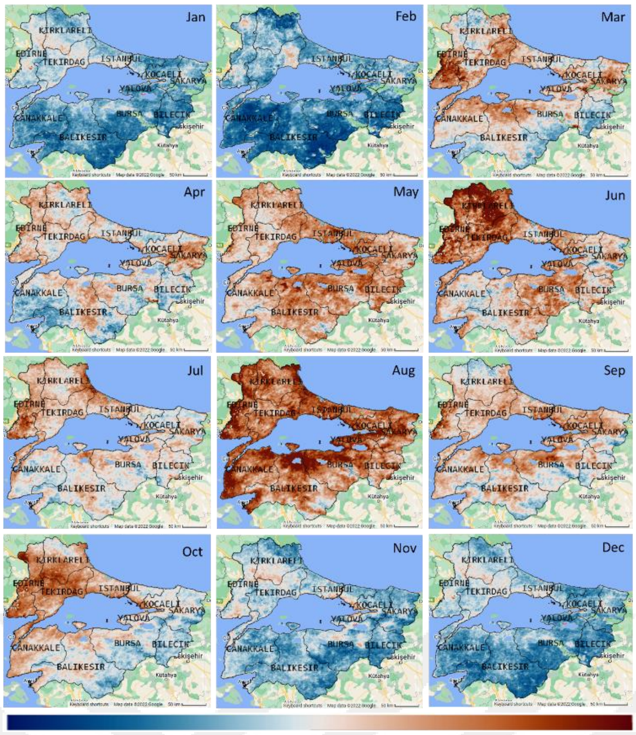

Figure A.5 : Monthly averaged MODIS MAIAC AOD for 2004.

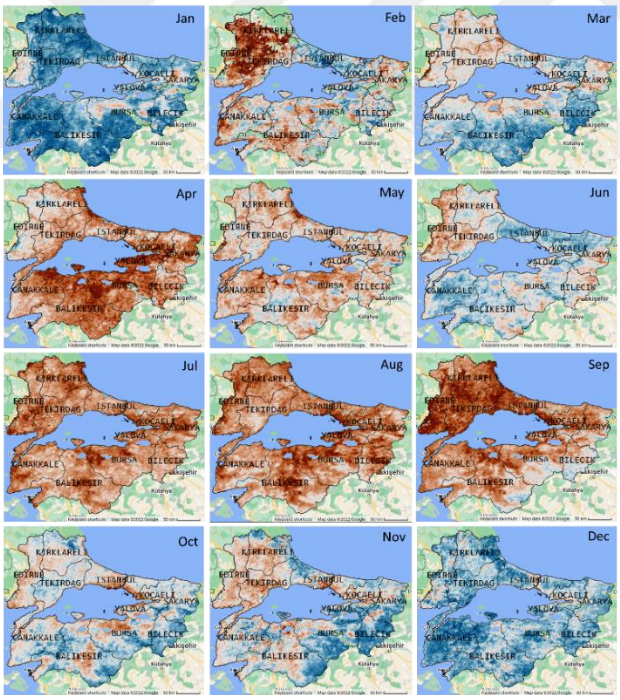

Figure A.6 : Monthly averaged MODIS MAIAC AOD for 2005.

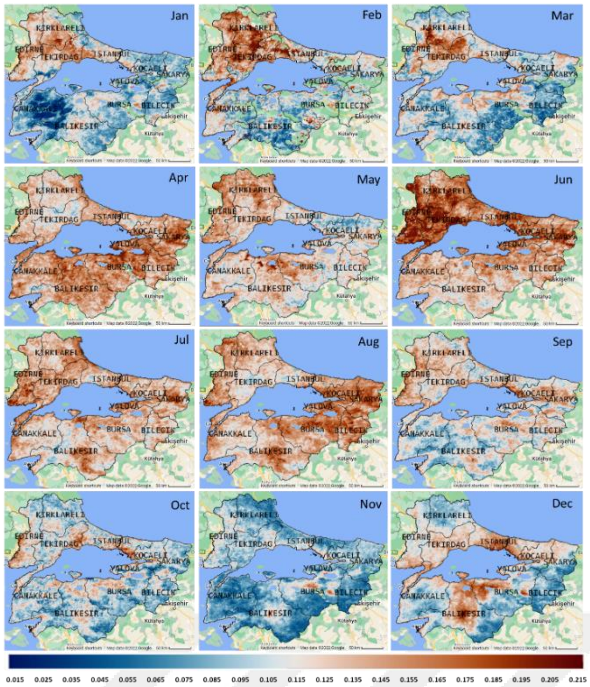

Figure A.7 : Monthly averaged MODIS MAIAC AOD for 2006.

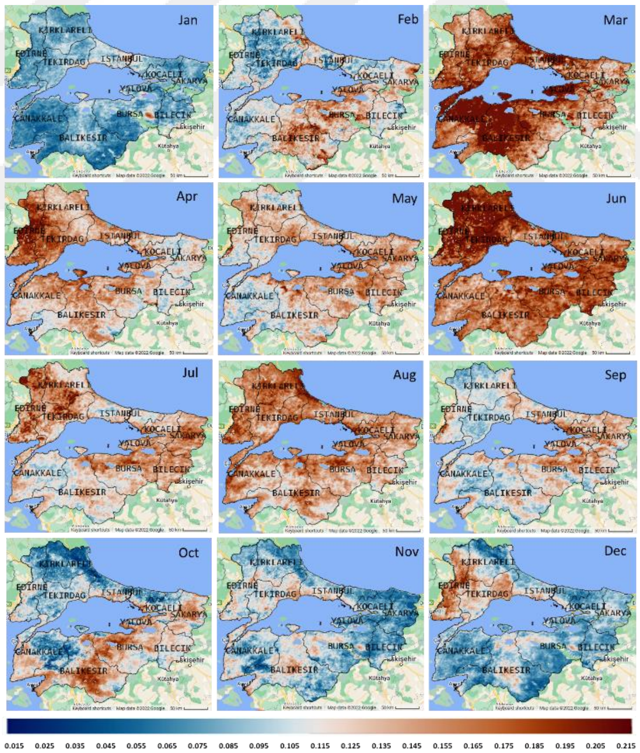

Figure A.8 : Monthly averaged MODIS MAIAC AOD for 2007.

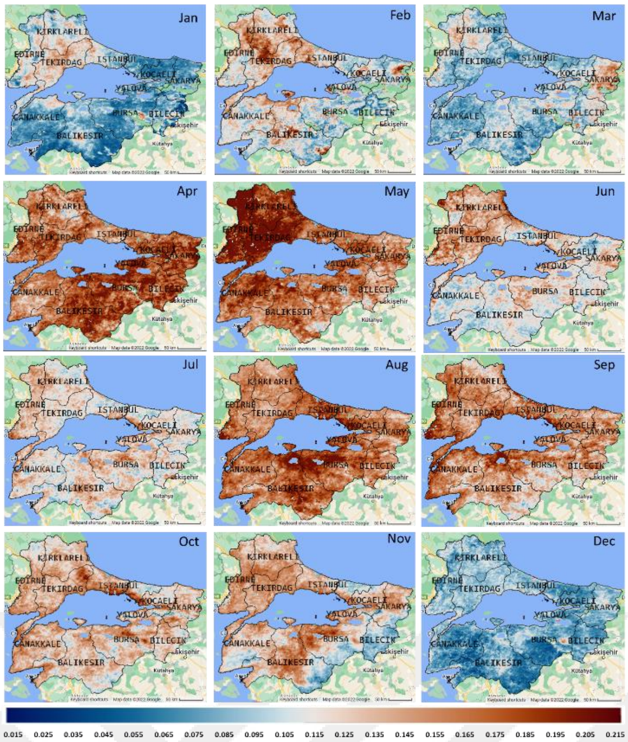

Figure A.9 : Monthly averaged MODIS MAIAC AOD for 2008.

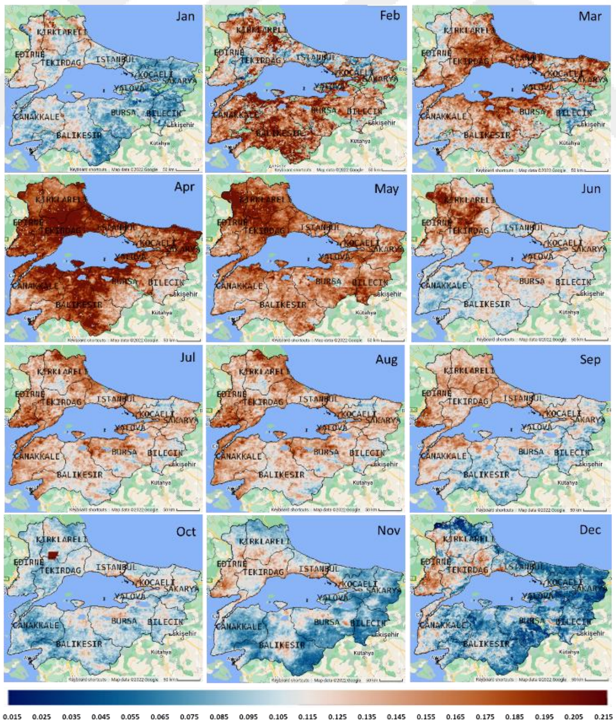

Figure A.10 : Monthly averaged MODIS MAIAC AOD for 2009.

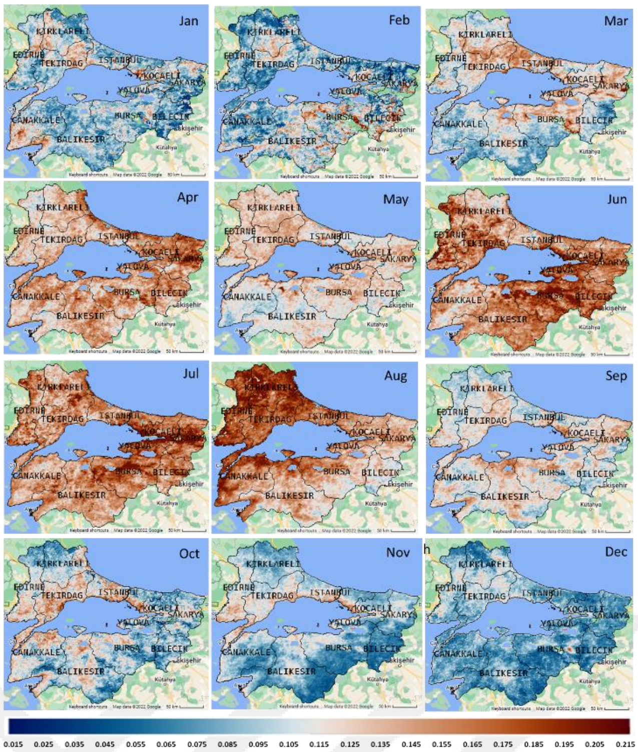

Figure A.11 : Monthly averaged MODIS MAIAC AOD for 2010.

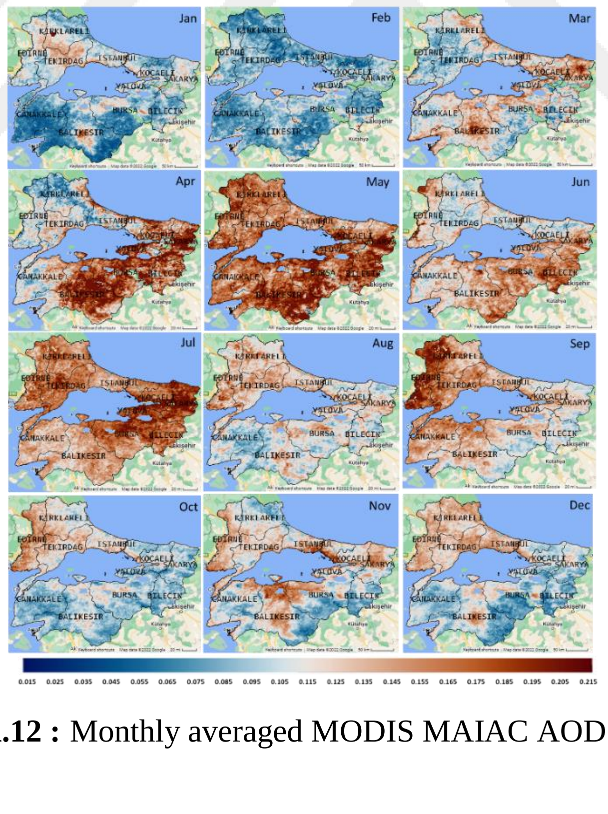

Figure A.12 : Monthly averaged MODIS MAIAC AOD for 2011.

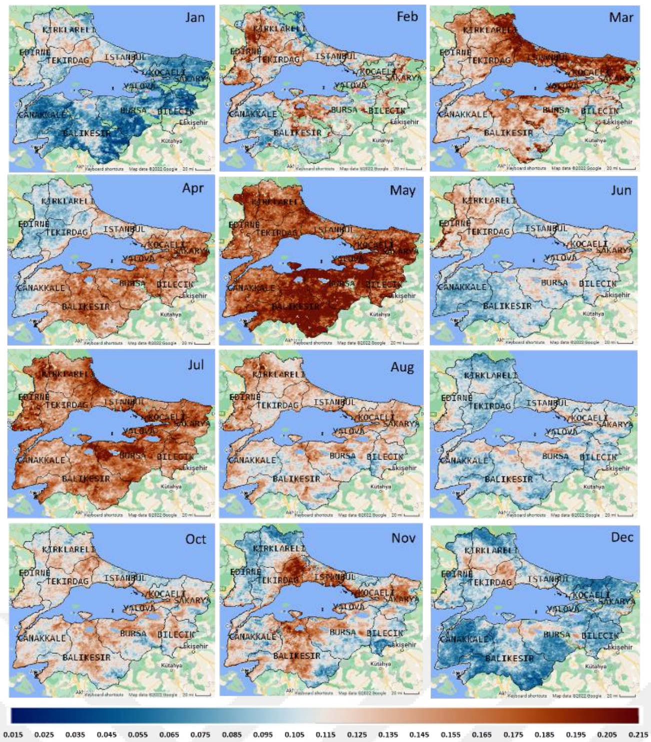

Figure A.13 : Monthly averaged MODIS MAIAC AOD for 2012.

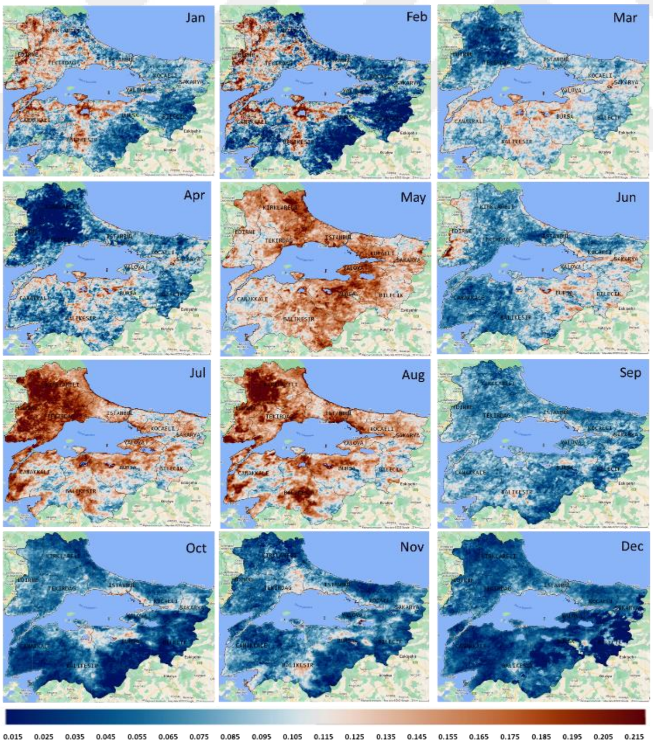

Figure A.14 : Monthly averaged MODIS MAIAC AOD for 2013.

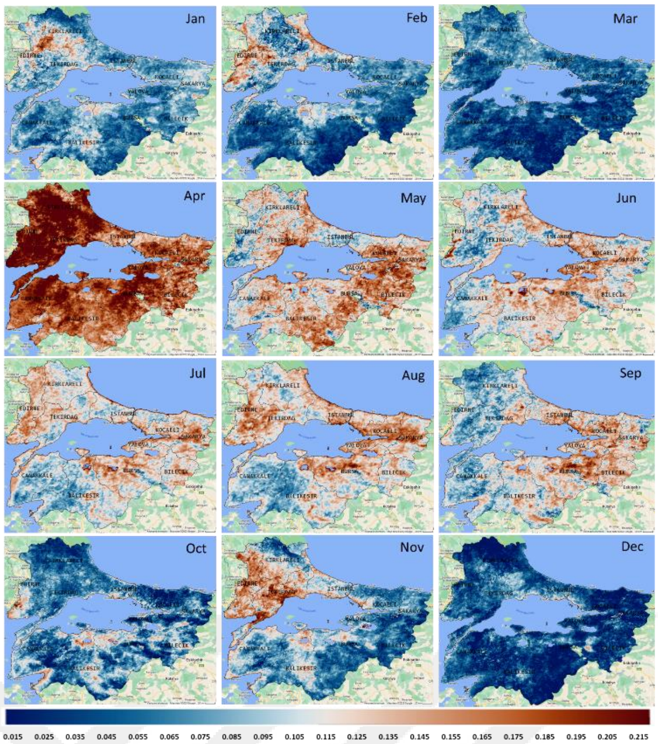

Figure A.15 : Monthly averaged MODIS MAIAC AOD for 2014.

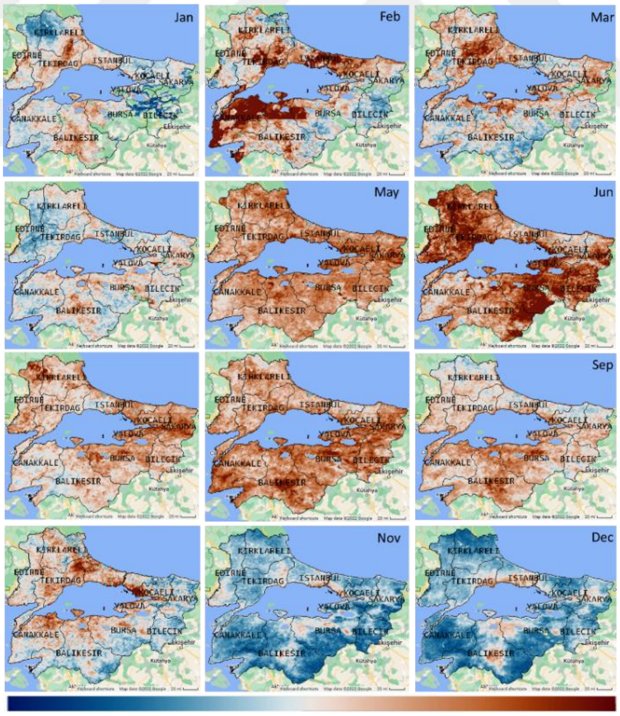

Figure A.16 : Monthly averaged MODIS MAIAC AOD for 2015.

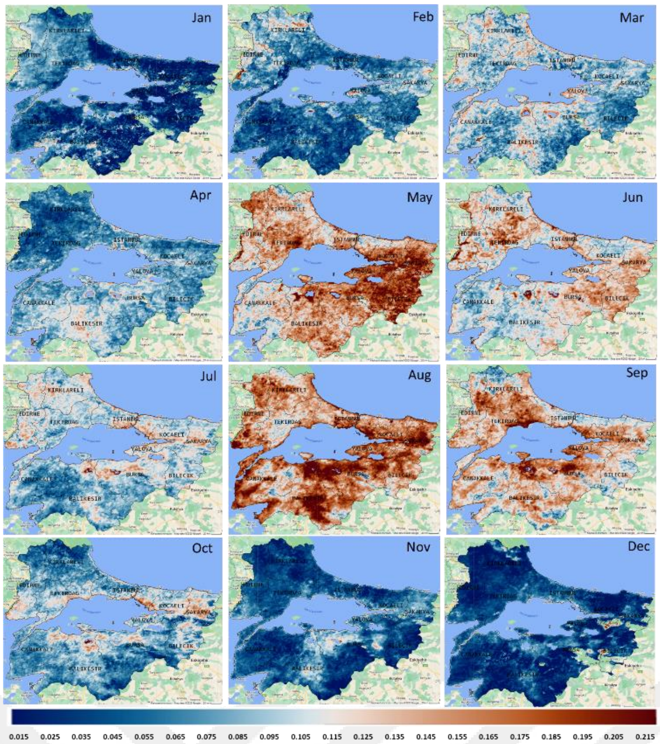

Figure A.17 : Monthly averaged MODIS MAIAC AOD for 2016.

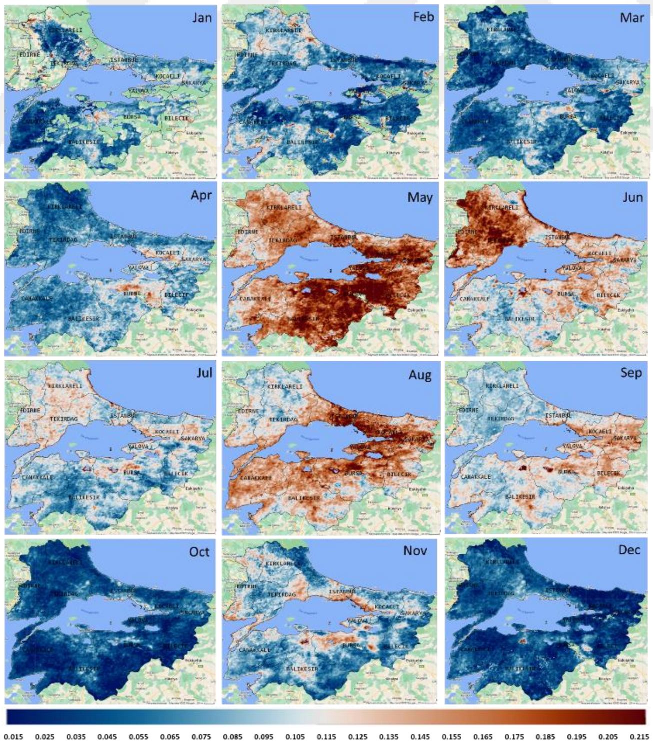

Figure A.18 : Monthly averaged MODIS MAIAC AOD for 2017.

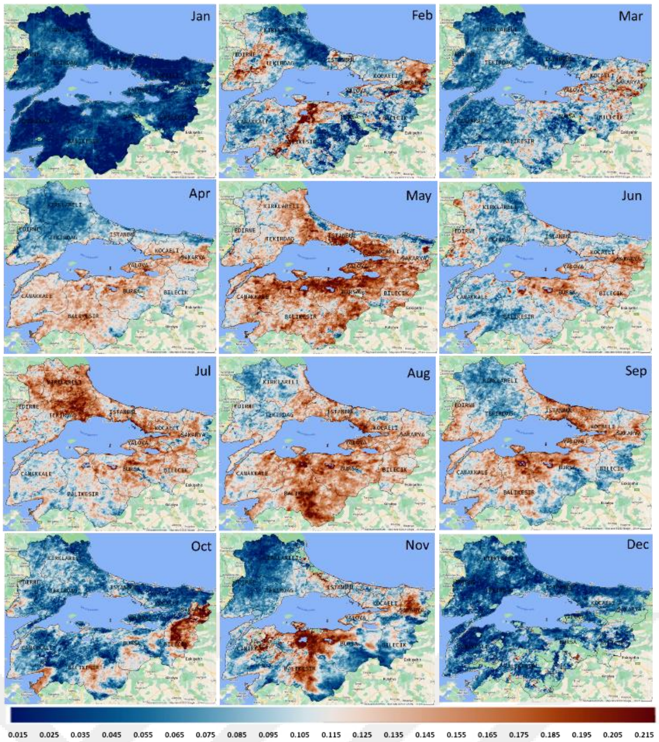

Figure A.19 : Monthly averaged MODIS MAIAC AOD for 2018.

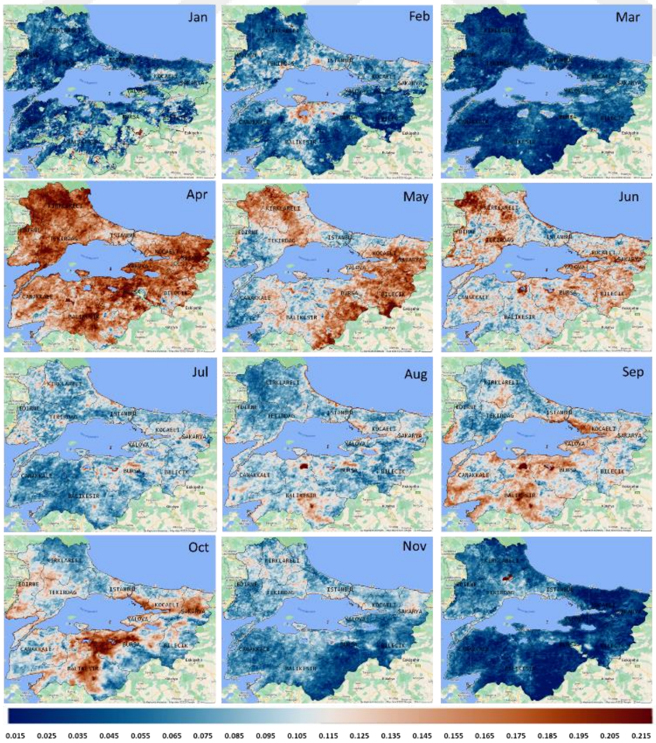

Figure A.20 : Monthly averaged MODIS MAIAC AOD for 2019.

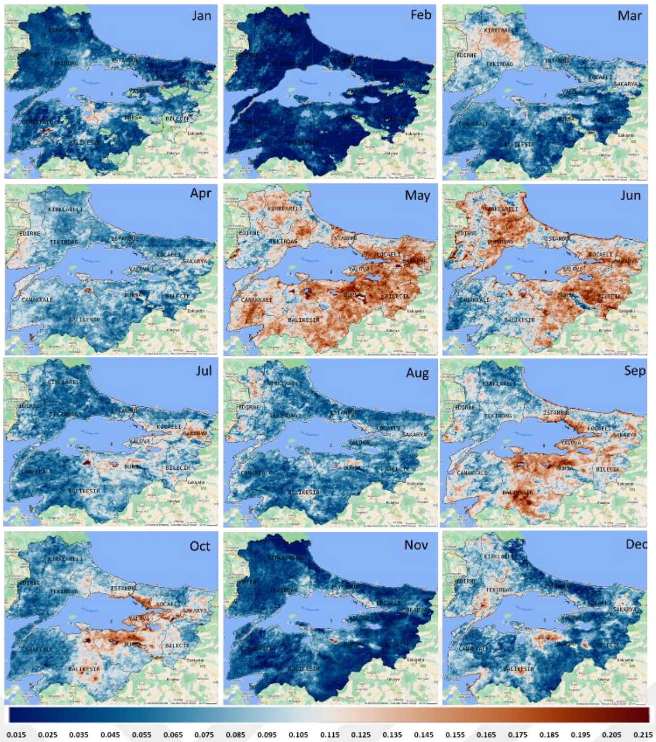

Figure A.21 : Monthly averaged MODIS MAIAC AOD for 2020.

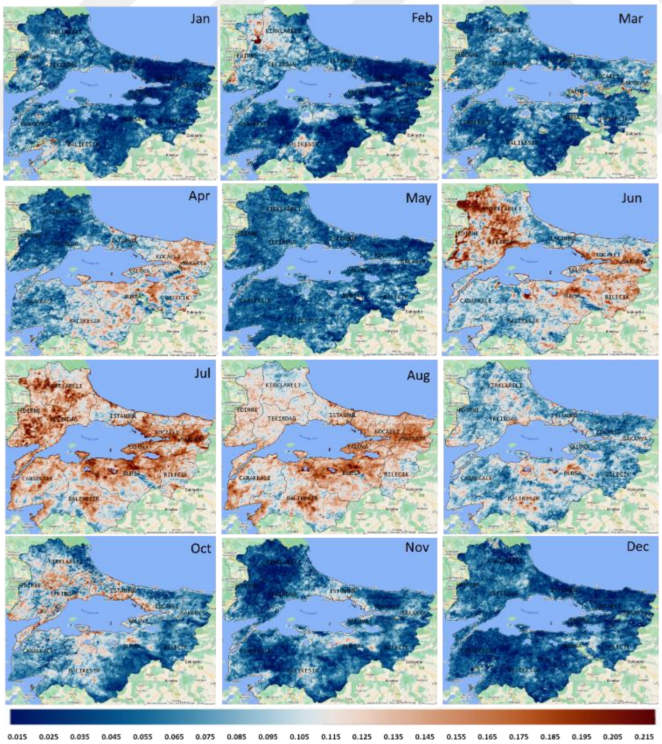

Figure A.22 : Monthly averaged MODIS MAIAC AOD for 2021.

APPENDIX B

Table B.1 : Annual variation of aerosol pollution levels in Bursa (2000-2021).

Year	Percentage statistics Level 1 %	Level 2 %	Level 3 %	Level 4 %	Year	Percentage statistics Level 1 %	Level 2 %	Level 3 %	Level 4 %
2000	36.4	35.98	21.76	5.86	2011	28.57	46.94	19.05	5.44
2001	34.09	42.8	15.91	7.2	2012	27.15	49.34	17.55	5.96
2002	34.09	42.8	15.91	7.2	2013	33.99	43.79	16.99	5.23
2003	26.32	41.75	24.56	7.37	2014	26.85	45.3	19.46	8.39
2004	30.61	43.2	19.73	6.46	2015	27.45	45.42	20.92	6.21
2005	27.15	42.27	22.34	8.25	2016	31.65	43.04	18.99	6.33
2006	28.67	43.67	20.67	7	2017	25.99	38.49	26.97	8.55
2007	28.7	42.9	19.44	8.95	2018	25.66	38.49	26.97	8.88
2008	29.47	41.39	20.86	8.28	2019	33.88	41.45	20.07	4.61
2009	27.42	44.82	20.74	7.02	2020	35.63	41.88	15.31	7.19
2010	28.91	45.24	18.71	7.14	2021	29.44	48.39	18.55	3.63

Table B.2 : Annual variation of aerosol pollution levels in Sakarya (2000-2021).

Year	Percentage statistics Level 1 %	Level 2 %	Level 3 %	Level 4 %	Year	Percentage statistics Level 1 %	Level 2 %	Level 3 %	Level 4 %
2000	33.8	31.48	24.54	10.19	2011	26.24	43.73	20.91	9.13
2001	34.19	38.89	18.38	8.55	2012	26.74	43.96	19.78	9.52
2002	27.34	32.03	30.86	9.77	2013	36.46	43.32	14.44	5.78
2003	27.34	42.97	21.48	8.2	2014	25.75	42.16	25	7.09
2004	29.12	47.13	17.62	6.13	2015	26.57	43.17	24.35	5.9
2005	27.82	37.5	24.6	10.08	2016	29.23	44.62	19.62	6.54
2006	27.55	43.02	21.13	8.3	2017	32.08	41.51	18.87	7.55
2007	31.16	41.44	19.86	7.53	2018	27.24	35.82	28.73	8.21
2008	30.51	39.34	23.9	6.25	2019	29.93	43.07	18.25	8.76
2009	32.95	43.18	17.05	6.82	2020	37.55	40.79	14.44	7.22
2010	27.69	45	20.38	6.92	2021	30.49	45.74	19.28	4.48

Table B.3 : Annual variation of aerosol pollution levels in Bilecik (2000-2021).

	Percentage statistics					Percentage statistics			
Year	Level 1 %	Level 2 %	Level 3 %	Level 4 %	Year	Level 1 %	Level 2 %	Level 3 %	Level 4 %
2000	38.1	40.48	15.71	5.71	2011	36.33	37.83	18.73	7.12
2001	38.86	39.3	15.72	6.11	2012	30.55	45.09	19.27	5.09
2002	30.19	37.74	24.15	7.92	2013	41.11	42.51	12.54	3.83
2003	29.46	44.57	15.5	10.47	2014	31.07	40	21.43	7.5
2004	37.21	38.37	17.44	6.98	2015	34.6	39.92	19.01	6.46
2005	35.34	41.77	17.27	5.62	2016	34.08	40.82	20.97	4.12
2006	32.82	41.6	20.23	5.34	2017	35.16	36.26	20.51	8.06
2007	32.07	43.45	18.97	5.52	2018	28.52	40.43	22.02	9.03
2008	30.39	44.52	18.73	6.36	2019	36.82	39.35	17.33	6.5
2009	34.94	42.38	16.73	5.95	2020	41.07	34.29	19.64	5
2010	33.07	43.58	18.29	5.06	2021	32.9	44.59	18.18	4.33

Table B.4 : Annual variation of aerosol pollution levels in Tekirdag (2000-2021).

	Percentage statistics					Percentage statistics			
Year	Level 1 %	Level 2 %	Level 3 %	Level 4 %	Year	Level 1 %	Level 2 %	Level 3 %	Level 4 %
2000	29.58	40	20.83	9.58	2011	26.76	42.96	21.48	8.8
2001	32.1	42.8	17.7	7.41	2012	30.41	47.97	15.88	5.74
2002	29.41	39.34	21.69	9.56	2013	32.09	48.31	15.88	3.72
2003	21.82	42.18	24	12	2014	25.29	45.98	21.46	7.28
2004	25.43	42.27	21.65	10.65	2015	32.88	42.37	19.66	5.08
2005	28.1	43.43	21.17	7.3	2016	36.67	41	17	5.33
2006	27.3	41.49	21.63	9.57	2017	35.92	40.85	16.9	6.34
2007	30.87	36.58	22.15	10.4	2018	33.33	44.44	17.04	5.19
2008	29.11	40.75	19.86	10.27	2019	36.7	39.06	18.52	5.72
2009	25.54	43.88	20.5	10.07	2020	45.27	35.14	12.84	6.76
2010	28.46	41.95	23.22	6.37	2021	31.98	44.53	18.22	5.26

Table B.5 : Annual variation of aerosol pollution levels in Kirklareli (2000-2021).

	Percentage statistics					Percentage statistics			
Year	Level 1 %	Level 2 %	Level 3 %	Level 4 %	Year	Level 1 %	Level 2 %	Level 3 %	Level 4 %
2000	32.77	34.03	21.85	11.34	2011	30	39.64	21.43	8.93
2001	33.33	37.04	19.34	10.29	2012	31.65	41.75	18.18	8.42
2002	26.82	39.85	20.69	12.64	2013	33.78	43.24	18.92	4.05
2003	27.82	40.14	21.48	10.56	2014	27.03	42.86	20.08	10.04
2004	27.17	39.13	24.28	9.42	2015	36.99	37.67	18.15	7.19
2005	24.44	45.56	22.22	7.78	2016	37.09	40.4	16.89	5.63
2006	29.18	45.55	18.15	7.12	2017	39.93	37.05	15.83	7.19
2007	34.54	36.18	14.8	14.47	2018	37.77	41.37	12.23	8.63
2008	29.97	39.72	21.6	8.71	2019	35.25	41.69	17.29	5.76
2009	25.93	41.48	23.33	9.26	2020	45.18	34.55	13.29	6.98
2010	28.24	42.75	22.14	6.87	2021	35.92	40.82	17.96	5.31

Table B.6 : Annual variation of aerosol pollution levels in Canakkale (2000-2021).

	Percentage statistics					Percentage statistics			
Year	Level 1 %	Level 2 %	Level 3 %	Level 4 %	Year	Level 1 %	Level 2 %	Level 3 %	Level 4 %
2000	35.48	43.55	14.92	6.05	2011	34.33	47	15.33	3.33
2001	33.7	43.59	16.12	6.59	2012	37.22	45.31	13.92	3.56
2002	38.59	38.26	14.09	9.06	2013	39.87	46.2	9.18	4.75
2003	29.37	47.85	16.83	5.94	2014	31.77	47.49	15.38	5.35
2004	33.66	45.63	17.15	3.56	2015	33.76	51.27	11.46	3.5
2005	27.83	53.4	15.21	3.56	2016	41.43	42.37	11.84	4.36
2006	35.08	44.92	14.1	5.9	2017	44.05	39.55	13.18	3.22
2007	37.89	39.13	18.01	4.97	2018	31.49	46.75	16.88	4.87
2008	33.66	43.69	15.86	6.8	2019	41.31	40.98	14.43	3.28
2009	32.67	44.67	20	2.67	2020	48.75	35.63	11.25	4.38
2010	35.33	44	16	4.67	2021	35.4	46.72	13.14	4.74

Table B.7 : Annual variation of aerosol pollution levels in the Eastern side of Istanbul (2000-2021).

	Percentage statistics					Percentage statistics			
Year	Level 1 %	Level 2 %	Level 3 %	Level 4 %	Year	Level 1 %	Level 2 %	Level 3 %	Level 4 %
2000	33.49	42.45	16.98	7.08	2011	26.59	50.79	13.89	8.73
2001	35.78	44.5	14.22	5.5	2012	30.28	45.42	18.31	5.99
2002	28.4	42.8	18.8	10	2013	31.52	48.55	14.13	5.8
2003	24.42	47.29	19.38	8.91	2014	25.3	49.41	18.58	6.72
2004	27.88	44.24	21.19	6.69	2015	29.39	48.47	15.65	6.49
2005	28.46	45.06	18.18	8.3	2016	33.92	44.52	14.84	6.71
2006	26.95	42.19	22.27	8.59	2017	38.1	40.29	16.12	5.49
2007	30.39	42.4	18.37	8.83	2018	30.16	50	13.1	6.75
2008	27.74	47.08	16.06	9.12	2019	35.4	42.34	16.06	6.2
2009	25.48	46.01	19.77	8.75	2020	41.64	39.41	13.75	5.2
2010	28.85	44.66	20.55	5.93	2021	41.1	39.83	13.56	5.51

Table B.8 : Annual variation of aerosol pollution levels in the Western side of Istanbul (2000-2021).

	Percentage statistics					Percentage statistics			
Year	Level 1 %	Level 2 %	Level 3 %	Level 4 %	Year	Level 1 %	Level 2 %	Level 3 %	Level 4 %
2000	29.32	41.88	18.32	10.47	2011	27.35	49.15	16.24	7.26
2001	37.75	39.71	14.71	7.84	2012	28.95	46.24	18.05	6.77
2002	29.11	37.97	20.68	12.24	2013	39.46	39.08	15.71	5.75
2003	28.02	45.26	20.26	6.47	2014	29.17	44.58	19.17	7.08
2004	30.12	44.58	18.88	6.43	2015	33.04	43.04	12.61	11.3
2005	28.33	45.83	17.5	8.33	2016	36	40.8	18.4	4.8
2006	26.69	44.92	19.49	8.9	2017	41.22	35.92	17.96	4.9
2007	31.97	40.52	16.73	10.78	2018	28.95	39.04	23.68	8.33
2008	31.13	38.91	23.74	6.23	2019	34.78	41.9	18.18	5.14
2009	31.4	42.98	19.42	6.2	2020	41.08	37.34	16.18	5.39
2010	28.81	41.1	23.31	6.78	2021	37.96	39.35	18.06	4.63

Table B.9 : Annual variation of aerosol pollution levels in Kocaeli (2000-2021).

	Percentage statistics					Percentage statistics			
Year	Level 1 %	Level 2 %	Level 3 %	Level 4 %	Year	Level 1 %	Level 2 %	Level 3 %	Level 4 %
2000	35.12	34.15	22.93	7.8	2011	27.89	47.81	15.14	9.16
2001	41.18	33.03	18.1	7.69	2012	26.3	46.3	18.89	8.52
2002	26.1	37.75	24.5	11.65	2013	39.41	37.92	17.1	5.58
2003	27.82	41.94	21.37	8.87	2014	27.09	45.42	19.12	8.37
2004	31.23	45.45	15.81	7.51	2015	30.12	44.02	20.46	5.41
2005	26.94	39.18	24.49	9.39	2016	32.68	42.8	20.23	4.28
2006	23.65	50.62	17.43	8.3	2017	36.22	34.65	22.83	6.3
2007	31.77	39.71	19.13	9.39	2018	28.11	39.36	22.89	9.64
2008	30.97	38.81	23.51	6.72	2019	29.7	41.35	20.68	8.27
2009	31.5	43.7	18.9	5.91	2020	38.89	44.05	11.51	5.56
2010	28.51	43.37	19.68	8.43	2021	33.63	43.05	16.14	7.17

Table B.10 : Annual variation of aerosol pollution levels in Yalova (2000-2021).

	Percentage statistics					Percentage statistics			
Year	Level 1 %	Level 2 %	Level 3 %	Level 4 %	Year	Level 1 %	Level 2 %	Level 3 %	Level 4 %
2000	31.5	37.5	24	7	2011	26.45	49.59	17.77	6.2
2001	35.89	39.71	17.7	6.7	2012	27.27	45.85	19.76	7.11
2002	25.21	41.6	22.69	10.5	2013	32.69	44.23	16.92	6.15
2003	26.97	39.83	24.48	8.71	2014	24.58	49.58	18.33	7.5
2004	28.46	43.9	16.67	10.98	2015	27.09	45.42	22.31	5.18
2005	24.22	43.5	21.97	10.31	2016	28	45.2	20	6.8
2006	22.18	47.7	23.01	7.11	2017	33.47	41.74	18.18	6.61
2007	28.14	41.83	22.43	7.6	2018	24.57	45.26	20.69	9.48
2008	27.24	41.25	21.01	10.51	2019	29.72	46.18	16.87	7.23
2009	24.79	47.06	23.53	4.62	2020	35.16	46.88	13.67	4.3
2010	21.19	49.15	19.49	10.17	2021	27.14	50.95	18.1	3.81

Table B.11 : Annual variation of aerosol pollution levels in Balikesir (2000-2021).

	Percentage statistics					Percentage statistics			
Year	Level 1 %	Level 2 %	Level 3 %	Level 4 %	Year	Level 1 %	Level 2 %	Level 3 %	Level 4 %
2000	38.91	40.47	16.34	4.28	2011	29.19	50.62	15.53	4.66
2001	34.51	46.83	14.44	4.23	2012	27.27	45.85	19.76	7.11
2002	35.14	39.62	18.21	7.03	2013	35.63	47.50	13.44	3.44
2003	28.98	48.73	15.92	6.37	2014	27.76	51.42	15.14	5.68
2004	32.28	48.42	15.82	3.48	2015	32.82	45.82	16.41	4.95
2005	28.57	53.02	14.92	3.49	2016	36.58	44.25	13.86	5.31
2006	35.09	45.96	14.91	4.04	2017	37.27	40.91	19.39	2.42
2007	31.07	45.86	16.86	6.21	2018	26.56	44.38	21.88	7.19
2008	27.69	50.15	16.92	5.23	2019	36.83	41.90	15.87	5.40
2009	28.57	51.75	15.24	4.44	2020	41.14	40.84	13.51	4.50
2010	32.17	51.27	14.65	1.91	2021	35.29	45.59	15.44	3.68

Table B.12 : Annual variation of aerosol pollution levels in Edirne (2000-2021).

	Percentage statistics					Percentage statistics			
Year	Level 1 %	Level 2 %	Level 3 %	Level 4 %	Year	Level 1 %	Level 2 %	Level 3 %	Level 4 %
2000	27.02	37.90	22.98	12.10	2011	27.27	41.96	18.18	12.59
2001	28.23	39.11	20.97	11.69	2012	30.23	40.51	21.54	7.72
2002	24.18	41.39	20.51	13.92	2013	30.56	47.84	16.28	5.32
2003	23.53	39.45	23.18	13.84	2014	24.10	43.88	24.46	7.55
2004	26.21	41.03	22.41	10.34	2015	34.19	40.00	20.65	5.16
2005	21.84	50.17	19.45	8.53	2016	34.29	42.54	17.46	5.71
2006	26.16	42.65	20.79	10.39	2017	36.52	38.91	19.11	5.46
2007	29.15	37.62	17.24	15.99	2018	40.42	41.81	13.94	3.83
2008	25.99	44.74	21.38	7.89	2019	36.39	41.97	15.41	6.23
2009	27.21	42.05	22.61	8.13	2020	40.76	40.45	14.33	4.46
2010	26.91	45.82	18.91	8.36	2021	33.07	41.25	18.29	7.39

CURRICULUM VITAE

Name Surname : Paria ETTEHADI OSGOUEI

EDUCATION:

- **B.Sc.:** 2010, Tabriz Azad, Faculty of Engineering, Department of Computer Engineering (Information technology engineering)
- **M.Sc. :** 2014, ITU, Informatic instititute, Communication systems Department (Satellite communication and remote sensing)

PUBLICATIONS, PRESENTATIONS AND PATENTS ON THE THESIS:

Papers

- **Ettehadi Osgouei, P.;** Kaya, S.; Sertel, E; Alganci U. (2019). Separating Built-Up Areas from Bare Land in Mediterranean Cities Using Sentinel-2A Imagery. Remote Sens. 2019, 11 (3), 345.
- **Ettehadi Osgouei, P.;** Roberts, G.; Kaya, S.; Bilal, M.; Dash, J.; Sertel, E. (2022) Evaluation and comparison of Modis and Viirs Aerosol Optical Depth (AOD) products over regions in the Eastern Mediterranean and the Black Sea. Atmos. Environ. 2022, 268, 118784.

Conferences

- **Ettehadi Osgouei, P.;** Kaya, S.; Sertel, E;, (2019). Evaluation of Satellite AOD Observations for Monitoring Air Quality. International Symposium on Applied Geoinformatics (ISAG-2019), Volume 1 - No. 1, ISBN: 978-975- 461-564-7/2019, pages: 291/614.
- **Ettehadi Osgouei, P.;** Kaya, S.; Sertel, E; Alganci U. (2019). Improved Urban Land Cover/Use Mapping Using Sentinel-2A Imagery. International Symposium on Applied Geoinformatics (ISAG-2019), Volume 1 - No. 1, ISBN: 978-975-461-564-7/2019, pages: 296/614

OTHER PUBLICATIONS, PRESENTATIONS AND PATENTS:

- Kaya, S.; **Ettehadi Osgouei, P.**; Alganci, U.; Seker, D.Z.; Gazioglu, C., (2015). Evaluation of vegetation density changes in suburban area: A case study of Istanbul metropolitan area. Asian Association on Remote Sensing.
- **Ettehadi Osgouei, P.;** Sertel, E; Kabadayı M. E. (2022). Integrated usage of historical geospatial data and modern satellite images reveal long-term land use/cover changes in Bursa/Turkey, 1858–2020. Sci Rep 12, 9077 (2022). https://doi.org/10.1038/s41598-022-11396-1

- Kabadayı M. E.; **Ettehadi Osgouei, P.;** Sertel, E; (2022). "Agricultural Land Abandonment in Bulgaria: A Long-Term Remote Sensing Perspective, 1950–1980" Land 11, no. 10: 1855. https://doi.org/10.3390/land11101855.
- Sertel, E; Ekim B.; **Ettehadi Osgouei, P.;** Kabadayı M. E. (2022). "Land Use and Land Cover Mapping Using Deep Learning Based Segmentation Approaches and VHR Worldview-3 Images" Remote Sensing 14, no. 18: 4558. https://doi.org/10.3390/rs14184558.